THE EFFECTS OF DOPING AND PROCESSING ON THE THERMOELECTRIC PROPERTIES OF PLATINUM DIANTIMONIDE BASED MATERIALS FOR CRYOGENIC PELTIER COOLING APPLICATIONS

By

Spencer Laine Waldrop

A DISSERTATION

Submitted to
Michigan State University
in partial fulfillment of the requirements
for the degree of

Materials Science and Engineering — Doctor of Philosophy

2017

ABSTRACT

THE EFFECTS OF DOPING AND PROCESSING ON THE THERMOELECTRIC PROPERTIES OF PLATINUM DIANTIMONIDE BASED MATERIALS FOR CRYOGENIC PELTIER COOLING APPLICATIONS

By

Spencer Laine Waldrop

The study of thermoelectrics is nearly two centuries old. In that time a large number of applications have been discovered for these materials which are capable of transforming thermal energy into electricity or using electrical work to create a thermal gradient. Current use of thermoelectric materials is in very niche applications with contemporary focus being upon their capability to recover waste heat. A relatively undeveloped region for thermoelectric application is focused upon Peltier cooling at low temperatures. Materials based on bismuth telluride semiconductors have been the gold standard for close to room temperature applications for over sixty years. For applications below room temperature, semiconductors based on bismuth antimony reign supreme with few other possible materials.

The cause of this difficulty in developing new, higher performing materials is due to the interplay of the thermoelectric properties of these materials. The Seebeck coefficient, which characterizes the phenomenon of the conversion of heat to electricity, the electrical conductivity, and the thermal conductivity are all interconnected properties of a material which must be optimized to generate a high performance thermoelectric material. While for above room temperature applications many advancements have been made in the creation of highly efficient thermoelectric materials, the below room temperature regime has been stymied by ill-suited properties, low operating temperatures, and a lack of research.

The focus of this work has been to investigate and optimize the thermoelectric properties of platinum diantimonide, $PtSb_2$, a nearly zero gap semiconductor. The electronic properties

of $PtSb_2$ are very favorable for cryogenic Peltier applications, as it exhibits good conductivity and large Seebeck coefficient below 200 K. It is shown that both n- and p-type doping may be applied to this compound to further improve its electronic properties. Through both solid solution formation and processing techniques, the thermal conductivity may be reduced in order to increase the thermoelectric figure of merit. Further reduction in thermal conductivity using other novel approaches is identified as an area of promising future research. Continued development of this material has the potential to generate a suitable replacement for some low temperature applications, but will certainly further scientific knowledge and understanding of the optimization of thermoelectric materials in this temperature regime.

I would like to dedicate this work to my family. Without their love, support, and encouragement this would not have been made.

ACKNOWLEDGMENTS

I am reminded and grateful for the many people who have played a role in helping me to this point in life. I would first like to thank my advisor Dr. Donald Morelli for allowing me this opportunity to study thermoelectrics these past four years, his thoughtfulness and guidance, and his willingness to allow me to explore any topic no matter how reaching it was. I would also like to thank my committee members Dr. Tim Hogan, Dr. Wei Lai, and Dr. Thomas Bieler for their assistance and direction.

I would like to thank my past and current lab mates, Dr. Gloria Lehr, Dr. Steve Boona, Dr. Xu Lu, Dr. Vijay Ponnambolam, Mr. Daniel Weller, and Mr. Spencer Mather for their help and insight. I would like to thank Dr. Dale Hitchcock for providing me a model of a graduate student and being my first research mentor. I would also like to thank Dr. Terry Tritt for first introducing and stirring in me an excitement and enthusiasm for solid state physics.

I also need to single out and thank two colleagues and friends who have had a very special role in helping me through these past four years. I'd like to thank Dr. Winston Carr for his never ending patience, insightful conversations spanning everything from thermoelectrics to economics, and, of course, the proper way to wear a beard. To Dr. Jared Williams I would like to thank him for his friendship these past six years. He was always there to offer insight or critique, to help with a hard problem or study for a test, to debate an issue or philosophize on end, and to offer a word of encouragement whenever it was needed.

I would also like to acknowledge and thank my family for their love and support through these four years. First, to my mother, who raised me to persevere through anything, value the small things in life, and know that we can make it through anything together. To my

father, who taught me how to slow down, to value honor, and to never turn back unless it's for a good night's rest. To my sister, who always had my back, but never forgot to teach me humility every chance she got. And finally, to my wife, who taught me to love life again and to always keep the child at heart.

Finally, I would like to acknowledge that this research was funded by the Air Force Office of Scientific Research under the Multi-University Research initiative (MURI), Cryogenic Peltier Cooling, Contract No. FA9550-10-1-0533.

TABLE OF CONTENTS

LIST OF TABLES

LIST OF FIGURES

Chapter 1

Introduction

1.1 Thermoelectric Effects

For over 150 years three effects of materials, the so-called thermoelectric effects, have been studied due to their potential for applications in everyday life. These effects allow for the targeted conversion of heat into electrical energy, or vice versa, electrical energy into heat.

Seminal to these effects is the Seebeck effect discovered in 1821 by Thomas Seebeck [1]. The Seebeck effect describes the generation of a voltage between the junctions of two dissimilar materials held at differing temperatures. This effect is best visualized in its application with thermocouples, as seen in Figure 1.1.

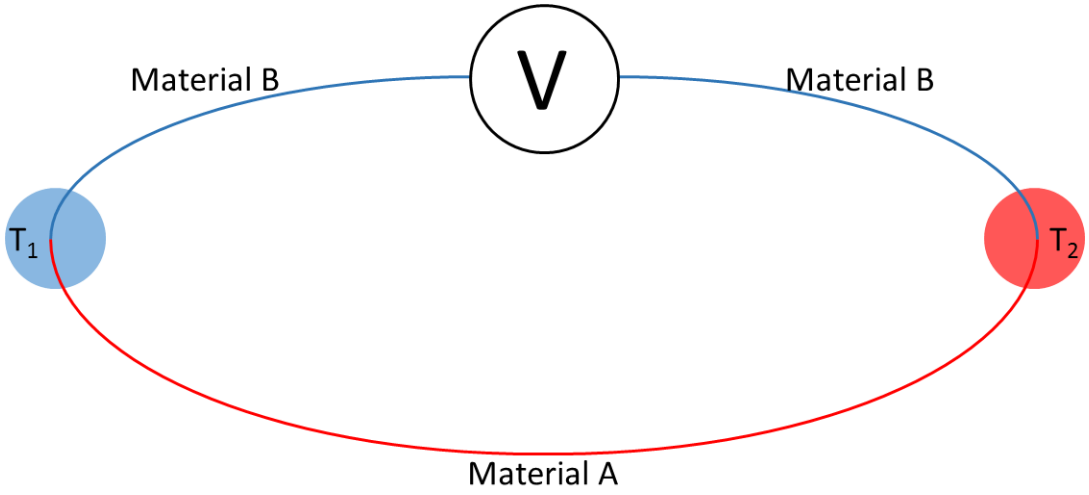

Figure 1.1: Schematic of thermocouple displaying Seebeck Effect

The Seebeck effect is governed by the movement of electrons in a material due to the occurrence of a temperature gradient across it. The additional thermal energy on one side of the material causes a net migration of the electrons in response to their increased momentum. Turning our attention back to the thermocouple in Figure 1.1 we can see how this effect generates a voltage. Depending upon the properties of material A and B their electrons will respond to the addition of thermal energy with differing magnitude and create a voltage potential. This effect is summarized by the equation:

$$\Delta V = -\alpha_{AB}\Delta T \tag{1.1}$$

where ΔV, is the voltage generated, α_{AB}, is the Seebeck coefficient of the additive contribution of the pair of materials A and B, and ΔT, the temperature difference. Each material will have a Seebeck coefficient dependent upon its own properties which will contribute to the overall parameter α_{AB}.

In what can be thought of as the inverse of the Seebeck effect is the Peltier effect, which

was discovered in 1834 by Jean Peltier [2]. Peltier found that when a current is passed between two dissimilar conjoined materials a cooling or heating effect is found at their junction. In 1838 when Lenz was able to freeze water or melt ice depending upon the direction of the current between two dissimilar materials he discovered the relationship between heat flow, the current, and a coefficient depending upon the material. This relationship is given by the equation:

$$\dot{Q} = (\Pi_A - \Pi_B)I \tag{1.2}$$

where $\dot{Q}$, is the heating or cooling generated, Π, is the Peltier coefficient, and I is the current. Direct measurement of the Peltier coefficient of a material presents difficulties due to irreversible heating processes that happen during this phenomenon.

Finally in 1854 William Thomson, known as Lord Kelvin, discovered the Thomson effect [3]. This reversible effect defines the heat absorbed or rejected by a material due to a parallel temperature gradient and current. This effect is given by the equation [4]:

$$\dot{q} = \tau_A I(dT/dx) \tag{1.3}$$

where $\dot{q}$ is the heat absorbed per unit length, τ_A is the Thomson coefficient, I is the current, and dT/dx is the temperature gradient. Thomson additionally, using thermodynamic arguments, was able to relate the Seebeck coefficient and the Peltier effect using the Onsager relationships [5]. One of the Kelvin relations is given by the equation:

$$\tau_A - \tau_B = T(d\alpha_{AB}/dT) \tag{1.4}$$

which gives the relation between the Thomson coefficient and the differential of the Seebeck coefficient at a temperature. The other Kelvin relation is much more applicable to experimental work and gives the relation between the Seebeck coefficient and the Peltier coefficient:

$$\Pi_{AB} = \alpha_{AB} T \tag{1.5}$$

This relation allows for the conversion between the much easier to measure quantity α and the Peltier coefficient.

The relations and equations above have all been dependent upon the junction of two dissimilar materials, A and B, but it is advantageous to express these relations as dependent upon only one material. To this effect superconducting materials, which have a Seebeck coefficient of zero, have been utilized as a reference to determine the Seebeck coefficient for a single material. In this manner standardized values have been determined for many materials, against which an unknown Seebeck coefficient can be measured.

1.2 Application of the Thermoelectric Effects

The thermoelectric effects can be utilized for numerous applications. The most widely used, thermocouples, allows for the accurate measurement of temperatures across a wide range depending upon the materials utilized. In 1909 and 1911 Altenkirch derived the maximimum efficiency of thermoelectric power generators and coolers [6, 7] and in 1954 Julian H. Goldsmid opened up the possibility of using semiconductors as coolers, paving the way for further research in the field [5]. While the research and development of thermoelectric power generators and coolers has had periods where little progress took place, this area is now the

most widely researched in the thermoelectric effects.

1.2.1 Power Generation

The vast majority of thermoelectric device research is directed towards the recovery of waste heat. This is due to the need of increased energy sustainability and environmental consciousness in our future world. As a growing number of global entities industrialize and expand, the energy usage of prior global power users has remained nearly constant which is supporting this drive for increasing power generated through renewable means [8, 9]. This pressure for increased energy usage from industrialization is further fueled in relation to the expectation of an increased global population [10, 11]. With this increased energy usage much, if not a majority, of the energy produced will be wasted as rejected heat. Thermoelectric power generation modules make it possible for a fraction of this rejected heat to be harvested and recirculated resulting in a significant potential reduction in the amount of total energy production required.

Recovery of waste heat from the exhaust of automobiles is a potential application which has garnered a significant amount of interest. This application would increase the gas mileage of vehicles by removing the need for an alternator, which generates electricity for the vehicle by sapping energy produced by the engine [12, 13]. However, this application has several disadvantages and an analysis of them highlights the many applications where thermoelectric power generators are better applied. Thermoelectric power generators are solid state devices without any moving parts, are scalable in size, and are extremely reliable in a steady state environment free of vibration. The majority of vehicles are however constantly in a state of flux, either heating up or cooling down due to being used multiple times a day and are also prone to the occasional sudden stop and ever constant vibrations. Putting aside the

diminished efficiency of thermoelectric generators outside of their peak temperature, the mechanical turbulence of a typical car ride and constant thermal cycling demonstrate how ill-suited thermoelectric generators are for vehicles.

Examining the drawbacks of generators in automobiles highlights the applications for which thermoelectric power generators are best suited: an environment where a constant temperature is maintained and is free of vibrations. Two applications where this environment may be found are in industrial power plants and in satellites using a radioisotope generator [14]. Satellites using radioisotope generators are an excellent example of the long term reliability of thermoelectric devices with the Voyager I and II spacecraft having operated for almost 50 years [15]. Several other applications of thermoelectric power generators, (i.e. wrist watches, cardiac pacemakers, recreational gear, etc.), have the potential for use in the future if the efficiency of these devices can be improved.

1.2.2 Peltier Cooling

The application of thermoelectric devices upon which this work is focused is in Peltier cooling. Peltier cooling utilizes the Peltier effect to generate a heat absorption on one side of a thermoelectric device that can offer targeted and precise refrigeration with all of the advantages which were highlighted for power generators. Other advantages of Peltier cooling devices are their low weight and small size when compared to mechanical cryocoolers. Mechanical cryocoolers are generally large, heavy devices which generate significant vibrations. Thus, for many applications, the use of these mechanical cryocoolers creates unsuitable operating conditions, (i.e. vibrations on an electronic component), or substantially increases the weight or space requirements of the application.

An exciting application of Peltier cooling is in the refrigeration of infrared focal plane

array detectors. Much of the impetus for this research has been for military usage in missile defense and forward looking infrared detectors [16]. For such applications reliability is of the utmost importance which lends some credence to using a Peltier cooler due to their inherent reliability. These detectors use materials such as HgCdTe, InSb, InGaAs, and VO_x, (Vandaium Oxide), with bandgap energies in the range of electromagnetic radiation such that an incident infrared photon will cause an electron hole pair to be generated in the material which creates the signal in these devices [17–19]. These detectors, however, need to be cooled to the tens of Kelvins such that the ratio of noise to signal is minimized. This noise is termed, "dark current", because an aberrant signal is generated not from an incident photon, but due to thermal excitation, which is why thermal energy must be kept within an acceptable range in these detectors [20].

Several other possible applications of Peltier coolers lie in spot cooling of X-ray astronomy detectors, laser equipment, medical equipment and transport, consumable food, residential and industrial electronics, and in heat generating mechanical processing machines [21]. However, as with the applications of thermoelectrics for power generation, Peltier cooling is also dependent upon the improvement of the efficiency or coefficient of performance, a metric of the cooling power of a device in ratio with the power it requires, of these devices [22].

1.3 Thermoelectric Device Performance

Both Peltier coolers and power generators have a similar device schematic, shown in Figure 1.2.

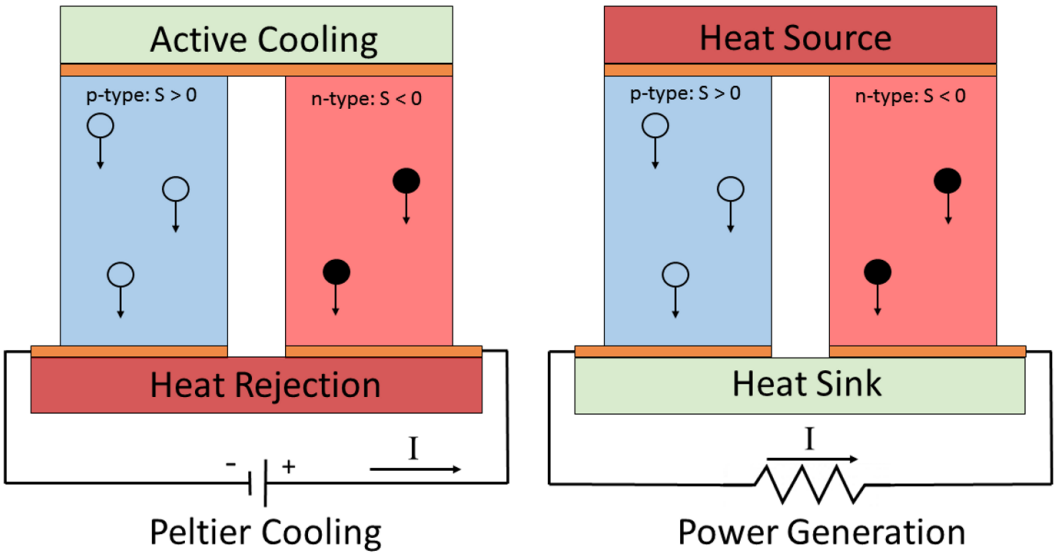

Figure 1.2: Schematic of Peltier Cooler and Thermoelectric Power Generator

As can be seen from the figure both devices consist of p- and n-type legs that are connected electrically via a metal connector with an insulating layer between heat source and sink. This allows for the thermoelectric legs to be electrically in series while thermally in parallel [23]. The distinction between p- and n-type materials is due to their dominant charge carrier which gives rise to a positive Seebeck coefficient in the p-type material and a negative Seebeck coefficient in the n-type material; the specific arrangement of n- and p-legs in series allows for a current to flow. A further description of p- and n-type materials is given in the following section.

In examining the Peltier cooler a standard thermodynamic metric for evaluating the performance of a cooler is the coefficient of performance, (COP), ϕ, which is a metric defined by the ratio of cooling performed to the electrical power input [24]. The cooling power, Q_c, is a result of the Peltier effect transporting thermal energy through the material, a backward flow of thermal energy through the material limited by the thermal conductivity of the

material, and approximately half of the joule heating due to a current passing through the leg. The equation that defines this is:

$$Q_c = (\alpha_p - \alpha_n)IT_c - K\Delta T - \frac{1}{2}I^2R \tag{1.6}$$

Where I is the current input, T_c is the cold side temperature, K is the thermal conductance of the legs, ΔT is the temperature differential across the legs, and R is the electrical resistance of the legs.

The power supplied to perform the cooling, W, is simply the electrical power: P=IV. The voltage supplied is composed of two parts; the part to overcome the Seebeck voltage generated by a temperature differential across the material and the part to overcome the electrical resistance of the leg:

$$W = IV = I[(\alpha_p - \alpha_n)\Delta T - IR] \tag{1.7}$$

The COP of a device is then:

$$\phi = \frac{Q_c}{W} = \frac{(\alpha_p - \alpha_n)IT_c - K\Delta T - \frac{1}{2}I^2R}{I[(\alpha_p - \alpha_n)\Delta T - IR]} \tag{1.8}$$

Several device optimization parameters can be solved for using equations 1.6 - 1.8, such as the current to be used for maximum cooling power or the maximum ΔT that can be generated given a set of material properties [25, 26].

$$Q_{max} = \frac{\alpha^2 T^2}{2R} \tag{1.9}$$

$$\Delta T_{max} = \frac{ZT_c^2}{2} \tag{1.10}$$

Using an optimal current input the ϕ_{max} can be obtained:

$$\phi_{max} = \frac{T_c}{\Delta T} \frac{\sqrt{1 + ZT_{Avg}} - \frac{T_h}{T_c}}{\sqrt{1 + ZT_{Avg}} + 1} \tag{1.11}$$

where the figure-of-merit, Z, for the thermoelectric module is used, which is distinct from the often cited thermoelectric material figure-of-merit z. It is found that as Z increases the COP also increases, Figure 1.3, thus Z, which is only dependent upon properties of the materials used, should be attempted to be maximized [4].

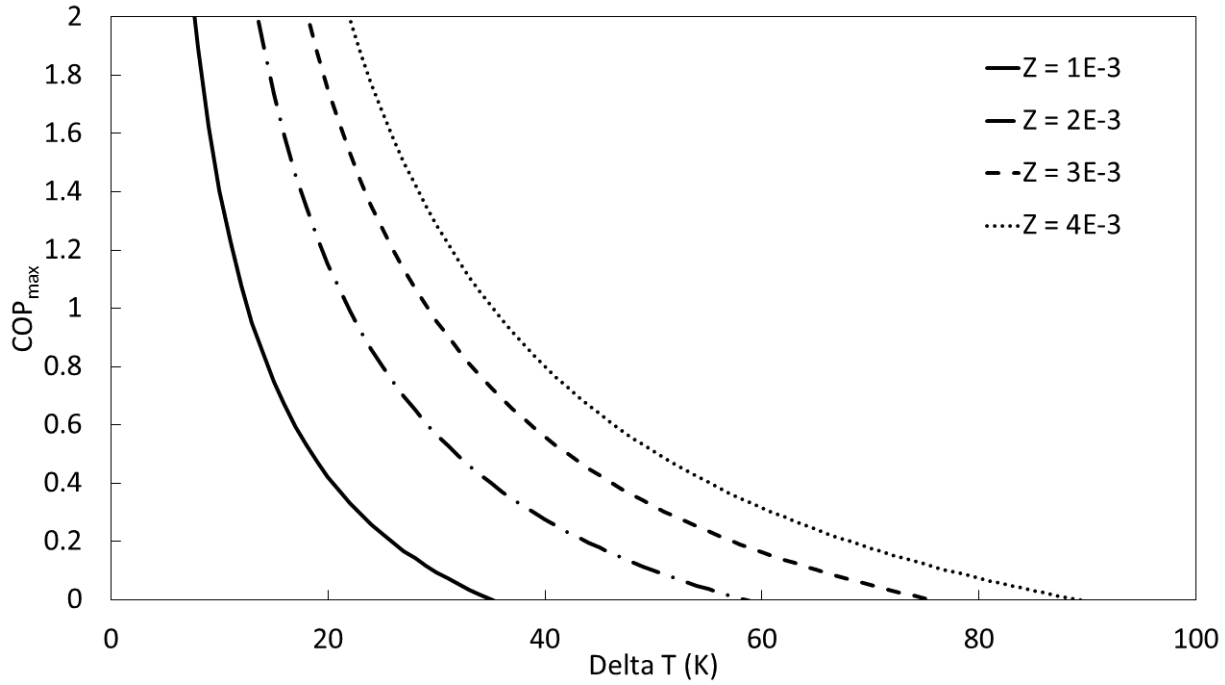

Figure 1.3: COP vs. Delta T with Hot Side Temperature of 300 K

In the development and engineering of new materials to be used in Peltier coolers, and thermoelectric devices in general, it would be quite cumbersome to use the Z for the thermoelectric module to compare and quantify the potential of individual materials. It is therefore

advantageous to define a material specific figure-of-merit z [27]:

$$z = \frac{\alpha^2 \sigma}{\kappa} \tag{1.12}$$

Where σ is the electrical conductivity, ($\rho = 1/\sigma$, the electrical resistivity), and κ is the thermal conductivity. The thermoelectric module Z is found to be a rather complicated mean of the two z's of the legs and further complicating study, contact resistances can be included resulting in a reduced effective Z. Additionally, the geometry of the legs should be optimized by the equation [24]:

$$\frac{l_p S_n}{l_n S_p} = \left(\frac{\sigma_p \kappa_p}{\sigma_n \kappa_n} \right)^{1/2} \tag{1.13}$$

where l is the length of the leg and S is the cross-sectional area. When the thermoelectric properties of both the p- and n-type materials are similar, Z is effectively the mean of z of the legs and materials can be optimized separately, but when the properties begin to differ these geometric arguments begin to play a more important role. This effect can become so large that at extremely low temperatures a superconducting material may be better suited for one of the legs than the typical semiconductor [23].

In the above description the so called thermoelectric properties α, σ, and κ have been assumed to be constant with temperature, however this is not the case in real materials and devices. Thus, it is helpful to examine a material at a mean operating temperature, which then gives a unitless figure-of-merit, zT:

$$zT = \frac{\alpha^2 \sigma}{\kappa} T_M \tag{1.14}$$

As a result of the dependence on average operating temperature of maximized Z, and therefore maximum ΔT of cooling, a Peltier cooler would only be applicable for a small range of temperatures. To tackle this issue thermoelectric modules may be cascaded such that multiple layers of modules can be tailored for maximum COP in a specific ΔT range and an overall increased ΔT can be achieved [28]. The main drawback to this system is that with each subsequent stage there is an increased cooling load required with not only the heat from the source, but also the heat generated from the preceding stages. In addition to generating a greater temperature drop across the module a multi-staged cascade may be used to increase the COP of a module [29]. If the COP of each stage is assumed to be the same the overall COP of the module may be given as [24]:

$$\phi_N = \frac{1}{(1+1/\Phi)^N - 1} \quad \text{where} \quad \Phi = N(\phi + 1/2) - \frac{1}{2} \tag{1.15}$$

It is found in practical use that for the majority of applications a two stage module is sufficient instead of increased spending on larger cascade modules as shown in Figure 1.4 [30]. It is additionally found that for temperature decreases that are well below the maximum ΔT that a single staged module is sufficient, but when the necessary temperature drop approaches the maximum then a two stage cascade may increase the overall COP greatly.

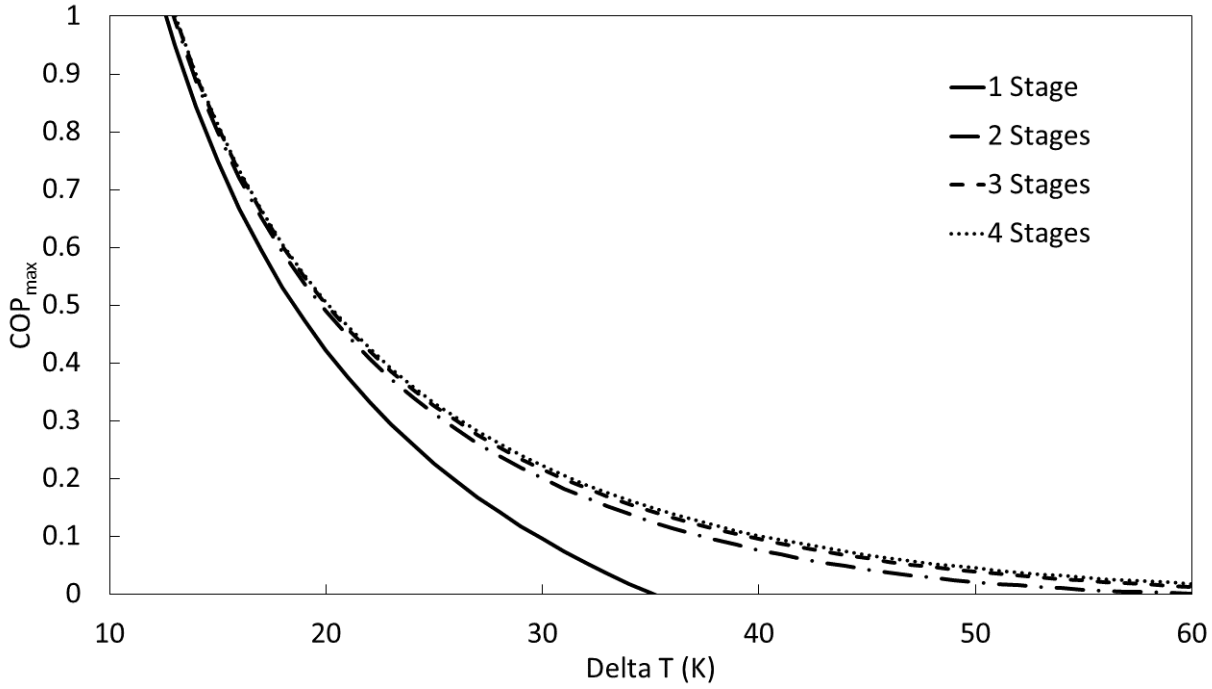

Figure 1.4: Multi-Stage Device COP vs. Delta T with Hot Side Temperature of 300 K and Z of 10^{-3} K

1.4 Electronic Transport

While the three thermoelectric effects, Seebeck, Peltier, and Thomson effect allow for the use of thermoelectric coolers and power generators, they are not the only properties of interest in the search for increased zT. These other parameters include the electrical conductivity, σ and the thermal conductivity, K. This section will attempt to establish a base of information on the properties of a material that determine the zT and ultimately how those properties may be manipulated such that more effective and efficient devices may be created.

1.4.1 Energy-Band Diagrams and Material Types

The Drude model presented by Paul Drude in 1900 predicts the motion of electrons based upon a kinetic gas theory [31]. It is a classical model where the electrons are imagined as

a sea of charges interacting with only the ionic cores of atoms and acted on by an electric field. The Drude model had many successes, especially with metals, in predicting things like the electrical resistivity of a material and the Wiedemann-Franz law. The model, however, fell short in some ways with a predicted electronic heat capacity much larger than that experimentally observed in metals.

In 1928 Sommerfeld introduced quantum theory to electronic transport using Fermi-Dirac statistics instead of the classical Maxwell-Boltzman statistics used by Drude [32]. Additionally in 1928 Felix Bloch mathematically described the periodic potentials that interact with electrons in a crystalline solid with Bloch functions [33]:

$$\Psi_{\mathbf{k}}(\mathbf{r}) = e^{i\mathbf{k}\cdot\mathbf{r}} u_{\mathbf{k}}(\mathbf{r}) \tag{1.16}$$

where $\Psi_{\mathbf{k}}(\mathbf{r})$ is the wavefunction of an electron, $\mathbf{k}$ is the crystal wave vector of the electron, $\mathbf{r}$ is distance, and $u_{\mathbf{k}}(\mathbf{r})$ is a function with the same periodicity as the crystal. These wavefunctions are the eigenfunctions which satisfy the Schrodinger equation for the available states of the electron:

$$\left(-\frac{\hbar^2}{2m}\nabla^2 + U(\mathbf{r})\right)\Psi = \mathbf{E}\Psi \tag{1.17}$$

where $\hbar$ is the reduced Planck's constant, m is the mass of the electron, and $U(\mathbf{r})$ is the periodic potential due to the crystal lattice. Due to the periodic nature of the crystal the wave vector $\mathbf{k}$ can always be represented within the first Brillouin zone and another possibly further elucidating version of Bloch's theorem is [34]:

$$\Psi(\mathbf{r}+\mathbf{R}) = e^{i\mathbf{k}\cdot\mathbf{r}}\Psi(\mathbf{r}) \tag{1.18}$$

which demonstrates that for any translationally moved wavefunction $\Psi(\mathbf{r} + \mathbf{R})$ there exists a wave vector $\mathbf{k}$ which will relate this new wavefunction to a wavefunction within the first Brillouin zone. This wave vector $\mathbf{k}$ may be plotted versus energy to give rise to the extremely useful representation of the available energy states of a material as the energy band diagram.

A schematic representation of an energy band diagram is shown in Figure 1.5.

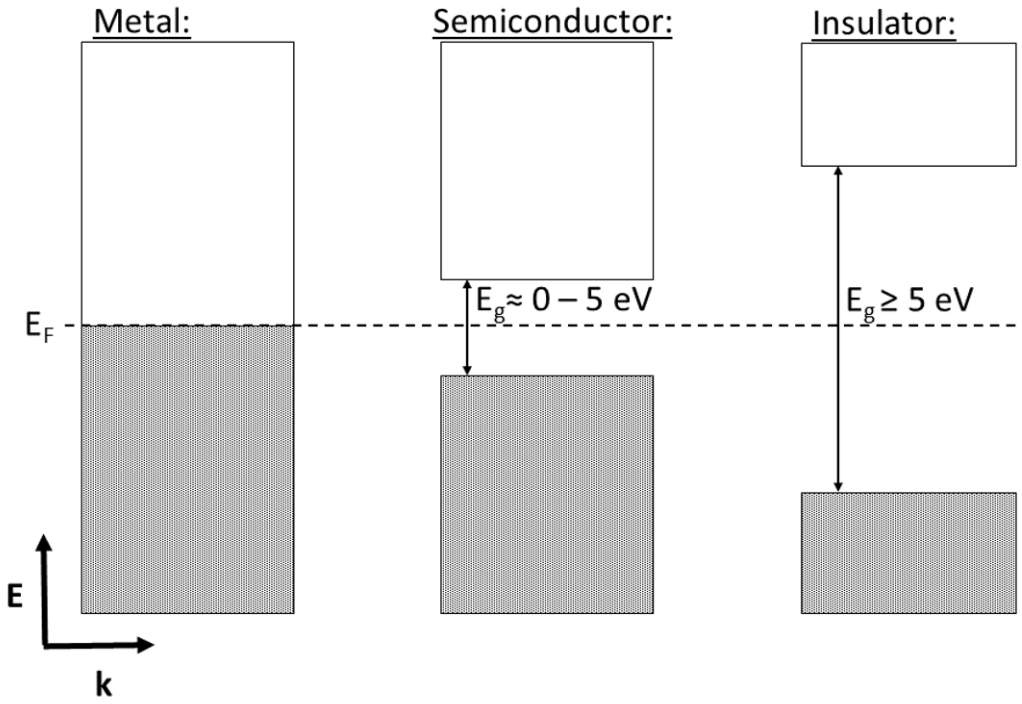

Figure 1.5: Schematic Energy Band Diagram for Metals, Semiconductors, and Insulators

This figure shows the underlying differences in the energy band diagram of metals, semiconductors, and insulators and demonstrates why the electronic properties of these categories of materials vary so dramatically. The energy band diagram of a metal is shown to have fully occupied electronic states up to the Fermi energy, E_F, which is well within the middle of a band. As was shown by Sommerfeld the charge carriers that are within a few k_BT of the Fermi energy are those that are able to electronically conduct. In the metal there are

a plethora of carriers and available empty energy states around the Fermi energy and thus its electronic properties reflect this; prominently a very high electrical conductivity. It is in semiconductors and insulators where a band gap, or a region of non-overlapping energy states where carriers are unable to populate, exists. In the insulator this band gap is so large that at terrestrial temperatures carriers will not have enough energy to populate free, empty states, in the conduction band. This is reflected in the electronic properties of insulators and most prominently in an extremely low electrical conductivity. In the semiconductor the band gap is found to be within range of thermal energy supplying greater than the band gap energy to carriers, such that an electron may be able to populate a free energy state in the conduction band. This gives rise to a wide range of electronic properties that semiconductors may adopt.

Stemming from the concept of the energy band diagram is that of the effective mass of a charge carrier and that of the conduction of charge by holes. The effective mass is the curvature of a band extrema, either the minima of the conduction band, or the maxima of the valence band. In one dimension, this may be expressed as [23]:

$$m^* = \hbar^2 \left[\frac{\partial^2 \mathbf{E}}{\partial \mathbf{k}^2} \right]^{-1} \tag{1.19}$$

While in reality the inertial effective mass is a tensor, which gives the effective mass of carriers in the different directions of k-space, it is instructive to examine it as though a scalar for discussion. When the curvature of these band extrema are negative, as in the conduction band, the effective mass will be negative and the charge carriers are electrons in this case. When the curvature is positive, as in the valence band, the charge carriers are holes. Holes are quasi-particles, because their significance is due to the lack of an electron. Conduction

by holes is still performed by the migration of electrons, but it is the absence of an electron, which entails a positive charge, that is moving through a real material.

1.4.2 Electrical Conductivity

The ability of a material to conduct these charge carriers is defined as the electrical conductivity, σ, one of the properties of a material that determines the figure-of-merit, zT:

$$\sigma = ne\mu_e + ph\mu_h \tag{1.20}$$

where n is the electron concentration, e is the electronic charge, μ_e is the electron mobility, p is the hole concentration, h is the hole charge, and μ_h is the hole mobility. For most temperature ranges and purposes of thermoelectric materials it is advantageous to only have one type of charge carrier conducting in a material. When both carriers are present this mode of conduction is called bipolar conduction.

To begin the description of the electrical conductivity it is important to understand that, for the vast majority of equations concerning carrier concentration, only slight modification is required to switch between equations for electrons and holes. Therefore, in this description only the equations for electron concentration will be expressed.

Utilizing Fermi-Dirac statistics the electron concentration in a material is given by:

$$n = \int_0^\infty f_n(E)g(E)dE \tag{1.21}$$

where $f_n(E)$, the Fermi-Dirac distribution, and $g(E)$, the density of states for an electron

in the energy band, are:

$$f_n(E) = \frac{1}{e^{\frac{E-E_F}{k_B T}} + 1} \tag{1.22}$$

$$g(E) = \frac{8\pi\sqrt{2}}{h^3} m^{*3/2} \sqrt{E - E_c} \tag{1.23}$$

where k_B is the Boltzmann constant, m^* is the effective mass of the charge carrier, h is Planck's constant, E_c is the conduction band minima, and E_F is the Fermi energy. The Fermi energy is defined as the energy, at absolute zero, where all of the states below this energy are occupied and none above it are. The Fermi-Dirac distribution gives the probability of an electron existing in an energy state and is shown in Figure 1.6 for various temperatures.

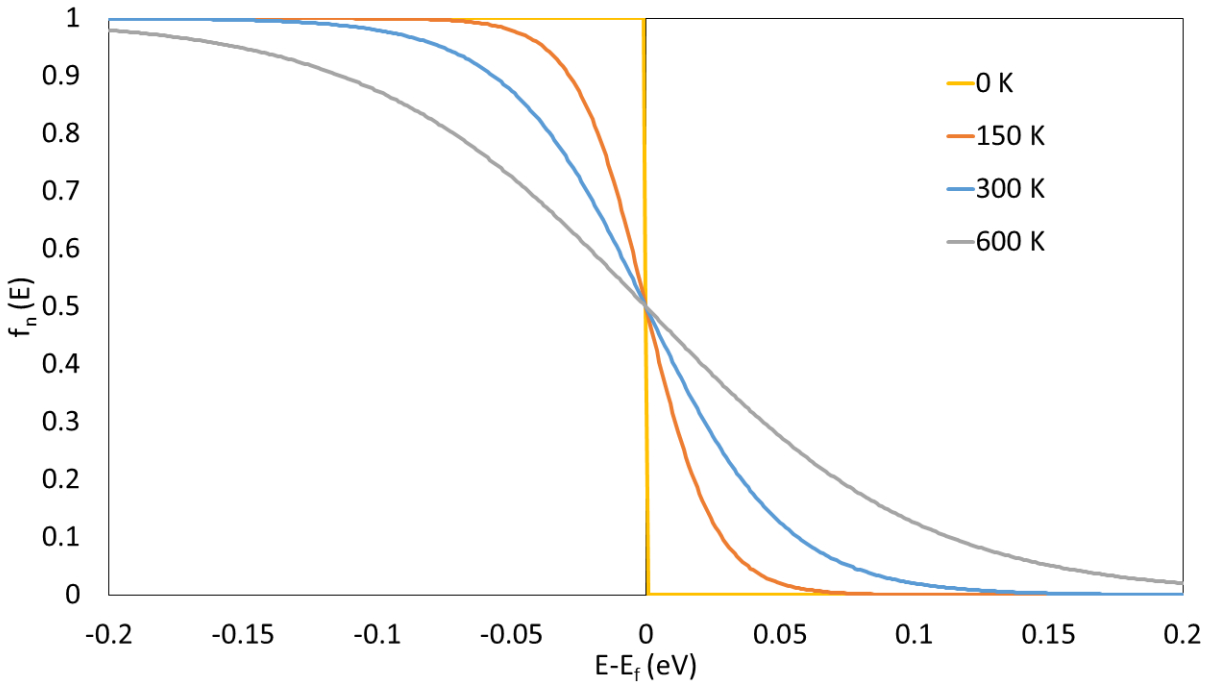

Figure 1.6: Fermi-Dirac Distribution for Multiple Temperatures

Observing the Fermi-Dirac distribution at 0 K it is found that there is a jump discontinuity at energy equal to the Fermi energy. For all energies below the Fermi energy the probability of an electron existing in this state is 100 % and above this energy equal to 0 %.

At non-zero temperatures the distribution is found to be continuous and varying between the values of 0 and 1 for energies approaching the Fermi level. This creates a non-zero potential of a charge carrier to exist in an energy state above the Fermi energy when at non-zero temperature. Of note is the increase in variance at higher temperatures, which results in a further increased potential of finding a charge carrier in higher energy states.

The equation for carrier concentration can thus be given as:

$$n = \frac{8\pi\sqrt{2}}{h^3} m^{*3/2} \int_0^\infty \frac{\sqrt{E - E_c}}{e^{\frac{E-E_F}{k_B T}} + 1} dE \tag{1.24}$$

which may be simplified to:

$$n = N_c \frac{2}{\sqrt{\pi}} F_{1/2}(\eta) \quad \text{where} \quad \eta = \frac{E_F}{k_B T} \tag{1.25}$$

and

$$N_c = 2 \left(\frac{2\pi m^* k_B T}{h^2} \right)^{3/2} \tag{1.26}$$

where $F_{1/2}(\eta)$ is the Fermi-Dirac integral and η is the reduced Fermi energy. For an intrinsic semiconductor, one in which there has been no doping, the number of electrons and holes are equal due to the fact that as electrons are populated across the bandgap they generate an equal number of holes from their absence. This result is stated in the law of mass action:

$$n * p = n_i^2 \tag{1.27}$$

where n_i is the intrinsic carrier concentration. This concentration may be obtained by

combining equations 1.27 and a simplified 1.24 to obtain:

$$n_i(T) = \sqrt{N_c N_v} e^{\frac{-E_G}{2k_B T}} \tag{1.28}$$

This shows that the intrinsic carrier concentration is dependent upon the effective masses of the charge carriers, due to the dependence of N_c and N_v upon the effective mass, as well as upon the energy bandgap. For a given temperature the intrinsic carrier concentration will be lower in a large bandgap material than for a low bandgap material. The ratio of the effective masses is often more important than their absolute value. This will affect the electrical conductivity, as seen in Equation 1.20, as well as the other thermoelectric properties in the intrinsic regime. The Fermi energy of a material is also dependent upon the ratio of these effective masses such that:

$$E_{f,int.} = E_v + \frac{1}{2}E_G + \frac{3}{4}k_B T \ln\left(\frac{m_v}{m_c}\right) \tag{1.29}$$

where the Fermi energy is dependent upon the energy at the top of the valence band, E_v, half of the energy of the bandgap, and then adjusted by the natural log of the ratio of the effective masses. In the majority of materials this addition will only affect the Fermi level by a small amount and for most purposes an assumption of the Fermi level lying in the middle of the band gap will be a sufficient approximation.

As mentioned earlier, the electronic properties of semiconductors can vary over a wide range. This is in part due to the variation in bandgaps in these materials, but also to the effect of extrinsic doping. Doping is the process of substituting elements in a compound with elements containing a differing number of valence electrons. In the most simplistic view the dopant atom will be adding or subtracting electrons from the material system thereby

directly affecting the carrier concentration. There are two categories of dopants, n-type, where the dopant has additional valence electrons relative to that of the atom for which it is substituting, and p-type, where the dopant has fewer valence electrons. Often, these dopants will not have a very high solubility in the parent material, but this is not needed to affect a dramatic change in the electronic properties. An often used example of extrinsic doping is with silicon where phosphorous may act as an n-type dopant and boron may act as a p-type. When these atoms are substituted the result is a change in the energy band diagram where the Fermi energy may be shifted closer to the valence or conduction band depending upon the addition of p-type or n-type dopant. The Fermi energy is shifted depending upon if electrons or holes were added to the system, because this will affect the probability of an energy state being filled. The equation for this shift is given by:

$$E_f = E_{f,int.} + 1/2k_BT\ln\left(\frac{n}{p}\right) \tag{1.30}$$

where the n and p in this equation may not be the same as that for an intrinsic semiconductor.

The dopants, referred to as donors for n-type materials, and acceptors for p-type materials, require an activation energy before they contribute carriers to the system. These activation energies are quite low compared to the bandgap and thereby ionize at temperatures much lower than intrinsic carriers. The equation for the electron carrier concentration in this region of ongoing ionization is:

$$n \approx \sqrt{\frac{N_D N_c}{2}} e^{-E_D/2k_BT} \quad \text{when} \quad N_D \gg \frac{1}{2}N_c e^{-E_D/k_BT} \gg N_A \tag{1.31}$$

where N_D is donor concentration and E_D is the activation energy of a donor. Once

the temperature has increased beyond the region where ionization is occurring the carrier concentration is given as:

$$n = \frac{1}{2}\left[(N_D - N_A) + \sqrt{(N_D - N_A)^2 + 4n_i^2}\right] \tag{1.32}$$

where N_A is the acceptor concentration. This equation can be simplified to $n \approx N_D$ given that $N_D \gg N_A$ and $|N_D - N_A| \gg n_i$.

The extrinsic semiconductor can be doped so heavily that the Fermi level is within 1 - 2 k_BT of a band edge. When this occurs the semiconductor is referred to as degenerate and the carrier concentration is very large, similar to that found in a metal, over a wide range of temperatures. However, for the extrinsic semiconductor that is non-degenerate the carrier concentration is small at low temperatures but increases as donors or acceptors are ionized with increasing temperature. As the temperature increases, the activation energy for all donors or acceptors is met and a region of saturation occurs where no new carriers are being populated to charge carrying energy states. At temperatures above the saturation region intrinsic charge carriers will begin populating across the bandgap and carrier concentration will again increase.

As can be seen in equation 1.20, the carrier concentration is only part of the electrical conductivity. The other variable is the mobility of that charge carrier, which is defined from the drift velocity of carriers in response to an electric field, $v_d = \mu\mathbf{E}$. The mobility may be given as:

$$\mu = \frac{e\bar{\tau}}{m^*} \tag{1.33}$$

where $\bar{\tau}$ is the average scattering time. This average scattering time is dependent upon

the dominant scattering mechanism in a material for a given temperature, but may be given by Matthiessen's rule:

$$\frac{1}{\tau} = \frac{1}{\tau_{lattice}} + \frac{1}{\tau_{impurities}} + \frac{1}{\tau_{defects}} + ... \tag{1.34}$$

where $\tau_{lattice}$ is the scattering of charges due to the lattice ions, $\tau_{impurities}$ is the scattering due to impurities, and $\tau_{defects}$ is the scattering due to defects in the crystal lattice.

Lattice scattering is due to the interaction between charge carriers and phonons traveling through the crystal lattice. As temperature increases more phonons are generated in the lattice, which corresponds to more scattering of carriers, thus, as temperature increases the dominant scattering mechanisms in materials becomes that from the lattice. It is found that in this case mobility depends on temperature as: $\mu_{lattice} \propto T^{-3/2}$.

Impurity scattering however is the low temperature dominant scattering mechanism compared to lattice scattering. Impurity scattering is found to depend upon the average thermal velocity of charge carriers, meaning that the more energy a carrier has the less likely it is to be scattered. Thus, at low temperatures, where the thermal velocity is low, more impurity scattering will occur than at high temperatures where thermal velocity is high. The proportionality for this type of scattering is: $\mu_{impurity} \propto T^{3/2}$.

The scattering due to crystal defects is given as an example of a scattering mechanism where the scattering rate is constant due to either an ordered or disordered defect causing the scattering of a carrier. Another scattering mechanism found in degenerate semiconductors, or for non-degenerate semiconductors that are at temperatures in the intrinsic regime, where a high carrier concentration is obtained, is electron-electron scattering where the carriers in a material will begin to scatter off of each other. This only begins to play a role at very

high carrier concentrations, but can become the dominant scattering mechanism at high temperatures, or in heavily doped semiconductors.

There are many more types of scattering mechanisms in materials, but for this work these are found to often be the dominant scattering mechanisms of importance at observed temperatures. The result of the switch between ionized impurity scattering, which decreases as temperature increases, and acoustic phonon scattering, which increases as temperature increases, is that there typically will be a maximum in the mobility over a temperature range.

How the electrical conductivity of a material ultimately responds to changes in carrier concentration and mobility will differ in all materials and will be greatly affected by the material synthesis and processing. However, a few generalizations may be made. Typically, the electrical conductivity of a non-degenerate, extrinsically doped semiconductor will increase as dopant carriers are populated, but will at higher temperatures begin to decrease as acoustic phonon scattering begins to dominate. For the degenerate semiconductor the electrical conductivity follows a trend that is much like that of a metal. Starting at low temperature with a high conductivity, due to the high carrier concentration, there will be a downward trend as acoustic phonons become a more dominant scattering mechanism.

1.4.3 The Seebeck Coefficient

The thermoelectric effects, with which this work began, are the foundation for the operation of thermoelectric materials. The most direct of which to measure is the Seebeck effect and namesake coefficient. As defined previously, the Seebeck coefficient is a reflection of the response of electrons to a temperature gradient. The Seebeck coefficient is defined such that an n-type material in open circuit conditions under a temperature gradient will generate a voltage potential such that the electric field is pointed in the direction of the cold side,

(the side with a negative charge buildup). This creates a negative Seebeck coefficient for an n-type material and the inverse for a p-type material.

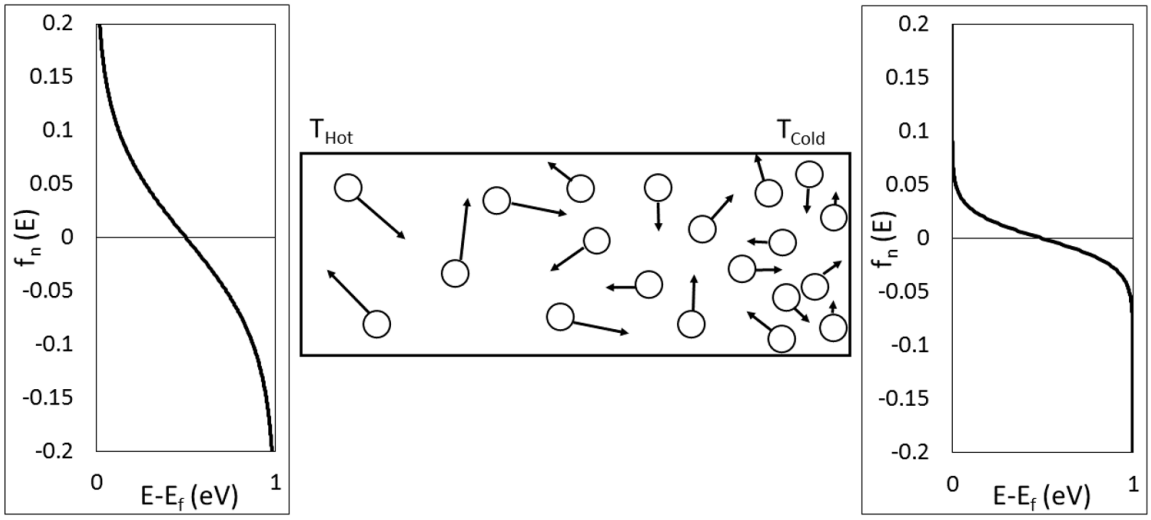

Figure 1.7: Schematic of Open Circuit Seebeck Effect

As was introduced in the previous section the Fermi-Dirac function will also have a gradient along the material due to the temperature differential. Using Boltzmann transport equations, an equation can be obtained where the Seebeck coefficient is dependent upon the integral of the partial derivative of the Fermi-Dirac function, density of states, energy, and scattering terms. Ioffe was able to simplify the equation to [35]:

$$\alpha = -\frac{k_B}{e}\left[\frac{\left(\frac{5}{2}+\lambda\right)F_{3/2+\lambda}(\eta)}{\left(\frac{3}{2}+\lambda\right)F_{1/2+\lambda}(\eta)} - \eta\right] \tag{1.35}$$

where λ is a term dependent upon the scattering mechanism, η is again the reduced Fermi energy, $\frac{E_F}{k_B T}$, and $F_{3/2+\lambda}$ and $F_{1/2+\lambda}$ are Fermi-Dirac integrals. This is assuming a single parabolic band model with a single energy dependent carrier relaxation time. The scattering dependent λ is equal to $-1/2$ for acoustic phonon scattering dominant energies and equal to $3/2$ for ionized impurity scattering dominant energies.

Examining the Seebeck coefficient for metals the equation for the Seebeck coefficient can be greatly simplified. The Mott-Jones equation gives the Seebeck coefficient for this class of materials as [36]:

$$\alpha = -\frac{\pi^2 k_B}{3e}\left(\frac{k_B T}{E_F}\right)\left(\frac{3}{2}+\lambda\right) \tag{1.36}$$

Examining this equation, the dependence of the Seebeck coefficient on $k_B T/E_F$ is immediately obvious. This is due to the fact that only those electrons that are within a few $k_B T$ of the Fermi energy will contribute to the effect.

To better examine the dependence of the Seebeck coefficient to the carrier concentration in semiconductors the following equation can be shown [37]:

$$\alpha = \frac{\pi^2}{3}\frac{k_B}{e}k_B T\left[\frac{1}{n}\frac{dn(E)}{dE}+\frac{1}{\mu}\frac{d\mu(E)}{dE}\right]_{E=E_F} \tag{1.37}$$

This equation shows that an increased Seebeck coefficient can be obtained by either having a large energy dependence of the carrier concentration or mobility at the Fermi energy. To obtain the former there needs to be a large change in the density of states at the Fermi energy and to obtain the latter a strong energy dependent scattering mechanism is required [38]. This additionally shows the dependence of the Seebeck coefficient on carrier concentration and carrier mobility. As carrier concentration and mobility increase the Seebeck coefficient is found to decrease.

Just as with the electrical conductivity, when bipolar effects begin to play a role in the intrinsic regime of a material, the Seebeck coefficient will be altered due to the mixed

conduction effects. The equation for this effect is given as [23]:

$$\alpha = \frac{\alpha_n \sigma_n + \alpha_p \sigma_p}{\sigma_n + \sigma_p} \tag{1.38}$$

Here the Seebeck coefficient contribution of electrons and holes is given and weighted by the electrical conductivity of those charge carriers. The first important point is that for thermoelectric applications it is best to have a material of only one carrier type. Any contribution of an additional carrier will only serve to decrease the overall Seebeck coefficient, because α_n and α_p have opposite signs. The next point to take note of is the dependence on the mobility of the individual carriers. If a material does have bipolar conduction occurring, then the contribution of the carriers may not be proportional. For example, if the electrons in a material have a much higher mobility than the holes, then the material may be n-type for similar electron and hole carrier concentrations.

If a degenerate, i.e. heavily doped, semiconductor with parabolic bands is assumed, with only one carrier type, then the following may be obtained [39]:

$$\alpha = \frac{8\pi^2 k_B^2}{3eh^2} m^* T \left(\frac{\pi}{3n}\right)^{2/3} \tag{1.39}$$

which shows even more directly the dependence of the Seebeck coefficient on the carrier concentration and the effective mass. Thus, typically for high Seebeck coefficient in extrinsically doped, degenerate semiconductors a low carrier concentration and high effective mass are desired. This trend in transport properties is directly contrary to what is required for high electrical conductivity and is one of the so-called "contra-indicated" properties that thermoelectric materials possess.

1.4.4 The Power Factor

The thermoelectric power factor of a material is the numerator in the figure-of-merit equation:

$$P.F. = \alpha^2\sigma \tag{1.40}$$

where $P.F.$ is the power factor. It is found that the power factor depends on the square of the Seebeck coefficient and the electrical conductivity. As mentioned earlier these two properties have contra-indicated components. As the carrier concentration increases the electrical conductivity is found to increase, but the Seebeck coefficient concurrently decreases. Additionally, if the mobility of a carrier is decreased the Seebeck coefficient tends to increase, however, the electrical conductivity will decrease. The contra-indication of these properties results in a maximization of the power factor at certain carrier concentrations assuming mobility is unchanged. This relationship is called the Pisarenko relationship and is shown in Figure 1.8.

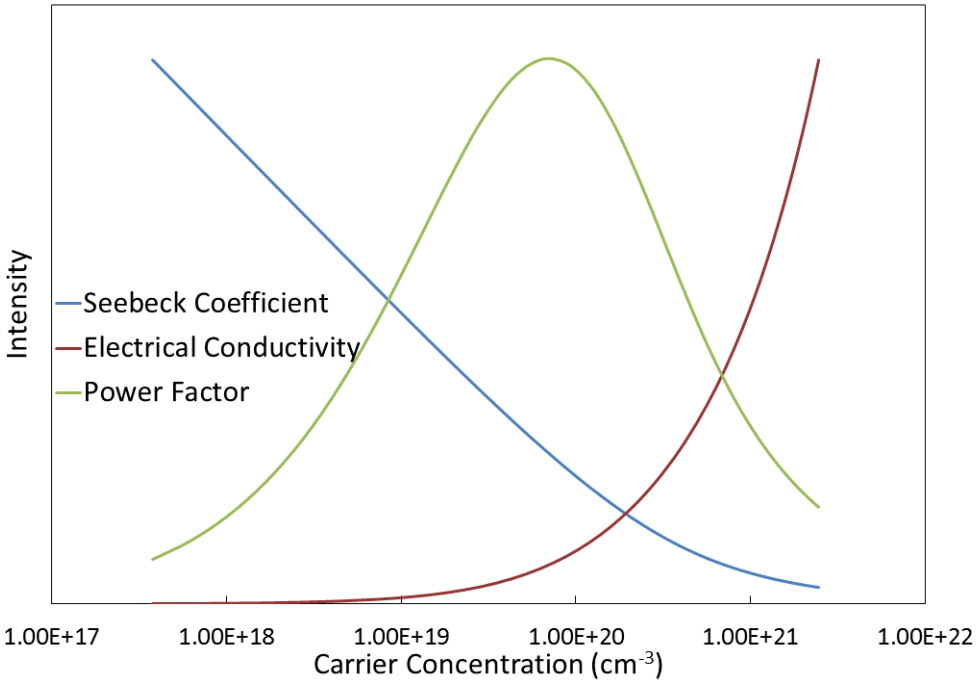

Figure 1.8: Diagram of Power Factor, Seebeck Coefficient, and Electrical Conductivity versus Carrier Concentration

This figure graphically demonstrates how the power factor will be maximized at a particular carrier concentration for a given material. For most material types a carrier concentration in the range of 10^{19} to 10^{21} yields a maximized power factor. Current and advanced techniques to increase power factor concentrate on band engineering to increase band degeneracy, carrier concentration doping with elements or materials which generate a minimum increase in carrier scattering, and preferential carrier scattering mechanisms leading to optimization [40]. However, as will be seen in the following section, a maximized power factor will not always relate to a maximized zT.

1.5 Thermal Transport

The flow of heat through a material is governed by Fourier's law of heat conduction which shows that the power conducted per unit area is proportional, by thermal conductivity, κ, to the ratio of the temperature difference over the distance of separation:

$$\frac{\Delta Q}{\Delta t A} = -\kappa \frac{\Delta T}{\Delta X} \tag{1.41}$$

Where $\Delta Q/\Delta t$ is the power conducted, A is the area through which the heat flux is traveling, ΔX is the distance of separation, and κ is the thermal conductivity. There are many components to thermal conductivity including more exotic forms of heat conduction like electronic spin waves, however in the study of thermoelectrics the majority are represented by the electronic and lattice contributions.

1.5.1 Electronic Thermal Conductivity

The electronic thermal conductivity, as suggested by its name, is an effect mediated by the flow of electrons in a material. This effect is dependent upon the electrical conductivity of a material and is defined by the Wiedemann-Franz law:

$$\kappa_e = L_0 \sigma T \tag{1.42}$$

where L_0 is the Lorenz number. The Lorenz number is well defined for metals based upon a free-electron model with little variation from the definition: $L_0 = \frac{\pi^2}{3}\left(\frac{k_B}{e}^2\right) = 2.44 * 10^{-8}\ W\Omega K^{-2}$. However, in many semiconducting materials this value can vary due to additional scattering mechanisms.

1.5.2 Lattice Thermal Conductivity

The other majority component to the thermal conductivity in thermoelectric materials is the lattice contribution, mediated by the quasi-particle phonon. The phonon is a quantization of the energy transmitted by thermal vibrations through a crystal lattice and was given its name by Peierls in 1929 [41]. Earlier work by Debye on a continuum lattice examined heat conduction by lattice vibrations [42]. This work was foundational and is still very useful to examine, however, it erroneously resulted in an infinite thermal conductivity. Peierls solved this issue with the correction that higher order terms in the harmonic solutions would yield a phonon mean free path before being scattered. The lattice contribution is defined by:

$$\kappa_l = \frac{1}{3} c_v v l_t \tag{1.43}$$

where κ_l is the lattice contribution to thermal conductivity, c_v is the specific heat per unit volume, v is the speed of sound in the material, and l_t is the mean free path of the phonon. The specific heat and mean free path shown above are dependent upon both temperature and the wavelength of phonons.

One of the successes of the Debye model was to describe the specific heat with a high degree of accuracy. Debye assumed that there were 3N vibrational states for N atoms in a material and that a maximum vibration frequency would be met, f_m, which yielded a temperature, the Debye temperature, which corresponded to the temperature of the highest normal mode in a lattice [43]:

$$\Theta_D = \frac{h f_m}{k_B} \quad \text{where} \quad v_m = v \left(\frac{3N}{4\pi V} \right)^{1/3} \tag{1.44}$$

where Θ_D is the Debye temperature and N/V is the number density of atoms. Debye was able to define the specific heat at constant volume as:

$$c_v = 9Nk_B \left(\frac{T}{\Theta_D}\right)^3 \int_0^{\Theta_D/T} \frac{x^4 e^x}{(e^x - 1)^2} dx \tag{1.45}$$

where $x = \hbar\omega/k_B T$. This solution leads to two temperature regions of interest: that below the Debye temperature and that above the Debye temperature. Below the Debye temperature the specific heat reduces to a $c_v \propto T^3$ dependency and above the Debye temperature a saturation effect of all available modes occurs termed the Dulong-Petit limit where $c_v \approx \frac{3R}{M}$, with R being the gas constant and M the molar mass.

The mean free path of a phonon is determined by scattering mechanisms in the solid, $l_t = v\tau$. Mattheisen's rule of scattering can again be used, only this time for phonons, to understand how one scattering mechanism will dominate over others:

$$\frac{1}{\tau_{Tot.}} = \frac{1}{\tau_B} + \frac{1}{\tau_I} + \frac{1}{\tau_U} + ... \tag{1.46}$$

where τ_{Tot} is the combined scattering rates, τ_B is the boundary scattering rate, τ_I is scattering due to impurities, and τ_U is the scattering due to the Umklapp process.

At low temperatures boundary scattering will dominate due to the long wavelength phonons at those temperatures. In the perfect crystal the mean free path of phonons will be approximately the smallest dimension of the crystal, L, [44] and the scattering rate can be approximated by [45]:

$$\tau_B^{-1} \approx \frac{v_s}{L} \tag{1.47}$$

This type of scattering can be manipulated by the introduction of additional boundaries or interfaces. Reduction of particle size by a variety of methods, such as ball milling, melt-spinning, and spark plasma sintering can yield greatly reduced lattice contributions due to additional interfacial scattering of phonons [46].

Scattering from impurities is primarily due to disturbances in the periodic arrangement of atoms in the lattice and how this affects the propagation of phonons. These disturbances can occur through mass difference in solid solution formations, lattice vacancies, crystal dislocations, and even the inclusion of differing isotopes of elements [47–50]. The scattering rate arising from these mechanisms can be defined by [51]:

$$\tau_I^{-1} = \frac{V\Gamma}{4\pi v^3}\omega^4 \tag{1.48}$$

where V is the volume of the unit cell, ω is the wavelength, and Γ is the mass-fluctuation scattering parameter. The mass-fluctuation parameter contains a ratio of the change in mass to the mass of the unsubstituted atom squared, which highlights that large differences in mass will scatter phonons at a higher rate. This scattering mechanism additionally has a large dependency upon the frequency, $\tau_I^{-1} \propto \omega^4$, which incidentally is very similar to the relation for Rayleigh scattering of photons.

Phonon scattering by phonon-phonon interactions takes place by two different processes each involving the interaction of three phonons. The first is termed a normal "N-" process which is a non-thermally resistive scattering mechanism whereby the phonon-phonon interaction momentum is conserved [52]. As this process is non-thermally resistive it does not contribute to the total thermal conductivity. The second process termed Umklapp, or U-process, however, does contribute to an increased scattering rate and thereby a reduction

in the lattice contribution.

Umklapp scattering is a process whereby the resultant interaction of two phonons results in a third phonon outside of the first Brillouin zone. A reciprocal lattice vector returns the phonon to inside the 1st Brillouin zone resulting in a net backwards phonon flux [53]. The temperature dependence of the scattering rate for this mechanism was given by Peierls as [41]:

$$\tau_U^{-1} \propto T^n e^{\Theta_D/mT} \tag{1.49}$$

Slack further quantified this relationship with the following equation [54]:

$$\tau_U^{-1} \approx \frac{\hbar\gamma^2}{Mv^2\Theta_D}\omega^2 T e^{-\Theta_D/3T} \tag{1.50}$$

where γ is the Grüneisen parameter, and M is the average atomic mass. The parameter of note here is the dependency of the scattering rate on the first order of temperature.

The total scattering rate is then given as:

$$\tau_{Tot.}^{-1} = \frac{v_s}{L} + A\omega^4 + B\omega^2 T e^{-\Theta_D/3T} \tag{1.51}$$

From this it can easily be seen that the boundary scattering effects have a more dominant effect at low temperatures, with impurity scattering becoming larger as temperature increases, and finally Umklapp scattering beginning to have a more dominant role at $T > 0.1\Theta_D$.

With both the specific heat and the scattering rate dependencies defined a few generalizations of the lattice thermal conductivity may be made. At low temperatures, where the

specific heat goes as T^3, and boundary scattering is dominant, the thermal conductivity will also go as a T^3 dependency which has simply been depressed due to the constant boundary scattering. As temperature increases impurity scattering also begins to increase which leads to further suppression of the thermal conductivity. As temperature approaches the Debye temperature, the thermal conductivity will peak at a maximum value. Once the Debye temperature has been met the specific heat will stay constant as the Umklapp scattering process begins to dominate. In this region the thermal conductivity will decrease with a T^{-1} dependency, matching the behavior observed by Eucken in 1911 [55].

1.6 Material Selection and Enhancement of zT

In the selection of materials for thermoelectric applications a material must be selected that can balance all of the contra-indicated properties which comprise the figure-of-merit. To summarize the requirements of high zT a material needs a high Seebeck coefficient, a high electrical conductivity, and a low total thermal conductivity. An insulator will typically display very low thermal conductivity and a high Seebeck coefficient because of the large band gap. However, insulators will, again because of the large band gap, have a very low electrical conductivity. The case for metals is slightly more muddled, however, metals typically have low Seebeck coefficients, and high electrical and thermal conductivities. Thus, it is the semiconductor which has been identified and most widely researched for its potential in thermoelectric application [56]. Semiconductors may exhibit a wide array of electrical properties over a large range of temperatures. They additionally may be modified to greatly reduce their thermal conductivities. Above all else it is the large degree of tuning and tailoring that may be performed on semiconductors that makes them attractive for use as thermoelectric

materials.

As was stated before, the contra-indicated properties of the Seebeck coefficient and electrical conductivity require a tuning of the carrier concentration for power factor optimization, however for high zT the additional parameters of κ_e and κ_l must also be addressed. The relationship between κ_e and σ is direct, and any decrease in κ_e comes at the expense of a decrease in σ, and vice-versa. Additionally, many methods of lowering κ_l will negatively affect the power factor by the introduction or exacerbation of scattering effects. It is beneficial to rearrange the equation for zT to simplify these connections:

$$zT = \frac{\alpha^2}{L_0 + \frac{\kappa_l}{\sigma T}} \tag{1.52}$$

This equation removes the dependency on the electrical contribution to thermal conductivity because of the direct connection between it and the electrical conductivity. It additionally highlights the importance of the ratio of the lattice thermal conductivity to the electrical conductivity and the importance of a high Seebeck coefficient. The higher the electrical conductivity the lower the ratio of $\kappa_l/\sigma T$ will become. In the case where this quantity becomes much less than 1, the zT equation simplifies to $zT \approx \alpha^2/L_0$. Unfortunately in this case the material has such a metallic electrical conductivity that its Seebeck coefficient will typically be very low.

Another way in which equation (1.52) may be interpreted is to attempt to minimize the lattice contribution. However, in the process of minimizing κ_l the likely result will be to increase the intensity and number of scattering events for electrons, as well as phonons, resulting in a dramatic decrease in mobility and thereby a subsequent reduction in the electrical conductivity and the power factor. The interplay of these properties can be displayed

in an expanded form of the Pisarenko plot which was shown before in Figure 1.8, where it becomes clear that it is not a simple matter of tuning the carrier concentration to the maximum power factor and then decreasing the lattice contribution to thermal conductivity. It is thus beneficial to begin by selecting materials with favorable properties and then to take a refined approach to optimizing the variables in zT.

Slack proposed a paradigm of the optimal properties with which a material may be selected in his phonon-glass electron-crystal model [57]. In this model Slack states that the phonon mean free path should be that found in amorphous glasses, and the mobility of carriers should be that found in single crystals. Under these criteria Slack proposed a term, U, the weighted mobility where $U = \mu \left(\frac{m^*}{m_0}\right)^{3/2}$ and R, where $R = U/\kappa_l$. Using these terms Slack came to the conclusion that for high zT the best materials will have a high mobility, a high effective mass, and a low lattice contribution to thermal conductivity. This R term could then be a filtering term to distinguish materials with high zT values. In his survey Slack found no material with R values high enough to result in zT values of unity from 77 to 300 K, but outlined the requirements for zT values as high as 4 at room temperature.

A material parameter, B, given the moniker "quality factor", is an attempt to define the exact properties of a material which will result in a high zT. This was first introduced by Chasmar and Stratton, named the material factor, β [58], and later reworked by Nolas and Goldsmid [23]. Taking into account the changes in mobility with doping and carrier band degeneracy the quality factor was given Snyder et al. as [59]:

$$B = \frac{2k_B^2\hbar}{3\pi}\frac{C_l N_v}{m_I^* \Xi^2 \kappa_l} T \tag{1.53}$$

where N_v is the valence band degeneracy, C_l is the longitudinal elastic constant, m_I^* is

the conductivity effective mass, and Ξ is the deformation potential. The band degeneracy relates back to the concept of energy band diagrams, where the bottom of the conduction band or the top of the valence band may be comprised of several overlapping bands. It is seen from the above equation that a high band degeneracy with low conductivity effective mass is preferred. This comes contrary to what is typically desired for the effective mass and contrary to what Slack proposed. The parameter C_l is a measure of the resistance of a material to elastic deformation under an applied force and can be thought of as the stiffness of the atomic bonding, and for high quality factor, should be maximized. Finally, the term, Ξ, which is a measure of the deformation potential of energy bands created by the interaction of phonons with the band structure, should be minimized.

The lattice contribution to thermal conductivity in the Umklapp scattering dominated region, can be approximated as [60, 61]:

$$\kappa_l \propto \frac{M v_s^3}{T V^{2/3} \gamma^2} \left(\frac{1}{N^{1/3}} \right) \tag{1.54}$$

where M is the average mass, V is the unit cell volume, γ is the Gruneisen parameter, and N is the number of atoms in the primitive unit cell. This equation is especially useful for the selection of a material because it highlights the importance of having a large number of atoms in the primitive unit cell and having a high Gruneisen parameter, which is a measure of the anharmonicity of bonding [62].

A final aspect of material selection that will be mentioned here is selection based upon the electronic band gap. Early work by Chasmar and Stratton found a band gap of 6 $k_B T$ maximized thermoelectric performance in an indirect gap material with Mahan later expanding that to 10 $k_B T$ with similar values being found for direct gap materials [58,

63, 64]. Taking the midpoint of these values at 8 k_BT the optimum band gap at 150 K is approximately 0.1 eV and at 300 K is approximately 0.2 eV. Thus, for low temperature applications and zT maximization a low bandgap material is desired. This can be intuitively understood by the requirement for one carrier type to be present in a material for the desired temperature. If the bandgap of a material is too low for a desired operating temperature, then intrinsic carriers will be populated and the Seebeck coefficient will be decreased. There is more room for optimization if the bandgap is larger than this 6-10 k_BT guide through carrier concentration doping. Thus, for the work contained herein a low band gap material will be preferred for low temperature thermoelectric applications.

Chapter 2

Experimental

2.1 Materials Synthesis

2.1.1 Furnace Reaction Method

For this work there were three main steps in the synthesis and processing of materials. The first was the reaction of elements to form the desired compound. This step typically consisted of a heating phase to supply the required thermal energy to allow for chemical reaction between the different elements. The second step consisted of any post reaction powder processing required by the particular project. This would entail any particle size reduction attempts by ball milling or any material annealing required. The final step in the synthesis procedure was a densification step whereby a dense pellet was created capable of having transport measurements taken upon it.

As the specific experimental synthesis parameters varied for many of the materials examined a general guideline of what was performed will be given here. For the majority of materials the initial reaction was facilitated by furnace heating. For all materials examined, stoichiometric amounts of the elements were sealed in an evacuated quartz ampoule. The elements used were supplied from either Sigma Aldrich or Alfa Aesar with a purity of at

least 99.99 %. The elements were placed in a furnace which was heated to 800 °C for 4 days. The reacted compounds were then quenched to room temperature in a water bath. After the initial reaction samples were typically very porous with low densities, thus for transport properties measurements a subsequent densification step was necessary.

Samples were ground via mortar and pestle to prepare for X-ray diffraction and either material processing or densification depending upon the project. Between the initial reaction, any post-reaction processing, and densification every sample was analyzed by X-ray diffraction on a Rigaku Miniflex-II using Cu-K_α radiation to ensure phase purity.

For projects which entailed particle size reduction a ball milling step was performed using a SPEX MixerMill 8000D or a MixerMill 8000M in either a stainless steel ball milling jar and media or a zirconium oxide, (zirconia), milling jar and media. The duration of milling time differed between projects and will be given in the discussion of the applicable projects. Samples which were annealed were again placed back into an evacuated quartz ampoule, heated to their reaction temperature, and held for a specified time.

The final step in material synthesis was densification by spark plasma sintering, SPS, for all projects in this work. A Thermal Technology model 10-4 system SPS machine was used for early samples and a Dr. Sinter spark-plasma-sinter 211LX was used for later samples. To prepare samples for sintering, a mortar and pestle were used to pulverize samples which had not been ball milled. The powder was then loaded into a graphite die with graphite foil spacers between two plungers which acted to give uniaxial pressure on the sample and to apply a path of electric current through the sample. The die and plungers were stationed between two water cooled graphite rams. A schematic representation and picture of the SPS system is shown in Figure 2.1.

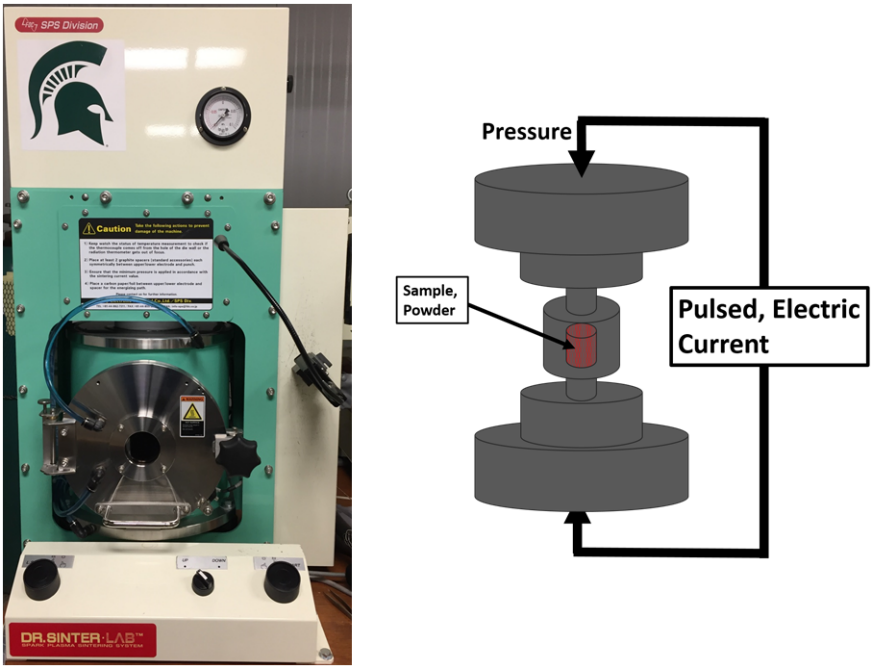

Figure 2.1: Schematic of Spark Plasma Sinterer

SPS, or pulsed electric current sintering, is differentiated from other types of sintering by the pulsed direct current which is applied across the sample. This pulsed electric current results in two effects which create sintering in the sample. One of these is joule heating due to the passage of a current through an internally resistive sample. The other effect is the arcing of electric current between neighboring particles [65, 66]. Through these two effects samples with densities higher than 95% density were obtained. The final densified sample is in the shape of a cylindrical puck and must be cut to perform transport properties measurement upon.

2.1.2 Flux Synthesis

In the Conclusions and Future Directions chapter a material system will be presented which used an entirely different initial chemical reaction than other samples. This material contained the element phosphorous which has a low boiling point that made a furnace reaction

method impossible due to the failure of quartz ampoules when phosphorous vaporizes. To synthesize this material a flux method was utilized. For this method a secondary material was added to the reactants which acted as a solvent for the desired compound. This stabilized the mixture and allowed for the desired product to react [67].

The synthesis procedures outlined here were based upon the work by Odile et al. [68]. Stoichiometric amounts of elements were sealed in an evacuated quartz tube with 85 wt% tin added as the flux. The heating profile for this reaction consisted of an initial ramp to 250 °C at 1.0 °C per minute with a dwell time at this temperature of 12 hours. Another ramp was performed up to 1000 °C at 0.5 °C per minute with a dwell time of 2 days. A slow cooling step was performed at a rate of 5 °C per hour to 550 °C to allow the desired compound to form. Once the furnace had cooled to 550 °C a water quench to room temperature was performed.

Samples were ground via mortar and pestle and examined with X-ray diffraction for the desired product. To liberate the product from the tin flux a reaction with 6 molar hydrochloric acid was performed. The reaction with hydrochloric acid will generate the creation of tin chloride, a salt, and hydrogen gas. Thus, the generation of bubbles due to hydrogen gas formation was an indication that the reaction was proceeding. When hydrogen production ceased it was assumed that the reaction was complete. Finally, the mixture was washed with distilled water to dissolve and remove the tin chloride salt. The remaining material after the wash should be the desired product. After this step typical powder processing and densification procedures were resumed.

2.2 Material Characterization Techniques

2.2.1 X-ray Diffraction

X-ray diffraction was performed to characterize the phase purity of powderized samples. This technique allows for the analysis of the crystal structure of a sample due to the diffraction of X-ray radiation from atoms in the lattice. Due to the periodic nature of atoms in crystal lattices the spacings between planes of atoms can be examined by the angle with which X-ray radiation diffracts.

As X-ray radiation is diffracted from the crystal lattice these waves may interact by either constructive or destructive interference. In destructive interference the waves are completely "out-of-phase" meaning that the crest of one wave is perfectly aligned with the valley of the wave it is interacting with. Mathematically this is expressed as when the phase of one wave in a set is at an odd multiple of π relative to the other wave. X-rays in this arrangement are said to destructively interfere and have an amplitude of zero which does not generate any signal in X-ray diffraction. Constructive interference however occurs when waves are perfectly "in-phase", which may differ by an even multiple of π. In this instance the crests of both waves perfectly align which results in a doubling of the amplitude of the resultant wave. It is these constructively interfering waves which generate the signal in X-ray diffraction.

Since it is constructively interfering diffracted beams which generate the output signal in X-ray diffraction the spacing between planes of atoms and the angle with which they constructively interfere is given by Bragg's law:

$$n\lambda = 2d_{hkl}sin(\theta) \tag{2.1}$$

where λ is the wavelength of incident X-ray radiation, d_{hkl} is the spacing between planes of atoms, and θ is the angle of incident X-ray radiation in relation to the atomic plane. A schematic representation of this is given in Figure 2.2.

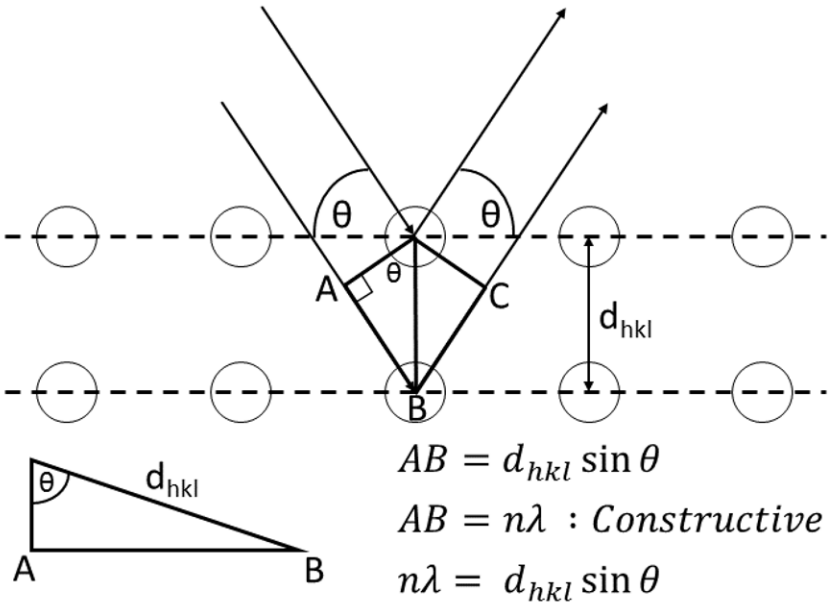

Figure 2.2: Schematic of Bragg Diffraction

A desktop Rigaku Miniflex II using Cu-K_α radiation with a wavelength of $\lambda = 1.54$ Å was used. To determine the lattice parameter of samples an internal silicon standard was added to account for any offset in 2θ due to systematic error or a height offset of the diffracted powder. For this work the samples examined all had cubic crystal structures, thus the lattice parameters were all equal, a = b = c, and all internal angles equal to 90°. Using reciprocal space d_{hkl} parameters where h, k, and l are the Miller indices of planes, the lattice parameter could be obtained by:

$$\frac{1}{d_{hkl}^2} = \frac{h^2 + k^2 + l^2}{a^2} \tag{2.2}$$

To analyze the particle size reduction effects of ball milling X-ray diffraction was again utilized. Particle size reduction results in a broadening of the observed peaks for a material. The width of the peak, taken at half the maximum intensity, can be related to the particle size by the Debye-Scherrer equation [69]:

$$L = \frac{K\lambda}{\beta cos(\theta)} \tag{2.3}$$

where L is the crystallite size, K is the shape factor, β is the broadening at half maximum, and θ is the 2θ position at which the peak maximum occurred. The shape factor is very often close to unity but depends upon the shape of the crystallite. When determining the broadening at half maximum it is important to subtract any instrumental broadening, which may occur due to several factors including imperfectly monochromatic radiation production from the machine and a non-infinitesimally small diffraction surface.

However, a reduction in crystallite size is not the only sample effect which can lead to broadened X-ray peaks. The other factor occurs due to any internal strain effects in the crystal lattice. These can arise from lattice distortion from dislocations, concentration gradients, and several other factors which cause a displacement of atoms from their most thermodynamically stable position. The Debye-Scherrer equation is unable to separate the peak broadening due to lattice strain from the reduction of crystallite size, however the Williamson-Hall equation has made these two effects separable and is given by [70]:

$$\beta cos(\theta) = \frac{K\lambda}{L} + 4\epsilon sin(\theta) \tag{2.4}$$

Using this equation it is possible to plot $\beta cos(\theta)$ vs. $sin(\theta)$ to obtain the y-axis offset which can be solved for to obtain the crystallite size. This method gives an average crystallite

size and should be confirmed with additional methods to quantify exact crystallite sizes. The technique is nevertheless a powerful tool for comparison between similar samples given differing processing conditions.

2.2.2 Low Temperature Transport Property Characterization

To measure the thermoelectric properties of each sample a diamond saw was used to cut samples into a parallelepiped of typical dimensions: 3 mm x 3 mm x 8 mm. These samples were then measured on an in-house built Janis liquid nitrogen-flow cryostat from 80 to 350 K. Two key concerns for the accurate measurement of transport properties are good electrical contacts between the sample and the measuring devices and good thermal contact and sinking between the sample and the heat source and sink. To ensure good electrical and thermal contact samples were soldered onto a copper base, which additionally acted as a heat sink, and to the top surface of the sample an 800 Ω resistor was soldered. A copper sheet was wrapped around the resistor to allow for good thermal contact between the resistor and the sample and to also be a conduit for the current input. A Keithley 2400-LV Sourcemeter was used to source a known current through the resistor. A Keithley 2001 multimeter was used to measure the voltage drop across the resistor. With the known current input into the resistor, and the voltage drop across it, the power output, in the form of Joule heating, was able to be calculated. A current input, again using a Keithley 2400-LV Sourcemeter, was soldered onto the copper sheet wrapped around the resistor which allowed for the propagation of current down the sample and output through the copper base. For all measurements a steady state heat flux condition was created by holding the powered resistor on for at least ten minutes prior to any measurement. To measure the conduction of heat through the sample two copper-constantan thermocouples were soldered onto the surface

of the sample perpendicular to the flow of heat taking care to span the entire breadth of the face of the sample. A Keithley 2182A Nano voltmeter was used to measure the voltage generated by the thermocouples which could then be interpreted as the temperature of the sample at that point. To reduce the loss of heat by conduction the cryostat was placed under a vacuum of approximately 10^{-5} torr. A schematic representation of this setup used to measure thermal conductivity, electrical resistivity, and the Seebeck coefficient is given in Figure 2.3.

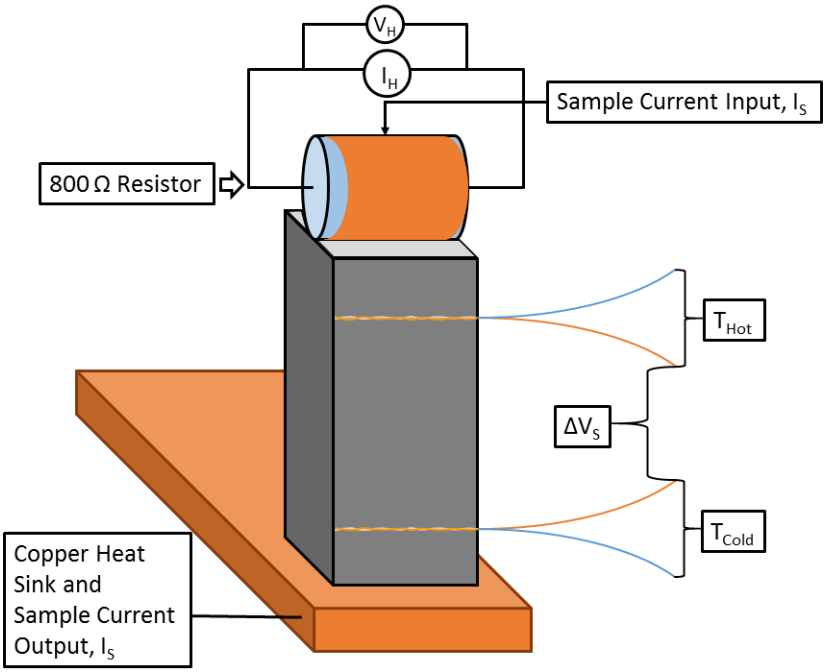

Figure 2.3: Schematic of Cryostat Measurement Setup

To determine the thermal conductivity of a sample the thermal conductance was first determined by:

$$K_M = \frac{V_H I_H}{\Delta T} \tag{2.5}$$

where K_M is the measured conductance, V_H is the voltage drop across the resistor, I_H is

the current passed through the resistor, and ΔT is the measured temperature drop between the thermocouples. $V_H I_H$ is the power in the form of Joule heating generated by the resistor. It is assumed that all of this heat is conducted into the top surface of the sample, further highlighting the importance of good thermal contact. According to the Stefan-Boltzmann law a certain amount of this heat will be lost as radiative energy as it propagates through the sample. This law is given by: $P = \epsilon \sigma A T^4$, where P is the radiative heat lost, ϵ is the emissivity of the sample, σ is the Stefan-Boltzmann constant, A is the surface area of the sample, and T is the temperature of the sample. Thus, the actual thermal conductance of the sample is the measured component minus the radiative heat loss. To account for this loss in samples with unknown emissivity a standard glass sample was used to determine the typical radiative loss:

$$K_{Rad} = 0.00146 * \left(\frac{T}{300}\right)^3 \tag{2.6}$$

where K_{Rad} is the radiative heat loss. Using this term the total thermal conductivity of the sample could be found from the equation:

$$\kappa = (K - K_{rad}) * \frac{L}{S} \tag{2.7}$$

where L is the thermocouple probe separation and S is the area of the sample. The dependency of the conductivity to the dimensions of the sample highlight the importance of having accurate dimensional measurement. To reduce the inherent error in the thermocouple separation measurement the thermocouples should be separated as far as possible while still allowing space for heat and electrical current flow to be homogeneous. To account for this thermocouples were soldered onto the sample surface a minimum of 2 mm away from the

ends of the sample. Thus, a typical thermocouple probe separation was approximately 5-6 mm. The error in this measurement is still estimated to be up to 10% due to inaccuracy in dimension measurement, system error, and the radiative heat loss term.

To determine the Seebeck coefficient of samples the voltage drop obtained between the copper contacts of the thermocouples were measured using a Keithley 2000 multimeter with the heater energized. With the known voltage and temperature drop between thermocouple probes the Seebeck coefficient may be directly obtained from: $\alpha = \frac{V_S}{\Delta T}$, where V_S is the voltage drop between copper leads from the thermocouples and the ΔT is the same temperature drop between the thermocouples as before. The error in this measurement is estimated to be 5% due to inherent inaccuracy in measuring the temperature gradient and the relatively low voltages generated due to the Seebeck effect.

The four probe electrical resistivity measurement method was used for samples where again the voltage drop along the sample was measured between the copper leads of the thermocouples. For this measurement the sample current is sourced in one direction and then reversed to account for any contact resistances or the generation of a Seebeck voltage from Joule heating. The equation describing this is:

$$\rho = \frac{V_S}{I_S} * \frac{S}{L} \tag{2.8}$$

where I_S is the current passed through the sample. Sample dimensions are found to play a role in evaluating another measured property which further highlights the need for accurate sample dimensional measurement. The error in this measurement is also estimated to be 5% primarily due to dimensional measurement.

2.2.3 Hall Effect Measurement

The Hall effect is due to the presence of an orthogonal force, the Lorentz force, acting on moving charge carriers in the presence of a magnetic field [71]. This force is dependent upon the electric field acting on the charge carriers and the magnetic field by:

$$\mathbf{F} = q\left[\mathbf{E} + (\mathbf{v} \times \mathbf{B})\right] \tag{2.9}$$

where $\mathbf{F}$ is the Lorentz force, $\mathbf{E}$ is the electric field, $\mathbf{v}$ is the drift velocity of carriers, and $\mathbf{B}$ is the magnetic field. The cross product of $\mathbf{v}$ and $\mathbf{B}$ yields a transverse component which causes a migration of charge carriers to one side of a sample. This buildup of charge generates a measurable voltage across the sample. This voltage is termed the Hall voltage and is given as:

$$V_H = \frac{IB}{nte} \tag{2.10}$$

where I is the current, t is the thickness of the sample, and n is the charge carrier concentration. A Hall coefficient, R_H, may then be defined as:

$$R_H = \frac{V_H t}{IB} = \frac{-1}{ne} \tag{2.11}$$

Using Hall testing the carrier concentration of a sample may be obtained and subsequently the carrier mobility may be determined by the relation: $\sigma = ne\mu$; in the single carrier system. A schematic representation of this system may be seen in Figure 2.4

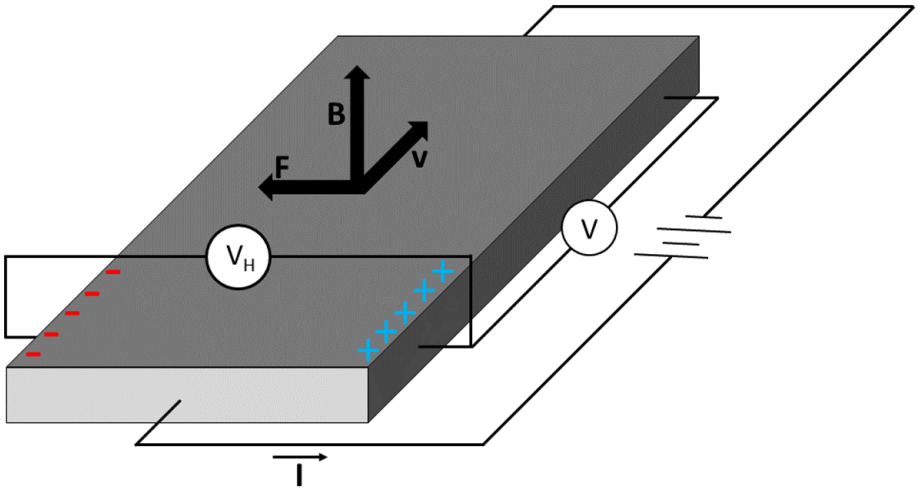

Figure 2.4: Schematic of Hall Effect Measurement Setup

To perform these measurements samples of dimensions ≈ 0.25 mm x 3 mm x 8 mm with a probe separation of approximately 5 mm were used. The thickness of samples was minimized to result in higher signal to noise ratios in obtaining the Hall voltage. Samples were mounted onto a flat copper base with 2 layers of cigarette paper to act as an electronic barrier, yet still provide good thermal contact. All sample contacts were soldered on to encourage good electrical contact with the sample. Magnetic fields ranging between 0 to 2 Tesla were used to measure the Hall voltage from 80 to 350 K as measured with a Lakeshore 421 Gaussmeter. The standard four probe electrical resistivity measurement method was used to determine the resistivity of the sample at all temperatures measured using a Lakeshore 370 AC Resistance Bridge. Samples were sealed in an evacuated atmosphere of approximately 10^{-5} torr with a liquid nitrogen flow to reach 80 K. A Lakeshore temperature control meter was used to stabilize the system at each temperature.

Chapter 3

Background on $PtSb_2$

3.1 Low Temperature Thermoelectric Materials

Thermoelectric materials research for low temperature applications, typically room temperature and lower, is an area of the field with relatively less work compared to the mid temperature and high temperature regions of application. Since the 1950's the reigning material for room temperature applications has been Bi_2Te_3. Work by Goldsmid and Douglas established Bi_2Te_3 [5, 72, 73] with zT values approaching unity around room temperature. Over the past sixty years further work devoted to doping and solid solution alloying with Sb_2Te_3 have been able to increase the zT of this material to values above unity up to temperatures of 500 K [74–76]. Possibly of even more importance, Bi_2Te_3 and its alloys have the capability of assuming p- and n-type properties such that a thermoelectric module may be made from the same base compound. This is highly beneficial because of the need to have similar thermal expansion coefficients for the materials in a thermoelectric module to avoid cracking from thermal cycling stresses. This has made Bi_2Te_3 the "go-to" material for commercial application and use near room temperature.

These optimized Bi_2Te_3 alloys are limited to use around room temperature due to a drop-off of their properties outside of this region. At temperatures lower than 250 K other

materials have been found to have superior properties. Work by Smith and Wolfe established the solid solution of bismuth and antimony as a material which shows superior properties to Bi_2Te_3 at temperatures between 20 and 220 K [77]. Work with Bi-Sb alloys has been able to show further enhancement due to the presence of a magnetic field, but even in a zero field, this n-type material, with a Bi rich composition of 15% Sb, showed a figure-of-merit maximized at 80 K with a zT ≈ 0.5 [78].

Further work in the low temperature region for thermoelectrics has been sparse due to the dominance of these two compounds. A material that has shown promise as a potential low temperature candidate is $CsBi_4Te_6$. This layered material, which is structurally distinct from Bi_2Te_3, shows superior zT to Bi_2Te_3 at low temperatures until approximately 275 K with a maximum at 225 K of zT ≈ 0.8 [79].

FeSi first garnered interest due to its unusual magnetic properties [80], but later showed a very large Seebeck coefficient of approximately 500 μV/K at 50 K [81]. This large Seebeck coefficient was shown to be from a phonon-drag effect, which correlated to a large thermal conductivity at the same temperature. Many attempts have been made to dope FeSi to enhance its thermoelectric properties, with the best dopant being found to be iridium [82]. This dopant showed a maximized zT = 0.12 for planetary milled samples at 100 K.

Other possible materials for low temperature application include those of the intermediate valence systems such as $CePd_2Pt$ with a zT approaching 0.3 below room temperature and YbScAl [83, 84]. These systems allow for the chemical pressure tuning of the electronic properties by simple substitution methods and make use of a complex electronic structure with very sharp electronic density of states due to f-shell electrons. However, they still show lower performance than the Bi-Sb alloys examined so long ago.

For further enhancement of the figure-of-merit at low temperature extensive work should

be performed on known, as well as, unknown materials. The serendipitous finding of $CsBi_4Te_6$ as a superior thermoelectric demonstrates the possibility that there are still material candidates as yet unknown for low temperature applications.

3.2 $PtSb_2$

3.2.1 Crystal Structure and Phase Diagram

$PtSb_2$ is a semiconducting material which crystallizes in the cubic pyrite structure with space group ($Pa\bar{3}$). To start, a comparison to the rocksalt, NaCl, structure may be made. Pt atoms occupy the cation Na sites in a face centered cubic arrangement, with positions: (0, 0, 0), (1/2, 1/2, 0), (1/2, 0, 1/2), and (0, 1/2, 1/2). The anion site is occupied by an Sb dimer pair with positions: ±(x, x, x), ±(-x, x+1/2, 1/2-x), ±(1/2+x, 1/2-x, -x), and ±(1/2-x, -x, 1/2+x) with internal parameter x = 0.375 [85]. The Sb dimers are oriented parallel to the <111> directions with a Sb-Sb separation of 2.78 Å [86]. The lattice parameter through theoretical calculations and experimental work has been found to be $a = 0.644$ nm [85, 87]. Platinum atoms are octahedrally coordinated with 6 bonded antimony atoms while antimony atoms are tetrahedrally bonded to three platinum atoms and one other antimony atom. Figure 3.1 shows a schematic of the pyrite crystal structure generated from the software Vesta [88].

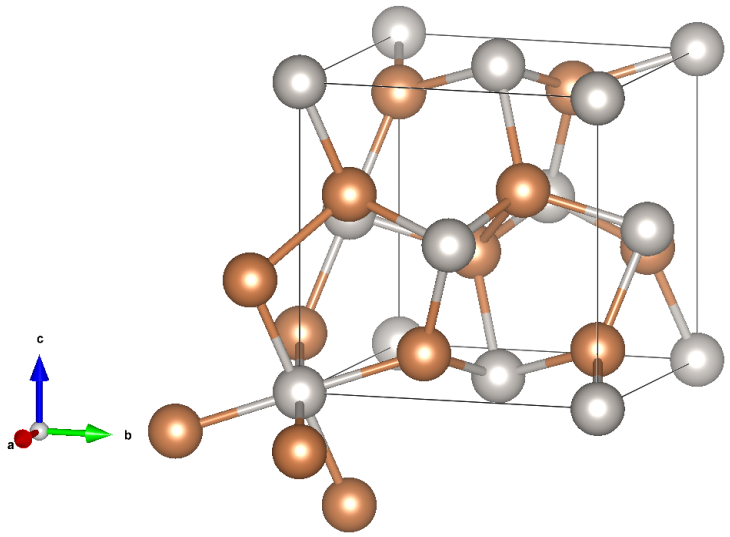

Figure 3.1: Schematic of Pyrite Crystal Structure Showing Pt - Sb Local Bonding

Visible in this schematic is the distortion of the octahedral coordination of Pt where the angles between Sb-Pt-Sb groups are no longer 90°. Due to this distortion local symmetry is reduced from cubic to trigonal and it can also be seen that there is a rotation of the octahedral axis away from the cubic lattice of approximately 24° [89].

$PtSb_2$ shares the pyrite crystal structure with several compounds, the namesake compound, FeS_2, CoS_2, $MnTe_2$, $RuSe_2$ and $RuTe_2$, $AuSb_2$, $PdAs_2$ and $PdSb_2$, and $PtPn_2$, where Pn = S, As, Sb, and Bi [90] [91]. The most exciting of these from the thermoelectric point of view are the Pd and Pt based pyrite compounds due to the possibility of making a variety of solid solutions which could lead to a reduction in the lattice thermal conductivity.

Using nuclear magnetic resonance Mallick and Emtage determined the likely formal valence state of $PtSb_2$ to be $Pt^{2-}Sb_2^{+}$ [92]. This valence state points to nearly only covalent bonding in $PtSb_2$, which is what would be expected due to the small difference in their Pauling electronegativities, χ, Pt(2.28) and Sb(2.05). The Sb-Sb dimers would be expected to be entirely covalent and the Pt-Sb bond dipole would be very small with a $\Delta\chi = 0.23$ which

would lend itself to being almost entirely covalent bonding [93]. Work by Lutz et al. have shown that $PtPn_2$ compounds going down the column of the periodic table have increasingly stronger bonding which further supported the claim of primarily covalent bonding in this system [94]. With the strong bonding found in $PtSb_2$ it is unsurprising that this compound has a high melting point of 1226 °C [95]. Itkin and Alcock presented the phase diagram of $PtSb_2$ where it is found that $PtSb_2$ forms by a congruent phase transformation from the liquid phase at an atomic% Sb of 66.7% to the intermetallic $PtSb_2$ [96]. The phase diagram for $PtSb_2$ is shown in Figure 3.2.

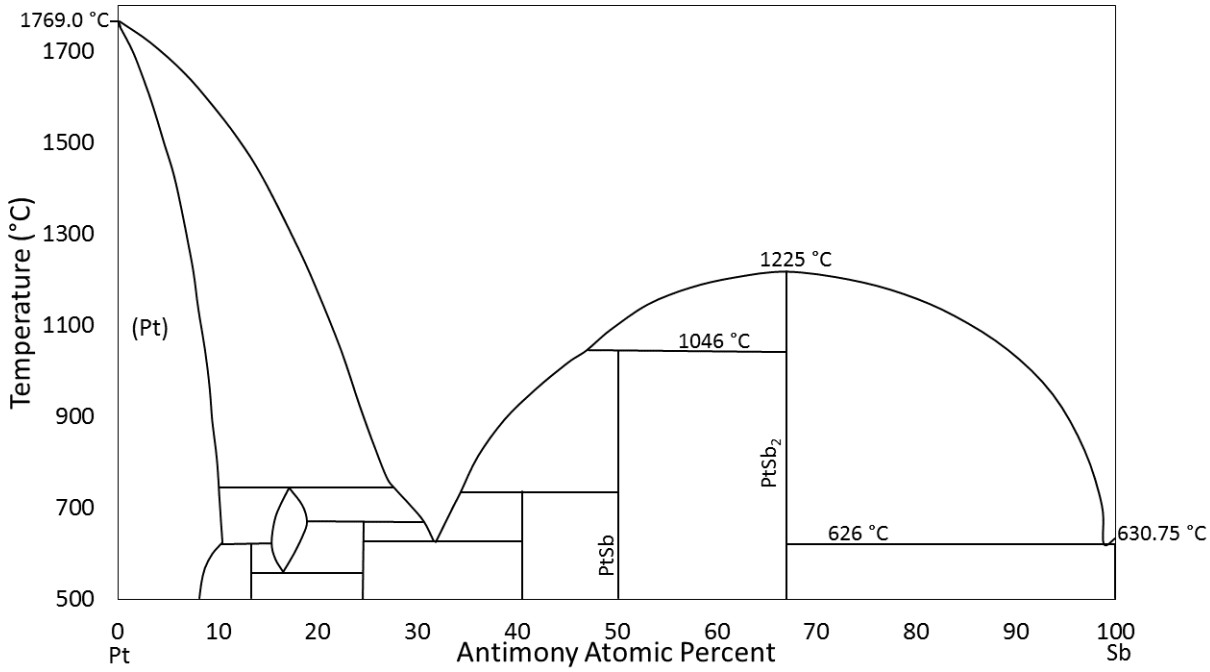

Figure 3.2: Schematic Phase Diagram of the Pt-Sb System

3.2.2 Electronic Structure and Transport Properties

Much of the early work with $PtSb_2$ was performed on single crystals to determine the electronic properties of the compound. This early work established that $PtSb_2$ is a narrow-gap semiconductor with a bandgap of approximately 0.1 eV [97–99]. Work by Damon et al.

examined the magnetoresistance and piezoresistance of $PtSb_2$ single crystals to find a likely valence band maxima was located on the <100> directions [98]. Emtage built upon this work using theoretical modeling and made electronic band structure calculations that would last for the next 40 years. Emtage calculated that it is non-bonded d-orbitals that take part in the formation of the conduction and valence bands. He found that there are valence band maxima in the <100> directions and conduction band minima along the <111> directions, which give rise to an indirect bandgap of $E_G \approx 0.08$ eV. A schematic representation of the energy band diagram of $PtSb_2$ is given in Figure 3.3 modified from that generated by [100]. Damon et al. later supported the valence band maxima being on the <100> directions and further showed that this was from six ellipsoid bands which produced unequal inertial effective masses, m_1, m_2, and m_3 with ratios of 0.61:1:1.64 [101]. They additionally countered Emtage's earlier finding of an energy dependent band structure and gave a direct gap of $E_G > 0.4$ eV.

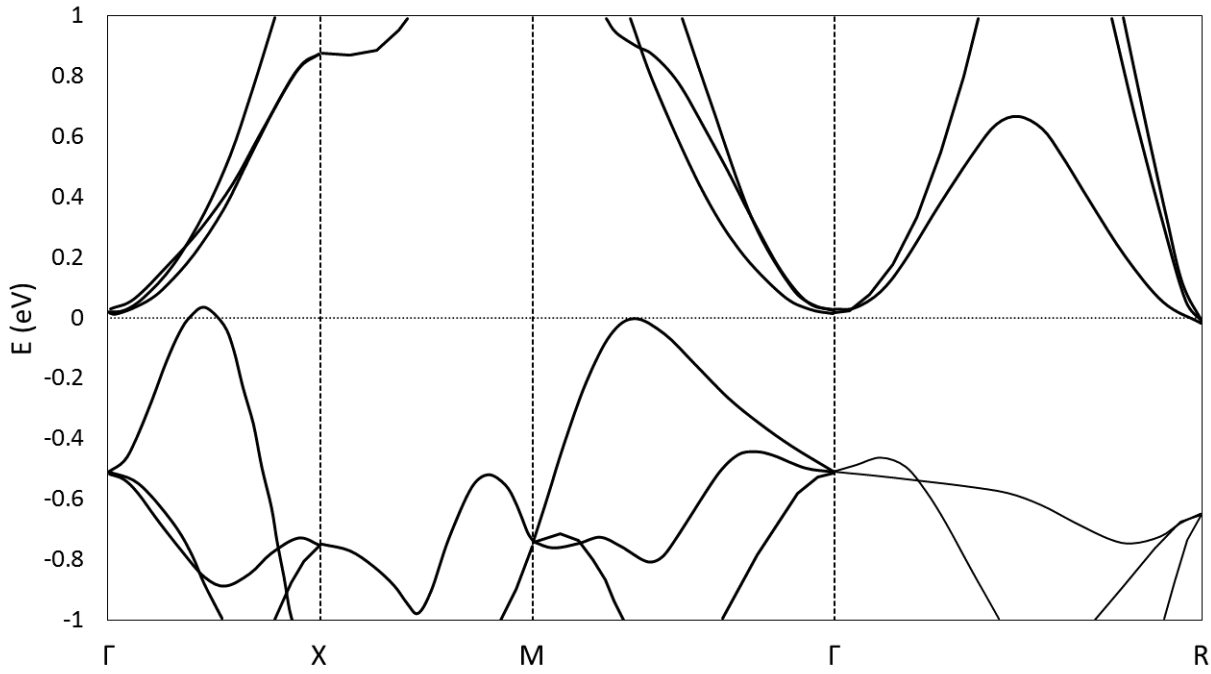

Figure 3.3: Schematic Energy Band Diagram of $PtSb_2$

Much of this early work on $PtSb_2$ on single crystals had an interesting finding that even when samples were undoped a large variation in carrier concentration and even dominant charge carrier was found. Several groups provided further validation of the energy gap being $E_G \approx 0.1$ eV and showed that acoustic phonon scattering was the dominant mechanism above 50 K, however found a large variation for many single crystal carrier concentrations ranging between $c.c. \approx 1 * 10^{16}$ to $1.5 * 10^{18}$ and also disagreed on the dominant carrier type [102–106]. These deviations are thought to have occurred because of variations in stoichiometry due to the loss of antimony when melting the compound in preparation for single crystal growth. More recent work on single crystal and polycrystalline samples showed that a non-stoichiometry due to antimony loss can create n-type samples at room temperature and below [100, 107].

Several doping experiments have been performed on $PtSb_2$ to examine its resultant behavior. Dargys and Kundrotas in 1983 examined the effects of tellurium doping on single crystals and found with low but, unfortunately, unspecified dopant concentration at T $\approx$ 25 K a very large Seebeck coefficient can be obtained at almost -800 $\mu V/K$ [108]. It was evident though that the $PtSb_2$ structure has a limited ability to incorporate dopants from the work of Laudise et al. and Bennett et al. In an attempt to make a magnetic semiconducting material Laudise et al. worked with the solid solution of $PtSb_2$ and the magnetic Heusler compound PtMnSb. However, with concentrations of x=0.25 and higher in $PtSb_{2-x}Mn_x$; secondary phases were found [109]. In the work by Bennett et al. the doping of several rare earth elements were attempted in $PtSb_2$. Again, it was found that secondary phases were produced from these dopants which in the case of $Pt_{1-x}Yb_xSb_2$ created a superconducting material [110]. This superconducting activity is thought however to have come from the secondary phase in the system of PtSb, which is superconducting at $T_c = 2.1$ K [111].

Successful p-type doping on the Pt site in $PtSb_2$ was obtained by Nishikubo et al. by Ir doping in a polycrystalline sample [112]. A large enhancement to the power factor was obtained largely from a decrease in electrical resistivity. A decrease in the Seebeck coefficient was found at low temperature, but above 300 K, in their lightest doped sample, the Seebeck coefficient surpassed the un-doped material. The power factor was found to be approximately 18 μW/cm-K^2 at 150 K for the un-doped sample with an increase to approximately 43 μW/cm-K^2 at 400 K. Diminished thermal conductivity was additionally found in the doped samples which ultimately gave an enhanced figure-of-merit.

Theoretical work by Mori et al. suggested that the origin of the large power factor found by Nishikubo et al. was due to a corrugated flat band structure found in $PtSb_2$ [113]. This work hearkened back to that of Emtage who found that a low energy barrier separated the maximum in the valence band between another high lying band which created a wide dispersive region separated by a 0.011 eV energy barrier. Typically, in a metal where the Fermi energy is within a band, to have a large Seebeck coefficient the Fermi energy must be near the band edge where the group velocities of electrons and holes will differ. This in turn reduces the carrier concentration which negatively affects the power factor. Mori et al. argued that due to the corrugated flat band structure in $PtSb_2$ hole doping did not cause a large decrease in the Fermi energy which left the large Seebeck coefficient intact. This can further be seen in theoretical work on electron and hole doping of $PtSb_2$ and experimental polycrystalline work on tellurium doping [114, 115].

A final consideration for $PtSb_2$ is due to its narrow bandgap. The small bandgap of only 0.1 eV creates the maximum in the Seebeck coefficient found at approximately 150 K due to the population of electrons at this temperature from the material entering into the intrinsic regime at this point. For the application of $PtSb_2$ at very low temperatures this

very narrow bandgap is ideal, but for applications approaching room temperature, a wider bandgap would be superior. This point was given by Mori et al. who concluded that the materials PtP_2 and $PtAs_2$ would be better candidates at higher temperatures due to their larger bandgaps. This point was proven by Kudo et al. when they examined rhodium doping of $PtAs_2$ [116]. The thermoelectric properties were examined from 2 to 600 K and found the Seebeck coefficient increased over the entire temperature range and a maximized power factor of 65 μW/cm-K^2 at approximately 440 K. Thus, the solid solution of $PtSb_2$ with these materials may be a route of engineering the bandgap in $PtSb_2$.

3.3 Nominally Undoped $PtSb_2$

3.3.1 Synthesis

As outlined in chapter 2 undoped $PtSb_2$ was synthesized by the solid-state reaction of elemental chunks of Pt and Sb in an evacuated quartz tube at 800 °C. Samples were allowed four days to react to completion and were subsequently quenched to room temperature via a water bath. A solid-state reaction was necessitated due to the high melting point of platinum and the end compound, 1769 °C and 1226 °C respectively. Neither the furnaces used in synthesis or the quartz tubes would have been able to facilitate such a high temperature to allow for the liquid state to have been met and subsequently water quenched. Additionally, due to the work of prior research it was known that many samples resulted in non-stoichiometry due to the loss of antimony from its high vapor pressure at the melting point of $PtSb_2$. Since antimony has a low melting point relative to platinum and $PtSb_2$ at 630 °C the synthesis was allowed to proceed by way of diffusion. At a furnace temperature of 800 °C antimony would melt and diffuse into and react with platinum to synthesize the desired end product.

Experimentation on reducing and prolonging the reaction time generated secondary phases with a decreased time and produced no benefit from prolonging the reaction time. To prepare samples for X-ray diffraction and subsequent densification via SPS a mortar and pestle was used to grind samples into a powder.

For nominal $PtSb_2$ two different SPS parameters were used to densify samples. In the early experimentation of this work the parameters were a slow ramp to 900 °C over 30 minutes where the sample was then held at this temperature for 30 minutes and then slowly cooled to room temperature over 30 minutes at a pressure of 40 MPa. This produced samples with greater than 95% theoretical density, but it was later found that a much shorter sintering time could be used while retaining the near theoretical density. The shortened SPS parameters were a ramp to 900 °C over 7 minutes with a dwell time of 10 minutes at 40 MPa of pressure. After the 10 minutes of sintering the current was turned off, the pressure was removed, and the sample was allowed to cool to room temperature limited by the rate at which the water cooled graphite dies could dissipate heat.

Cylindrical samples densified by SPS were then cut by diamond saw and either prepared for mounting on the cryostat, Hall measurement, or ground for XRD analysis as were all future samples.

3.3.2 Structural Properties

The X-ray diffraction pattern of $PtSb_2$ is shown in Figure 3.4 compared against the theoretical pattern generated from Vesta using the parameters obtained by Brese et al. [86, 88]. It was found that the obtained pattern matched well with previous literature and yielded a lattice parameter of $a = 0.643$ nm as determined by the inclusion of a silicon standard.

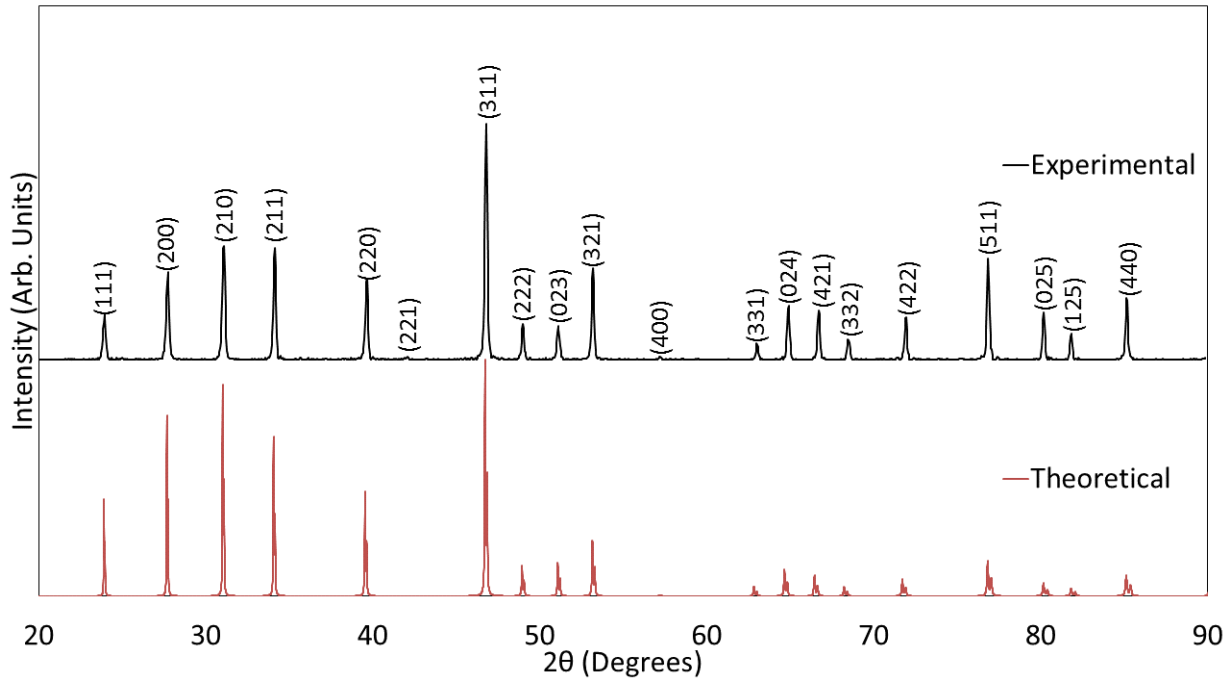

Figure 3.4: X-ray Diffraction Pattern of $PtSb_2$

At high 2θ double peaks may be observed in the theoretical pattern due to the inclusion of Cu-K_{α_2} peaks. These peaks have been removed from the experimental data for ease of analysis.

3.3.3 Electrical Properties

The Seebeck coefficient of $PtSb_2$ is shown in Figure 3.5 compared with data on polycrystalline samples by Johnston et al. and Nishikubo et al. [90, 112].

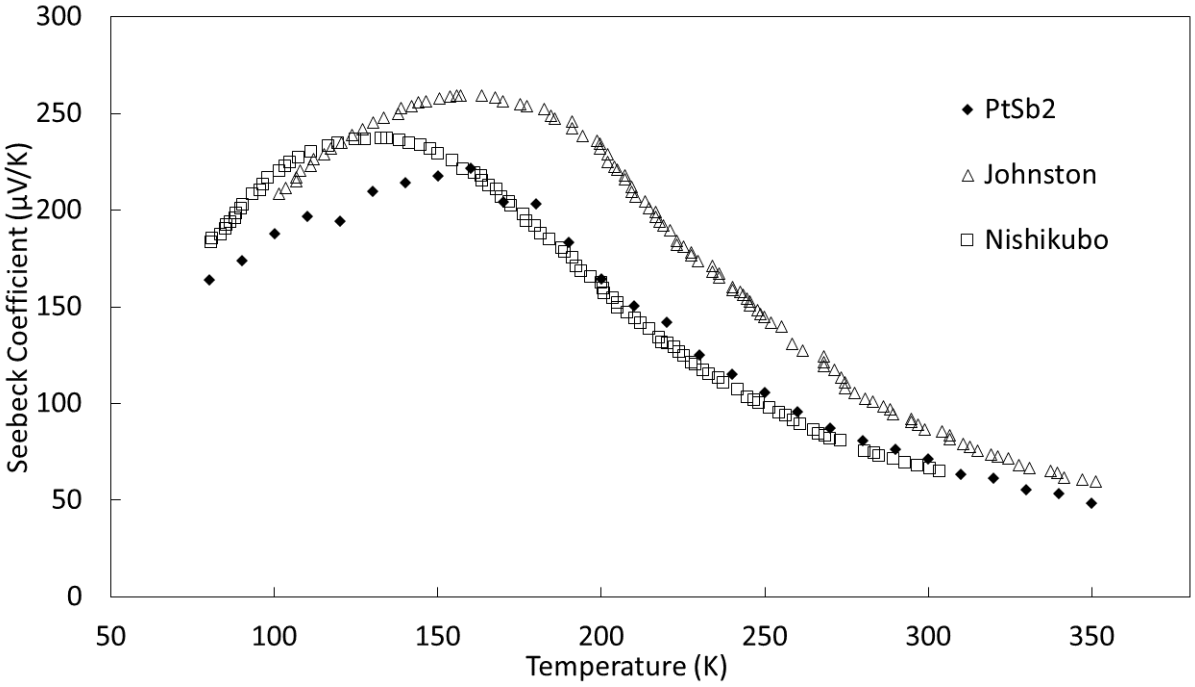

Figure 3.5: Seebeck Coefficient of $PtSb_2$

It is shown that using this synthesis procedure the same p-type Seebeck coefficient is found, however, its overall magnitude is shown to be diminished. Compared with the work of Nishikubo et al. it is seen that the peak in Seebeck coefficient found in that work was at a lower temperature, 130 K, than that found in this work, 150 K. This is indicative of a narrower bandgap in the work by Nishikubo et al. with the onset of bipolar conduction occurring at a lower temperature and is also indicative of a lower carrier concentration in their sample at this temperature due to the increased magnitude. However, above 160 K the magnitudes of both sets of data match and follow the same trend. Compared to Johnston et al. it is seen that the peak in Seebeck coefficient occurs at the same temperature, yet, it is only at high temperatures, > 300 K, that the magnitudes begin to converge, elsewhere the magnitude of the Seebeck coefficient is greater. The overall increased magnitude of Johnston's results is indicative of lower carrier concentration or a difference in mobility across

the entire temperature region measured. Though diminished compared to these other results the Seebeck coefficient found, from as prepared $PtSb_2$, is very large at low temperatures with a maximum at 160 K of 220 μV/K. This highlights the interest in this compound for low temperature Peltier coolers: few materials have such large Seebeck coefficients in the cryogenic temperature regime.

The electrical resistivity of undoped $PtSb_2$ is shown in Figure 3.6, also compared with the work of Johnston et al. and Nishikubo et al. It should be noted that the y-axis is in a logarithmic scale to show the wide ranging data.

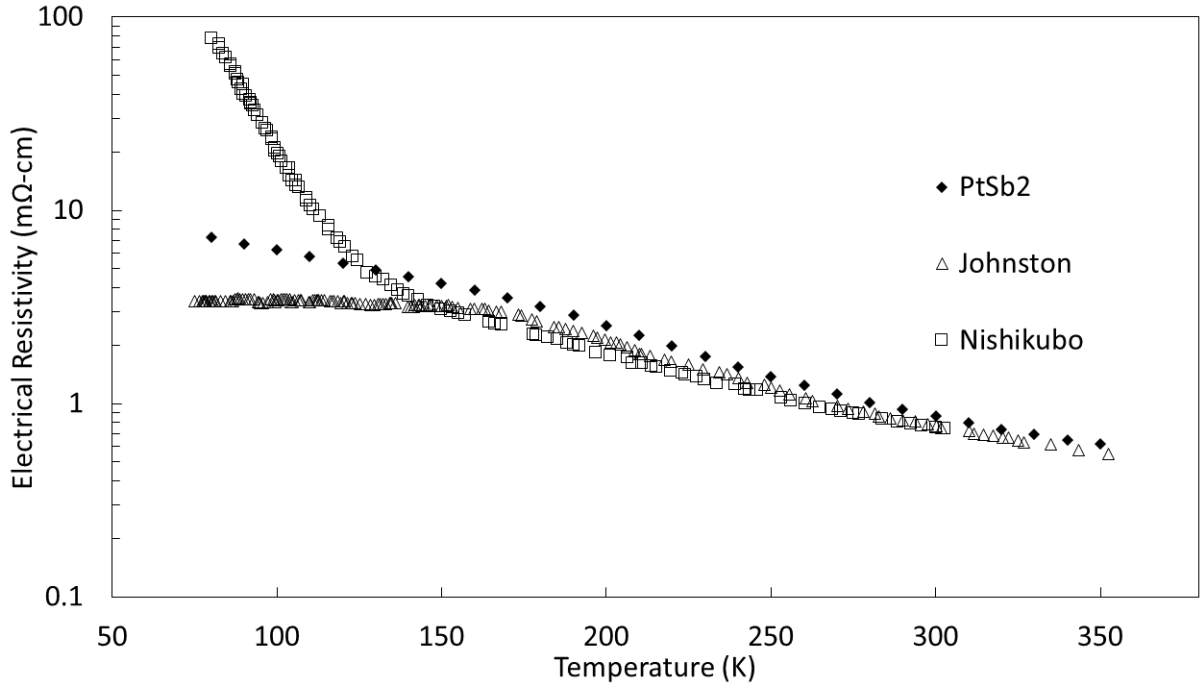

Figure 3.6: Electrical Resistivity of $PtSb_2$

Evidence for the lower carrier concentration of the Nishikubo et al. sample at low temperature can be gleaned from this figure. At 80 K the electrical resistivity found by Nishikubo is approximately an order of magnitude higher than that of this work and decreases rapidly until it matches the electrical resistivity of this work at approximately 130 K. The data of

Johnston et al. shows a relatively flat region until approximately 140 K, where it matches the values of this work and the work by Nishikubo et al. The flat portion of the work of Johnston et al. is thought to be in the extrinsic regime of carrier concentration which at 140 K enters the intrinsic regime and reduces the electrical resistivity.

Analysis of the electrical resistivity found from this work can best be done in conjunction with Hall effect data as shown in Figure 3.7.

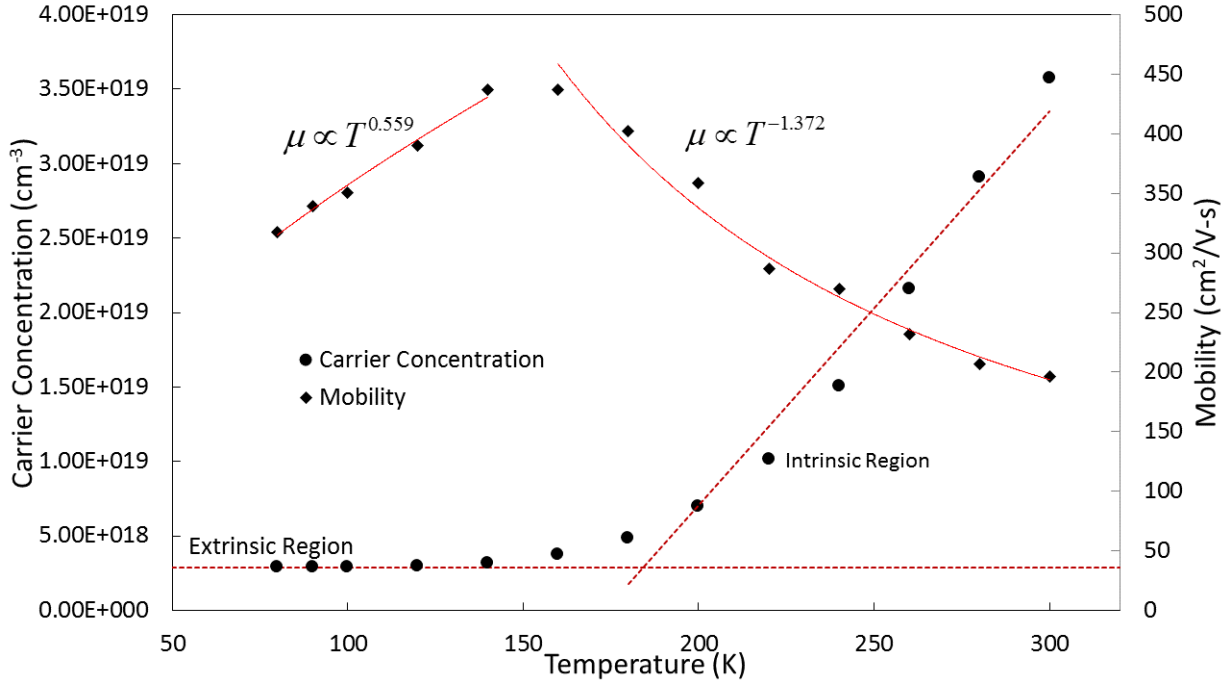

Figure 3.7: Carrier Concentration and Mobility of $PtSb_2$

It is found that the carrier concentration from 80 to 140 K is relatively unchanged, however the mobility in this temperature region is increasing with a $T^{0.5}$ dependency. This effect is what resulted in the decrease of the electrical resistivity in this region where the results of Johnston et al. did not. At approximately 150 K the carrier concentration began to increase rapidly. Fitting the curve where intrinsic carriers are being populated the band gap may be found to be $E_G \approx 0.16$ eV. While the carrier concentration is increasing the

mobility is found to decrease with a $T^{-3/2}$ temperature dependency. This is indicative of acoustic phonon dominant scattering as was also found by Reynolds et al. in this temperature regime [103]. As the mobility decreases by a factor of 2 from 140 K to 300 K the carrier concentration increases by an order of magnitude, which resulted in the observed continued reduction of the electrical resistivity in this temperature region.

3.3.4 Thermal Properties

The total thermal conductivity of $PtSb_2$ is shown in Figure 3.8 compared with that found by Nishikubo et al.

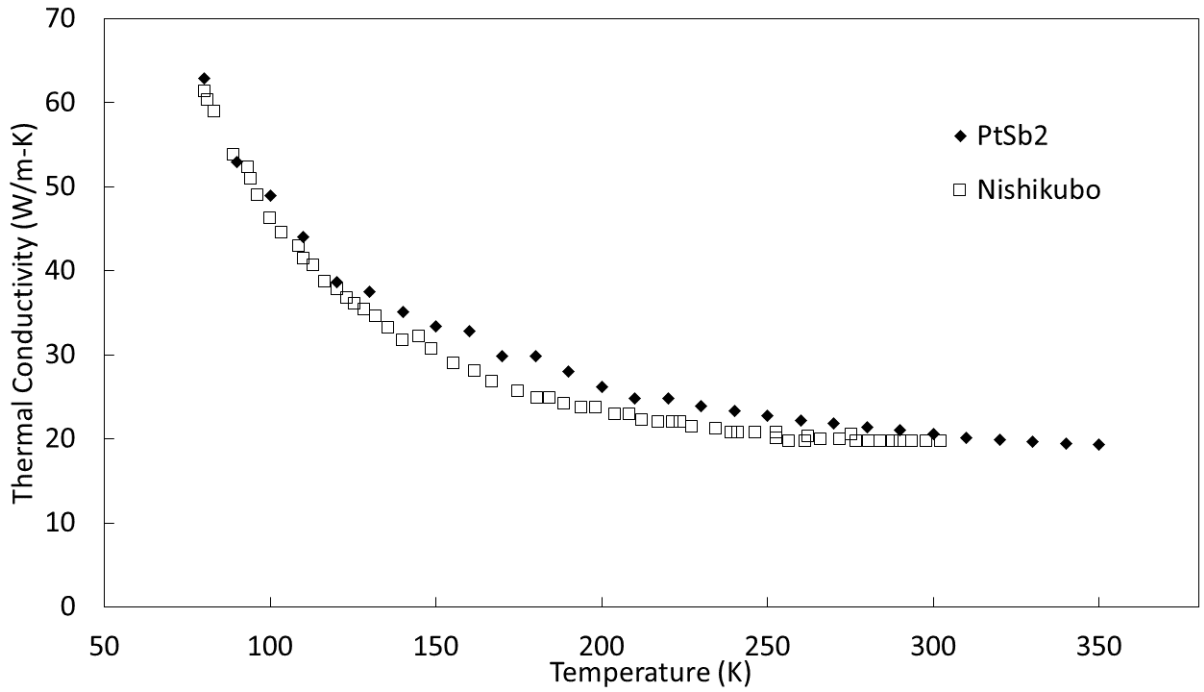

Figure 3.8: Total Thermal Conductivity of $PtSb_2$

Good agreement is found between the results of this work and that of Nishikubo et al. At 80 K the thermal conductivity is found to be very large at approximately 63 W/m-K. This is found to be the maximum over the temperature range examined due to the low

Debye temperature of this material. Above this temperature the specific heat is maximized and Umklapp scattering is the dominant scattering mechanism. The thermal conductivity is found to decrease with a $T^{-0.77}$ temperature dependency, which indicates a mix of scattering mechanisms over this temperature region. Compared with the standard commercial thermoelectric material Bi_2Te_3 this thermal conductivity is much too high and should be lowered for enhanced figure-of-merit.

Examination of the individual contributions to thermal conductivity in Figure 3.9 shows that the lattice contribution to thermal conductivity is dominant over the entire temperature range. The electronic contribution is determined using the Wiedemann-Franz law as described in section 1.5.1.

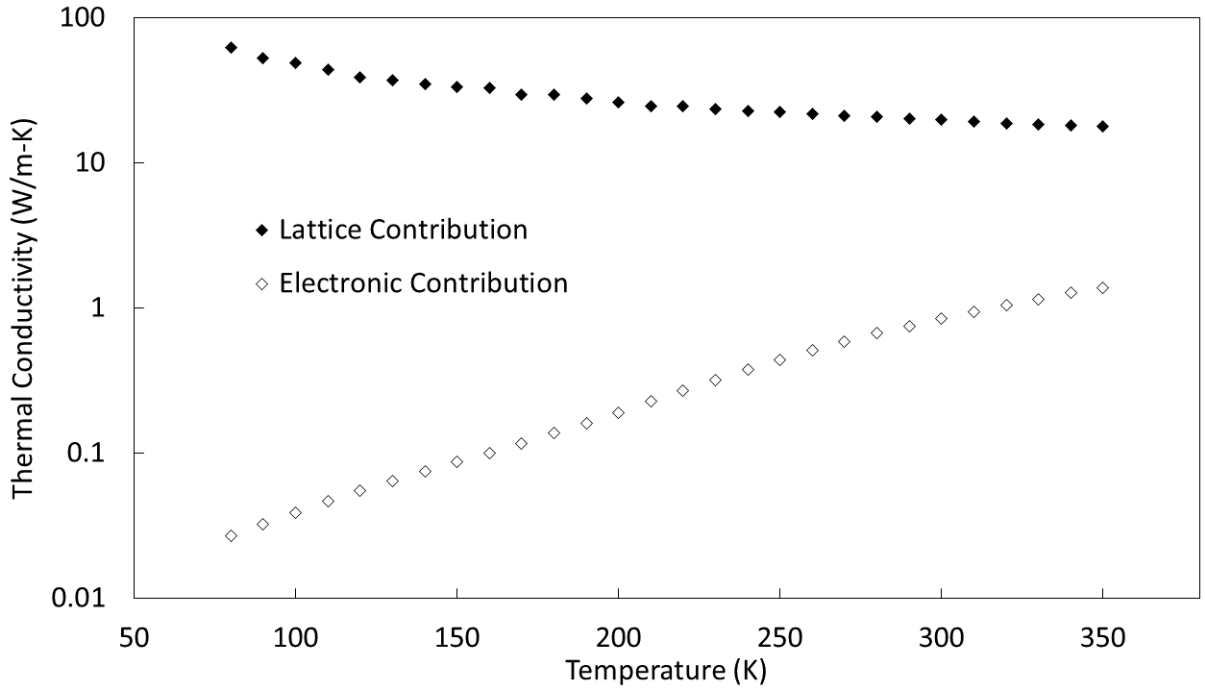

Figure 3.9: Lattice and Electronic Contributions to Thermal Conductivity of $PtSb_2$

The electronic contribution to thermal conductivity begins with a very low value at 80 K, where the electrical resistivity of $PtSb_2$ is at its maximum, and increases over the entire temperature range as the electrical resistivity is found to decrease. The lattice contribution

is found to be over an order of magnitude larger than the electronic contribution and will be an opportune parameter to minimize for figure-of-merit enhancement.

The magnitude of the figure-of-merit of nominal $PtSb_2$ is low for all temperatures measured, but reaches a maximum between 220 to 250 K at a value of zT ≈ 0.009. Compared to commercially maximized Bi_2Te_3 this value is almost two orders of magnitude too low. However, as will be shown in the forthcoming chapters several avenues of enhancement are possible in $PtSb_2$ that can increase its figure-of-merit substantially.

Chapter 4

Antimony Site Doping in $PtSb_2$

4.1 Background and Motivation

Electronic doping provides a "tuning knob" by which the carrier concentration and ultimately the power factor of a thermoelectric material may be optimized. There are several considerations when optimizing the power factor of a narrow bandgap material, which will be shown here, but this method has been proven to increase the figure-of-merit.

The most dramatic of these considerations occurs in the Seebeck coefficient. It is well known that as the carrier concentration of a material increases the Seebeck coefficient decreases, thus, when the nominally p-type $PtSb_2$ is p-type doped it is expected that this will increase the carrier concentration and subsequently decrease the Seebeck coefficient. However, an interesting effect occurs when a p-type material is doped with a donor atom. At high dopant concentrations the nominally p-type material will exhibit a negative Seebeck coefficient. This denotes that electrons are now the dominant charge carrier in this system as compared to the intrinsic holes. As the concentration of n-type dopant is decreased the magnitude of the Seebeck coefficient will increase due to fewer competing carriers and the peak in the Seebeck coefficient will shift to lower temperatures due to fewer intrinsic hole carriers needing to be populated to overcome the effect of the extrinsic electrons. At some very low

concentration, dependent upon the material and intrinsic carrier concentration, the Seebeck coefficient will reach a maximum in the magnitude of the negative Seebeck coefficient it will display. After this maximum has been met a subsequent decrease in the dopant concentration will not dope a sufficient concentration of electrons to create an n-type material, and the typical p-type Seebeck coefficient will re-emerge.

This chapter will focus on electronic doping on the antimony site of $PtSb_2$. In previous literature few dopants have been examined on the antimony site with even fewer making a comprehensive examination over low temperature. The work by Dargys and Kundrotas examined the effects of low dopant concentrations of tellurium on the antimony site. Their work found significant enhancement in the Seebeck coefficient at low temperature reaching approximately -800 μV/K as well as observing a change in dominant carrier type [108]. In the work by Nishikubo et al. it was stated that the power factor of Sn doped $PtSb_2$ was increased to approximately 20 μW/cm-K^2 [112]. Further, theoretical work by Saeed et al. showed the enhancement that may be found in electron and hole doped $PtSb_2$ at room temperature and higher [114].

With this prior research it was shown that significant improvements in the power factor may be made, thus it was the goal of this work to perform a comprehensive examination of the potential thermoelectric enhancement of $PtSb_2$ via n- and p-type dopants on the antimony site.

4.2 Experimental Methods

To examine the effects of n-type dopants selenium and tellurium were selected due to the additional valence electron that they have compared with antimony. To examine the effects

of p-type dopants tin, germanium, and indium were selected since they have fewer valence electrons than antimony. Samples with compositions $PtSb_{2-x}Dp_x$, where Dp = Se, Te, Sn, Ge, or In were synthesized with dopant concentrations ranging between $0 < x < 0.15$. While dopant concentrations varied, the n-type donor concentrations were kept low and p-type acceptor concentrations spanned the entire range due to variations in the electronic effects of each dopant. Samples were synthesized in the same manner as outlined for nominal $PtSb_2$ though it should be noted that tellurium doped samples utilized the SPS parameters which entailed the 30 minute dwell time while all other dopants utilized the shortened SPS parameters.

4.3 Tellurium Dopant Results and Discussion

4.3.1 X-ray Diffraction

The X-ray Diffraction patterns of tellurium doped $PtSb_2$ are shown in Figure 4.1.

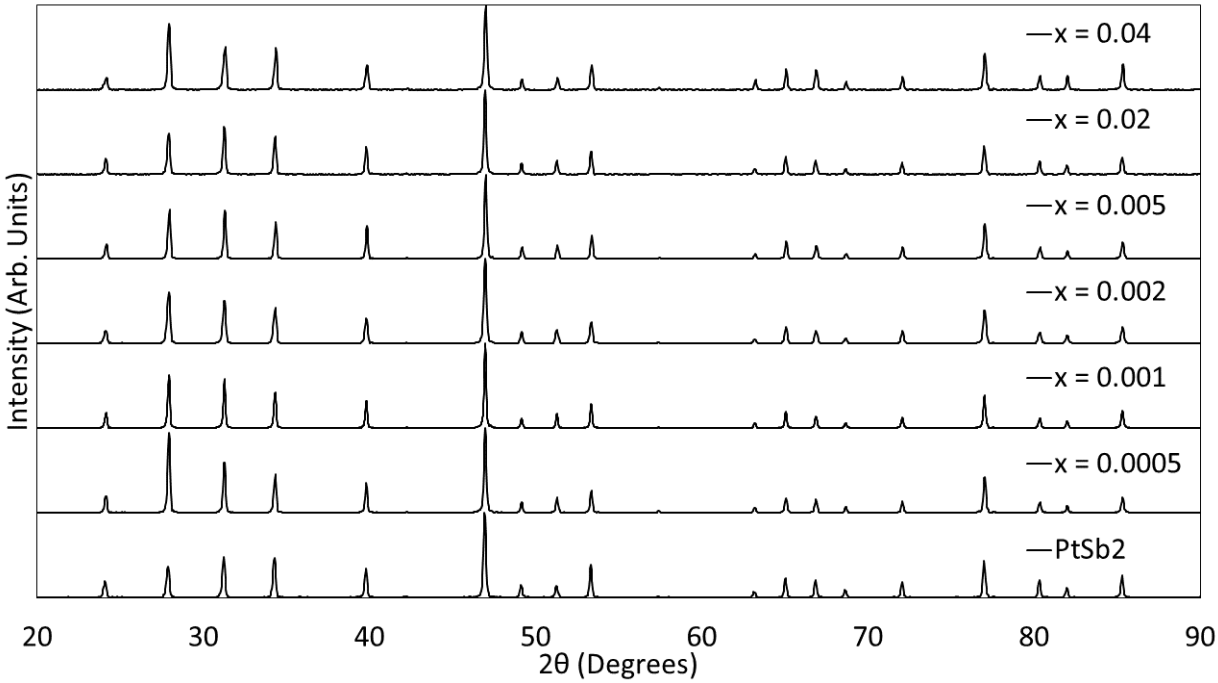

Figure 4.1: X-ray Diffraction of Tellurium Doped $PtSb_2$

It was found that there were no observable secondary phases with tellurium dopant concentrations of up to x = 0.04. It was additionally found that there were no shifts to lower 2θ values as tellurium dopant concentration increased which would be expected from an increasing lattice parameter. This is thought to be due to the low overall concentration of tellurium doped and the fact that the size difference between tellurium and antimony is small.

4.3.2 Electronic Properties

The results of low n-type dopant concentrations on a narrow bandgap semiconductor are shown very well by the results of tellurium doping. Examination of the Seebeck coefficient data in Figure 4.2 showed that a change in dominant charge carrier occurred with very low concentrations of tellurium dopant.

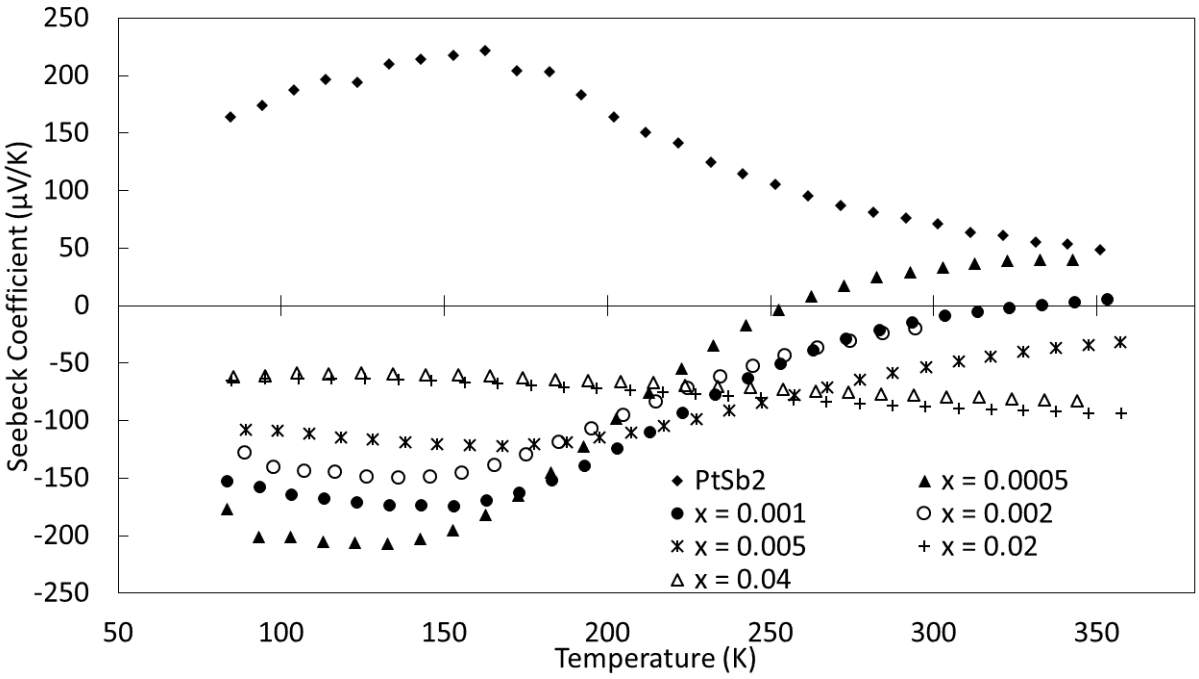

Figure 4.2: Seebeck Coefficient of Tellurium Doped $PtSb_2$

In the x = 0.02 and 0.04 samples an n-type sample was found with a low magnitude across all temperatures measured due to the high concentration of extrinsic carriers. With a reduction in the concentration of tellurium dopant it was found that the n-type character remained and further that the magnitude of the Seebeck coefficient was found to be increased at lower temperatures. These samples also showed a maximum, or peak in their trend, which decreased in temperature as dopant concentration was reduced. At low temperatures, in these low dopant concentration samples, the Seebeck coefficient increased with temperature until the thermal energy met that of the bandgap. At this temperature intrinsic hole carriers were then populated in the system which led to the competition of holes and electrons and caused a decrease in the magnitude of the Seebeck coefficient. At high enough temperatures, when the weighted contribution to the Seebeck coefficient of holes had surpassed that of electrons, the overall measured Seebeck coefficient was found to return to a positive value.

This effect was best shown in the x = 0.0005 sample with a maximum Seebeck coefficient of approximately -210 μV/K between 120 to 140 K. As temperature increased, and intrinsic carriers began to be populated, the sample became p-type between 250 and 260 K.

Comparing the results of the Seebeck coefficient with those of the electrical resistivity, shown in Figure 4.3, further evidence is shown for the bipolar conduction effects in this narrow bandgap material.

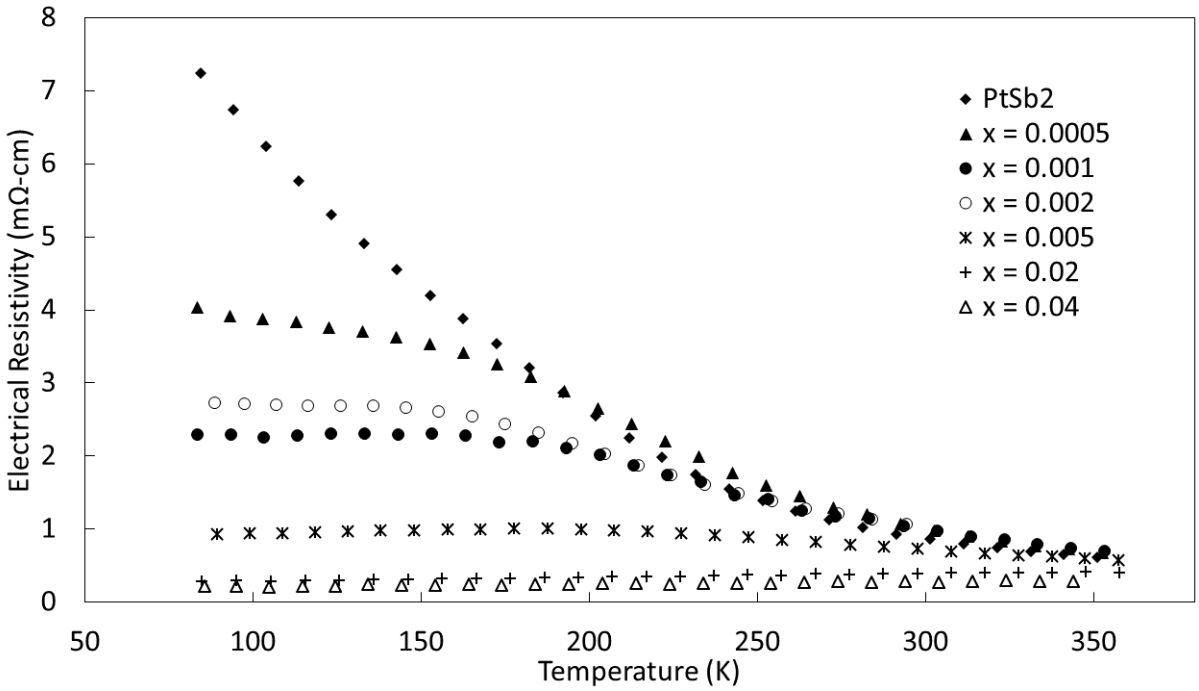

Figure 4.3: Electrical Resistivity of Tellurium Doped $PtSb_2$

Starting with the lightest dopant concentration of x = 0.0005 there is a marked reduction in the electrical resistivity at low temperatures compared with that of nominal $PtSb_2$. The effect of extrinsic doping is seen by the relatively flat trend in resistivity until such temperatures are met where intrinsic carriers begin to populate in the material. It was seen that at approximately 170 K the resistivity of this sample converged with that of undoped $PtSb_2$ at which point the intrinsic carriers were driving the electrical resistivity to lower

values. The electrical resistivity was found to be further reduced in the x = 0.001 and 0.002 samples illustrating the effect of increasing the dopant concentration. These samples again showed the onset of intrinsic carrier population at approximately 170 K with a change in the slope of their data that eventually converged with that of undoped $PtSb_2$. At the highest concentrations examined in this work, the x = 0.02 and 0.04 samples, a metallic electrical resistivity was found which was characterized by a flat trend. In these samples it was only at approximately 350 K where this data converged with that of the undoped $PtSb_2$.

The power factor of all doped samples showed enhancement at low temperatures. At 80 K undoped $PtSb_2$ has a power factor of 3.5 μW/cm-K^2 while that of the x = 0.04 sample is 17.5 μW/cm-K^2. As temperature increased the power factors of the lightly doped samples were maximized at varying temperatures, but the x = 0.02 and 0.04 samples, which showed the lowest electrical resistivity, were found to have a minimum between 120 to 130 K and then to progressively increase. The x = 0.04 sample showed the highest power factor at 350 K of approximately 24 μW/cm-K^2.

4.3.3 Thermal Properties

Examining the response of the thermal conductivity to n-type doping, shown in Figure 4.4, it was found that there was a general decrease as dopant concentration was increased.

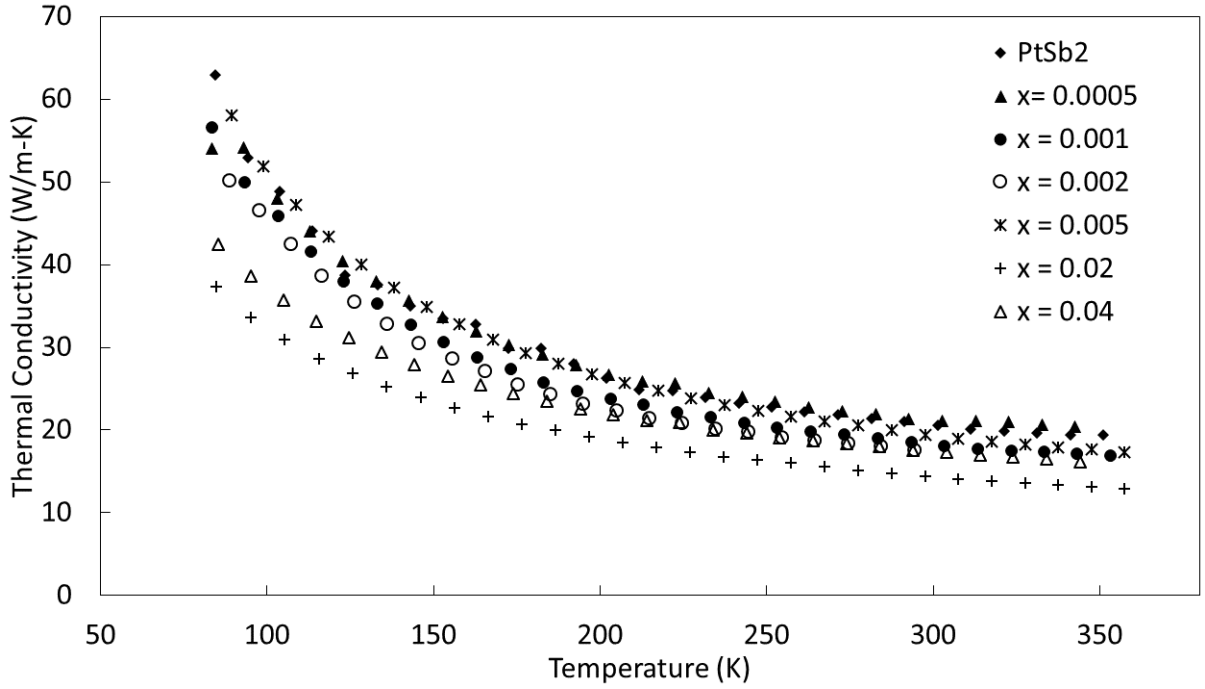

Figure 4.4: Thermal Conductivity of Tellurium Doped $PtSb_2$

At low temperatures the reduction was further pronounced due to the increased effect that ionized impurities have at low temperature compared to the effects of phonon-phonon scattering at higher temperatures. However, it was found that even with the reduction shown in these results further minimization techniques should be performed in future work.

Analysis of the electronic and lattice contributions to thermal conductivity showed that the lattice contribution was still the dominant contribution in this material. At low temperature the electronic contribution was over an order of magnitude less than the lattice contribution and as temperature increased the lattice contribution was still approximately five times as large as the electronic contribution at 350 K.

4.3.4 zT

The figure-of-merit of tellurium doped $PtSb_2$ is shown in Figure 4.5.

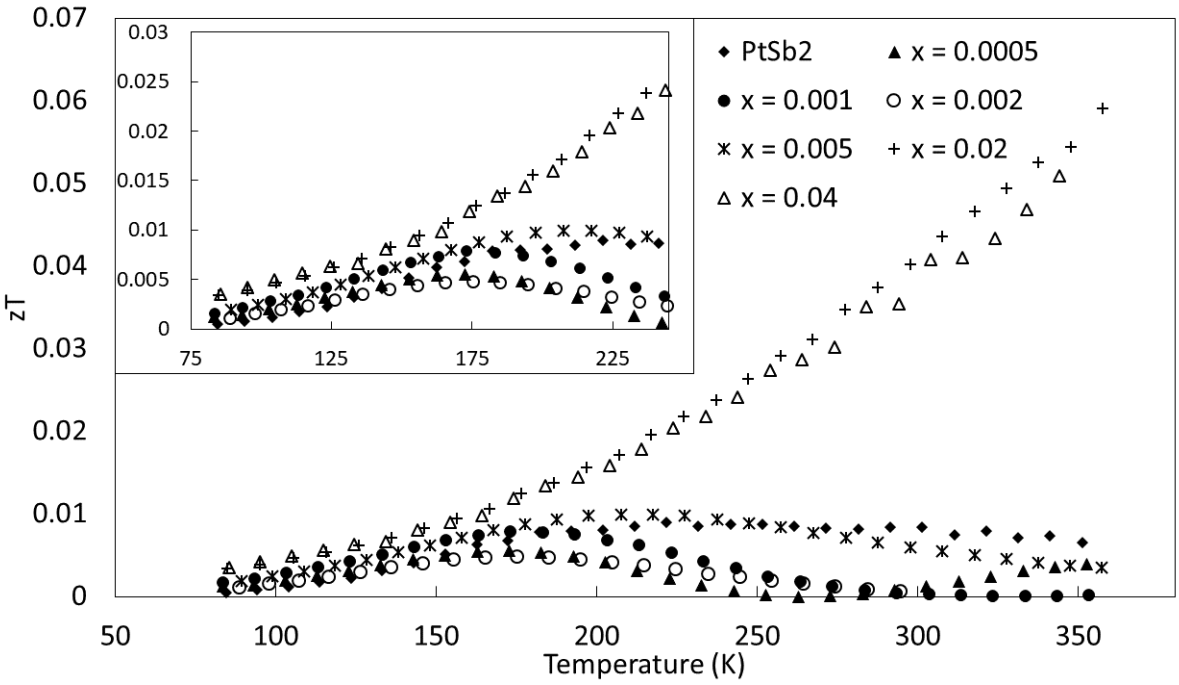

Figure 4.5: zT of Tellurium Doped $PtSb_2$

At low temperatures the figure-of-merit of all doped samples was found to be increased over that of the undoped $PtSb_2$. The overall magnitude of this enhancement was small at low temperature where this work was focused. At varying temperatures in all but the highest doped samples the figure-of-merit of undoped $PtSb_2$ eventually surpassed those of the doped samples. The most prominent values in this figure were those of the highest dopant concentrations, x = 0.02 and 0.04. These samples showed a large enhancement over that of undoped $PtSb_2$, most pronounced in the region around room temperature, achieving a zT of 0.059 at 350 K. Comparing this value to that of commercial Bi_2Te_3 puts this into perspective and shows that an enhancement of approximately 20 times is necessary for room temperature application. Comparison to that of Bi-Sb alloys at 80 K shows the need for several orders of magnitude improvement.

4.4 Selenium Dopant Results and Discussion

4.4.1 X-Ray Diffraction

The X-ray diffraction patterns obtained for selenium doping are shown in Figure 4.6.

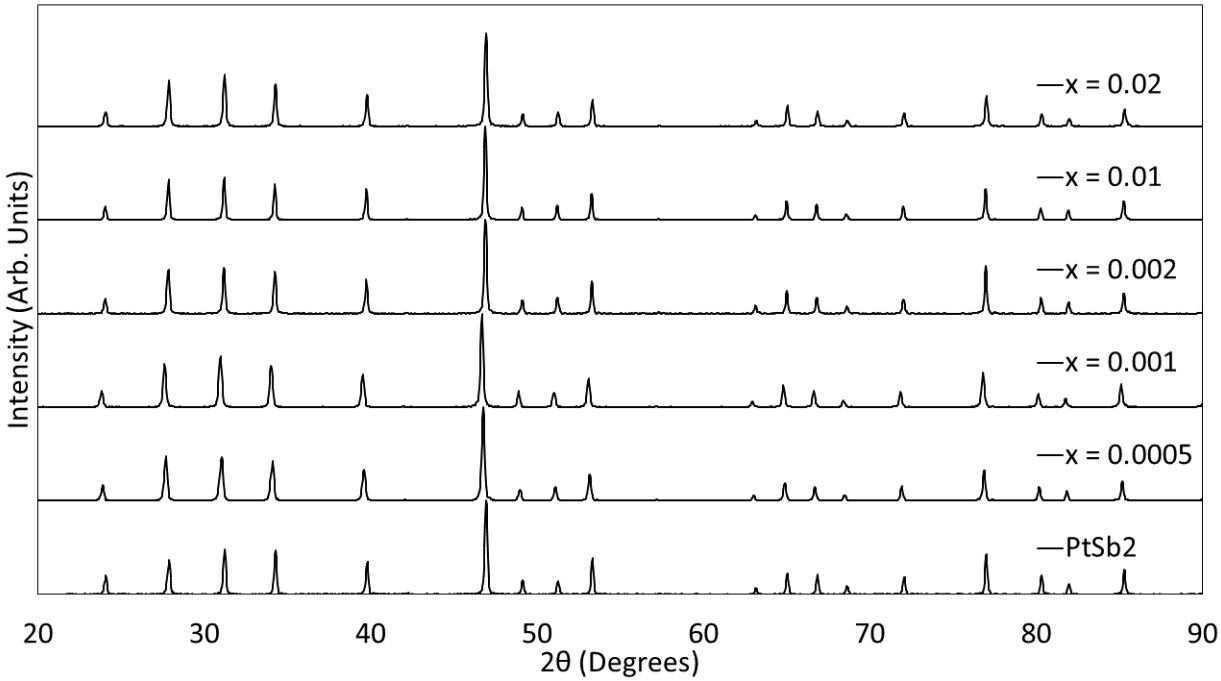

Figure 4.6: X-ray Diffraction of Selenium Doped $PtSb_2$

It was shown that for all selenium doping concentrations no secondary phases were present. Examination for a change in lattice parameter showed no shift, which was likely due to the low concentrations of dopant added in this work.

4.4.2 Electronic Properties

An examination of the Seebeck coefficient of selenium doped $PtSb_2$ may be made from Figure 4.7.

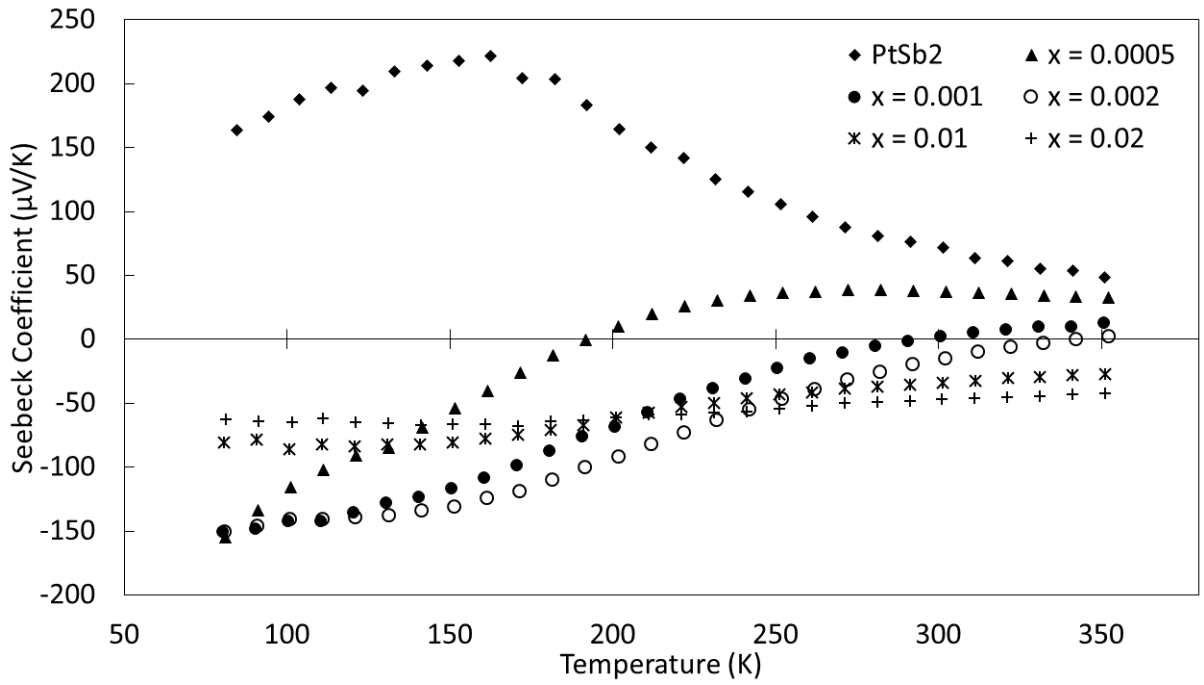

Figure 4.7: Seebeck Coefficient of Selenium Doped $PtSb_2$

It was found that as with tellurium doping the n-type selenium dopant generated a negative Seebeck coefficient for many doping concentrations. Examining the highest dopant concentrations first the x = 0.01 and 0.02 samples showed a fairly flat trend in Seebeck coefficient. It is of interest to note the cross over in the sample with the highest magnitude between the x = 0.01 and 0.02 samples between the temperatures of 190 to 210 K. This was due to the population of intrinsic carriers creating an overall decrease in the magnitude of the x = 0.01 sample more than the x = 0.02 sample due to the fewer number of extrinsic carriers in the x = 0.01 sample. Moving now to the x = 0.001 and 0.002 samples the effect of a low extrinsic carrier concentration being acted upon by the population of intrinsic carriers was seen. At low temperatures the Seebeck coefficient of these samples had a relatively large magnitude that decreased as intrinsic hole carriers were populated which competed with the extrinsically doped electrons. Finally, examining the x = 0.0005 sample it was found that

the maximum in the Seebeck coefficient was likely to occur at lower temperatures than were examined here.

Comparing these results with those of the tellurium doped samples an interesting effect may be observed. The x = 0.0005 composition for selenium doping versus the same composition for tellurium doping demonstrated that selenium was likely not doping as many extrinsic carriers into the $PtSb_2$ electronic structure as tellurium did. Evidence of this came from the result that the Seebeck coefficient did not have a maximum and was still decreasing at 80 K, as well as, the lower temperature at which the sample transitioned to p-type when compared to tellurium at this composition. Since the peak in the Seebeck coefficient for the selenium sample was at a temperature lower than 80 K its carrier concentration was likely lower than the tellurium sample. Additionally, the transition to p-type at a lower temperature indicated that fewer intrinsic carriers were required to dominate over the extrinsic carriers. Thus, it is likely that fewer extrinsic carriers were doped from selenium versus that of tellurium at the same composition.

Comparing the element tellurium to selenium it is found that beyond the size difference of the atoms the selenium atom has a Pauling electronegativity of $\chi = 2.55$, which is much larger than that of tellurium or antimony. The degree of electronegativity of an element is a characterization of the degree by which the element attracts electrons to itself. Thus, if the more electronegative selenium is doped into $PtSb_2$ it is less likely to fully donate the one additional valence electron to the material system than tellurium.

The electrical resistivity of selenium doped $PtSb_2$ is shown in Figure 4.8.

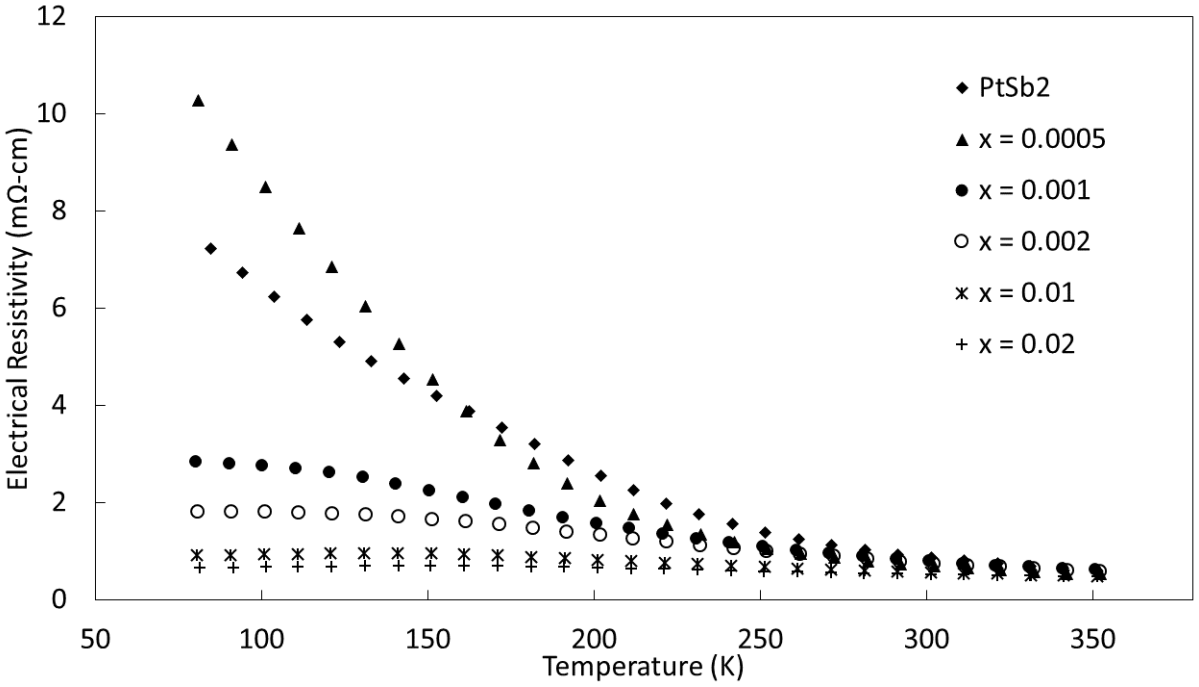

Figure 4.8: Electrical Resistivity of Selenium Doped $PtSb_2$

It was found that the electrical resistivity of the x = 0.0005 sample supported the claim that an effective decrease in the carrier concentration compared to Te at the same composition was observed. At low temperatures it was seen that the x = 0.0005 sample had a higher electrical resistivity than undoped $PtSb_2$, which is different from the tellurium doped sample with the same composition. This effect may have arisen from a decrease in the mobility or a decrease in the carrier concentration and Hall measurements would be a future route to probe this result. Examining those samples with a higher dopant concentration the more expected low temperature decrease in the electrical resistivity was observed. This data matched well with that found from tellurium doping and showed the same convergence of electrical resistivity towards that of undoped $PtSb_2$ as temperature increased.

4.4.3 Thermal Properties

The thermal conductivity of selenium doped samples is shown in Figure 4.9.

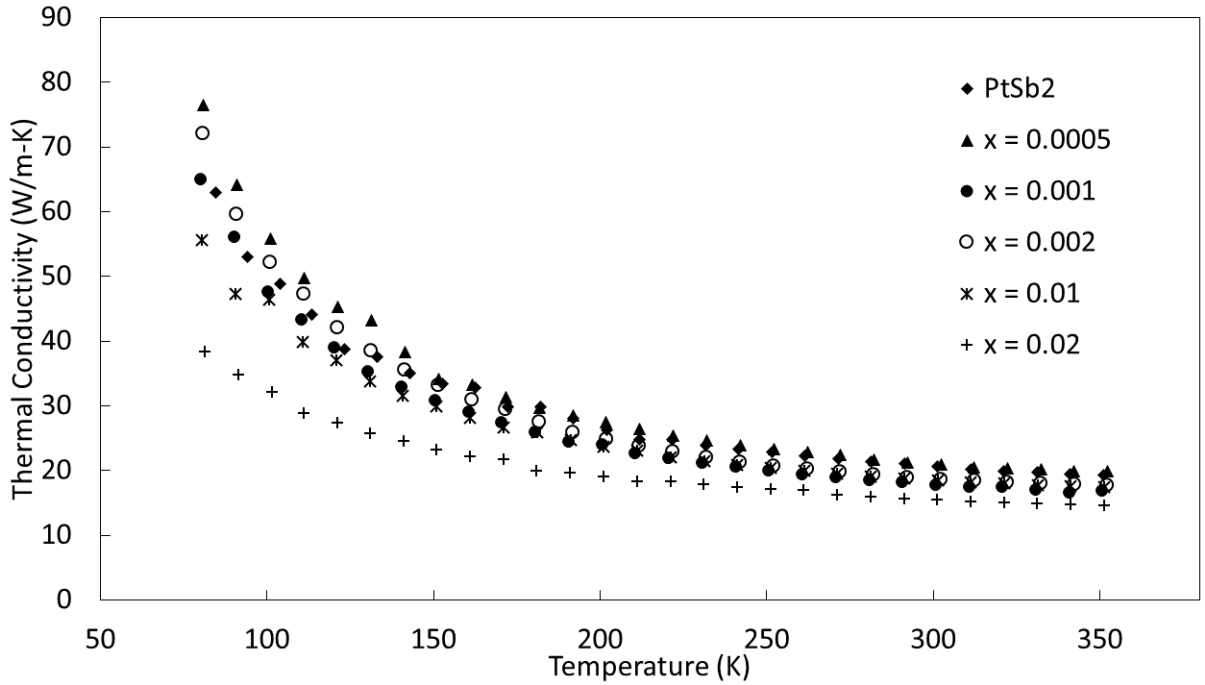

Figure 4.9: Thermal Conductivity of Selenium Doped $PtSb_2$

Relatively little change in the thermal conductivity was found for the low dopant concentrations examined. The outlier in this data set was found for the x = 0.02 sample. Comparison of the thermal conductivity of this sample with that of a similar tellurium dopant concentration showed very good agreement. Thus, it is not expected that this particular sample showed any larger decrease in the thermal conductivity than would be expected. These results along with those of tellurium highlight the importance of minimizing the thermal conductivity in future experimentation.

4.4.4 zT

The figure-of-merit of selenium doped samples is shown in Figure 4.10

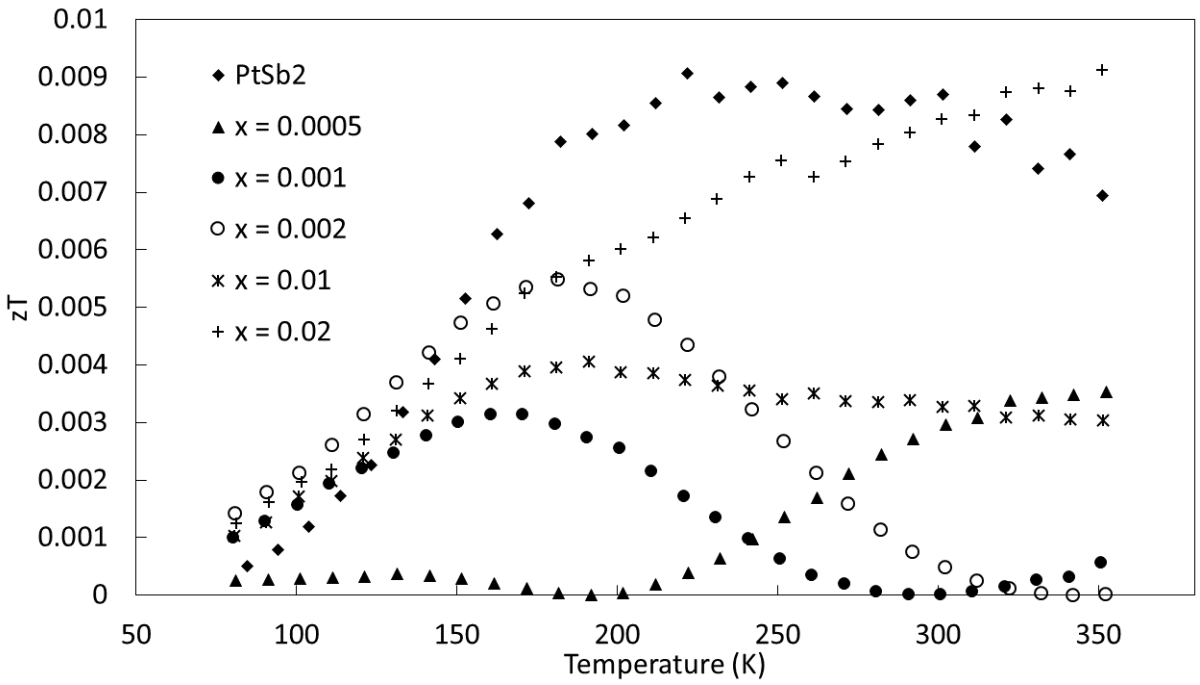

Figure 4.10: zT of Selenium Doped $PtSb_2$

The lackluster individual transport properties for selenium doping culminated in a reduced figure-of-merit for all dopant concentrations other than over a small temperature range at low temperature. From an examination of the power factor it is expected that further doping beyond the x = 0.02 concentration may lead to some enhancement, but the overall magnitude for these samples was low enough that it is unlikely a significant improvement in zT would be found before a solubility limit was met for selenium on the antimony site.

4.5 Tin Dopant Results and Discussion

4.5.1 X-Ray Diffraction

The X-ray diffraction patterns obtained for tin doping are shown in Figure 4.11.

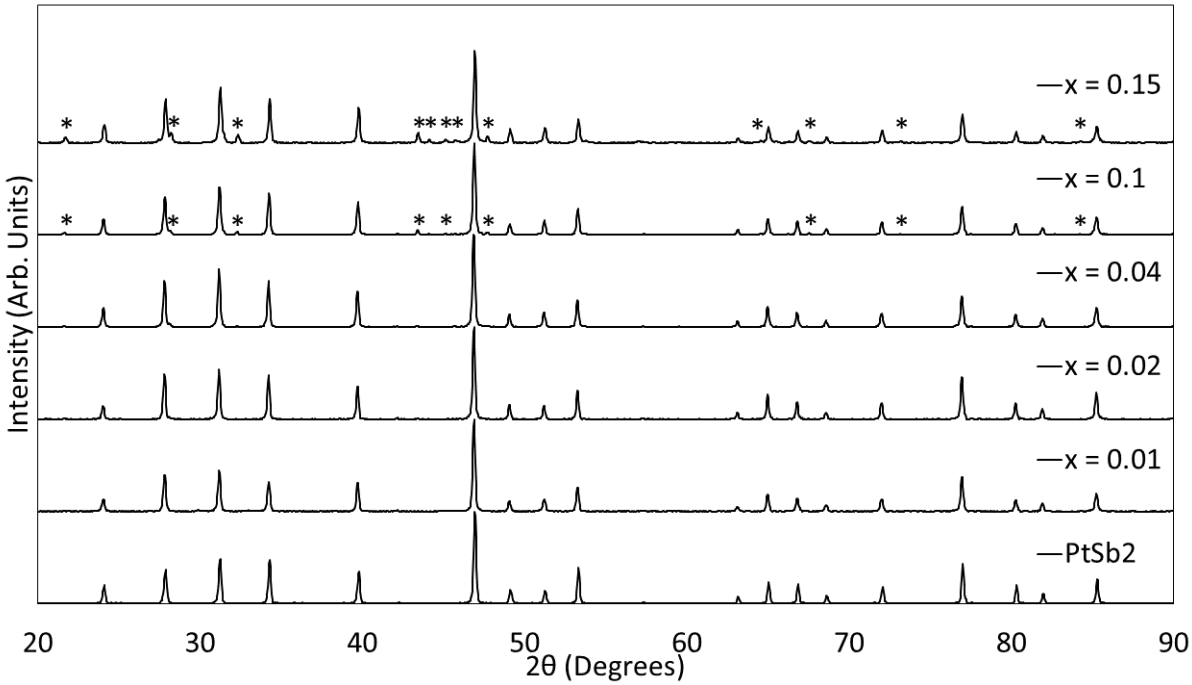

Figure 4.11: X-ray Diffraction of Tin Doped $PtSb_2$

It was found from this X-ray pattern that a likely solubility limit exists for tin doping on the antimony site in $PtSb_2$. Low concentrations of tin dopant showed no secondary phases present, however, at concentrations at and above x = 0.1, secondary phases of tin were found to exist demarcated by a star in the figure. There are no Pt-Sn phases which crystallize in the pyrite structure, thus it was not unexpected that there would be a solubility limit for tin dopant on the antimony site even with the similarity between the two elements. This resembled the limited solubility found by the work of Laudise et al. [109] and Bennett et al. [110] where secondary phases with low concentrations of dopant were found.

4.5.2 Electronic Properties

The Seebeck coefficient of tin doped $PtSb_2$ is shown in Figure 4.12.

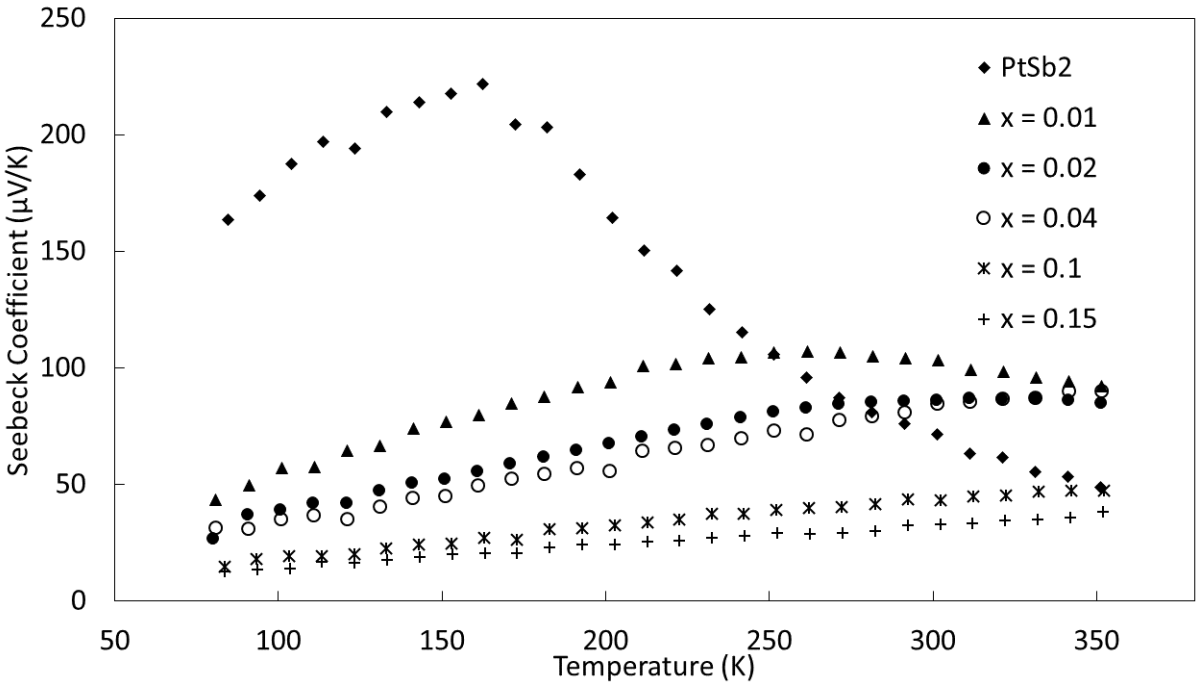

Figure 4.12: Seebeck Coefficient of Tin Doped $PtSb_2$

These results showed the effect of p-type doping on a nominally p-type material. It was found for all dopant concentrations examined that a decrease in the Seebeck coefficient was the result of an increase in the carrier concentration due to p-type doping. As the concentration of dopant was increased it was found that the Seebeck coefficient decreased in response. The maximum in the Seebeck coefficient for these samples was shifted to higher temperatures compared with undoped $PtSb_2$ and is only observable in the lowest doped sample of x = 0.01. This sample showed a maximum at approximately 250 K. Doping in the x = 0.01, 0.02, and 0.04 samples was found to decrease the magnitude of the Seebeck coefficient at low temperatures, but increase it over that of the undoped $PtSb_2$ at higher temperatures. This was due to the high concentration of extrinsic holes that had been doped into the system. Thus, when the Seebeck coefficient of the undoped $PtSb_2$ was decreasing due to the population of intrinsic carriers, the heavily doped x = 0.01 sample was

relatively unchanged with intrinsic carrier population and its Seebeck coefficient increased with temperature.

This conclusion was supported by the electrical resistivity data on these samples shown in Figure 4.13.

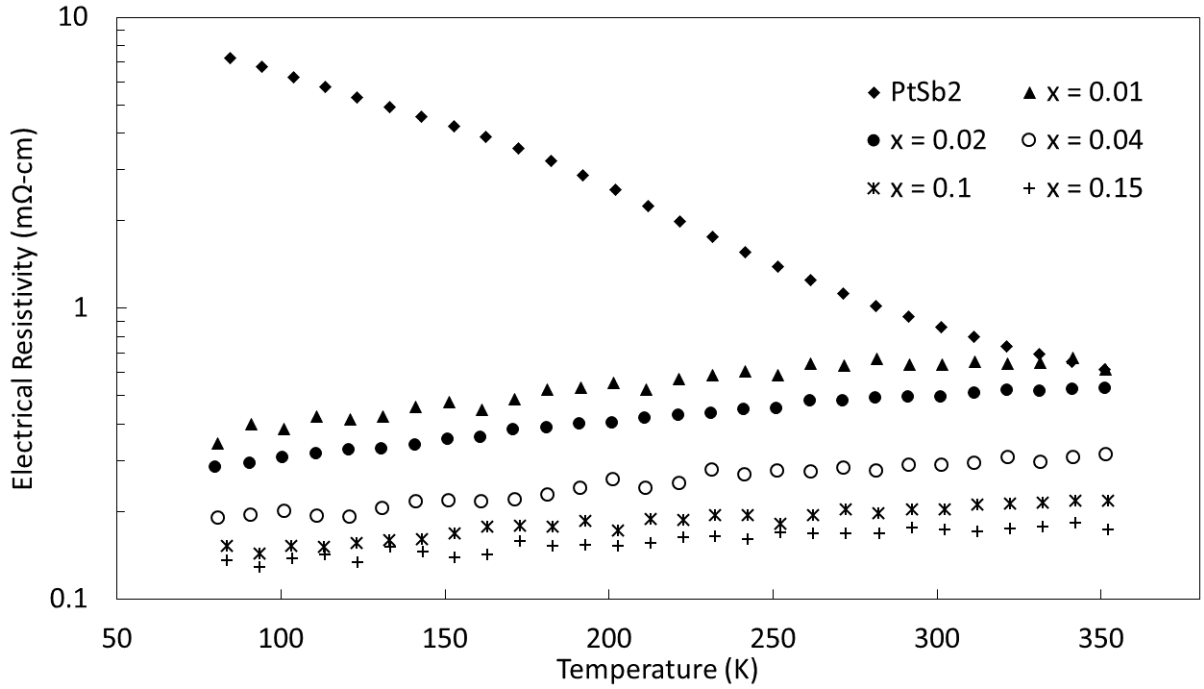

Figure 4.13: Electrical Resistivity of Tin Doped $PtSb_2$

It should be noted that the y-axis for this figure is given in a logarithmic scale to show the large change in the electrical resistivity demonstrated by these samples. At 80 K the electrical resistivity was reduced by a factor of 24 in the x = 0.01 sample. All doped samples showed a large reduction in electrical resistivity and displayed a metallic trend characterized by a linearly increasing electrical resistivity with increasing temperature. This positive trend was due to increasing scattering of carriers as temperature increased from phonons. In the x = 0.01 and 0.02 samples a convergence with undoped $PtSb_2$ was found at temperatures above room temperature, however for higher dopant concentrations the large extrinsic carrier

concentration reduced the electrical resistivity beyond that of undoped $PtSb_2$. The solubility limit of Sn in $PtSb_2$ was further exemplified by the similar electrical resistivities found in the x = 0.1 and 0.15 samples.

4.5.3 Thermal Properties

The thermal conductivity of Sn doped samples is shown in Figure 4.14.

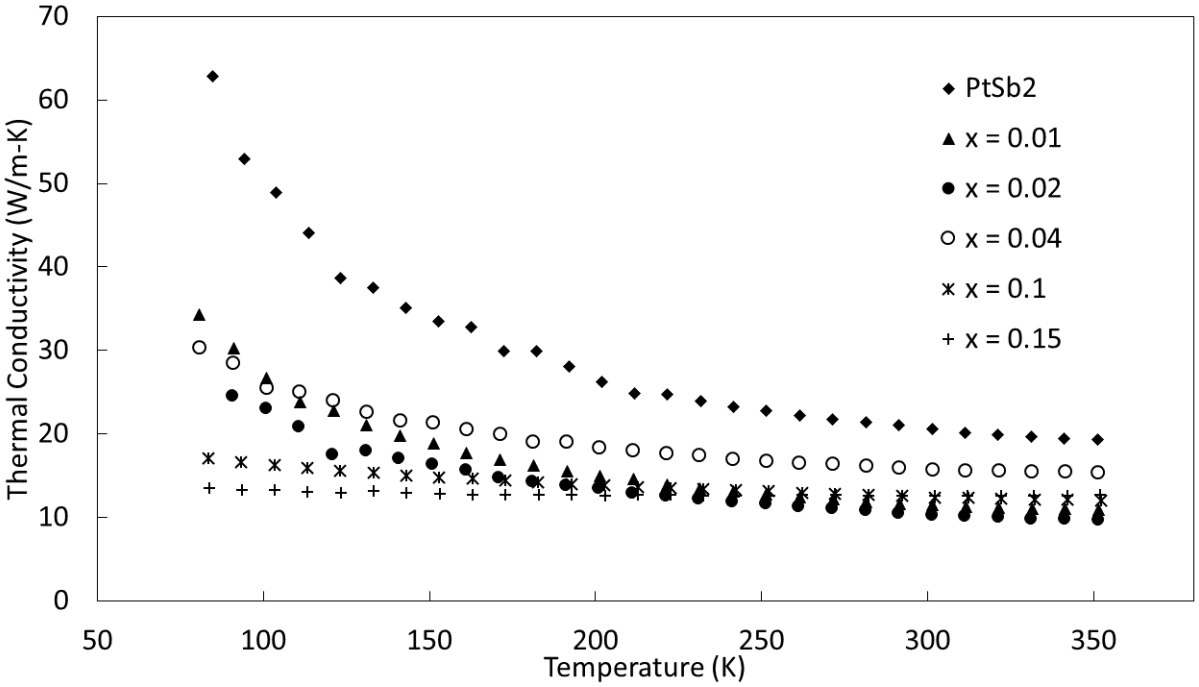

Figure 4.14: Thermal Conductivity of Tin Doped $PtSb_2$

Of note are the low temperature results in the highest dopant concentration samples, x = 0.1 and 0.15. These samples showed a low and flat trend, while all other samples showed a decreasing thermal conductivity with temperature. It is thought that the secondary phases in the highest Sn dopant samples caused additional boundary scattering and is likely the cause for the decreased thermal conductivity at low temperature.

Examination of these results would at first appear to show that Sn was able to reduce the

thermal conductivity superior to that found from tellurium or selenium doping. However, this was not the case, due to the increased dopant concentration examined in the work with Sn. In Figure 4.15 the reduction in thermal conductivity found for all antimony site dopants at 90 K is shown with the abscissa in a logarithmic scale.

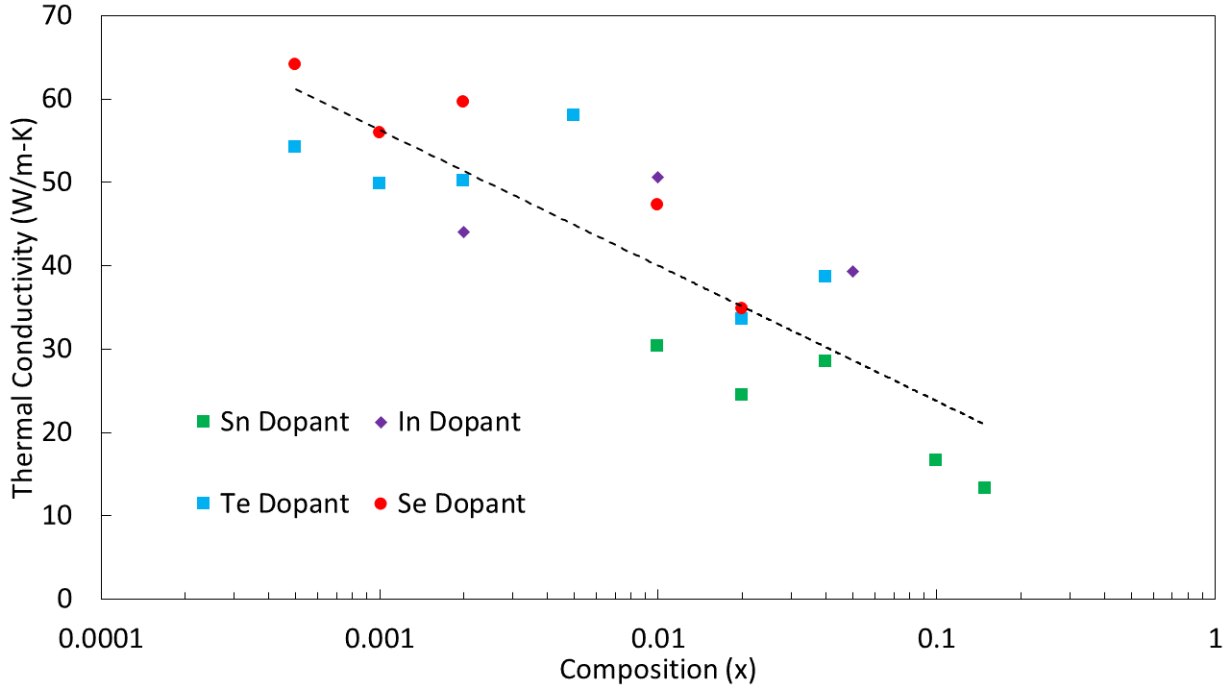

Figure 4.15: Thermal Conductivity of Te, Se, In and Sn Dopants at 90 K

This figure shows that, as a general trend, as dopant concentration increased the total thermal conductivity decreased. Thus, when comparing the overall reduction in thermal conductivity found for tellurium and selenium doping, for low dopant concentrations, with those of tin, for higher dopant concentrations, the larger reduction found for tin is more easily understood. The greater reduction in thermal conductivity found in higher dopant concentration samples is likely due to increased phonon scattering on impurities.

4.5.4 zT

The figure-of-merit of Sn doped $PtSb_2$ is shown in Figure 4.16.

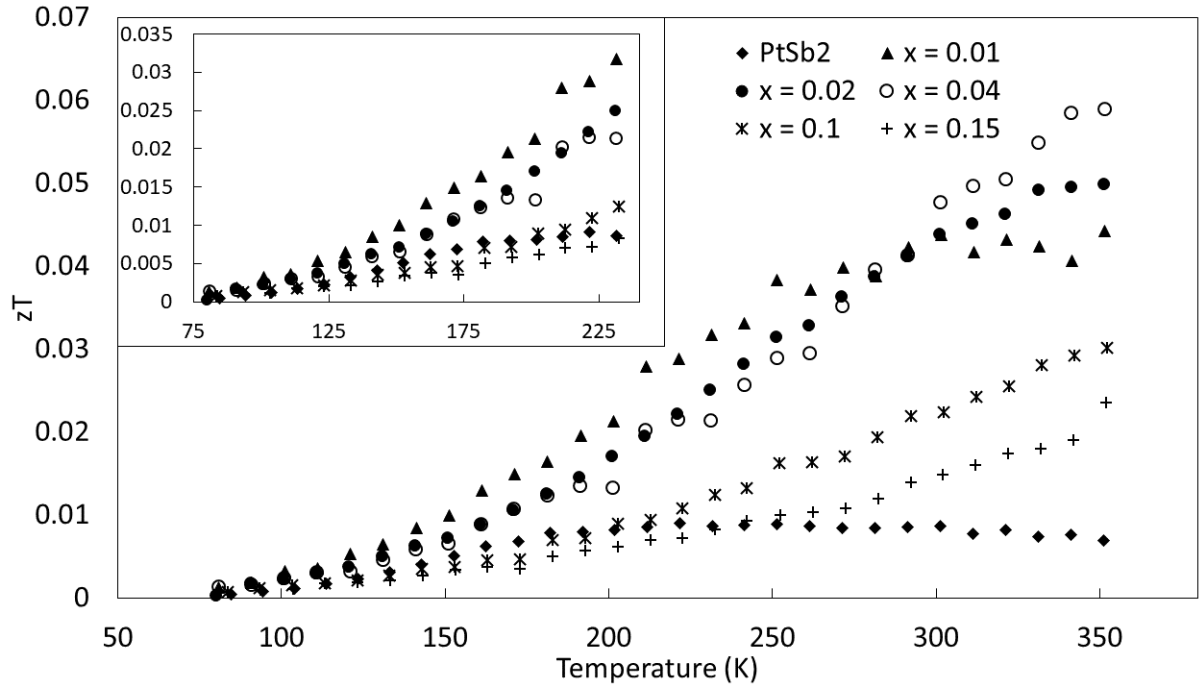

Figure 4.16: zT of Tin Doped $PtSb_2$

It was found that for all Sn doped samples that at room temperature and higher the figure-of-merit was enhanced to values similar to those obtained from tellurium doping. In the tellurium doped system a dopant concentration of x = 0.02 resulted in the highest zT at 350 K of approximately 0.059. In the tin doped system the highest zT was found in x = 0.04 again with a value of 0.059 at 350 K. At low temperatures the lightly doped samples of composition x = 0.01, 0.02, and 0.04 were found to have zT values larger than that of undoped $PtSb_2$. It should be noted again though that these values are very low when compared to the Bi-Sb alloys or commercialized Bi_2Te_3.

4.6 Germanium Dopant Results and Discussion

4.6.1 X-Ray Diffraction

The X-ray diffraction patterns of germanium doped $PtSb_2$ are shown in Figure 4.17.

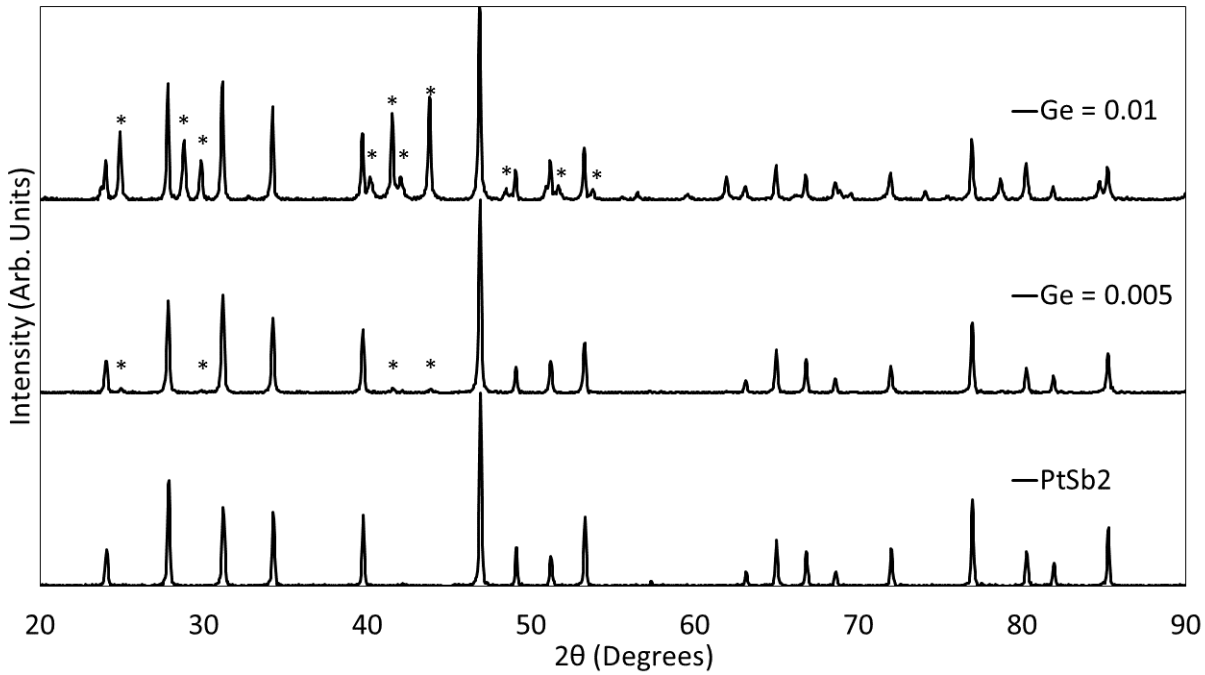

Figure 4.17: X-ray Diffraction of Germanium Doped $PtSb_2$

These X-ray diffraction patterns showed the very limited solubility of germanium in $PtSb_2$. In the lowest dopant concentration of x = 0.005 a secondary phase was found in the system and in the x = 0.01 sample a large amount of secondary phase was found. Comparison to the results of Sn doping in $PtSb_2$ would lead one to expect a solubility limit closer to a composition of x = 0.1, however, likely due to the greater size difference between germanium and antimony, a single phased sample was unable to be synthesized.

Due to the lack of single phased samples from germanium doping the transport properties of this dopant were not examined in this work.

4.7 Indium Dopant Results and Discussion

4.7.1 X-Ray Diffraction

The X-ray diffraction patterns of indium doped $PtSb_2$ are shown in Figure 4.18.

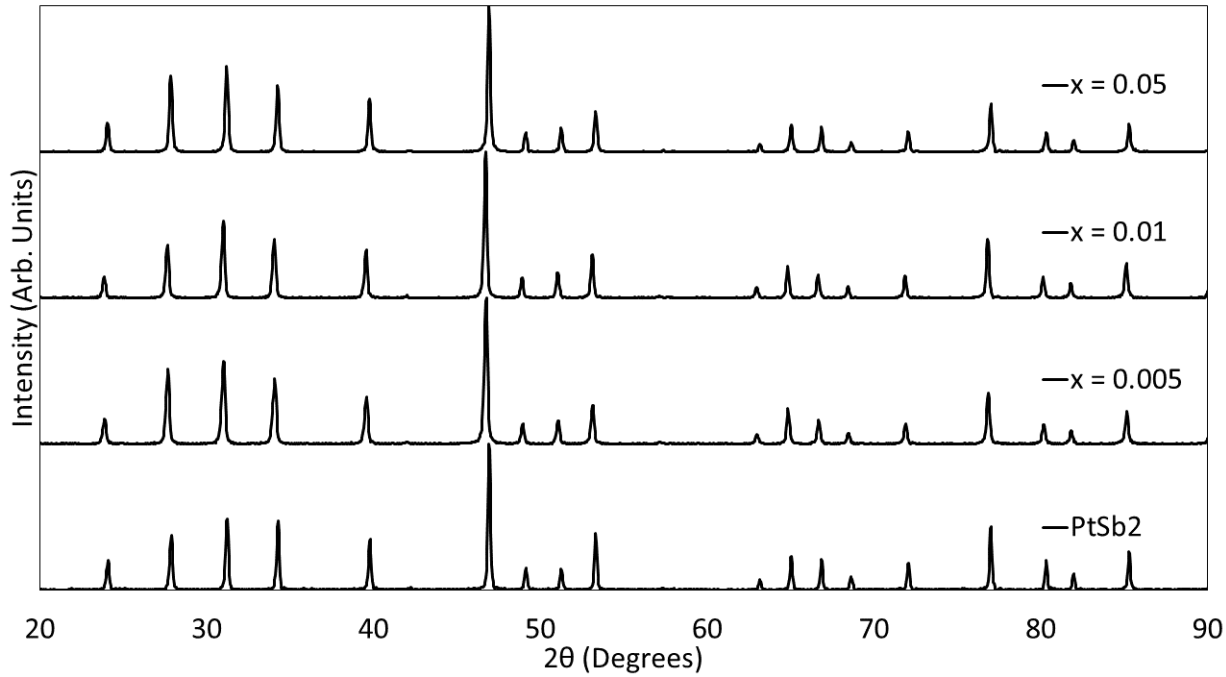

Figure 4.18: X-ray Diffraction of Indium Doped $PtSb_2$

The diffraction patterns for indium doping were found to coincide with that of the $PtSb_2$ structure. Extending to higher concentrations of dopant suggested a solubility limit for indium at the composition of x = 0.05, due to secondary phases of $PtIn_2$ at higher concentrations. For compositions of x = 0.05 or less no shift in the lattice parameter was found. It is likely that indium did not generate secondary phases at the very low concentrations that germanium did due to the greater size difference between antimony and germanium than antimony and indium.

4.7.2 Electronic Properties

The Seebeck coefficient for indium doped samples, shown in Figure 4.19, suggests that indium dopes onto the antimony site as a p-type dopant.

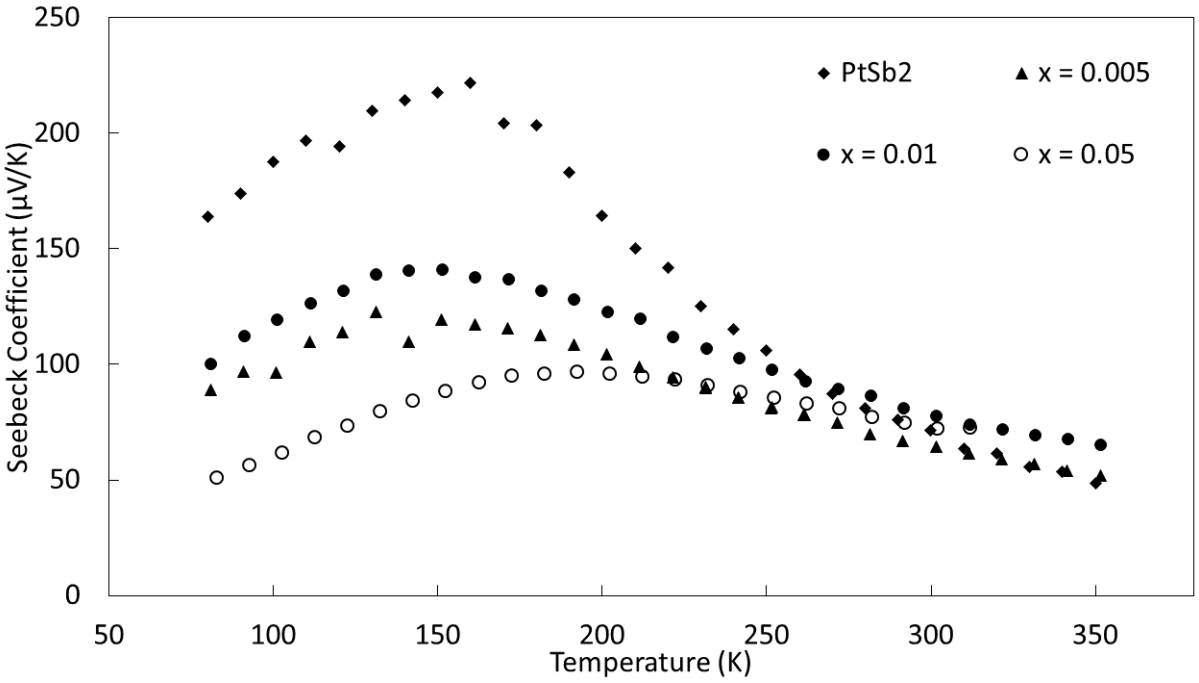

Figure 4.19: Seebeck Coefficient of Indium Doped $PtSb_2$

It was expected that indium would p-type dope in $PtSb_2$ due to indium containing two fewer valence electrons than antimony. The Seebeck coefficient behaved as expected from a p-type dopant with a general decrease in the magnitude and a slight shift in the temperature in peak Seebeck coefficient values towards higher temperatures.

Comparing indium with tin it was expected that indium would effectively dope two acceptor states for every atom of indium compared to the single acceptor state which was expected from tin doping. It can be concluded that this did not occur due to the larger magnitude in the Seebeck coefficient and the higher electrical resistivity for comparable doping compositions.

The electrical resistivity of indium doped $PtSb_2$ is shown in Figure 4.20.

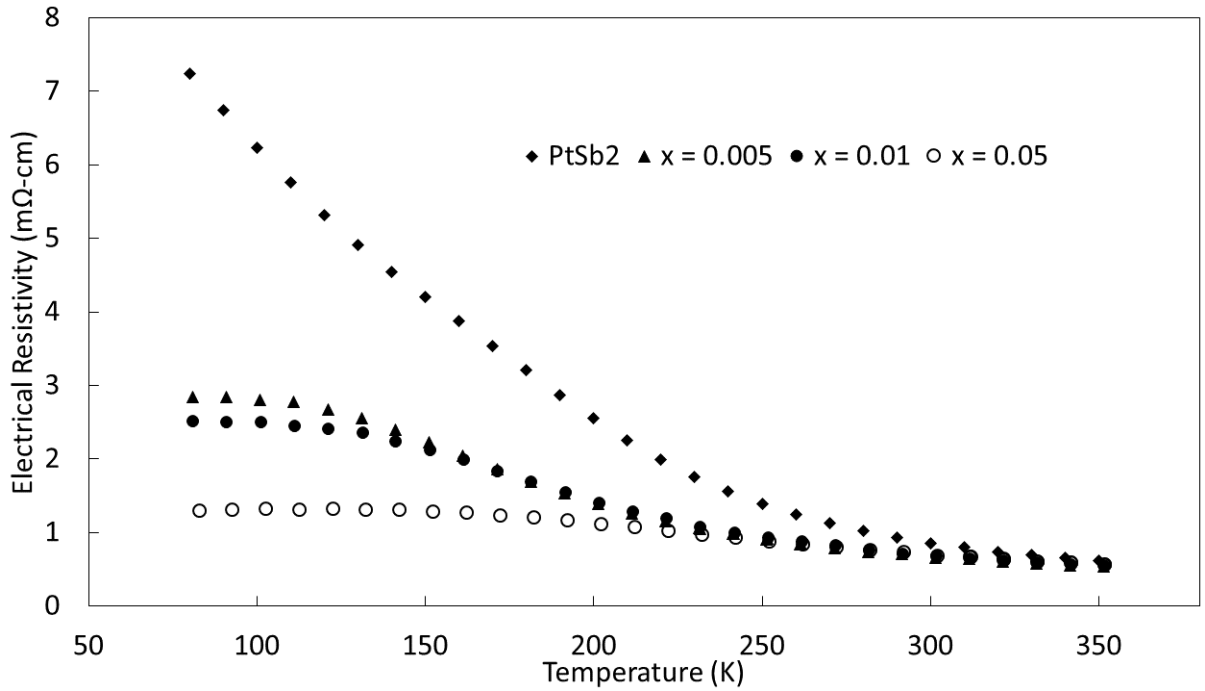

Figure 4.20: Electrical Resistivity of Indium Doped $PtSb_2$

The typical p-type doping behavior was again found in this data with a reduction in the electrical resistivity of these samples at low temperature. As temperature increased the electrical resistivity was found to converge to that of undoped $PtSb_2$ due to the onset of intrinsic carriers. To directly compare compositions of indium with those of tin the x = 0.01 composition is taken for discussion. At 80 K the indium x = 0.01 sample showed an electrical resistivity of 2.5 mOhm-cm while the tin x = 0.01 sample showed a value of 0.3 mOhm-cm, nearly an order of magnitude difference. Some of this difference may be due to increased scattering from the extra mass variance between indium and antimony as compared with tin and antimony. However, another consideration is that indium only has three valence electrons and it is being incorporated into a site for a tetrahedrally bonded element. It is likely that indium, with three valence electrons, was thermodynamically less

favorable to dope onto this tetrahedrally bonded site than tin, with four valence electrons, which ultimately caused a decrease in the effective carriers it doped per atom.

4.7.3 Thermal Properties

The thermal conductivity of indium doped $PtSb_2$ is shown in Figure 4.21.

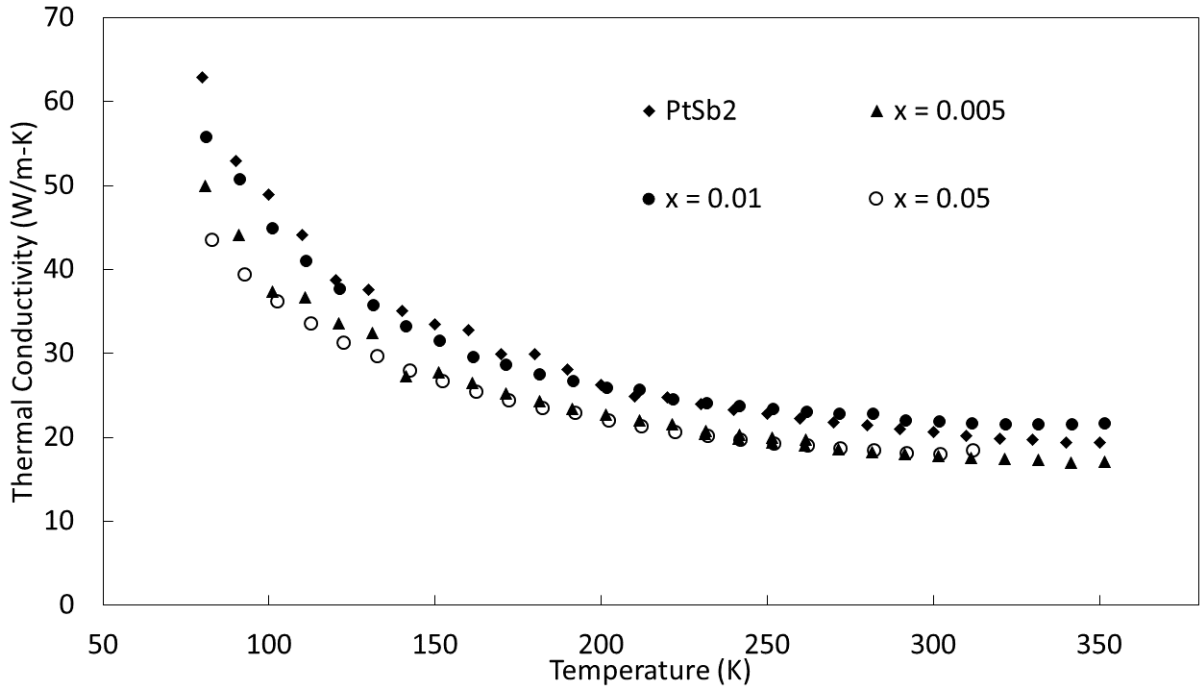

Figure 4.21: Thermal Conductivity of Indium Doped $PtSb_2$

The expected minor reduction in thermal conductivity was found for these lightly doped samples. With only a small decrease in the electrical resistivity the electronic contribution was not found to increase substantially and the impurity scattering introduced by doping suppressed the thermal conductivity across all temperatures measured.

4.7.4 zT

The resultant figure-of-merit values obtained for indium doped $PtSb_2$ is shown in Figure 4.22.

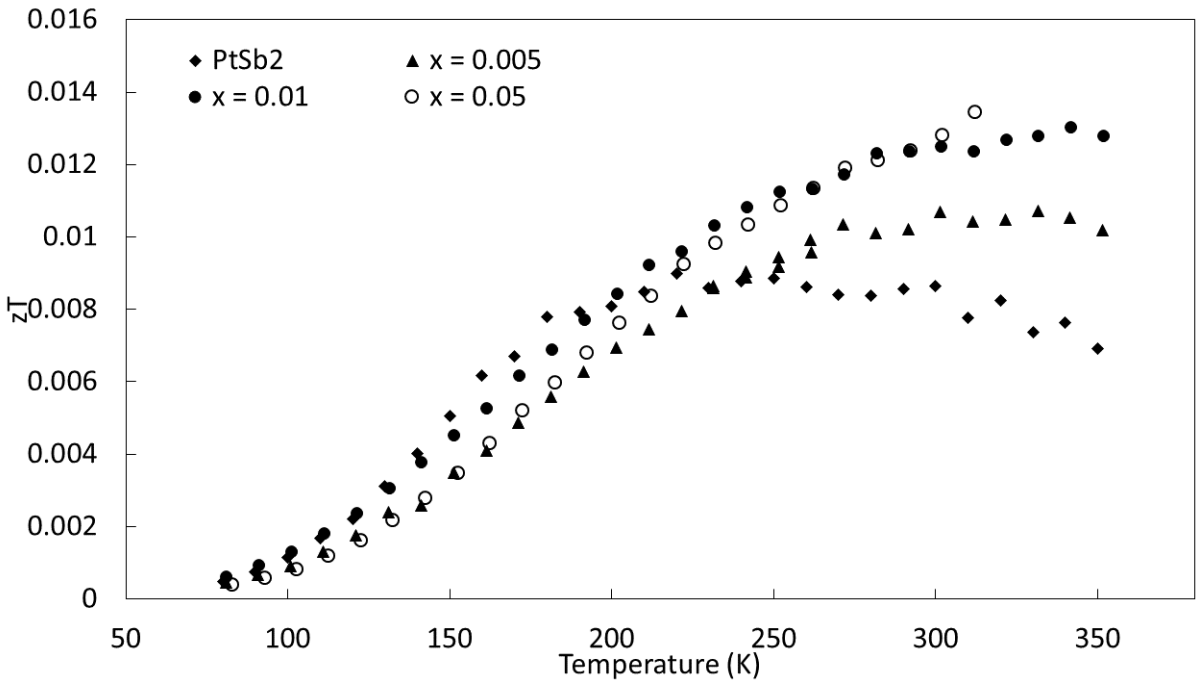

Figure 4.22: zT of Indium Doped $PtSb_2$

Due to the lackluster improvement in power factor at high temperature, from a decreased Seebeck coefficient and slightly reduced electrical resistivity, as well as a minor decrease in the thermal conductivity, the zT for indium doped samples showed only minimal enhancement above 200 K.

4.8 Conclusions

A comparison of the results found for tin and tellurium doping on the antimony site is enlightening of the effects of p- and n-type doping in a narrow bandgap system. Unlike materials with larger bandgaps the narrow bandgap system is in a state of intrinsic carrier population at much lower temperatures and thus is often characterized by the effects of bipolar conduction. The electrical conductivity is characterized by the conduction of both holes and electrons though both terms are weighted by their respective mobilities. The Seebeck

coefficient, on the other hand, is reduced due to bipolar conduction. When an extrinsic dopant of opposite type to the nominal material is introduced those extrinsic carriers will compete with the nominal carriers in establishing the Seebeck coefficient. Examining a system with a large dopant concentration, of opposite type to the nominal system and extrinsic carrier concentration much greater than the nominal carrier concentration, creates a change in the sign of the Seebeck coefficient and yields a low magnitude due to the large number of carriers. As the dopant concentration is decreased, the magnitude of the Seebeck coefficient is increased and a maximum is found due to the onset of intrinsic carrier population. As the dopant concentration is further decreased the Seebeck coefficient is expected to increase significantly, and the maximum will shift to lower temperatures, until such a concentration is met where there will be a sign change. Subsequent reduction in the dopant concentration will return the Seebeck coefficient to its nominal state. Refer to Figure 4.23 to examine this effect.

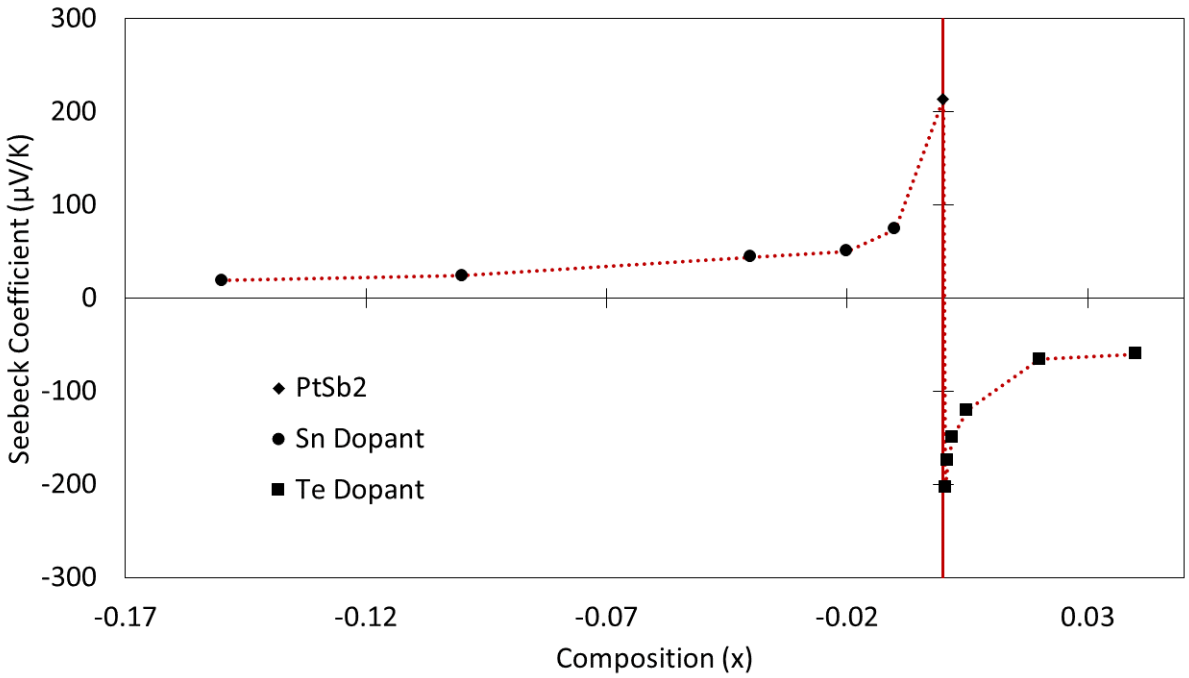

Figure 4.23: Effects of Dopant Concentration in Tellurium and Tin Doped $PtSb_2$

This figure shows the Seebeck coefficients at 140 K of varying concentrations of tin and tellurium doped $PtSb_2$, with an undoped sample for reference. The compositions of tin dopant are given as a negative on this figure to connote the loss of electrons with this dopant, while tellurium composition is positive to connote the gain of electrons. Examination of this figure displays the above mentioned effects for tellurium dopants. As the concentration of tellurium was reduced, the magnitude of the Seebeck coefficient increased and at some very low concentration would result in a maximized Seebeck coefficient for the electron dominant system. At any concentration less than this, the result would be a return to positive values. The effects of tin dopant displayed the typical decrease with increasing carrier concentration that is expected.

From the study of n- and p-type doping on the antimony site it was found that $PtSb_2$ could be made to assume a positive or negative Seebeck coefficient dependent upon the dopant. It was additionally found that a maximization in the power factor was observed for both donor and acceptor dopants in the lightly doped samples above room temperature. In both tellurium and tin doped samples the highest power factors occurred at 350 K with respective values of 24 μW/cm-K^2 and 26 μW/cm-K^2, both with the composition x = 0.04. At low temperatures, between 80 and 200 K it was found that n-type dopants resulted in enhancement while p-type dopants generated a decrease. Neither n- or p-type dopants were found to significantly decrease the thermal conductivity beyond that expected for an ionized impurity scattering site. It was additionally noted that the magnitude of the thermal conductivity was prohibitive to the generation of large figure-of-merits.

Ultimately, the figure-of-merits of n- and p-type doping on the antimony site led to enhancement in the tellurium and tin dopants primarily due to their power factor enhancement above room temperature. Thus, an endeavor to be presented in subsequent chapters is an

attempt to further increase the figure-of-merit by reducing the thermal conductivity while additionally tuning the carrier concentration to enhance the power factor.

Chapter 5

Platinum Site Doping in $PtSb_2$

5.1 Background and Motivation

From the results of electronic doping on the antimony site it was shown that the thermoelectric properties of $PtSb_2$ could be greatly affected with very low concentrations of dopant. Doping on the antimony site with elements of varying valence shell electron arrangements will largely create an alteration in the Sb p-shell. Doping on the Pt site, however, will largely alter the electronic configuration and the interaction of valence electrons in the Pt d-shell. From the work of Emtage et al. it was shown that the interaction of the 5d and 6s bands of platinum are what contribute to the minima of the conduction band being in the <111> direction as opposed to the minima being in the same k-space as the valence band maxima, the <100> direction [99]. This leads one to presume that alterations in the electronic structure of these 5d or 6s bands by electronic doping on the platinum site may affect the minima of the conduction band and may lead to even more dramatic effects than antimony site doping.

Prior work by Nishikubo et al. showed that the Pt site could successfully be doped with iridium which acted as a p-type dopant [112]. This generated a large decrease in the electrical resistivity and a decrease in the Seebeck coefficient. Similar to what was found for antimony

site doping, the electronic doping of iridium resulted in an increase in the power factor and a decrease in the thermal conductivity resulting in an increase in the figure-of-merit.

Beyond testing for possible routes to increase the figure-of-merit by p- or n-type doping on the platinum site there were two other routes examined here. The first examined was the effect of iron doping. It is well known that $FeSb_2$ is a narrow bandgap material which exhibits an extremely large Seebeck coefficient between -45 mV/K and -30 mV/K [117, 118]. This Seebeck coefficient is 2 to 3 orders of magnitude higher than the typical thermoelectric material and has generated a large amount of research and attention. $FeSb_2$ has been identified as a strongly correlated electron system which is characterized by a hybridization gap around the Fermi energy [119, 120]. This hybridization gap is due to the interaction of the conduction band with d- or f-bands and leads to a very large anisotropy of the density of states on either side of the gap [121, 122]. It is this large anisotropy in the density of states that leads to the large Seebeck coefficients in these materials [123].

Another route examined in this chapter was that of rare-earth doping with ytterbium. Several studies have shown the promising electronic properties of ytterbium compounds i.e. $YbAl_3$ and $YbAgCu_4$ [124–127]. Both of these compounds show large power factors at low temperature, behavior that is likely due to the intermediate valence state of Yb between the 2^+ and the 3^+ states. The chemical pressure tuning of the valence state of these compounds is another route which may be possible with Yb doping, though it is likely that only low concentrations of Yb would be soluble in the $PtSb_2$ structure which may limit the effects of this technique. A final possible route with rare-earth doping would be with cerium due to the similarity of the 4f configuration of Ce with that of Yb. Yb is found on the far end of the lanthanides with one less electron than a full f-shell and Ce is on the near end with one electron occupying the f-shell. Additionally, the Ce containing rare-earth compounds show

good electronic properties at low temperatures and are likely to have interesting effects as a dopant [128–130].

Thus, the effects of n- and p-type dopants, as well as iron and ytterbium doping on the platinum site will be examined in this chapter.

5.2 Experimental Methods

To examine the effects of transition metal doping on the platinum site the elements iron, silver, and niobium were selected. To examine the effects of rare-earth doping the element ytterbium was selected. Compounds with compositions $Pt_{1-x}Dp_xSb_2$ were synthesized where Dp = Fe, Ag, Nb, and Yb, with concentrations ranging between $0 < x < 0.1$. Samples were synthesized in the manner outlined in Chapter 2 without any post reaction processing. It should be noted that iron and ytterbium doped samples utilized the 30 minute dwell time SPS parameters while silver and niobium dopants utilized the shortened SPS parameters.

One final consideration was made for the ytterbium doped samples. Ytterbium is known to react with oxygen, thus care was taken with these samples to limit their exposure. This was especially important during the initial heat treatment during which sample reaction was taking place. During the heat treatment it was discovered that unless the silica, SiO_2, ampoules were coated with a layer of carbon the ytterbium would react with the oxygen in the sides of the ampoule. Thus, for all ytterbium containing samples a layer of carbon was coated on the inside of the silica ampoules by deposition from boiled ethanol.

5.3 Iron Dopant Results and Discussion

Iron has two fewer valence electrons than platinum, and would theoretically be a p-type dopant. However, that is only part of the reason to explore iron doping, the other being that $FeSb_2$ is a strongly correlated system that generates a large Seebeck coefficient. Therefore, to explore the possible generation of this effect in $PtSb_2$ iron doping was performed.

5.3.1 X-Ray Diffraction

X-ray diffraction data on iron doped samples is shown in Figure 5.1

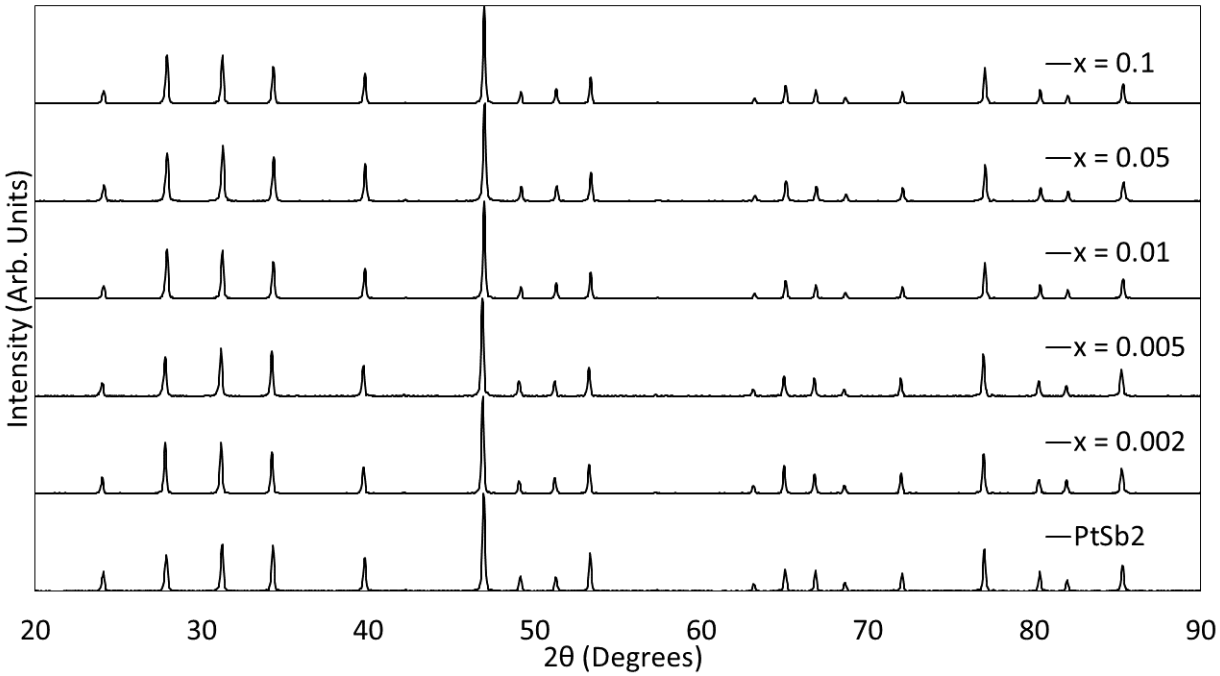

Figure 5.1: X-ray Diffraction of Iron Doped $PtSb_2$

It was found that for all dopant concentrations examined the single phase diffraction pattern for nominal $PtSb_2$ was observed. Due to the size difference between iron and platinum, when compared to germanium doping on the antimony site, it was surprising that while in the case of germanium no solubility was found, up to 5 atomic% of Fe can be incorporated

into the structure without the appearance of a secondary phase. However, $FeSb_2$ crystallizes in the orthorhombic marcasite structure, which is related to the pyrite structure of $PtSb_2$, and may have allowed a higher solubility limit for this dopant.

5.3.2 Electronic Properties

In Figure 5.2 the data obtained for the Seebeck coefficient of this dopant is shown.

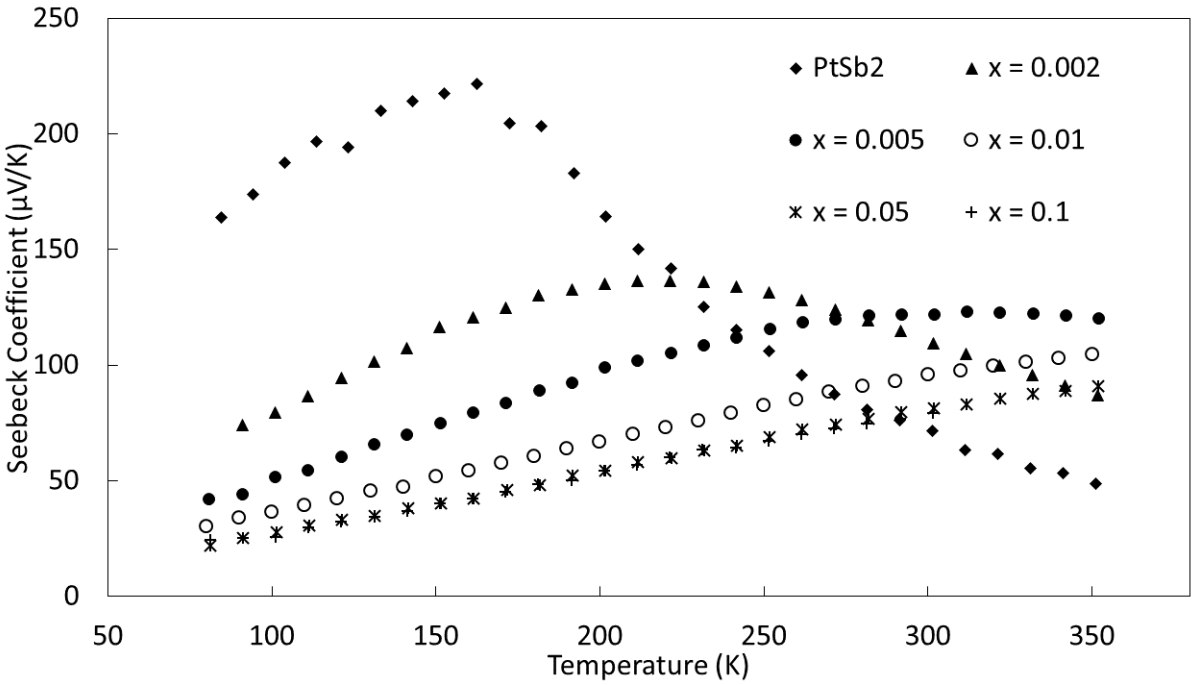

Figure 5.2: Seebeck Coefficient of Iron Doped $PtSb_2$

Iron doping was found to have the conventional effect of p-type doping in this material. With a slight dopant concentration, as in the x = 0.002 sample, a decrease in the nominal positive Seebeck coefficient was found. The maximum in the Seebeck coefficient was also found to be shifted to a higher temperature of approximately 225 K. At this temperature the Seebeck coefficient of this composition surpassed that of nominal $PtSb_2$. With increasing concentration of iron dopant a further decrease in the magnitude in the Seebeck coefficient

was found. In the x = 0.005 sample a further shifted maximum was found at approximately 300 K, and in concentrations higher than this the Seebeck coefficient was steadily increasing even up to 350 K.

Examining the electrical resistivity in Figure 5.3, further evidence of iron acting as a p-type dopant is shown. It should be noted that due to the large reduction in electrical resistivity a logarithmic scale on the ordinate was utilized.

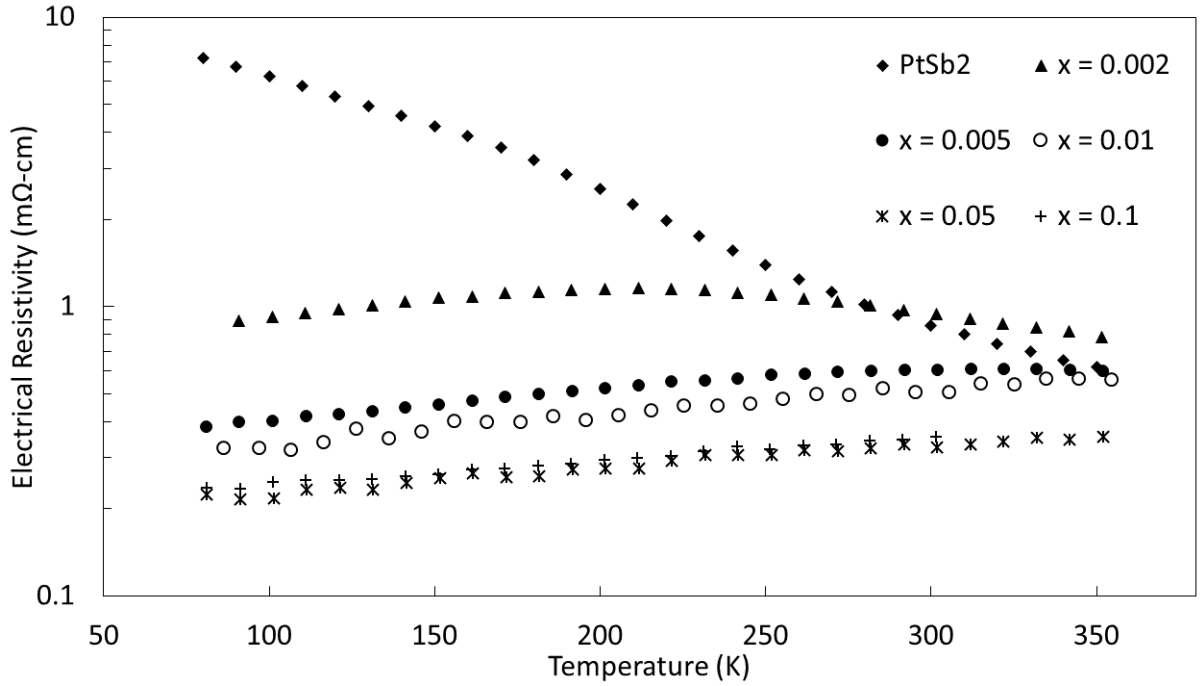

Figure 5.3: Electrical Resistivity of Iron Doped $PtSb_2$

Starting again with the lightest iron dopant, the x = 0.002 sample, almost an order of magnitude reduction in the electrical resistivity was found. A slight increase in resistivity with temperature was found until the onset of intrinsic carriers brought about a slight decrease starting at approximately 210 K. Further iron doping reduced the resistivity and generated a metallic trend.

A large enhancement was found in the power factors of these samples, shown in Figure 5.4.

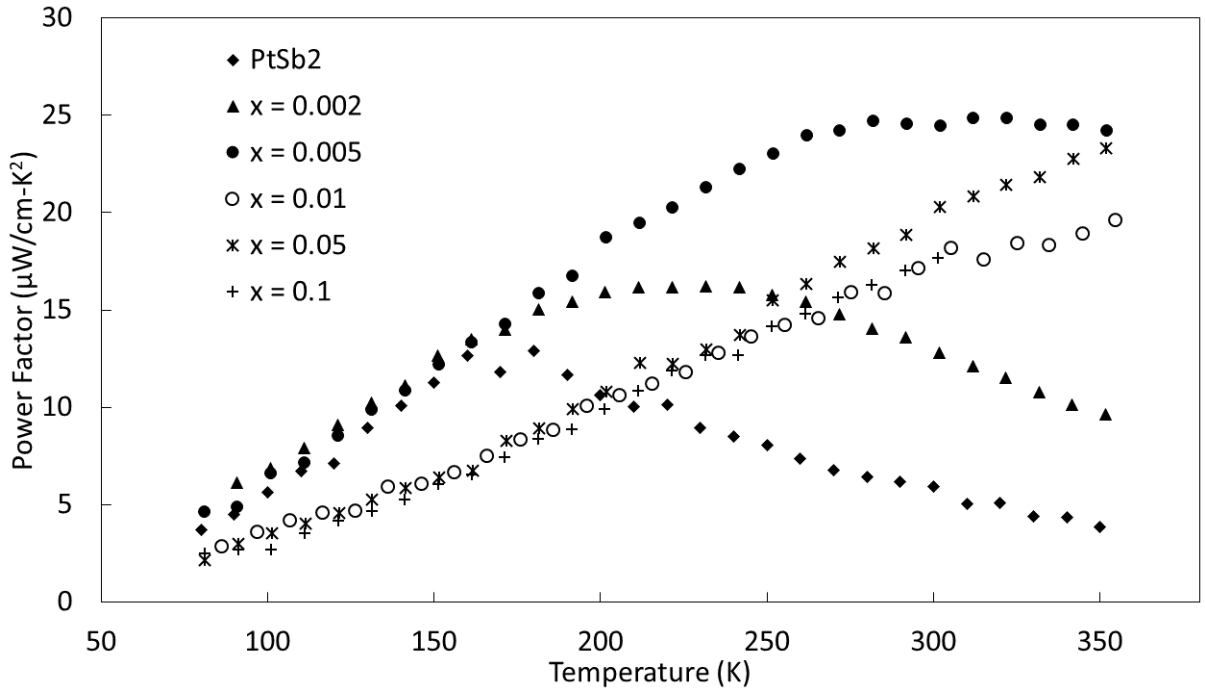

Figure 5.4: Power Factor of Iron Doped $PtSb_2$

These Fe doped samples all showed enhancement above 210 K, where the Seebeck coefficient of nominally undoped $PtSb_2$ was reduced due to the population of intrinsic carriers, and for the x = 0.01, 0.05, and 0.1 samples was found to still be increasing at 350 K. At low temperatures it was only the low dopant composition samples where the power factor was not suppressed relative to undoped $PtSb_2$, yet even for these samples the values were not greatly enhanced until above 210 K. The largest power factor obtained for the doped samples was approximately 25 μW/cm-K^2 from 280 to 320 K.

It is curious comparing this power factor with that of tin and tellurium dopants on the antimony site that all three samples showed maximum power factors of approximately 25 μW/cm-K^2 above room temperature. This indicates that there is relatively little change in the electronic band structure, other than p-type doping effects, from the dopant of iron in this system, where it was theorized that the 5d and 6s bands largely constitute the conduction

band minima. Since an element with a different d-shell valence electron configuration from that of platinum was doped here it was expected that more than the typical p-type doping effects would be found. It is possible that since iron was acting as a p-type dopant in this system this may have shifted the Fermi energy down to lower energies, away from the altered conduction band, which may have minimized any effects which otherwise would have been noted.

5.3.3 Thermal Properties

The thermal conductivity of iron doped $PtSb_2$ is shown in Figure 5.5.

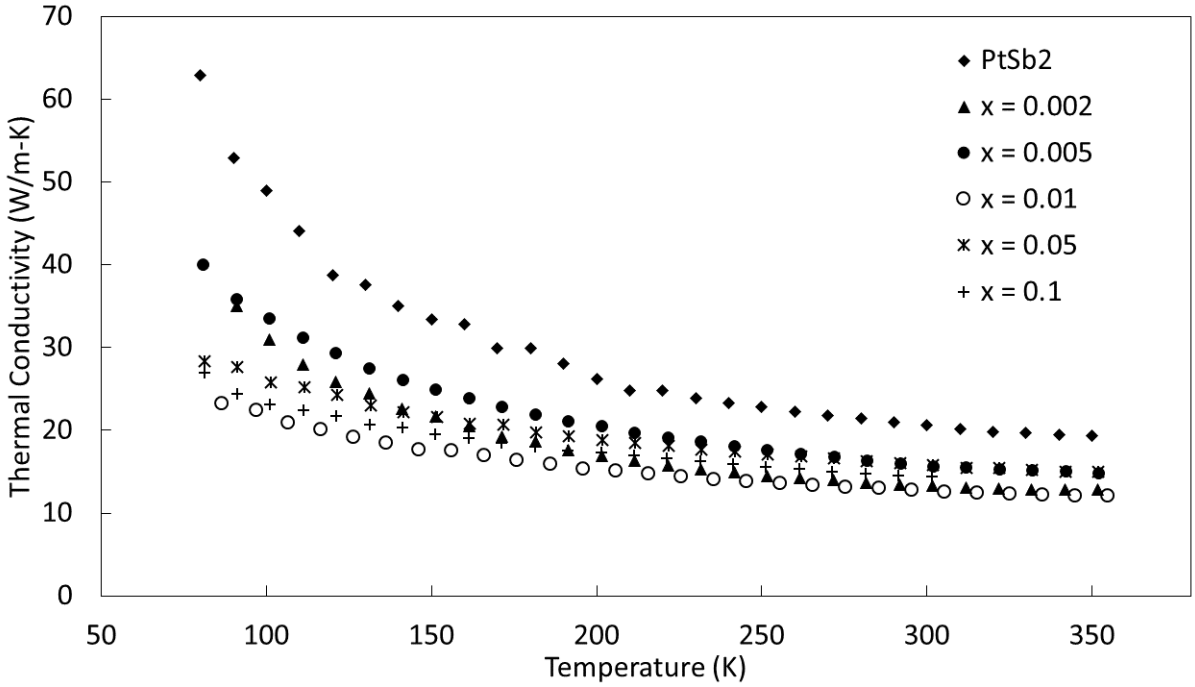

Figure 5.5: Thermal Conductivity of Iron Doped $PtSb_2$

As with other p-type dopants the effects on the thermal conductivity were minimal and resulted from ionized impurity scattering. The sample with the lowest total thermal conductivity was found to be the x = 0.01 sample due to the increased electronic contribution

from the further doped x = 0.05 and 0.1 samples.

5.3.4 zT

The resultant zT of iron doped samples is shown in Figure 5.6.

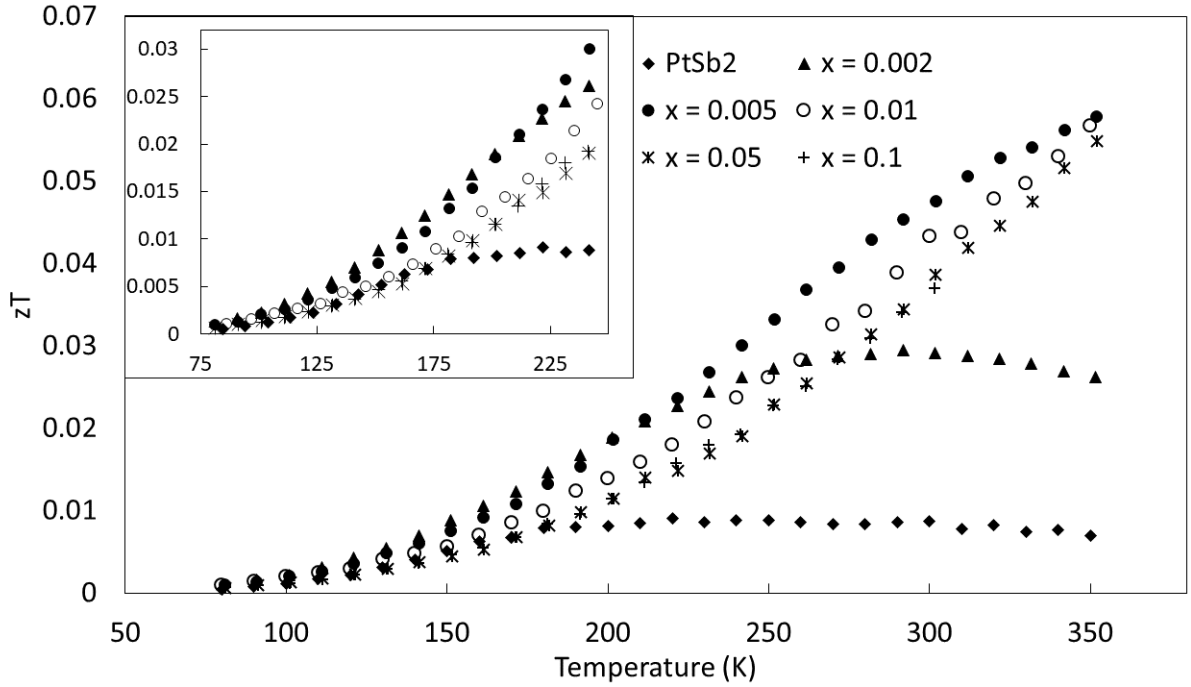

Figure 5.6: zT of Iron Doped $PtSb_2$

Very similar to the figure-of-merit found for tin and tellurium doped samples the iron doped samples showed large enhancement above room temperature. The maximum zT was obtained in the x = 0.005 sample at 350 K with a value of approximately 0.057, though the x = 0.01 and 0.05 samples were found to be within systemic error of this value. At low temperatures a slight enhancement of the figure-of-merit was found for doped samples. These results demonstrated that, as with doping on the antimony site, a large reduction in the thermal conductivity was needed for substantial zT values to be obtained.

5.4 Ytterbium Dopant Results and Discussion

5.4.1 X-Ray Diffraction

The X-ray diffraction patterns for ytterbium doped $PtSb_2$ are shown in Figure 5.7.

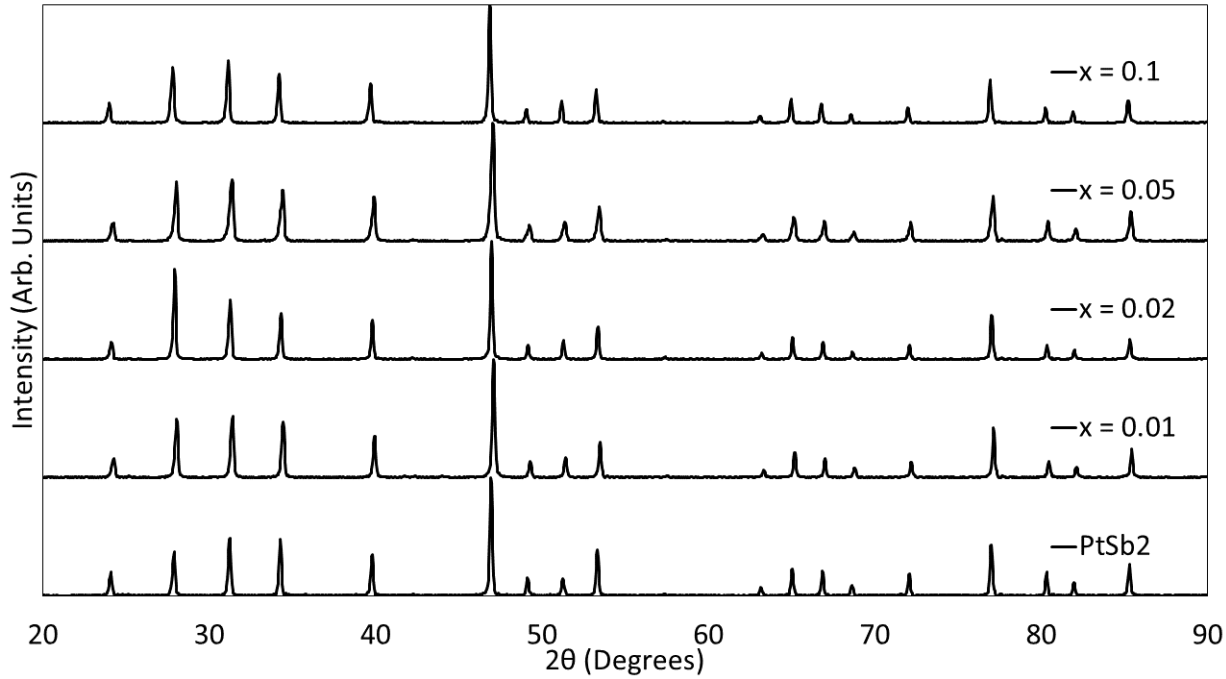

Figure 5.7: X-ray Diffration of Ytterbium Doped $PtSb_2$

Examination of these patterns shows no extraneous peaks corresponding to a secondary phase and no shift in the lattice parameter. It should be noted that the composition of x = 0.1 may be a solubility limit for ytterbium in the $PtSb_2$ structure due to the occurrence of secondary phases for any larger composition. In trials with higher compositions an x = 0.15 sample yielded secondary phases of antimony and a x = 0.2 sample yielded phases of platinum ytterbium, Pt_3Yb, and platinum antimony, PtSb. The finding of secondary phases in samples with high concentrations of ytterbium dopant matched what was found by Bennett et al. [110].

5.4.2 Electronic Properties

A comparison of the effect of varying concentrations of ytterbium dopant on the Seebeck coefficient may be found in Figure 5.8.

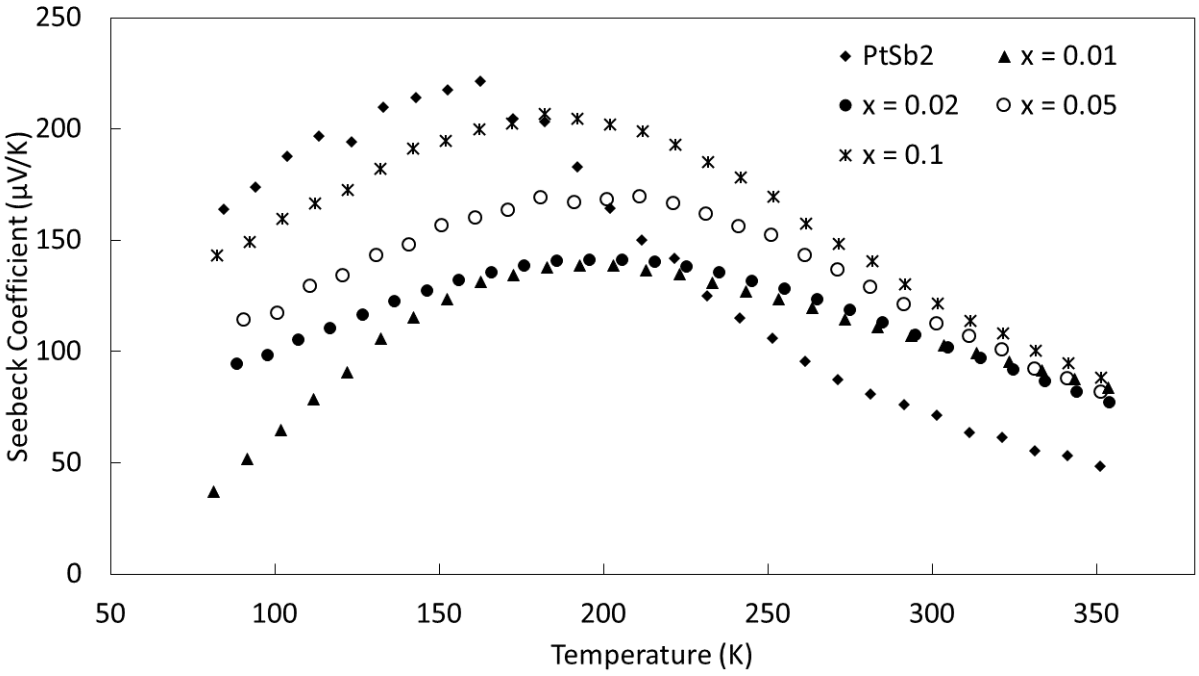

Figure 5.8: Seebeck Coefficient of Ytterbium Doped $PtSb_2$

First turning our attention to the lightest doped sample, the x = 0.01 composition, a significant decrease in the Seebeck coefficient and a slight shift in the maximum was found when compared to undoped $PtSb_2$. Moving to the next highest concentration, the x = 0.02 sample, an increase in the magnitude was found at low temperatures compared to the x = 0.01 composition, which at approximately 170 K met that of the x = 0.01 sample and followed the same trend as temperature increased. The x = 0.05 sample further increased the magnitude of the Seebeck coefficient across all temperatures measured, and showed the same range of temperatures where it was maximized. The final composition measured, the x = 0.1 sample, showed the largest Seebeck coefficient of the doped samples with a slight

shift in peak to lower temperatures of approximately 10 to 20 K, compared to the other compositions. As dopant concentration increased, the temperature at which the Seebeck coefficient of these samples surpassed undoped $PtSb_2$ decreased. At high temperatures all samples were found to converge to approximately 80 to 90 μV/K at 350 K.

From these results it was clear that for this dopant there was not simply an n- or p-type doping process occurring here. As was found from the results of Fe, Sn, and Te doping a p-type dopant will decrease the magnitude of the Seebeck coefficient, and shift the peak to higher temperatures as dopant concentration is increased. An n-type dopant will at high enough concentration change the sign of the material to negative, and with decreasing concentration lead to an increase in the magnitude, and a shift in the maximum to lower temperatures. However, with ytterbium doping the magnitude of the Seebeck coefficient initially dropped to a low value for low concentrations and subsequently increasing that concentration led to an increase in the magnitude.

Observing now the effects of ytterbium doping on the electrical resistivity in Figure 5.9 further evidence of this unusual transport behavior is shown.

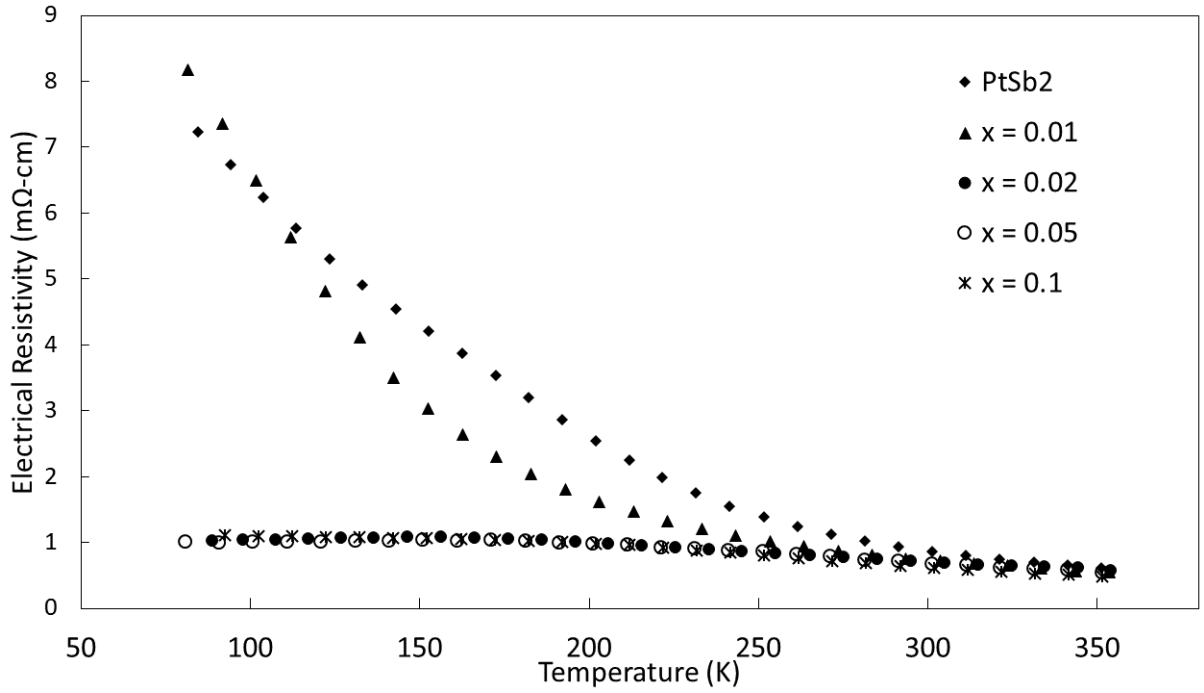

Figure 5.9: Electrical Resistivity of Ytterbium Doped $PtSb_2$

It was found that in the lowest dopant concentration sample, x = 0.01, between 80 and 110 K the electrical resistivity was higher than undoped $PtSb_2$ but quickly dipped below due to its steeply decreasing slope. At temperatures where intrinsic carriers began to be populated, the slope decreased and converged with the electrical resistivity of undoped $PtSb_2$ at approximately room temperature. All other dopant concentrations were found to have significantly decreased electrical resistivity at low temperature. All of these dopant compositions were found to display very similar electrical resistivities of approximately 1 mOhm-cm, which decreased slightly as intrinsic carriers were populated and converged with undoped $PtSb_2$, again at approximately room temperature.

If an element is doped into a material and it is not isoelectronic to the atom it is replacing, then a change in the electrical resistivity between differing dopant concentrations is expected. Thus, it was unusual that increasing concentrations of ytterbium caused no

significant change in the electrical resistivity between the x = 0.02, 0.05, and 0.1 samples. For this to happen there was either no change in the mobility of carriers and no change in the carrier concentration, or the changes in the mobility and the carrier concentration perfectly compensated each other.

Comparing the results of the Seebeck coefficient with the results from electrical resistivity, we see clear changes in the Seebeck coefficient in spite of the constant resistivity. The effects observed here may have their origin in the chemical-pressure driven intermediate valence behavior of Yb, which is known to produce large Seebeck coefficient in the cryogenic temperature range [84]. Further work to determine the cause of this effect would entail the use of Hall experimentation and magnetic measurements.

Turning to the power factor for these doped samples a large increase was found at low temperature. This is shown in Figure 5.10.

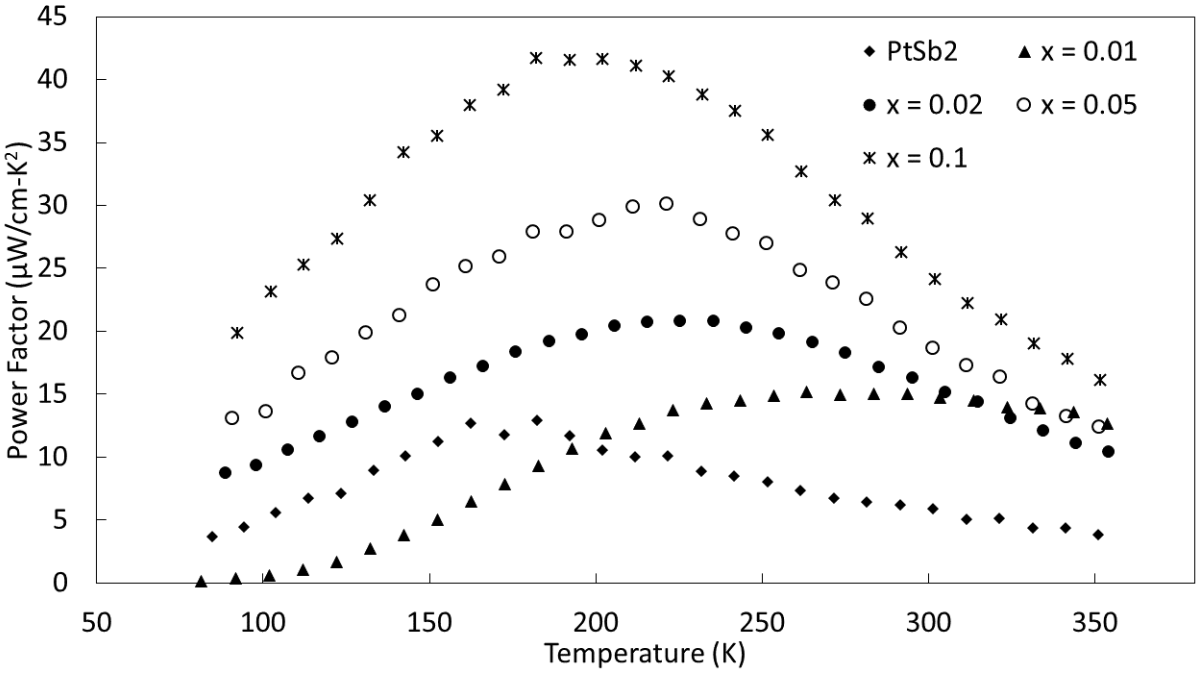

Figure 5.10: Power Factor of Ytterbium Doped $PtSb_2$

The maximized power factor was found in the x = 0.1 sample to have a value of approximately 42 μW/cm-K^2 between 180 to 200 K. This is the highest power factor for $PtSb_2$ found in this work and double the values found for other dopants in this temperature region. This power factor was even comparable to that of commercial Bi_2Te_3 in this temperature region. With the large enhancement found over undoped $PtSb_2$, and the increasing power factor with increasing Yb concentration, higher dopant concentrations were attempted. However, as outlined in the X-ray Diffraction section, higher concentration samples were unable to be synthesized without secondary phases.

5.4.3 Thermal Properties

The thermal conductivity of ytterbium doped $PtSb_2$ is shown in Figure 5.11.

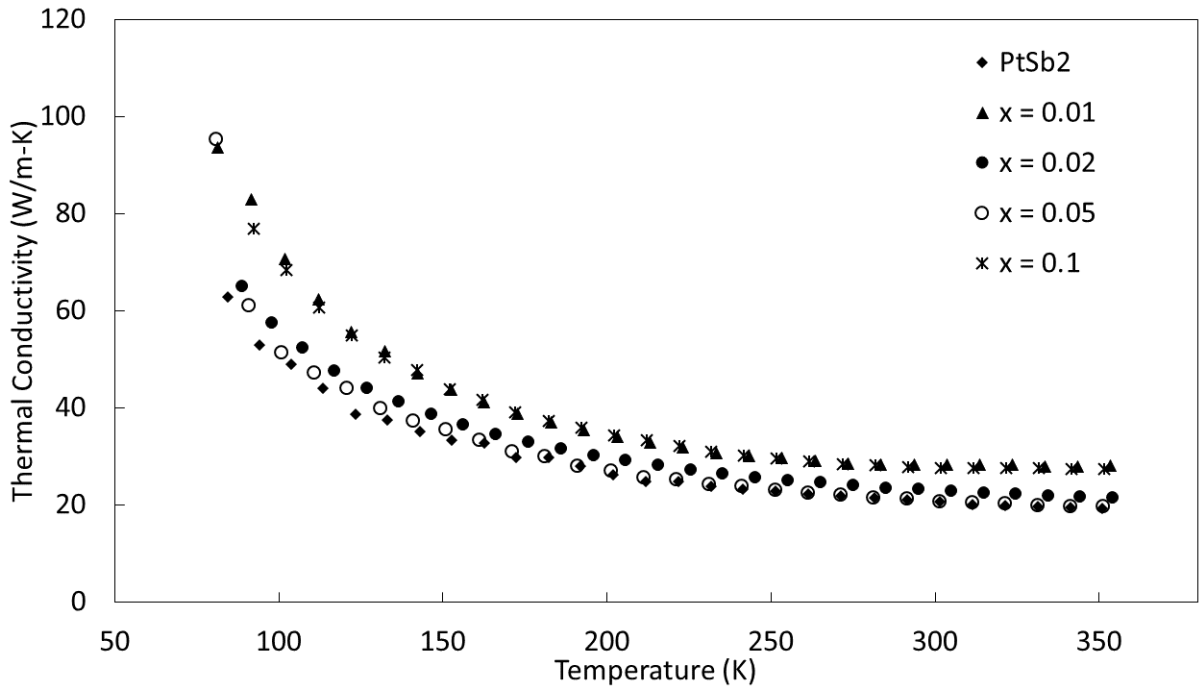

Figure 5.11: Thermal Conductivity of Ytterbium Doped $PtSb_2$

For all samples a small increase was found in the thermal conductivity and was most

prominent at low temperatures in the x = 0.01 and 0.1 samples. The electronic contribution to thermal conductivity was found to be increased relative to undoped $PtSb_2$, but was still more than an order of magnitude lower than the lattice contribution at room temperature and two orders of magnitude lower at 80 K. Ultimately, the lattice contribution to thermal conductivity was the major contributor to the increase in the total thermal conductivity in these samples.

5.4.4 zT

Turning our attention to the figure-of-merit of ytterbium doped samples in Figure 5.12.

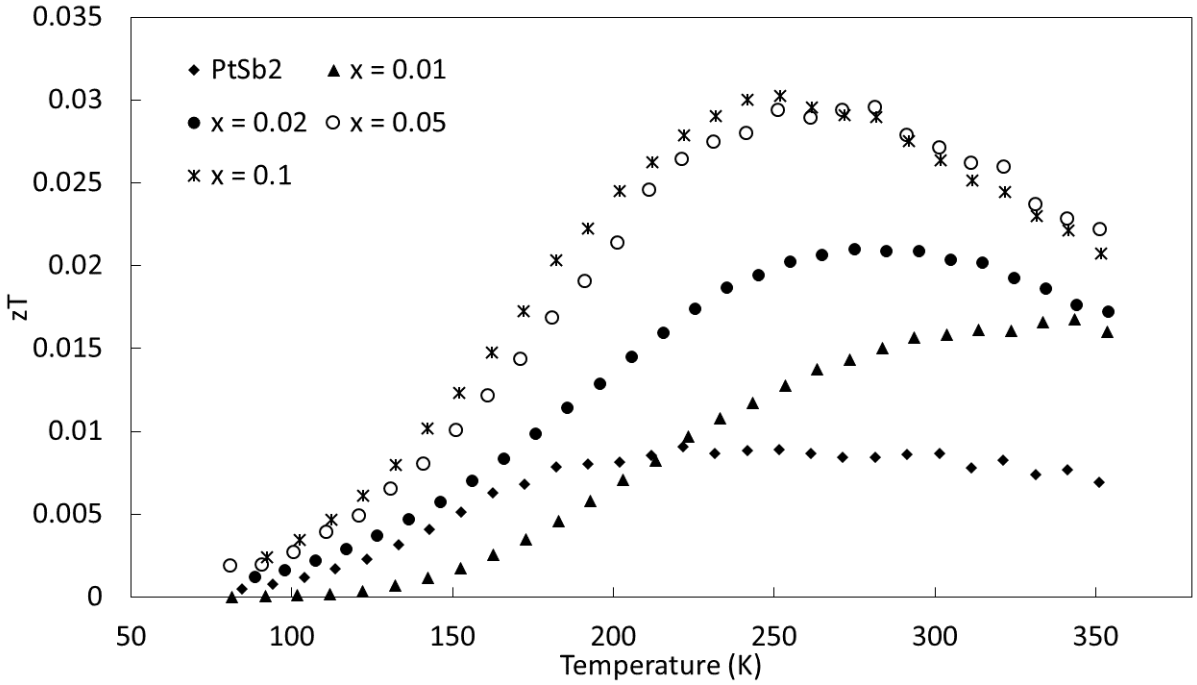

Figure 5.12: zT of Ytterbium Doped $PtSb_2$

The increased power factor of these samples ultimately resulted in an enhancement in the figure-of-merit most prominent below room temperature. The highest dopant concentration, x = 0.1, resulted in a zT = 0.03 at 250 K. Comparison of this result with those found previ-

ously for n- or p-type doping showed that this value was not uncommon at this temperature. For instance, tellurium doped samples showed zT = 0.027 and tin doped samples showed zT = 0.038 at 250 K. However, this enhancement was centered around the temperature region targeted by this research, and if a decrease could be made in the thermal conductivity, without affecting the electrical properties, the zT would be further enhanced.

5.5 Silver and Niobium Doping Results and Discussion

The transition metals, silver and niobium, were selected to examine the effects of doping on the platinum site with a large difference in number of valence electrons, nascent valencies, and electronegativities relative to platinum.

5.5.1 X-Ray Diffraction of Silver Doped Samples

Examining first the X-ray diffraction pattern for silver as a dopant it was found that with even the lowest concentrations of silver dopant there existed secondary phases.

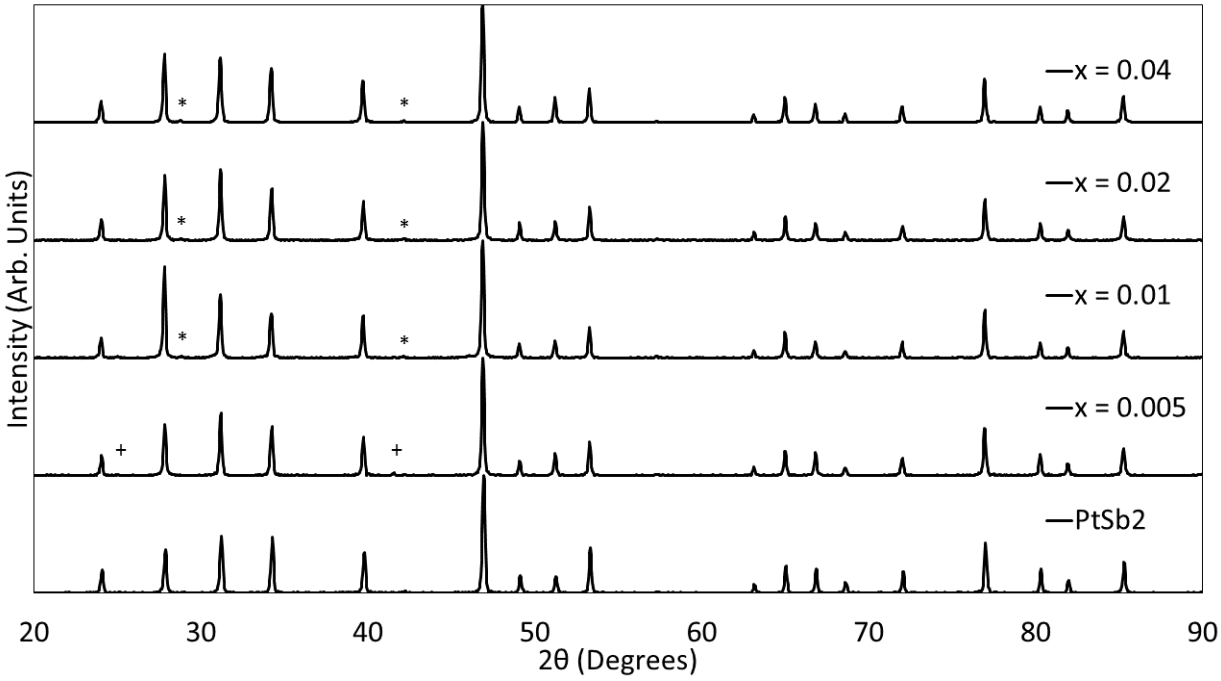

Figure 5.13: X-Ray Diffraction of Silver Doped $PtSb_2$

It was found that in the x = 0.005 sample a platinum antimony phase existed, demarcated with a cross, and in the higher dopant concentration samples an antimony phase was found, demarcated with an asterisk. It was unexpected that a low concentration of silver dopant would have this effect due to its proximity in the periodic table to platinum, however, a similar effect was seen with germanium doping on the Sb site.

5.5.2 Electronic Properties of Silver Dopant

The Seebeck coefficient measured for silver doping displayed the additional secondary phase in this material in Figure 5.14.

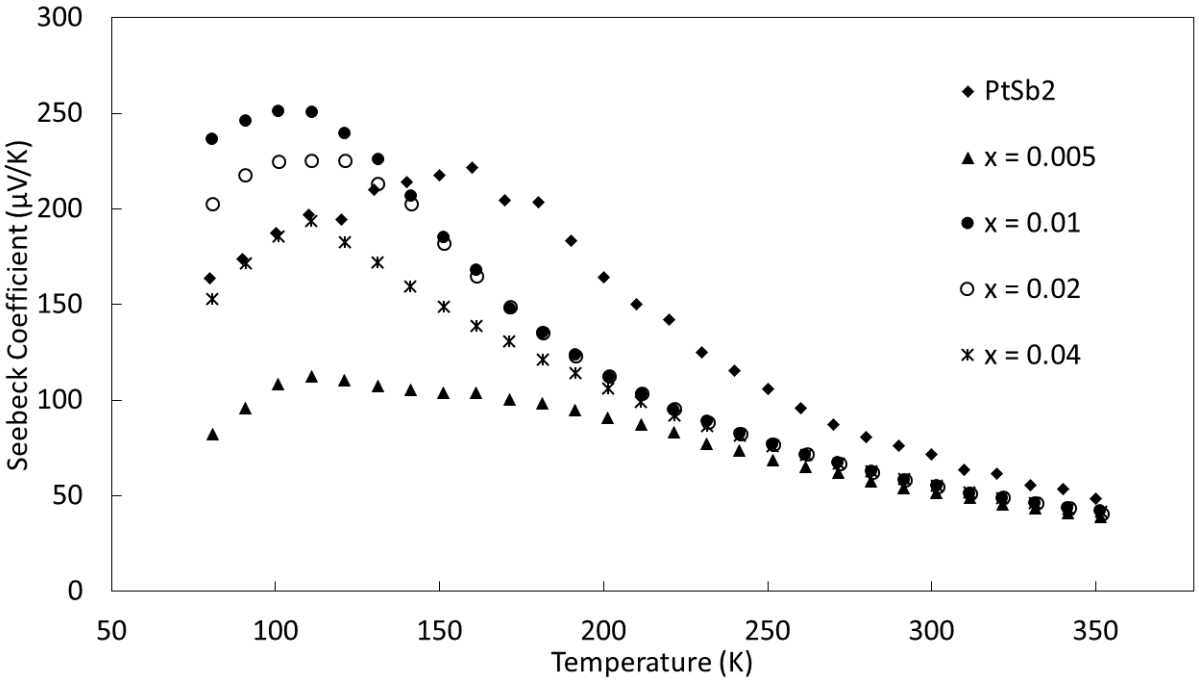

Figure 5.14: Seebeck Coefficient of Silver Doped $PtSb_2$

The lowest concentration, which displayed the secondary phase of platinum antimony, was found to have a greatly decreased Seebeck coefficient reflecting the incorporation of the metallic platinum antimony compound. Samples with larger dopant compositions showed a secondary phase of antimony which is reflected in the Seebeck coefficient by a shift in the temperature of the maximum to lower temperatures, as well as a slight increase in the magnitude. From the x = 0.01 sample to the x = 0.04 sample a decrease was found in the magnitude of the Seebeck coefficient, but no shift was found for the temperature at which the peak occurred.

Due to the secondary phases and impurities in this system, the expected n-type dopant behavior was not observed. A similar change in sign of the Seebeck coefficient as that found from tellurium doping on the antimony site was expected in these silver doped samples. However, a separate effect, ionized impurity scattering, was likely observed. It has been

shown that due to the large dependence of the Seebeck coefficient on the mobility of carriers that manipulation of the mobility, by increased scattering from ionized impurities, may result in an enhancement in the thermoelectric properties [131, 132]. This effect requires a balance between the enhancement in the Seebeck coefficient and the reduction in the carrier mobility, which Ioffe first theorized as a possible application [133]. It is theorized that those carriers which are lower in energy are preferentially scattered by the ionization of these impurity states and that this leads to an increase in the Seebeck coefficient [134].

An examination of the electrical resistivity displays the increased scattering from impurities in Figure 5.15.

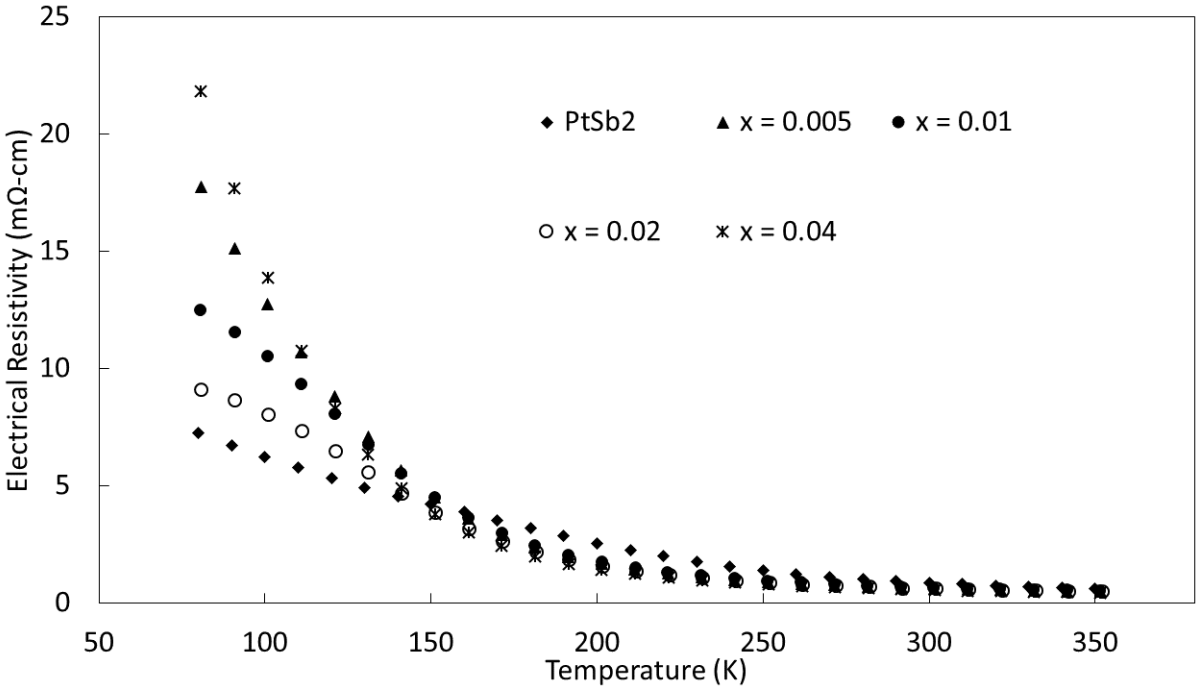

Figure 5.15: Electrical Resistivity of Silver Doped $PtSb_2$

It was found for all silver doped samples that the electrical resistivity was increased at low temperatures until the onset of intrinsic carriers brought about a reduction. This data demonstrated the lack of electronic doping from small concentrations of silver dopant. If

silver had been n-type doping on the platinum site, a similar electrical resistivity as that found from tellurium doping on the antimony site would be expected. In combination with the results for Seebeck coefficient, these results pointed toward a change in the mobility of carriers with the lack of a large change in carrier concentration, however, Hall experiments to determine carrier concentration and mobility would be required for a full examination.

An examination of the power factor displayed an overall reduction from the incorporation of secondary phases in this structure. The slight enhancement in the Seebeck coefficient at low temperatures did not offset the increase in the electrical resistivity.

5.5.3 Thermal Properties and zT of Silver Dopant

The thermal conductivity of these samples was found to be largely unaffected by the incorporation of impurities. All samples showed thermal conductivity values that were within the error of the system and thus the additional scattering from secondary phases was offset by their contribution to the thermal conductivity.

Ultimately, the figure-of-merit for these silver doped samples was found to be reduced for all compositions measured. Without a reduction in the thermal conductivity the lack of enhancement in power factor only produced a diminished zT for these samples.

5.5.4 X-Ray Diffraction of Niobium Doped Samples

Turning now to the doping of niobium on the platinum site the X-ray diffraction pattern of this dopant is given in Figure 5.16.

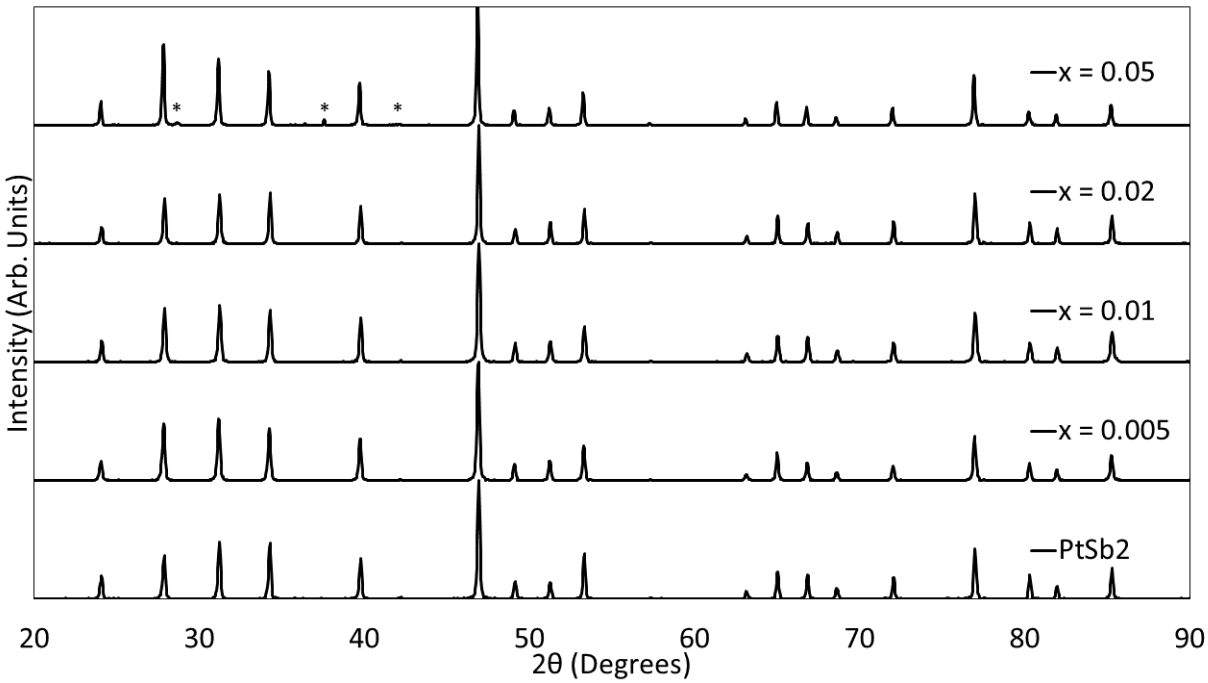

Figure 5.16: X-Ray Diffraction of Niobium Doped $PtSb_2$

Unlike the silver doped samples, the niobium dopant only showed an additional secondary phase of antimony in the x = 0.05 sample. However, as will be shown in the Seebeck coefficient and electrical resistivity data, it was very likely that a secondary phase was present in all samples which was simply too low of a concentration to generate a signal in X-ray diffraction. It was further found that for even greater concentrations of niobium, $x > 0.05$, that additional secondary phases were found on X-ray diffraction of niobium diantimonide, $NbSb_2$.

The Seebeck coefficient data for niobium doped samples is shown in Figure 5.17.

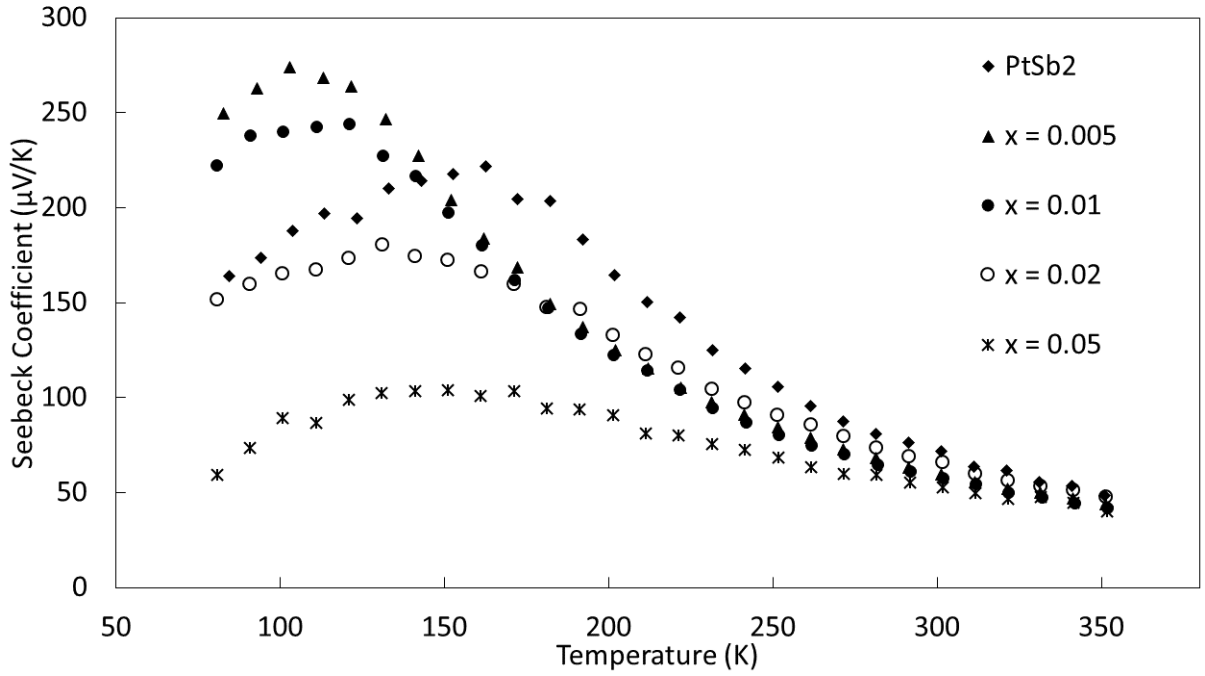

Figure 5.17: Seebeck Coefficient of Niobium Doped $PtSb_2$

A similar increase and shift of the peak in Seebeck coefficient to lower temperatures found from silver doping was also found here in the lowest concentrations. This pointed again towards the effects of ionized impurity scattering as a likely cause of this increase in the Seebeck coefficient at these low concentrations. As the concentration was increased the Seebeck coefficient was found to be diminished over all temperatures in the x = 0.02 sample. In the x = 0.05 sample where a secondary phase was readily observed in X-ray diffraction the Seebeck coefficient was found to be diminished due to the presence of antimony.

This scattering was again reflected in the electrical resistivity for these samples, shown in Figure 5.18.

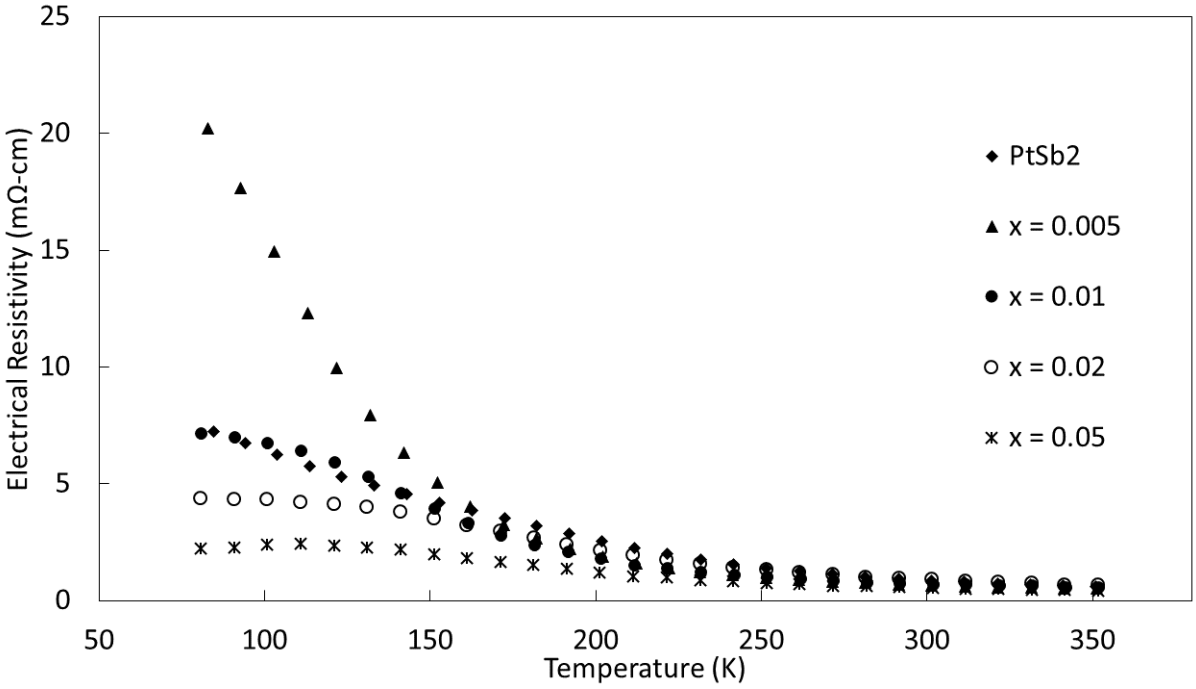

Figure 5.18: Electrical Resistivity of Niobium Doped $PtSb_2$

The large degree of scattering that was found for silver doping was again found for this data in the x = 0.005 sample. This gave further evidence of a secondary phase in this sample that was too low to be found in X-ray diffraction. As niobium concentration increased it was found that the electrical resistivity decreased due to the increasing concentration of secondary phases of antimony and niobium antimonide.

As with the silver dopant, the power factor of niobium doped samples was found to be reduced over all temperatures, except in the x = 0.01 sample, yet this was observed only at low temperatures. The increase for this sample was due to the enhanced Seebeck coefficient magnitude at low temperatures in combination with the relatively unchanged electrical resistivity of the sample compared to undoped $PtSb_2$.

5.5.5 Thermal Properties and zT

Similar to the silver doped samples these samples showed no significant change in thermal conductivity due to doping. Again, it is likely that the increased scattering due to secondary phase boundary scattering was offset by the thermal conductivity of those secondary phases.

The slight increase in power factor coupled with an unchanged thermal conductivity led to a slight enhancement of the figure-of-merit at low temperature in the x = 0.01 sample. All other samples for all temperatures measured showed a diminished zT due to a decreased power factor and an unchanged thermal conductivity.

5.6 Conclusions

In effect, there were three different studies performed on doping the platinum site of $PtSb_2$. The first examined here concerned iron doping in an attempt to incorporate the strongly correlated electron effects which are present in $FeSb_2$ to increase the Seebeck coefficient and thereby the figure-of-merit. It was found that iron acted as a p-type dopant on the platinum site and did indeed yield increased figure-of-merit, yet not by any incorporation of the effects found in $FeSb_2$. This however, gave further evidence of the enhancement potential of n- or p-type doping of transition metals.

The successful p-type doping of iridium and iron on the platinum site instigated an investigation for an n-type dopant, thus, silver, with an additional valence electron, was examined. Due to the generation of secondary phases the effect of this dopant was unable to be examined, however, the effects of ionized impurity scattering were observed for these samples. It was further found that niobium dopant produced a similar ionized impurity scattering effect, which resulted in a slight enhancement in the power factor at low temperatures.

The incorporation of rare earth dopants in $PtSb_2$ is an exciting avenue due to the curious results that may be obtained. While the figure-of-merit was not particularly enhanced at low temperature relative to simple electronic n- or p-type doping, the trend of the maximum in zT, which was a shift to lower temperature and an increase in magnitude, was exactly what was desired for this project. The thermal conductivity of this sample was, as with all of these samples, the largest hindrance to large figure-of-merit, but the power factor obtained by ytterbium doping was significantly enhanced at low temperature.

Further work on doping the platinum site of $PtSb_2$ could examine the effects of gold doping in an attempt to n-type dope on the platinum site. Another avenue would be a study into the effects of cerium doping on the platinum site and a comparison of those results with those found from ytterbium doping. Ultimately, future work on $PtSb_2$ should incorporate methods of reducing the thermal conductivity while also tuning the carrier concentration through doping on the platinum site, as well as, the antimony site.

Chapter 6

Methods to Reduce Thermal Conductivity

6.1 Background and Motivation

From the prior work on electronic doping it was determined that a large reduction in the thermal conductivity of $PtSb_2$ was required for significant enhancement of the figure-of-merit. Figure 6.1 displays the large reduction in thermal conductivity that would be required to generate significant zT values in $PtSb_2$. This figure shows the result of several hypothetical reductions in the total thermal conductivity on the zT assuming no reduction in the power factor from this effect.

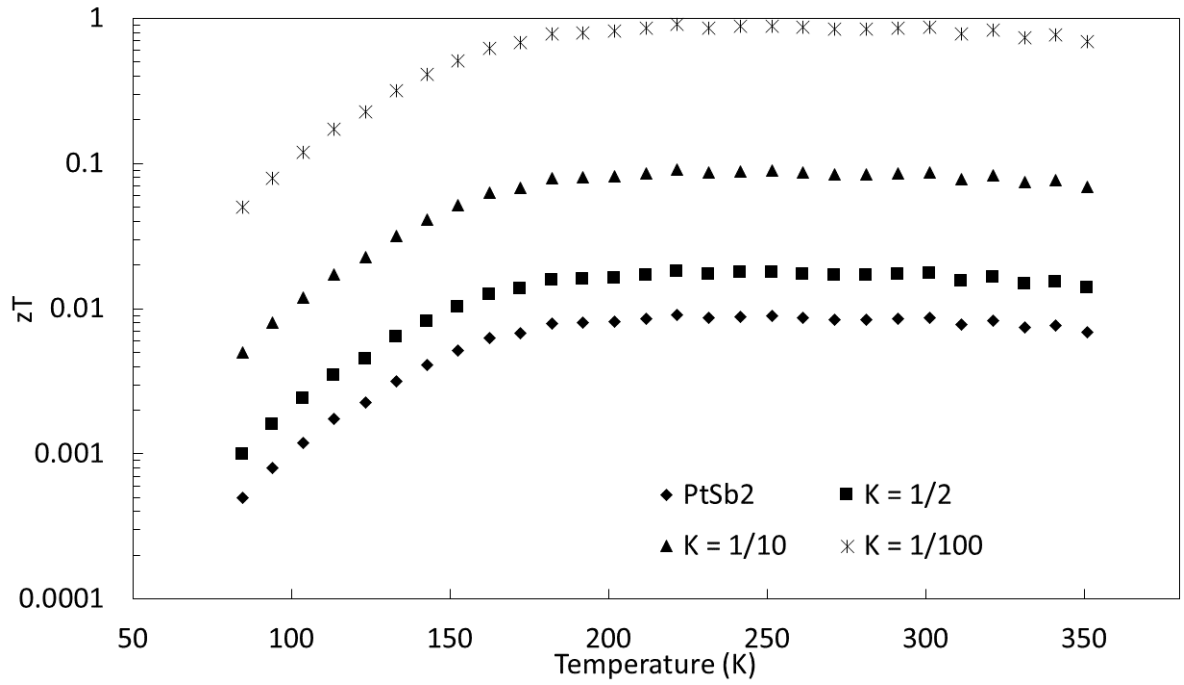

Figure 6.1: Thermal Conductivity Reduction required for high zT

This figure demonstrates that for un-doped $PtSb_2$ the total thermal conductivity would need to be reduced by two orders of magnitude to approach values of commercial Bi_2Te_3. In electronically doped samples, with optimized carrier concentration, a reduction in the thermal conductivity by a factor of 20 to 30 would still be required to result in near unity zT, again, independent of any modifications to the electronic properties.

Several methods of reducing thermal conductivity have been examined in prior research. One method is the generation of a solid solution of two elements or compounds, e.g. Si-Ge or $(PbTe)_x(PbSe)_{1-x}$. In this method elements with a difference in mass are alloyed together to cause point defect scattering. A large body of theoretical and experimental work has been performed to display the effectiveness of this procedure [135–138]. In the generation of a complete solid solution it is important for the two end compounds to have similar crystal structures otherwise it is likely that the materials will merely mix and generate a two

phased material. The more differences there are between the two end compounds the more scattering there will be, however, these large differences will make the full solid solution less thermodynamically favorable. For example, if a trigonal system with large lattice parameter is alloyed with a cubic system with small lattice parameter, then a large amount of strain will be present in the lattice even with low concentrations which may stop the formation of a full solid solution.

For $PtSb_2$ in the pyrite structure this means that other materials also in the pyrite structure should be targeted for their potential use because these materials in theory will more dependably form a solid solution. It has been shown that the materials: $PdAs_2$ and $PdSb_2$, and $PtPn_2$, where Pn = S, As, Sb, and Bi also crystallize in the pyrite structure [90, 91]. Thus, all of these materials would be possible candidate materials for use in the generation of a solid solution. The material $PdSb_2$ was selected due to its similar crystal structure and lattice parameter to $PtSb_2$, as well as to avoid using the toxic element arsenic and phosphorous with a low boiling point.

Another often used means of reducing the thermal conductivity is the reduction of particle size by ball milling or melt spinning [139–142]. Boundary scattering acts as a method to reduce the lattice contribution to thermal conductivity which is most prominent at low temperatures but will cause a reduction over all temperatures. The reason why particle size reduction affects low temperature thermal conduction to such a large degree is due to the length scale of the wavelength of phonons at low temperature. With low thermal energy, phonons will have a low frequency, and thereby a long wavelength. This long wavelength is scattered preferentially by those effects which are on the same length scale. Of these effects, grain boundaries will scatter these large length-scale, long wavelength phonons greater than some of the smaller length-scale effects like point defect scattering.

Thus, the effects of ball milling on the low temperature properties of $PtSb_2$ will be examined here. Further, electronic doping will be performed on ball milled $PtSb_2$ to enhance the electronic properties of these thermally tailored materials. In the course of examining ball milled $PtSb_2$ a series of experiments were performed to examine the effects of non-stoichiometry on the low temperature thermoelectric properties. It had previously been shown that at room temperature the dominant carrier type of $PtSb_2$ could be changed by the effects of non-stoichiometry, thus this was examined as a possible route of enhancement [100].

6.2 Experimental Methods

6.2.1 Solid Solutions with Palladium and Bismuth

To examine the reduction in thermal conductivity due to the generation of a solid solution in $PtSb_2$ the compound $PdSb_2$ was selected. Samples with the composition $Pt_{1-x}Pd_xSb_2$ were synthesized where x = 0.01, 0.05, 0.1, 0.25, 0.5, and 1.0. All samples were synthesized as outlined in the experimental section except for a variation in the SPS parameters which had to be altered due to the lower melting point of $PdSb_2$ of 678 °C [143]. With increasing concentrations of palladium substitution the SPS temperature was reduced incrementally to account for the reduction in melting point. The x = 0.01 and 0.05 samples were sintered at 850 °C, x = 0.1 sample at 800 °C, x = 0.25 sample at 700 °C and the x = 0.5 and 1.0 samples at 450 °C. All samples were sintered for 5 minutes with a pressure of 40 MPa.

6.2.2 Ball Milling and Electronic Doping in $PtSb_2$

To examine the reduction in particle size of $PtSb_2$ from ball milling, samples were synthesized using the typical furnace heat treatment, but before densification were ball milled in a stainless steel ball mill jar back filled with argon in increments of 10 minutes. The sample was examined with X-ray diffraction after each 10 minute increment of milling. A zirconium oxide jar and media was used for comparison with the results of the stainless steel jar and media for one examination. After 100 total minutes of milling, samples were densified by SPS at 500° C for three minutes at a pressure of 40 MPa. A reduction in sintering temperature was necessitated by the lowered melting point of ball milled samples due to the smaller particle size of the powder $PtSb_2$.

To examine the effects of electronic doping on ball milled $PtSb_2$ the two elements Sn and Te were again utilized for comparison with un-ball milled samples. The compositions examined were $PtSb_{2-x}Dp_x$ where Dp is either Sn or Te with compositions ranging between $0 < x \leqslant 0.15$ for tin dopant and $0 < x \leqslant 0.04$ for tellurium dopant. All samples required modified SPS parameters due to the reduction in the melting point of ball milled samples. These parameters entailed SPS at 500 °C for three minutes at a pressure of 40 MPa.

6.2.3 Non-Stoichiometric $PtSb_2$

To determine the effects of non-stoichiometry in $PtSb_2$, samples were synthesized with compositions of $PtSb_{2+x}$ and $-0.05 \leqslant x \leqslant 0.1$. These samples were synthesized using the furnace heat treatment and SPS parameters outlined in the experimental section.

6.3 Solid Solution Results and Discussion

6.3.1 X-Ray Diffraction

It is known that $PdSb_2$ crystallizes in the same pyrite structure as $PtSb_2$ with a very similar lattice parameter of 0.645 nm [85]. It was thus expected that a full solid solution between these two end compounds would form. Contrary to this expectation it was found that at concentrations of Pd of x = 0.1 and higher, the two end compounds failed to form a single phase and that the two phases of $PtSb_2$ and $PdSb_2$ were present in all of these high concentration samples. At concentrations lower than x = 0.1 no secondary phases were found, thus it is only the high concentration samples which are shown in Figure 6.2.

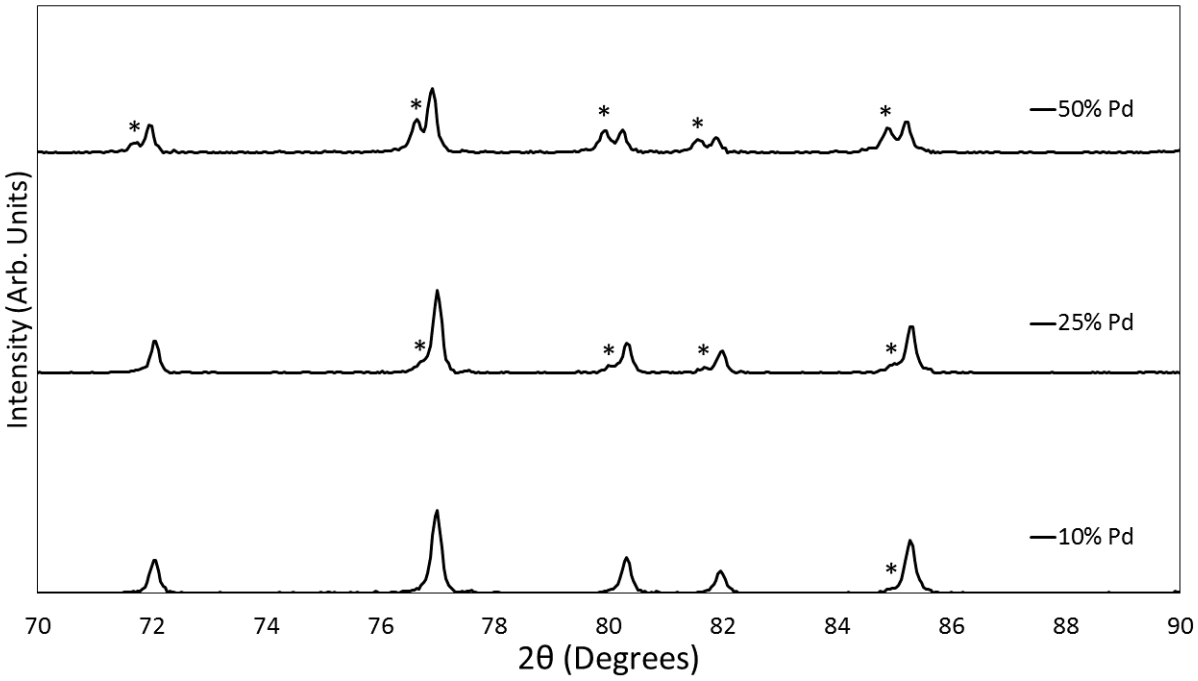

Figure 6.2: X-Ray Diffraction Patterns of Palladium Substituted $PtSb_2$

Observed in Figure 6.2 are the high 2θ peaks for the x = 0.1, 0.25, and 0.5 compositions where the $PdSb_2$ phase is demarcated with an asterisk.

6.3.2 Electronic Properties

When examining the electronic properties of palladium substituted $PtSb_2$ it is important to remember that in the x = 0.1 and higher concentrations there is evidence of two phases being present in these samples. It is expected that a full solid solution between these two compounds would generate differing electronic properties than those found from the alloying of these two compounds. Shown in Figure 6.3 are the Seebeck coefficients of these samples.

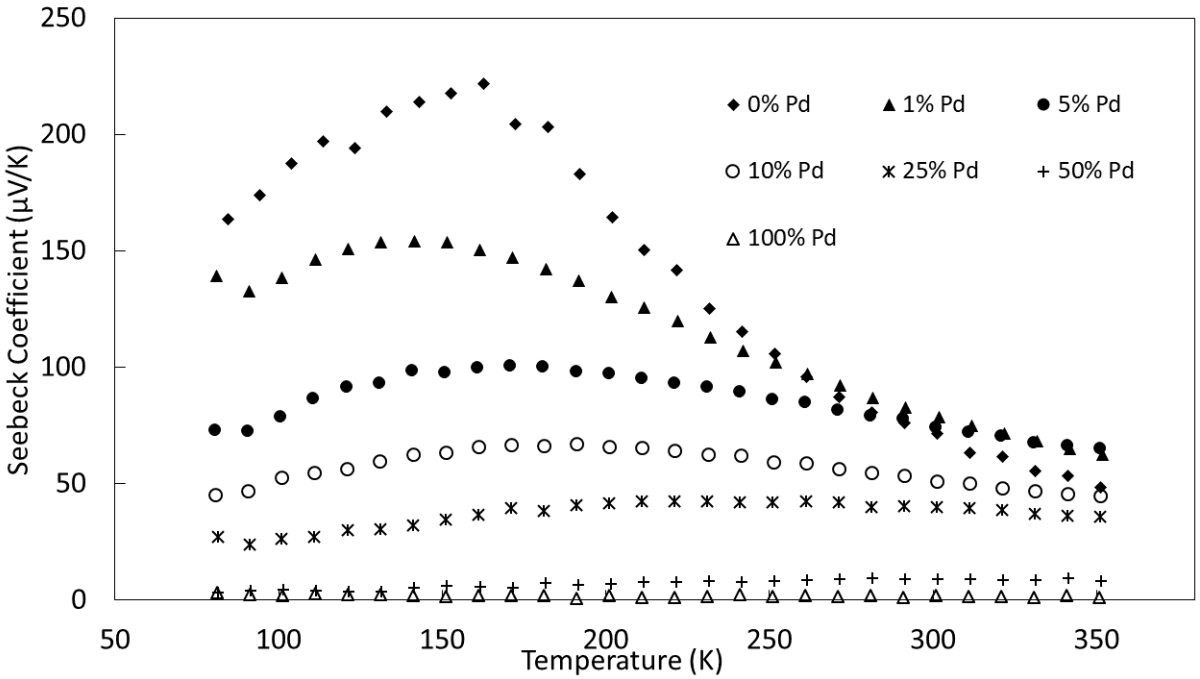

Figure 6.3: Seebeck Coefficient of Palladium Substituted $PtSb_2$

As the concentration of palladium substitution was increased a general decrease in the Seebeck coefficient was found. The temperature at which the peak in Seebeck coefficient occurred was generally found to slightly increase as concentration increased. In the x = 0.5 and 1.0 samples the Seebeck coefficient was found to be greatly decreased and exemplary of what would be expected of a metal. The Seebeck coefficient of $PdSb_2$ is found to range between one to three μV/K and is the expected very low value often found for metals. This is

consistent with band structure calculations, which predict metallic behavior for $PdSb_2$ [144]. Unlike p-type doped samples the Seebeck coefficient was not found to have any composition with a positive trend above room temperature. These samples appear to show an incremental decrease in the Seebeck coefficient with increased Pd substitution which would be expected from an increasing concentration of a metallic phase.

The electrical resistivity of palladium substituted samples is shown in Figure 6.4, with a logarithmic ordinate axis due to the large reduction displayed by the samples.

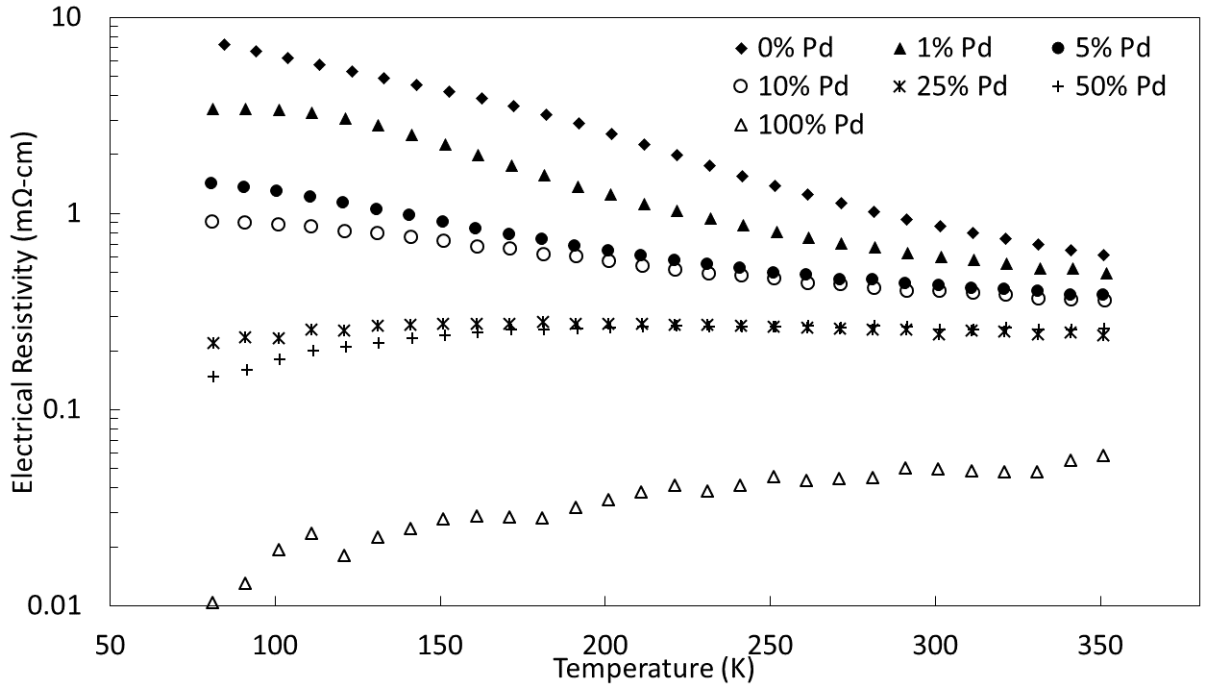

Figure 6.4: Electrical Resistivity of Palladium Substituted $PtSb_2$

It was found that $PdSb_2$ displayed a very low electrical resistivity, nearly three orders of magnitude less than $PtSb_2$, with a positive trend for all temperatures measured. It was found that as Pd composition was increased the electrical resistivity decreased due to the inclusion of the metallic secondary phase. Examining the trend of the electrical resistivity it was found that for low Pd concentration samples a decrease was found as temperature

increased due to the population of intrinsic carriers in the $PtSb_2$ phase. In the x = 0.25 and 0.5 samples this was replaced with an increasing with temperature electrical resistivity due to carrier scattering from the lattice.

Examining the carrier concentration and carrier mobility results from Hall experiments in Figure 6.5 it was found that a large change in the carrier concentration was what created the reduction in electrical resistivity for these samples.

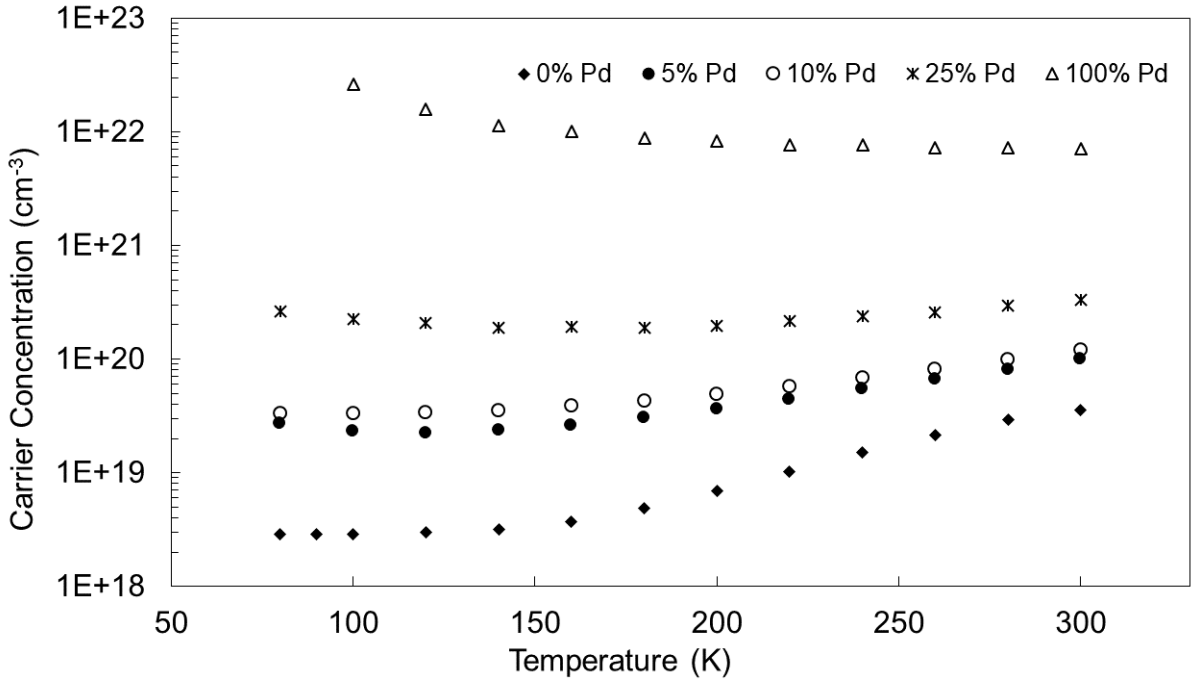

Figure 6.5: Carrier Concentration of Palladium Substituted $PtSb_2$

A large difference in carrier concentration between $PtSb_2$ and $PdSb_2$ from Hall experiments of nearly four orders of magnitude was found. As the concentration of the secondary phase, $PdSb_2$, was increased the carrier concentration was also found to increase. The onset of intrinsic carriers in the $PtSb_2$ phase was found for all Pd substituted samples further demonstrating that a solid solution was not generated. The mobility of these samples was shown to incrementally decrease with increasing palladium substitution which is what would

be expected from the addition of a secondary phase.

6.3.3 Thermal Properties

The thermal conductivity of the $Pt_{1-x}Pd_xSb_2$ samples studied here is shown in Figure 6.6.

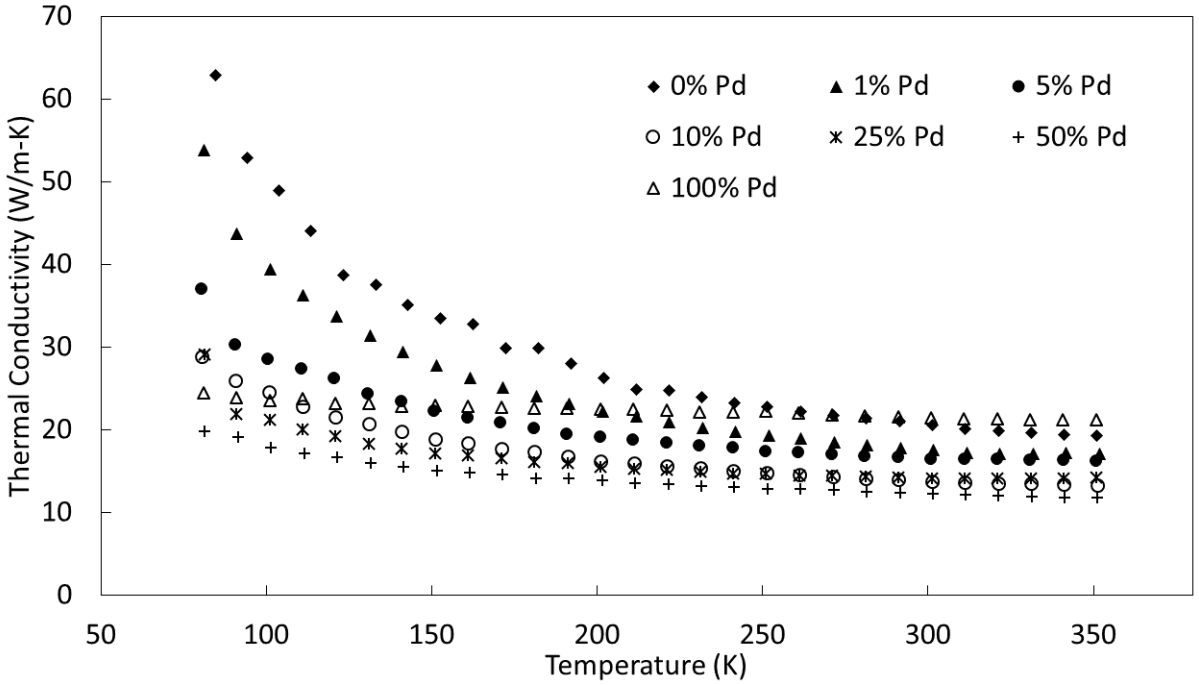

Figure 6.6: Thermal Conductivity of Palladium Substituted $PtSb_2$

It was found that as palladium composition was increased, a general decrease in the total thermal conductivity was found for all temperatures. The sample with the lowest thermal conductivity was the x = 0.5 composition, which would be the expected result from alloying. The total thermal conductivity of $PdSb_2$ was shown to be relatively flat across all temperatures measured with a small decrease as temperature increased. It was found for the $PdSb_2$ sample that the electronic contribution was on the order of the lattice contribution due to the extremely low electrical resistivity of the sample. The effects of Pd substitution were most prominent at low temperature, shown in Figure 6.7.

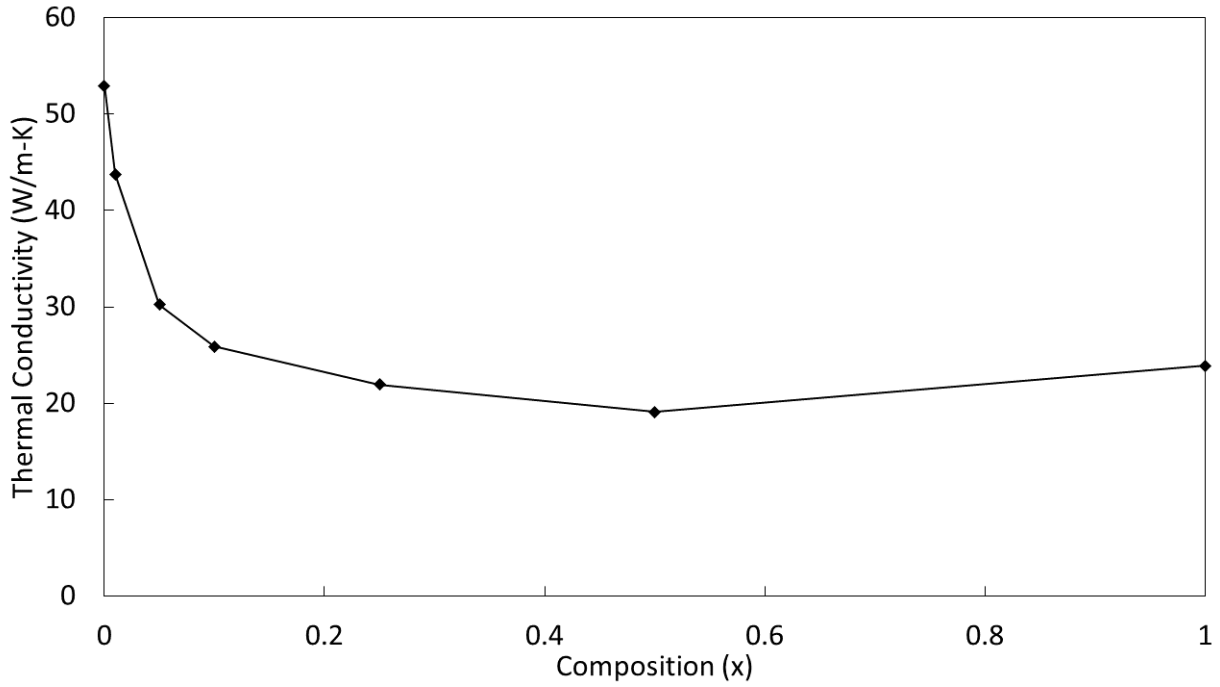

Figure 6.7: Thermal Conductivity of Palladium Substituted $PtSb_2$ at 90 K

A large reduction in total thermal conductivity with low concentrations of Pd substitution was observed, which extended to further reduction in the higher Pd substitution compositions. The expected lowest thermal conductivity was found for the x = 0.5 sample due to the large amount of scattering from the two phases present.

6.3.4 zT

The figure-of-merit of palladium substituted samples is shown in Figure 6.8.

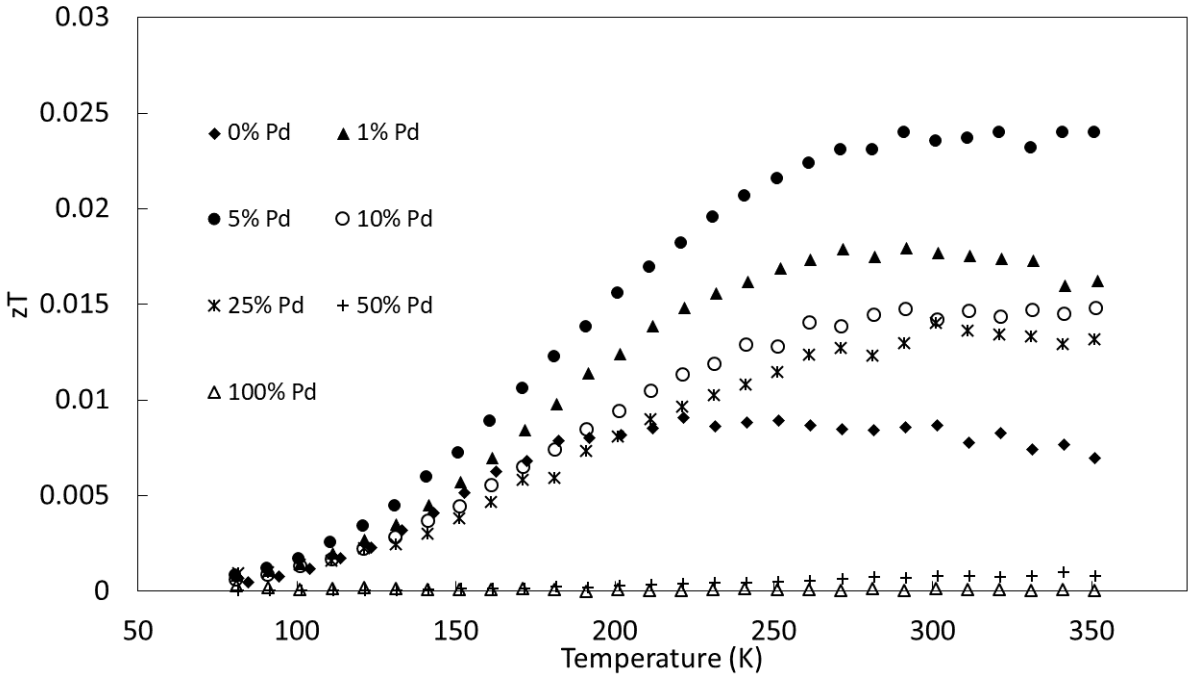

Figure 6.8: zT of Palladium Substituted $PtSb_2$

It was found that all samples with composition x $\leqslant$ 0.25 showed enhancement in the figure-of-merit. It was only in the x = 0.01 and 0.05 samples that the power factor was enhanced beyond nominal $PtSb_2$, but due to the large reduction in the thermal conductivity of the x = 0.1 and 0.25 samples an enhanced zT was still generated. Samples with concentrations x > 0.25 had such a reduced power factor that the lowered thermal conductivity did not offset this value and led to very low zT values.

While the enhancement to the figure-of-merit was only slight for these samples, these results demonstrated the interplay of thermal conductivity reduction and power factor manipulation found from alloying $PtSb_2$ with a metal. It is expected that if a full solid solution had been generated in this experimentation the resultant electronic properties, as well as thermal properties would be significantly different. Most notably the scattering mechanisms would be expected to change from a boundary scattering dominated system to point defect

dominated.

6.4 Ball Milling Results and Discussion

6.4.1 X-Ray Diffraction

To examine the effects of ball milling on the thermal conductivity of $PtSb_2$ a study was performed to examine the optimal time of milling to result in a minimized particle size. A sample of $PtSb_2$ was milled in increments of 10 minutes and shown in Figure 6.9 are the X-ray patterns for 0, 50, and 100 minutes of ball milling time.

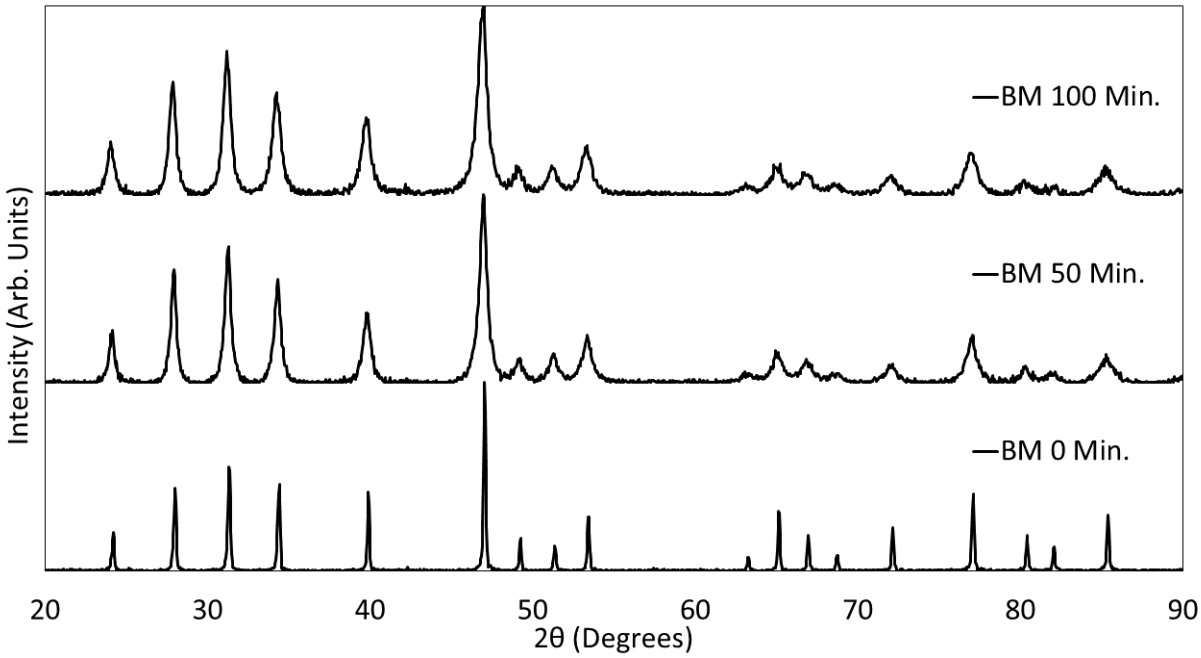

Figure 6.9: X-ray Diffraction of Ball Milled $PtSb_2$

A significant amount of peak broadening was observed in ball milled samples. As can be seen from the above figure, additional broadening was found when comparing 100 minutes of ball milling to only 50 minutes. As was discussed in the experimental section, the broadening

of a peak may be related to both particle size reduction, as well as increased strain in the material. To separate these effects and to determine how long samples should be milled to reach a minimum particle size the Williamson-Hall equation was employed. The results of this analysis are given in Figure 6.10 where particle size is given on the primary axis and full width at half maximum, FWHM, values are given on the secondary axis.

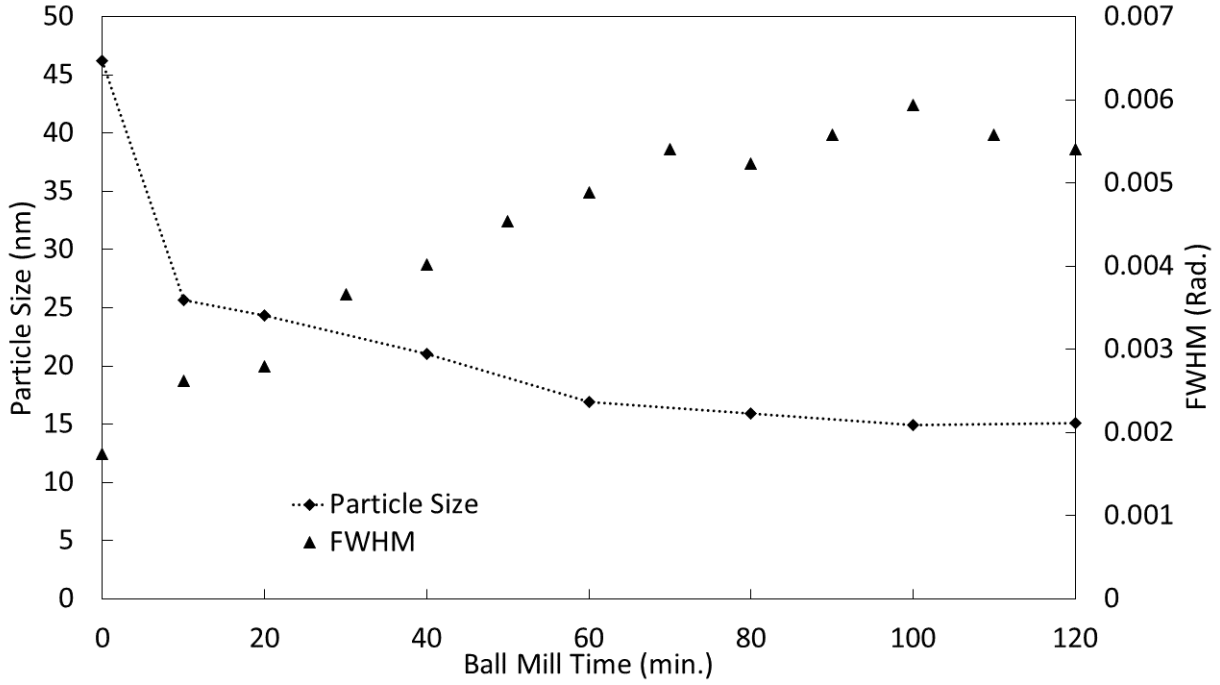

Figure 6.10: Particle Size of Ball Milled $PtSb_2$

Williamson-Hall analysis demonstrated that a large decrease in the particle size was found from only 10 minutes of ball milling. After 10 minutes subsequent milling generated further reduction until approximately 80 minutes where additional milling did not result in further reduction in particle size. Also in this figure is the FWHM of the (311) plane. It was found that the FWHM of this plane showed a slower broadening of its peak, however the broadening was again found to be maximized at approximately 80 minutes. The FWHM, again, contains information not only on particle size but also internal strain and is useful

as a secondary proof that milling should be stopped at 100 minutes. It should additionally be noted that to substantiate any quantitative particle size further experimentation should be performed, such as scanning electron microscopy analysis. However, for this study, the most important aspect was not the exact size of particles but the required time of ball milling to reach a minimized particle size. Thus, to account for error, it was assumed that to generate a minimized particle size in this material a ball milling time of 100 minutes should be performed.

6.4.2 Thermal Properties

As the objective of this study was to examine the reduction in thermal conductivity obtained from ball milling the thermal properties will be presented first. Shown in Figure 6.11 is the thermal conductivity of ball milled $PtSb_2$.

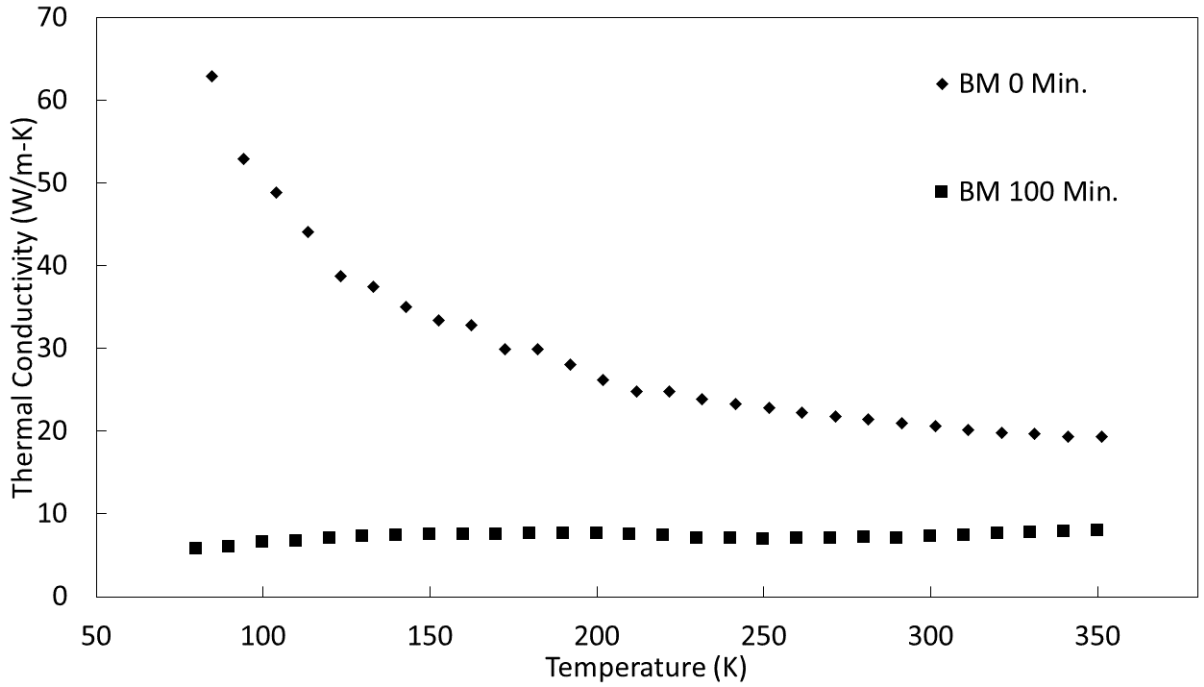

Figure 6.11: Thermal Conductivity of Ball Milled $PtSb_2$

A very large reduction in thermal conductivity was found from ball milling $PtSb_2$, most pronounced at low temperatures, which matched what was expected from theory. The reduction found at 80 K was slightly larger than an order of magnitude changing from approximately 63 W/m-K to 5.7 W/m-K. Unlike that found for nominal $PtSb_2$ a reduction from acoustic phonon scattering was not found as temperature increased, which is exemplary of Matthieson's rule in this sample. Matthieson's rule states that the largest scattering mechanism will dominate over other present mechanisms, which is what was found in these results. A large increase in boundary scattering from particle size reduction led to boundary scattering being the dominant mechanism for these temperatures. Thus, the typical reduction in thermal conductivity as temperature increased due to acoustic phonon scattering was not observed.

Comparing the lattice contribution to thermal conductivity versus the electronic contribution showed that the lattice contribution was the majority component to the total thermal conductivity for all temperatures examined, as well as, the largest contributor to the reduction observed here.

6.4.3 Electronic Properties

Focusing now on the electronic properties measured from ball milled samples an interesting result was observed in the Seebeck coefficient, shown in Figure 6.12.

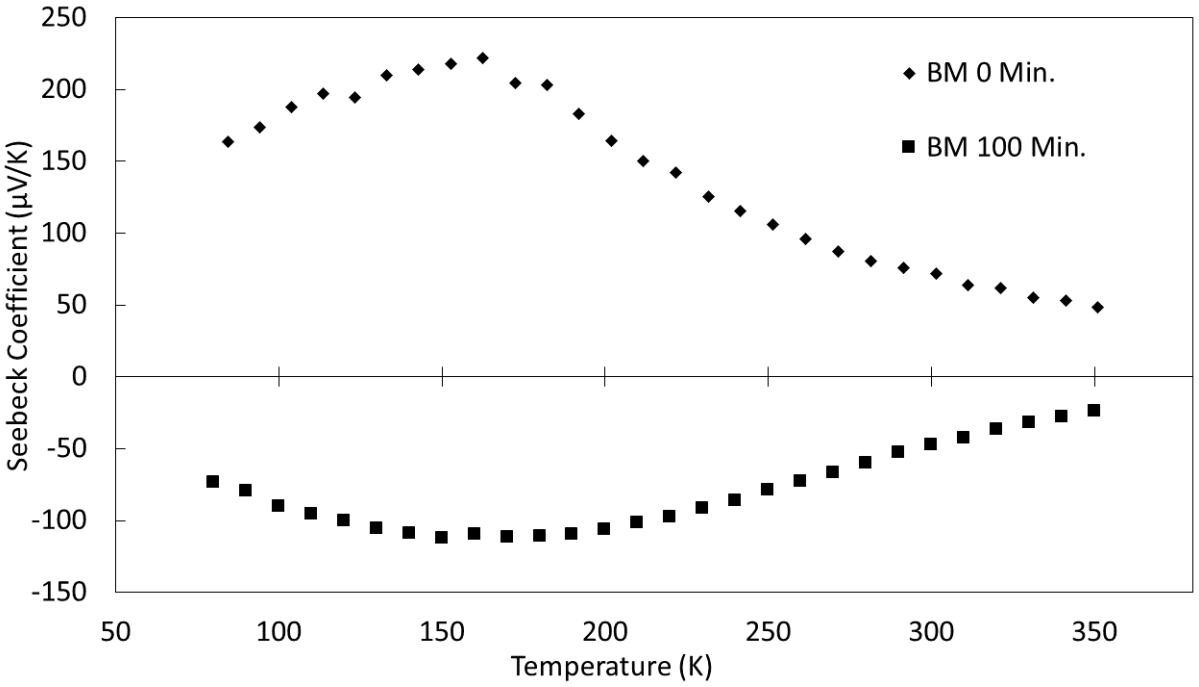

Figure 6.12: Seebeck Coefficient of Ball Milled $PtSb_2$

The most prominent effect of ball milling was a change in the sign of the Seebeck coefficient from p-type to n-type. This meant that the dominant carrier in the system had changed from holes in the nominally undoped system to electrons in the ball milled system. A similar change in type had been observed from n-type doping on the antimony site of $PtSb_2$, however such a change resulting from ball milling was very unexpected. It was additionally noted that the magnitude of the Seebeck coefficient had decreased, but the temperature where the peak was found remained the same. The existence of a peak in the Seebeck coefficient indicated the onset of intrinsic carriers in the system and that while a shift in the dominant carrier had been generated, the material remained a narrow bandgap semiconductor.

There were a few possible causes for the change in dominant carrier in this system. One possibility is that the stainless steel ball mill jar may have incidentally doped Fe into the sample from the high energy milling. Another possibility was that boundary scattering on

that length scale was preferential to holes and thereby dropped their contribution to the Seebeck coefficient. The last possibility was that antimony sublimated during SPS densification which had altered the electronic properties. This sublimation may have occurred due to the reduced melting point of ball milled $PtSb_2$.

Looking beyond the Seebeck coefficient, the electrical resistivity is shown in Figure 6.13.

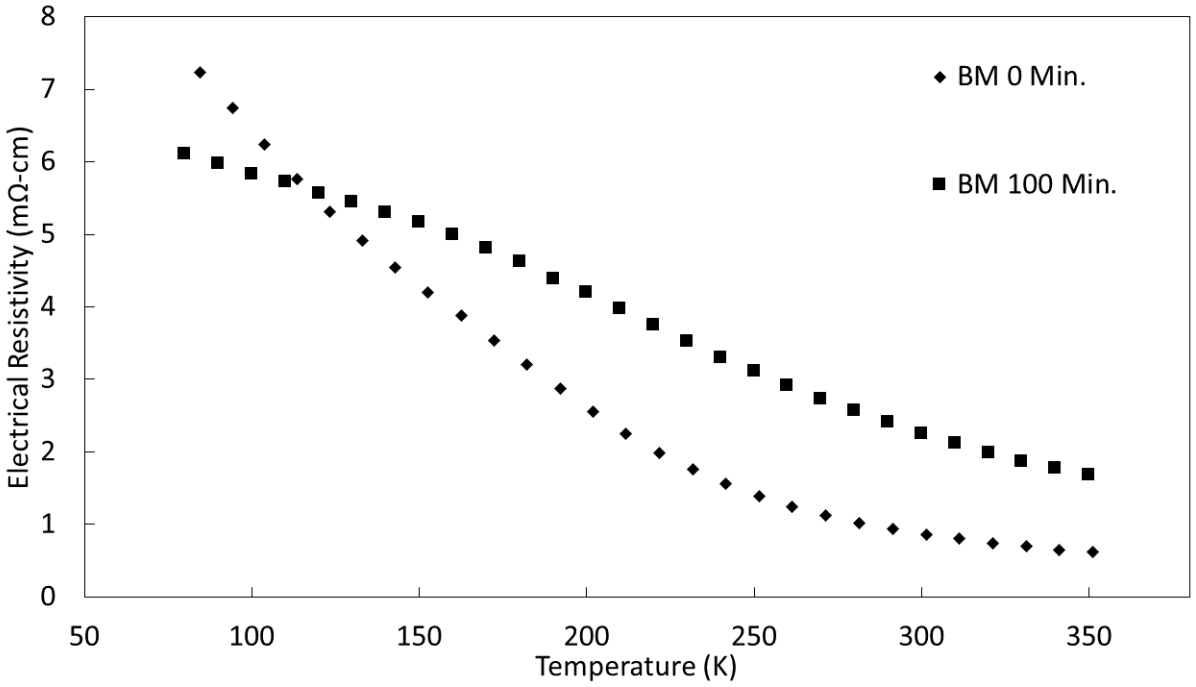

Figure 6.13: Electrical Resistivity of Ball Milled $PtSb_2$

A comparison of the electrical resistivity of ball milled $PtSb_2$ to nominal demonstrated an unexpected decrease in the electrical resistivity at low temperature. A reduced particle size will reduce the mean free path of charge carriers, as well as phonons, and increase the electrical resistivity by decreasing the charge carrier mobility. Thus, the decrease in electrical resistivity which was found at low temperatures was very odd. This result gave an indication of a change in the band structure of this sample. The trend of the electrical resistivity was found to decrease at a slower rate than un-ball milled $PtSb_2$ as temperature increased and

resulted in the expected increase in electrical resistivity.

From the results on the electronic properties it was expected that there was a significant change in the electronic band structure of the material. To examine how this affected the carrier concentration and mobility Hall experiments were performed on these samples. Shown in Figure 6.14 is the carrier concentration data obtained.

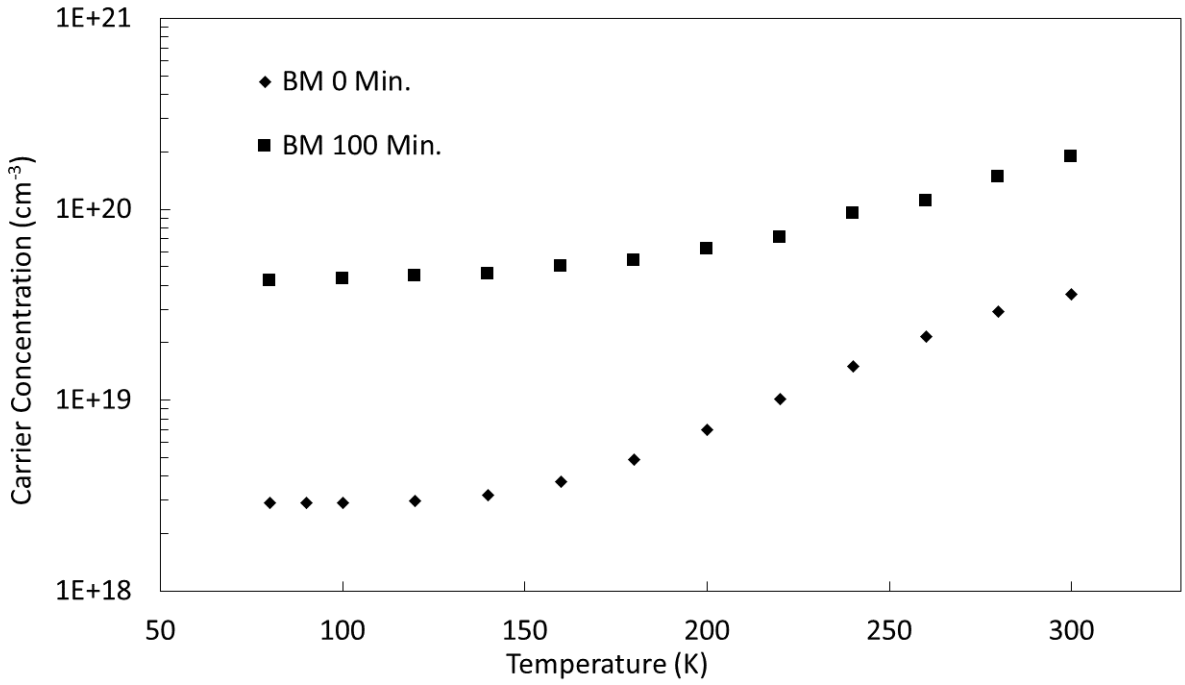

Figure 6.14: Carrier Concentration of Ball Milled $PtSb_2$

It was found that due to ball milling a large change in carrier concentration of approximately an order of magnitude had taken place. Both samples displayed the onset of intrinsic carriers at approximately 150 K and increased as temperature increased. The mobility was found to have been reduced dramatically from ball milling to approximately 30 cm^2/V-s at low temperature and remained relatively flat as temperature increased. Given these results the most likely cause of the change in dominant carrier type in the Seebeck coefficient and decreased electrical resistivity at low temperature was either iron doping from the milling or

the loss of antimony during densification.

From prior investigations in doping iron on the platinum site it was unlikely that the cause of the irregularities in the electronic properties were due to iron doping. In that study it was found that iron acted as a p-type dopant and would not produce a negative Seebeck coefficient when doped on the platinum site. However, to rule out the possibility of iron acting as a dopant a similar milling study was performed with a zirconium oxide ball mill jar and media, since it did not contain any iron, to determine if a similar effect to that found for the stainless steel jar and media would be observed.

The Seebeck coefficient of zirconium oxide milled $PtSb_2$ is shown in Figure 6.15.

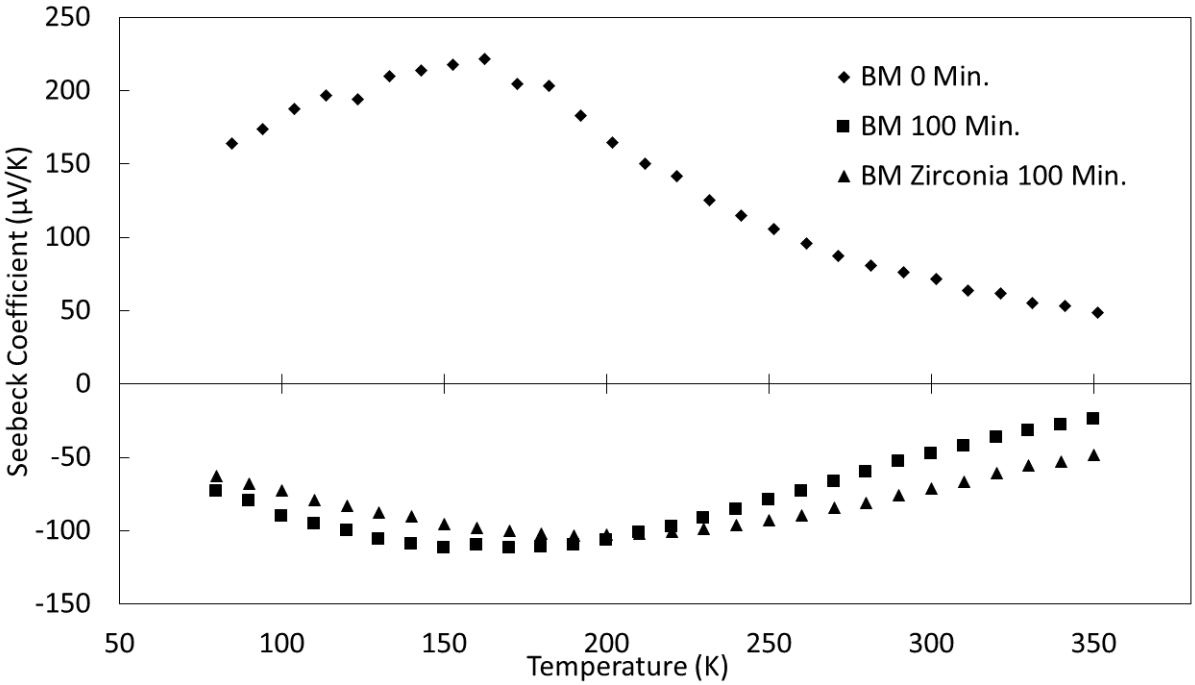

Figure 6.15: Seebeck Coefficient of Zirconium Oxide Ball Milled $PtSb_2$

It was found that the Seebeck coefficient of ball milled $PtSb_2$ using a zirconium oxide jar and media still produced a sign change. A slight shift in the temperature of the peak was observed but these results, coupled with the previous work on iron doping, motivated the

conclusion that the sign change was not due to iron deposition during ball milling.

Thus the most likely reason for the sign change was a change in the stoichiometry of $PtSb_2$ due to the loss of antimony during densification. Thus, a study of the effects of non-stoichiometry on $PtSb_2$ was performed.

6.5 Non-Stoichiometric $PtSb_2$ Results and Discussion

Prior experimental work demonstrated that antimony sublimation would occur during the synthesis of $PtSb_2$ while elemental precursors were undergoing a heat treatment to create a melt [102–106]. Samples synthesized in this manner showed large variations in their transport properties from this sublimation and unless specific methods were used to reduce antimony sublimation it would occur to some extent. Thus, when it was found that the melting point of $PtSb_2$ powder had been decreased from particle size reduction, the sublimation of antimony was identified as a possibility. To examine the degree to which antimony sublimation may have occurred in ball milled samples, and further to probe the possible thermoelectric enhancement of $PtSb_2$ by non-stoichiometry this study was performed.

6.5.1 X-Ray Diffraction

The X-ray diffraction pattern of non-stoichiometric $PtSb_2$ is shown in Figure 6.16.

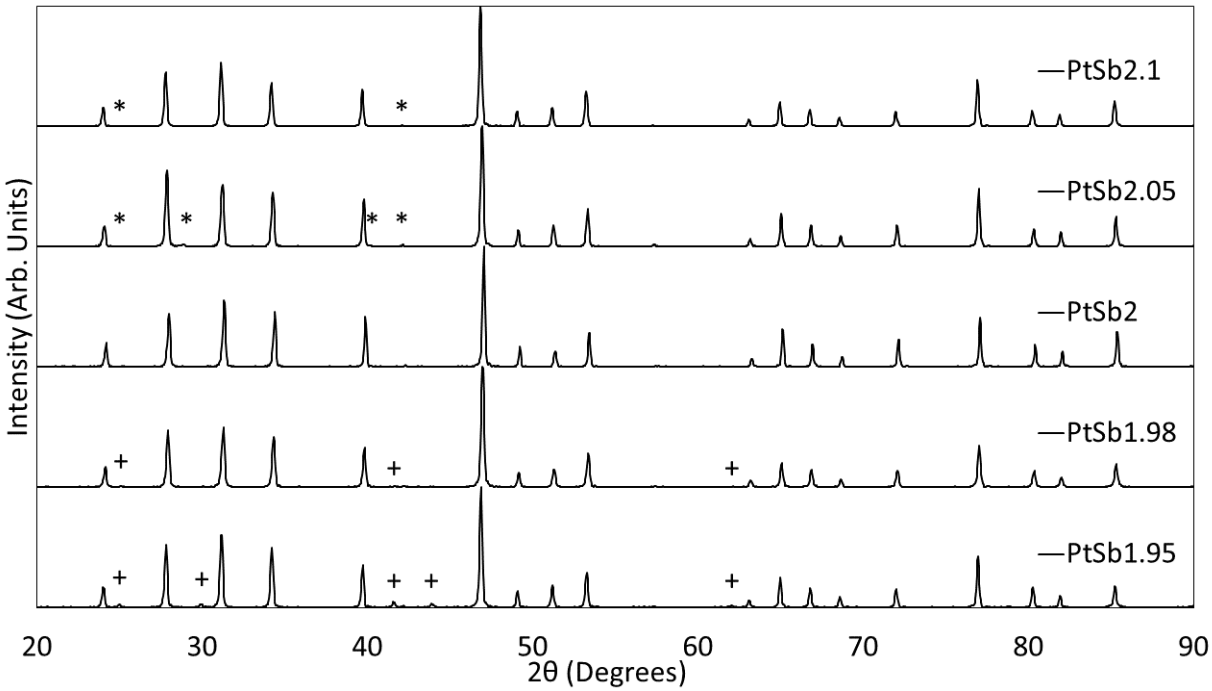

Figure 6.16: X-Ray Diffraction of Non-Stoichiometric $PtSb_2$

It was found that with antimony excess samples a secondary phase of antimony was observed demarcated with an asterisk and in antimony deficient samples a secondary phase of platinum antimony, PtSb, was observed demarcated with a cross. These results match well with what would be expected from their respective non-stoichiometry. Upon addition of a silicon standard no shift in the lattice parameter was observed which is in agreement with the formation of a secondary phase.

6.5.2 Electronic Properties

The Seebeck coefficient of non-stoichiometric $PtSb_2$ is shown in Figure 6.17.

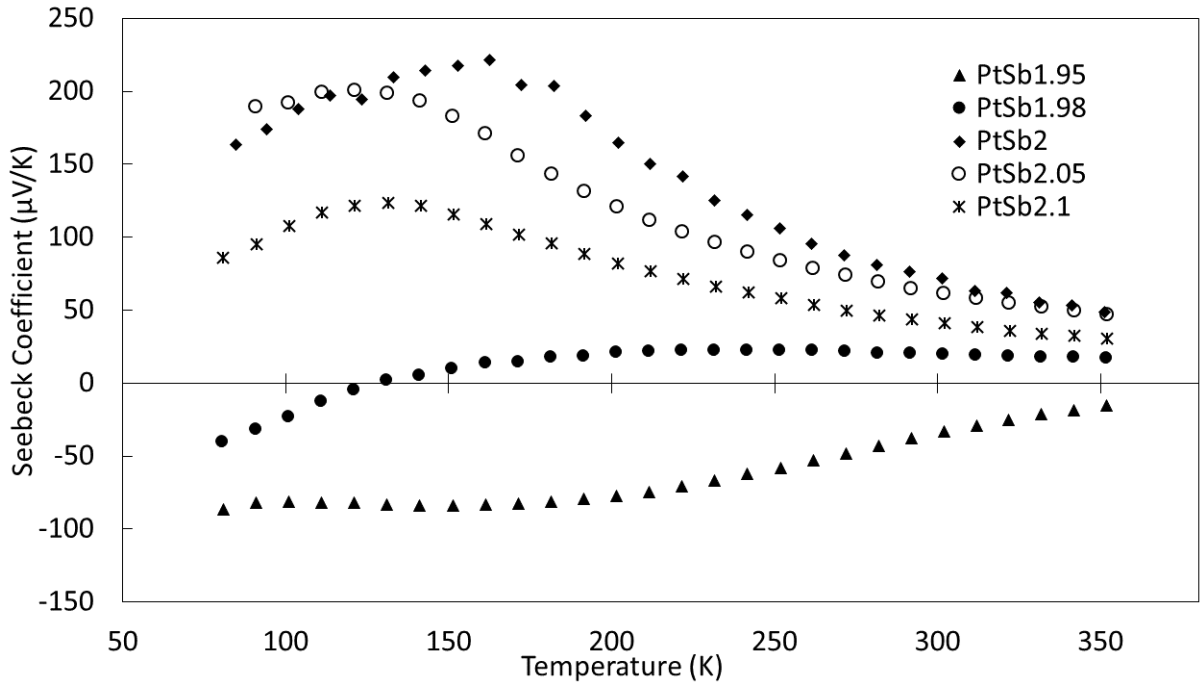

Figure 6.17: Seebeck Coefficient of Non-Stoichiometric $PtSb_2$

Examining the electronic properties of these non-stoichiometric samples good agreement was found with prior literature on non-stoichiometric $PtSb_2$ at room temperature [100]. In this prior work it was found that antimony deficiency led to the generation of a negative Seebeck coefficient at room temperature, which matched well with what was found here in the x = -0.05 sample. With a light deficiency of antimony a negative Seebeck coefficient was found at low temperatures as displayed in the x = -0.02 sample. As temperature increased, and intrinsic carriers were populated, this sample returned to positive values due to the large hole concentration generated by intrinsic carrier population. The x = -0.05 sample showed the results that were being probed for in this study. It was found that across all temperatures measured a negative Seebeck coefficient was generated from this composition of antimony deficiency in $PtSb_2$. This result matched well with the negative Seebeck coefficient generated from ball milled samples and was taken as strong evidence that ball milling caused a loss of

antimony during SPS from sublimation. Examining the antimony excess samples, a decrease in the magnitude of the Seebeck coefficient was found. The decrease in magnitude was observed to intensify as the concentration of antimony excess increased. A slight reduction in the temperature of the peak with a similar decreasing value as temperature increases was observed in these antimony excess samples.

Examining the electrical resistivity of non-stoichiometric $PtSb_2$ in Figure 6.18 a large amount of variability is found at low temperature.

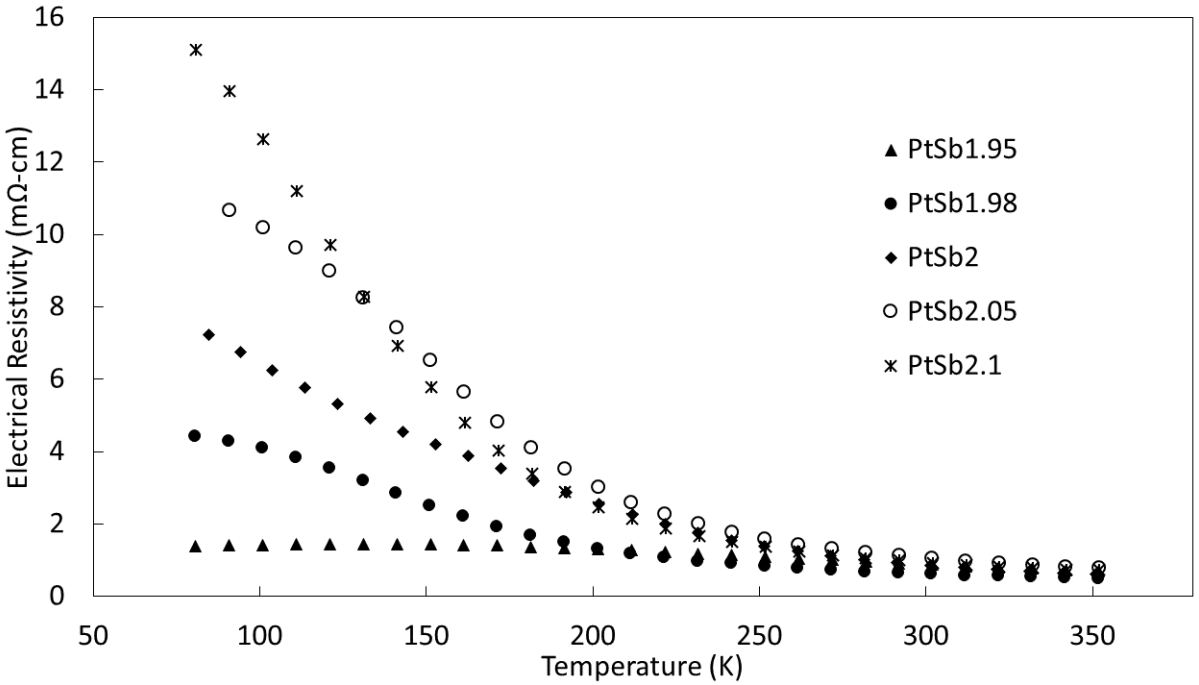

Figure 6.18: Electrical Resistivity of Non-Stoichiometric $PtSb_2$

At 80 K the electrical resistivity spans an order of magnitude between the most deficient sample and that with the largest antimony excess. Starting with the x = 0.1 sample a large increase in the electrical resistivity was found. As intrinsic carriers were populated in the $PtSb_2$ phase the electrical resistivity was found to decrease rapidly and match the value of stoichiometric $PtSb_2$ at approximately 200 K. As antimony content was decreased

the electrical resistivity at 80 K was also found to decrease relative to the x = 0.1 sample. In samples with antimony deficiency a reduction in the electrical resistivity was found at 80 K relative to stoichiometric $PtSb_2$. As antimony content was reduced to the x = -0.05 sample the trend of the electrical resistivity became flat across all temperatures measured. All samples were found to approach the electrical resistivity of stoichiometric $PtSb_2$ at temperatures above room temperature.

The results from studying the electrical resistivity suggest that, as with silver and niobium doping on the platinum site, ionized impurity scattering occurred in the antimony excess samples. The shift to lower temperatures of the peak in the Seebeck coefficient, the reduction in magnitude with increased antimony excess, and the large increase in the electrical resistivity at low temperatures all point towards ionized impurity scattering in these samples. In the antimony deficient samples a more complex mechanism is at play, but appears to be similar to n-type doping. Comparing the Seebeck coefficient of the x = -0.02 samples with that found for low dopant concentrations of selenium a similar result was found. The negative values at low temperatures which crossed the x-axis and became p-type as temperature increased were very similar to that found for selenium doping. The electrical resistivity of this sample also displayed similarity to n-type doping. Finally, the x = -0.05 sample displayed a Seebeck coefficient and electrical resistivity similar to lightly n-type doped samples.

6.5.3 Thermal Properties

The thermal conductivity of non-stoichiometric $PtSb_2$ is shown in Figure 6.19.

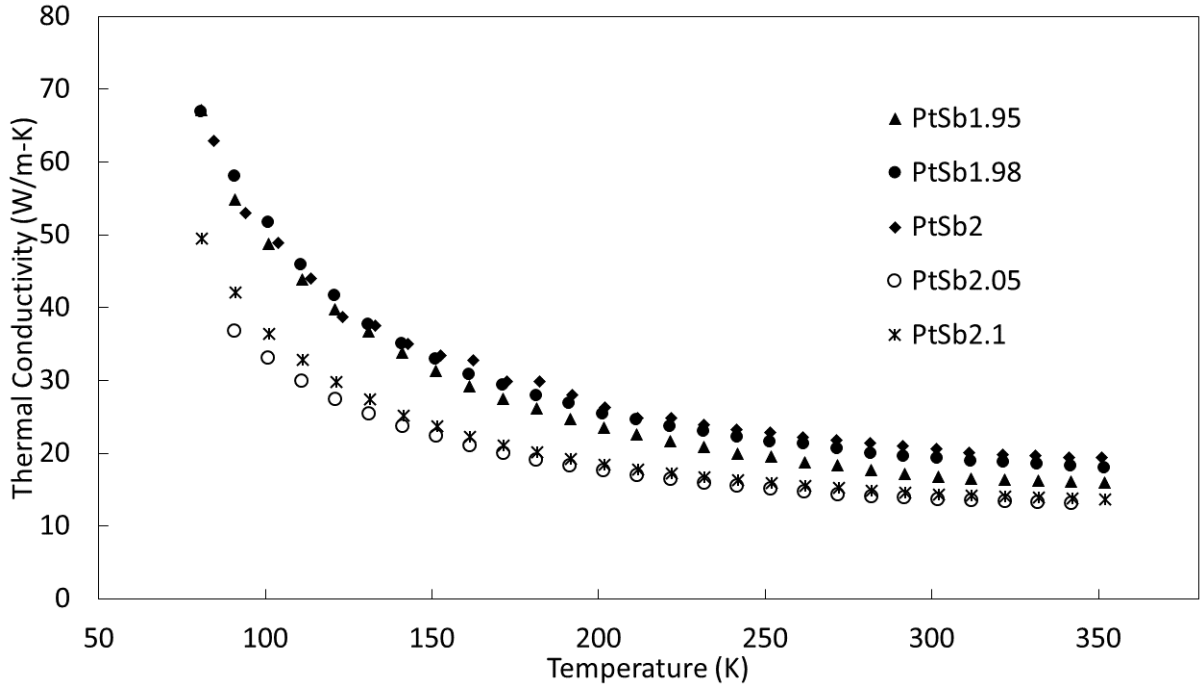

Figure 6.19: Thermal Conductivity of Non-Stoichiometric $PtSb_2$

From this data it was found that antimony deficient samples showed the same thermal conductivity as nominal $PtSb_2$ within the error of the system, however antimony excess samples showed a reduction across all temperatures measured. Examining just the lattice contribution to thermal conductivity it was found that these samples were dominated by the lattice contribution with the electronic contribution at least an order of magnitude less for all temperatures. Thus, it is likely that the antimony impurities in the excess antimony samples lead to greater phonon scattering than did the PtSb phase in antimony deficient samples.

6.5.4 zT

Figure 6.20 shows the resultant figure-of-merit for these non-stoichiometric samples.

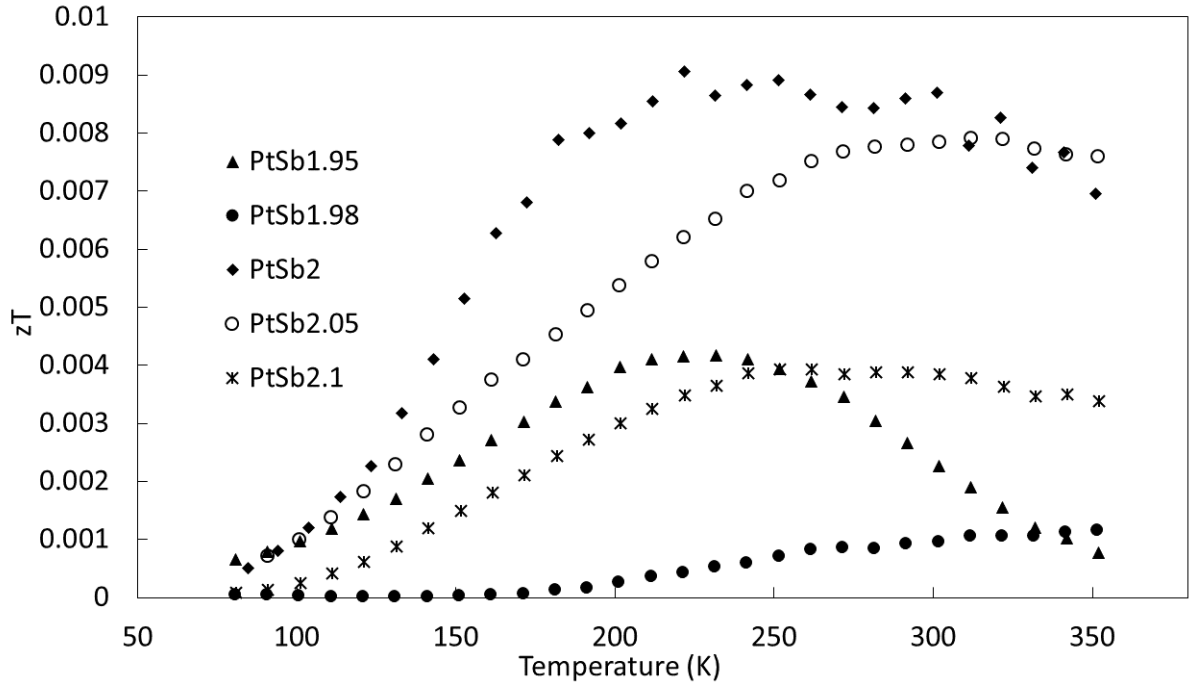

Figure 6.20: zT of Non-Stoichiometric $PtSb_2$

Drawing comparison to prior experimentation again, the antimony excess samples showed no improvement in the figure-of-merit just as the silver and niobium dopant samples showed no improvement. The antimony deficient samples when compared to n-type dopants showed the effects of light doping, which only had modest improvements in the zT. These antimony deficient samples however showed no improvement due to their low power factor.

Overall, the results of non-stoichiometric $PtSb_2$ demonstrated that manipulation of stoichiometry in this material is not a viable means of increasing the figure-of-merit. However, these findings served to solidify the interpretation of results on ball milled $PtSb_2$ and furthered the understanding of this narrow bandgap material.

6.6 Hole Doping Ball Milled $PtSb_2$

To capitalize upon the large reduction in thermal conductivity produced by ball milling $PtSb_2$, a study on tuning the carrier concentration was performed.

6.6.1 X-Ray Diffraction

The X-ray diffraction patterns obtained for Sn doped $PtSb_2$ are shown in Figure 6.21. A large number of samples were examined in this work and to better visually demonstrate the results of X-ray diffraction only a subset of the patterns obtained for these samples is shown.

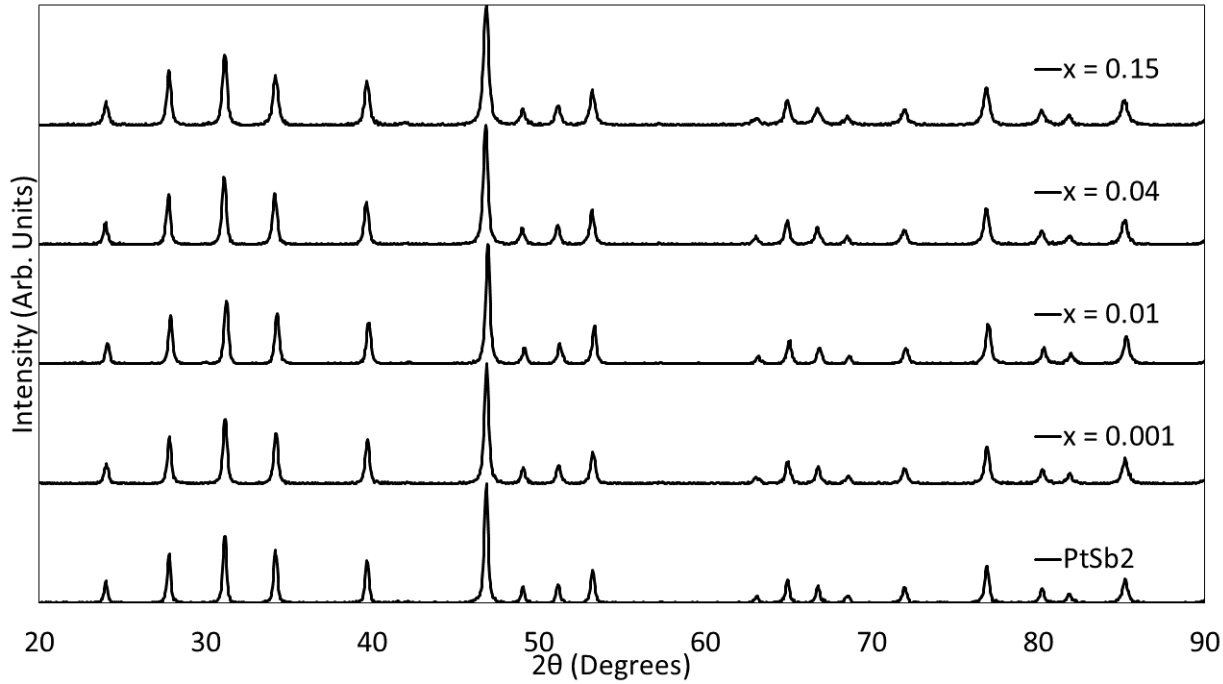

Figure 6.21: X-Ray Diffraction of Sn Doped, Ball Milled $PtSb_2$

In this figure the large amount of broadening due to ball milling is shown to be preserved for all Sn dopant concentrations. Examination with an internal silicon standard showed no shift in the lattice from the incorporation of Sn dopant. In Sn doped samples without any ball milling a secondary phase was found in compositions of $x \geqslant 0.1$, however, in these

ball milled samples only the single phase of $PtSb_2$ is observed for all concentrations examined here. It is possible that due to the broadening of peaks the amplitude of secondary phases were either suppressed to such a low value that they were insignificant, or that they were indistinguishable from the broadened peaks of $PtSb_2$. As will be shown, the electrical properties of these doped samples followed the expected trend from doping, thus it is likely the strained lattice of ball milled samples was able to incorporate a higher solubility of Sn dopant.

6.6.2 Electronic Properties

The Seebeck coefficient of Sn doped, ball milled $PtSb_2$ is shown in Figure 6.22 for a subset of samples measured. A subset is shown because if all of the data points for all of the samples were shown it would occlude the effects which are occurring in these samples. Thus, a subset is shown to better visualize the data. The samples included in the subset were selected to best demonstrate the trends from Sn doping.

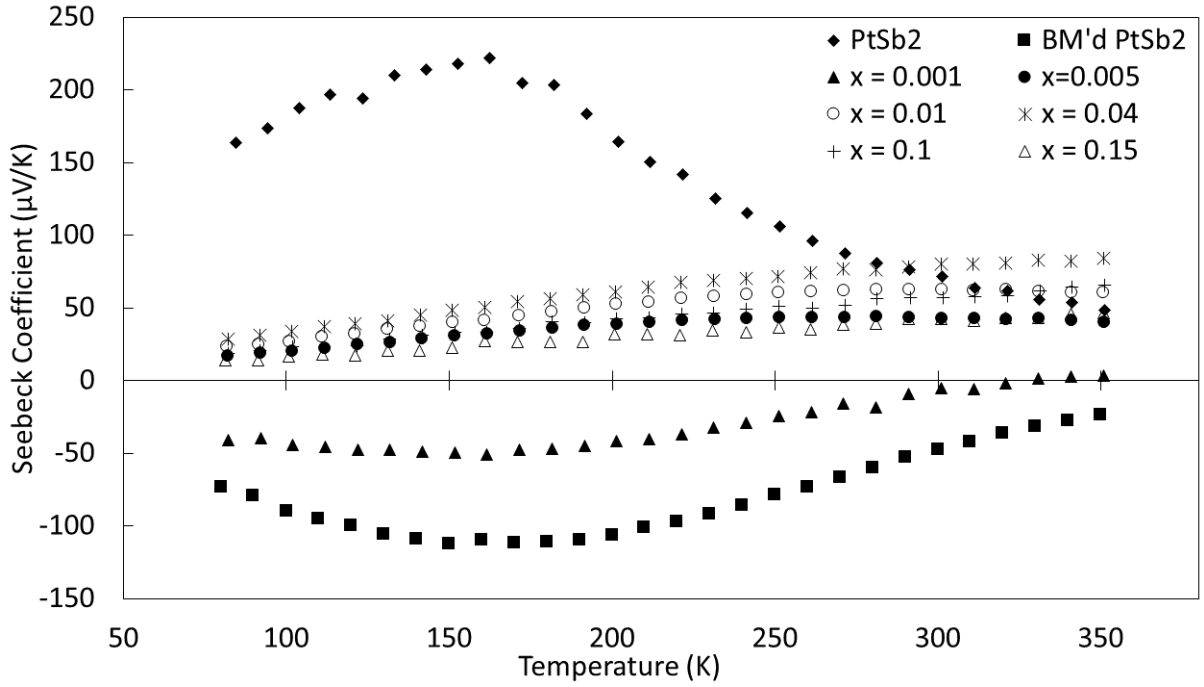

Figure 6.22: Seebeck Coefficient of Sn Doped, Ball Milled $PtSb_2$

The Seebeck coefficient of nominal $PtSb_2$ was shown in this figure as a reference point for the values obtained. The lowest concentration of tin doping in these samples, x = 0.001, showed a decrease in the magnitude of the Seebeck coefficient when compared with undoped, ball milled $PtSb_2$. The Seebeck coefficient of this sample approached zero and crossed over to become p-type at approximately 320 K. This sample demonstrated the effect of bipolar conduction with the doped holes competing with the electrons in this ball milled sample. As the tin dopant concentration was increased the sample became p-type due to the large number of doped holes in the system. This was seen from the transition in Seebeck coefficient between the x = 0.001 and 0.005 samples. A maximized Seebeck coefficient for all doped samples was found for the x = 0.04 dopant concentration. From the x = 0.01 to 0.04 sample an increase in Seebeck coefficient was found, but decreased from x = 0.04 to 0.1 and further still in 0.15. This effect was exemplary of the typically expected behavior of the Seebeck

coefficient in a bipolar conductor as the doped holes met a maximum value while competing with intrinsic electrons which upon further doping led to a reduction.

Comparing the Seebeck coefficients of all samples at 300 K, in Figure 6.23, this maximized Seebeck coefficient in the x = 0.04 sample is better observed.

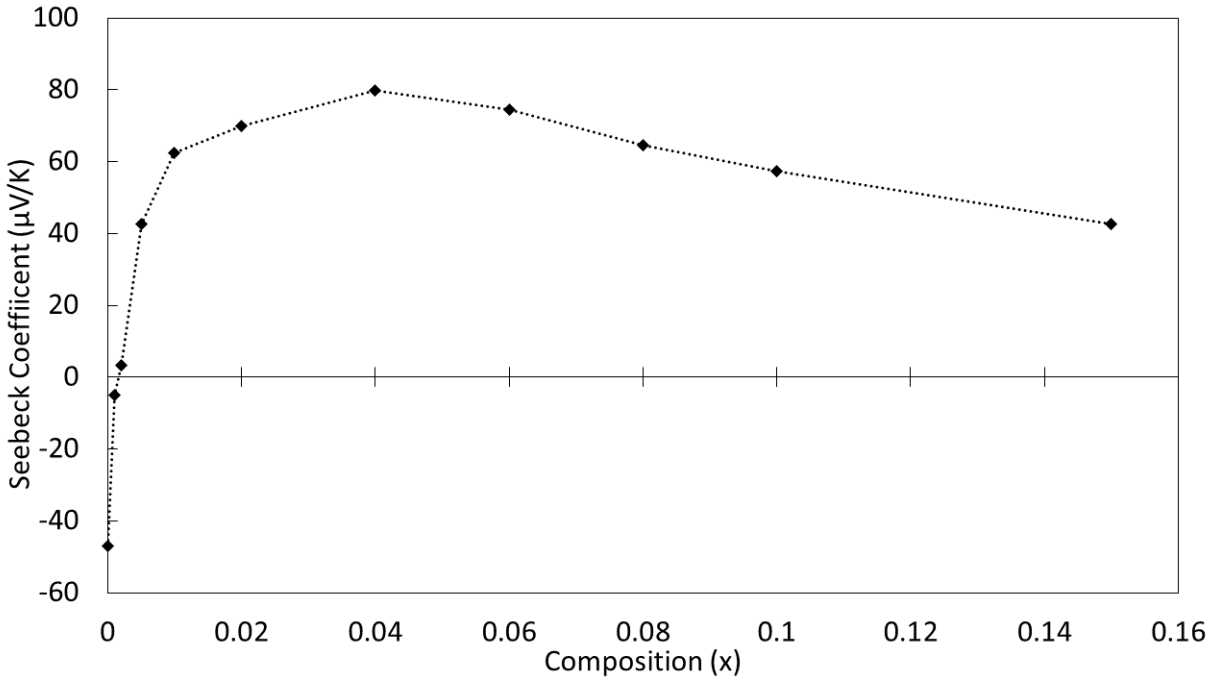

Figure 6.23: Seebeck Coefficient of Sn Doped, Ball Milled $PtSb_2$ at 300 K

In this figure the Seebeck coefficient of un-ball milled $PtSb_2$ was not included, but the undoped, ball milled sample is shown on the y-axis at a composition of x = 0. This figure clearly shows the effects of Sn doping on the Seebeck coefficient of ball milled $PtSb_2$. For the x = 0.001 sample the Seebeck coefficient was still negative because the mobility weighted Seebeck coefficient contribution from holes was not yet enough to surpass that of intrinsic electrons. As the dopant concentration was increased the Seebeck coefficient became positive and rose as the doped holes began to dominate in the system over electrons. At the x = 0.04 composition a maximum in the Seebeck coefficient for these samples was met and further

doping resulted in a reduction from an increased hole doped carrier concentration.

Examining the electrical resistivity in Figure 6.24 a similar effect was found.

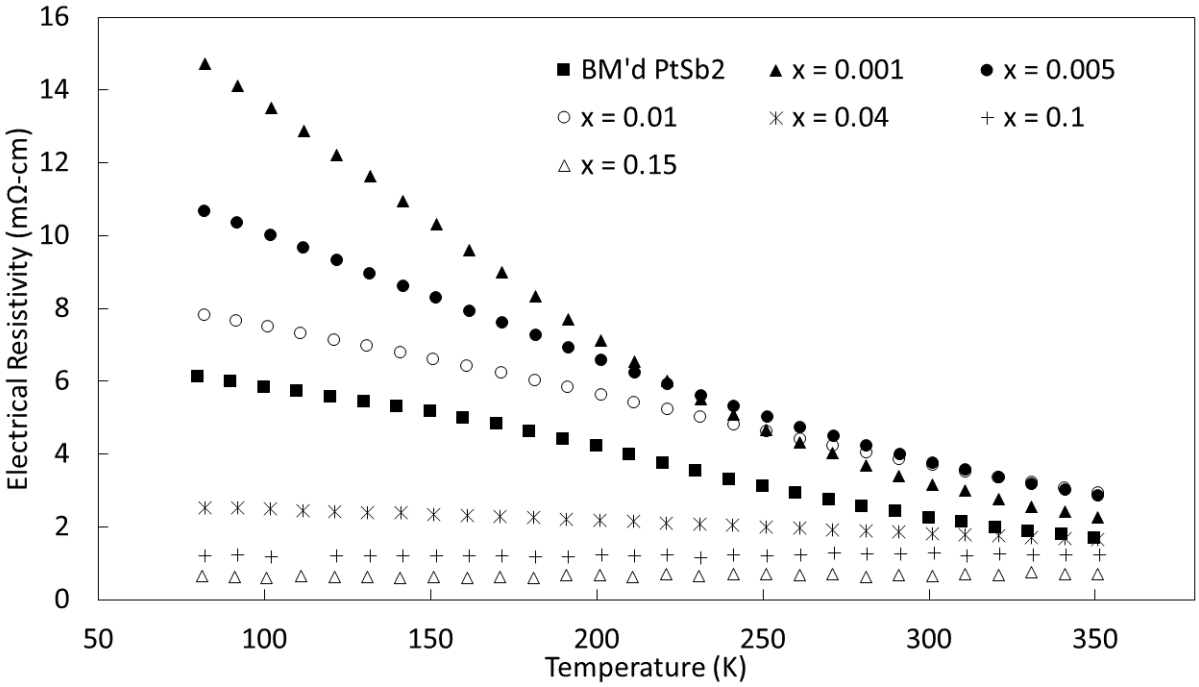

Figure 6.24: Electrical Resistivity of Sn Doped, Ball Milled $PtSb_2$

In this figure the electrical resistivity of nominal $PtSb_2$ is not shown to better visually demonstrate the data, however, reference should be made to Figure 6.13 for any comparison. An interesting result was found for low dopant concentration samples. The electrical resistivity was found to be increased in the x = 0.001, 0.005, and 0.01 samples. It was known from the Seebeck coefficient data that a bipolar conduction effect was occurring in all doped samples, but this result on its own would not increase the electrical resistivity. It is likely that these samples demonstrated an increased carrier scattering rate due to dopant impurities. As the Sn dopant concentration was increased it is likely that the mobility was not affected as greatly by an incremental increase in impurity as was the increase in the carrier concentration. However, to be certain of this interpretation, future work with these samples

would entail Hall experimentation to probe the mobility and carrier concentration.

Beginning with the x = 0.04 sample the electrical resistivity was found to be decreased from doping and in the x = 0.1 and 0.15 samples a similar electrical resistivity was found compared with previously doped samples. It was likely not a coincidence that the maximum in the Seebeck coefficient was found in the same sample that first demonstrated a reduced electrical resistivity. The reduced electrical resistivity was due to the large number of doped carriers in this system from these higher Sn dopant concentrations. Comparing the electrical resistivity values found for these dopant concentrations, the carrier scattering effects of ball milling were prominent. For the x = 0.04 composition the electrical resistivity of the un-ball milled sample was $\rho = 0.19$ mΩ-cm, while the ball milled sample was $\rho = 2.54$ mΩ-cm, an order of magnitude increase. This result was reflected in the other doped samples as well.

6.6.3 Thermal Properties

The thermal conductivity of Sn doped, ball milled $PtSb_2$ is shown in Figure 6.25.

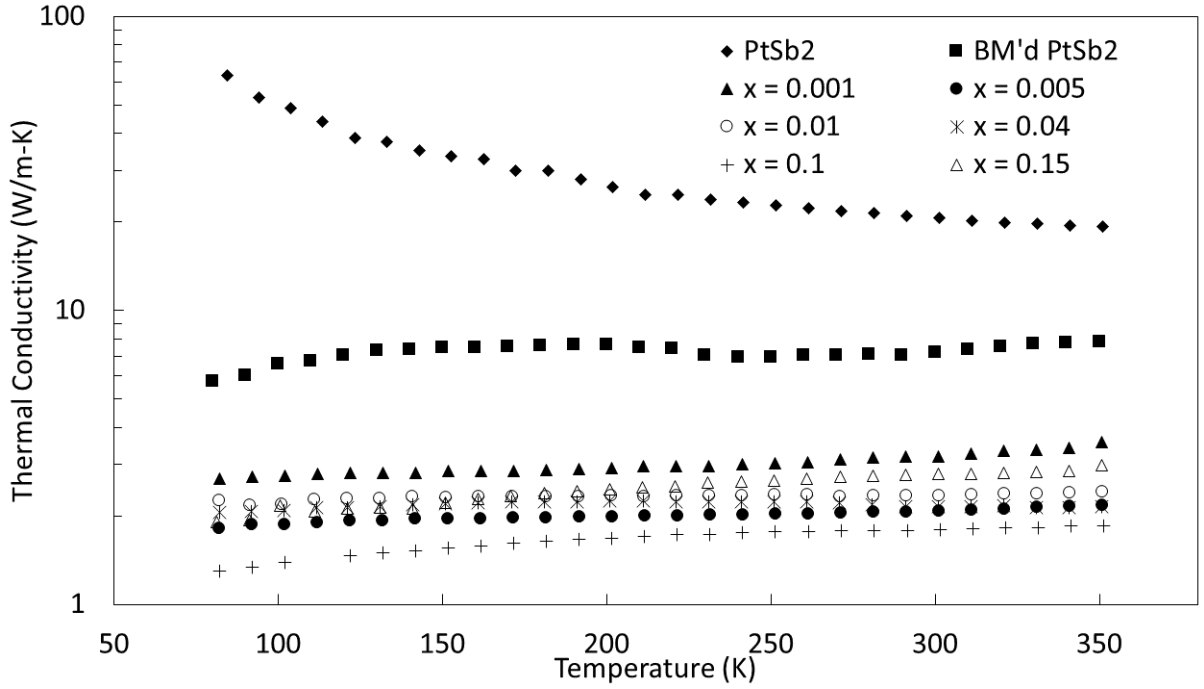

Figure 6.25: Thermal Conductivity of Sn Doped, Ball Milled $PtSb_2$

The large reduction in thermal conductivity from ball milling was found to be further reduced from point defect phonon scattering in these doped samples. To demonstrate the large reduction found from ball milling and doping in these samples the thermal conductivity of nominally undoped $PtSb_2$ is also shown. It was found for these Sn doped ball milled samples that the electronic contribution to the thermal conductivity began to comprise a significant portion of the total thermal conductivity. Thus, the reduction in the total thermal conductivity found from point defect scattering in these samples does not follow an incremental trend of further reduction from increasing Sn dopant concentration. In the x = 0.1 and 0.15 samples the electronic contributions are 12% and 15% of the total thermal conductivity at 80 K and reach 38% and 40% at 350 K, respectively. Comparison of the thermal conductivity of nominally undoped $PtSb_2$ with that of undoped ball milled $PtSb_2$ and the x = 0.04 sample at 80 K a reduction of approximately a factor of 30 was found for

nominal $PtSb_2$ and a factor of approximately 3 from ball milled $PtSb_2$. Recall from Figure 6.1 that this large reduction in thermal conductivity was what would be required to result in a competitive figure-of-merit for $PtSb_2$, dependent upon the effects of this minimization on the electronic properties.

6.6.4 zT

The figure-of-merit of Sn doped, ball milled $PtSb_2$ is shown in Figure 6.26.

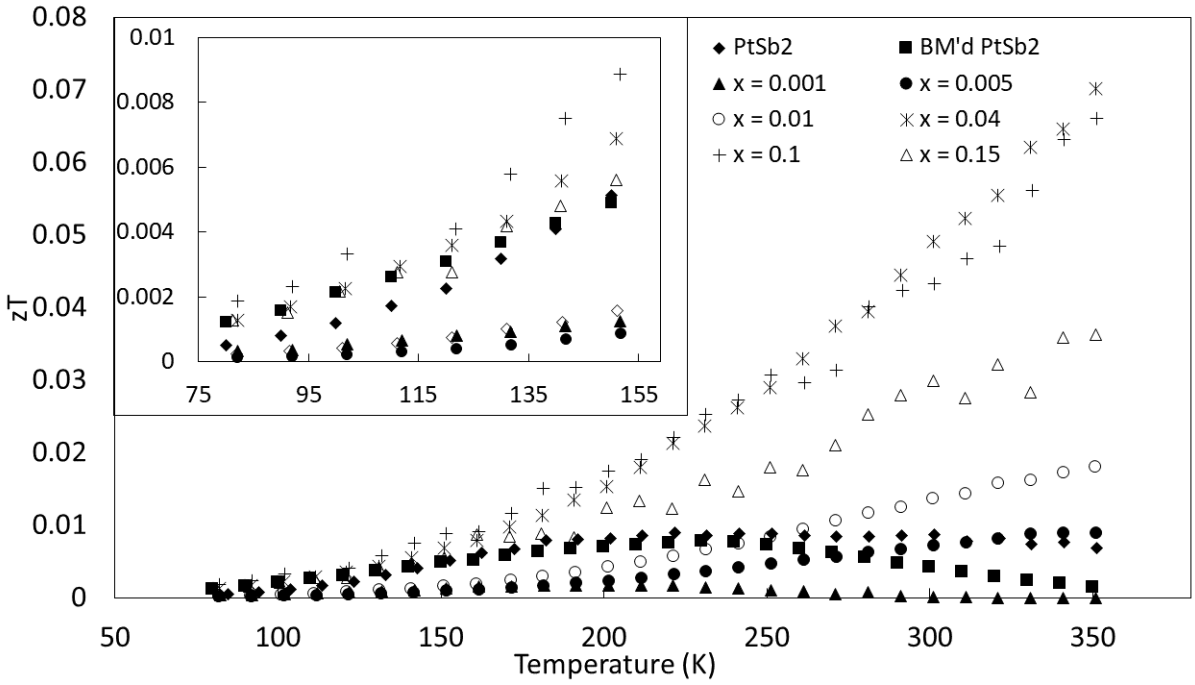

Figure 6.26: zT of Sn Doped, Ball Milled $PtSb_2$

The figure-of-merit of Sn doped ball milled samples showed a large enhancement over both nominally undoped $PtSb_2$ and undoped ball milled $PtSb_2$. The largest zT obtained in these samples was for the composition of x = 0.04 with a value of approximately 0.07 at 350 K. The x = 0.01 sample was elevated as well when compared with nominally undoped $PtSb_2$, as were samples not shown here of x = 0.06 and 0.08. At low temperatures, shown

in the inset, the x = 0.1 sample demonstrated the highest figure-of-merit, but not by a large magnitude compared with ball milled or nominally undoped $PtSb_2$.

As is the case with all thermoelectric materials, a reduction in the thermal conductivity by the introduction or exacerbation of a scattering mechanism will impact both the thermal, as well as, the electronic transport properties. Yet in the typical thermoelectric material this effect will often still result in an enhancement of the figure-of-merit. This effect was indeed found in this work as well, however the dramatic change in the sign of the Seebeck coefficient was atypical. While it is unrealistic to expect the power factor of a material to be unaffected from significant particle size reduction, if that had been found for these Sn doped, ball milled samples a very significant increase in the figure-of-merit would have been found. A comparison of the values found for the power factor of ball milled and un-ball milled $PtSb_2$ is shown in Figure 6.27.

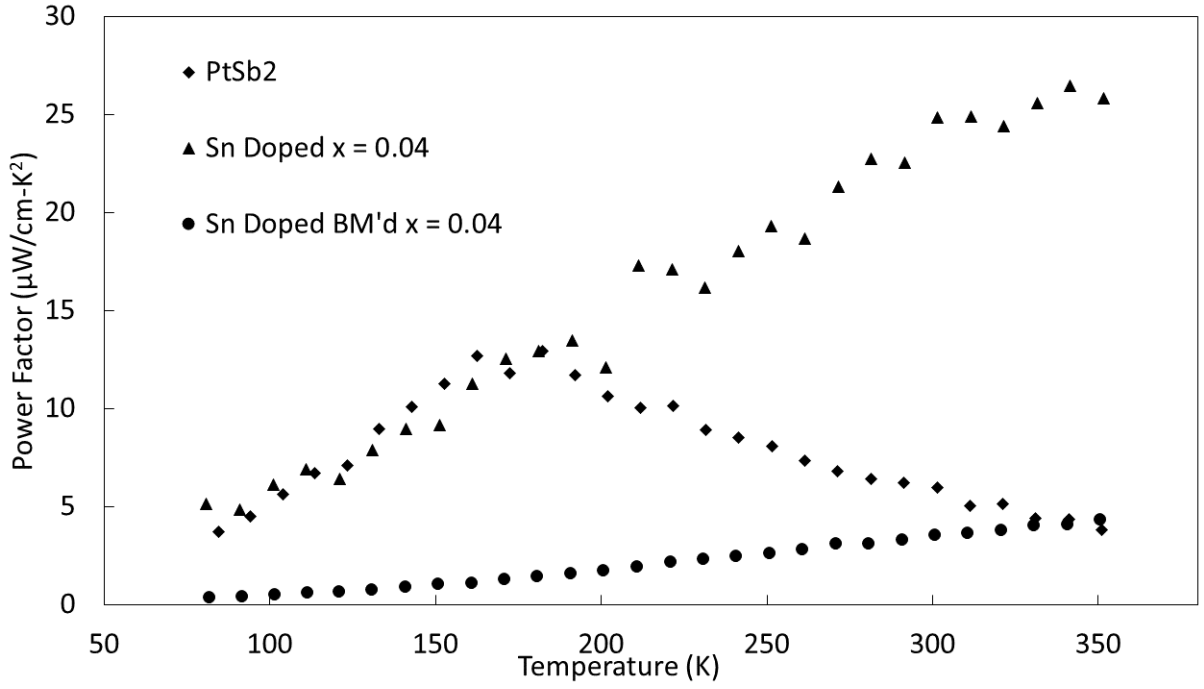

Figure 6.27: Power Factor of Sn Doped, Ball Milled and Un-Ball Milled $PtSb_2$

The dramatic decrease in the power factor due to ball milling was found to be the major limiting factor to large figure-of-merit. Upon analysis it was found that the large decrease in the power factor did not solely come from the change in the sign of the Seebeck coefficient in ball milled samples. In fact, since the Seebeck coefficient of ball milled samples returned to the p-type values found in Sn doped un-ball milled samples, the Seebeck coefficient of the x = 0.04 samples for ball milled and un-ball milled samples varied by less than 10% over all temperatures measured. The ball milled sample was even found to have an enhanced Seebeck coefficient compared to the un-ball milled sample for several temperature ranges. Thus, it was largely the reduction in the electrical resistivity found from additional boundary scattering which led to the large decrease in the power factor.

If the power factor was not reduced due to ball milling and could instead be further enhanced from doping, then substantial zT values could be obtained at low temperature. A purely hypothetical situation is presented where the best properties obtained from separate $PtSb_2$ projects are combined to show a projected zT possible. This zT with the combined best properties from measured samples is compared with $Bi_{0.88}Sb_{0.12}$ [77] and $Bi_{2-x}Sb_xTe_3$ [79] in Figure 6.28.

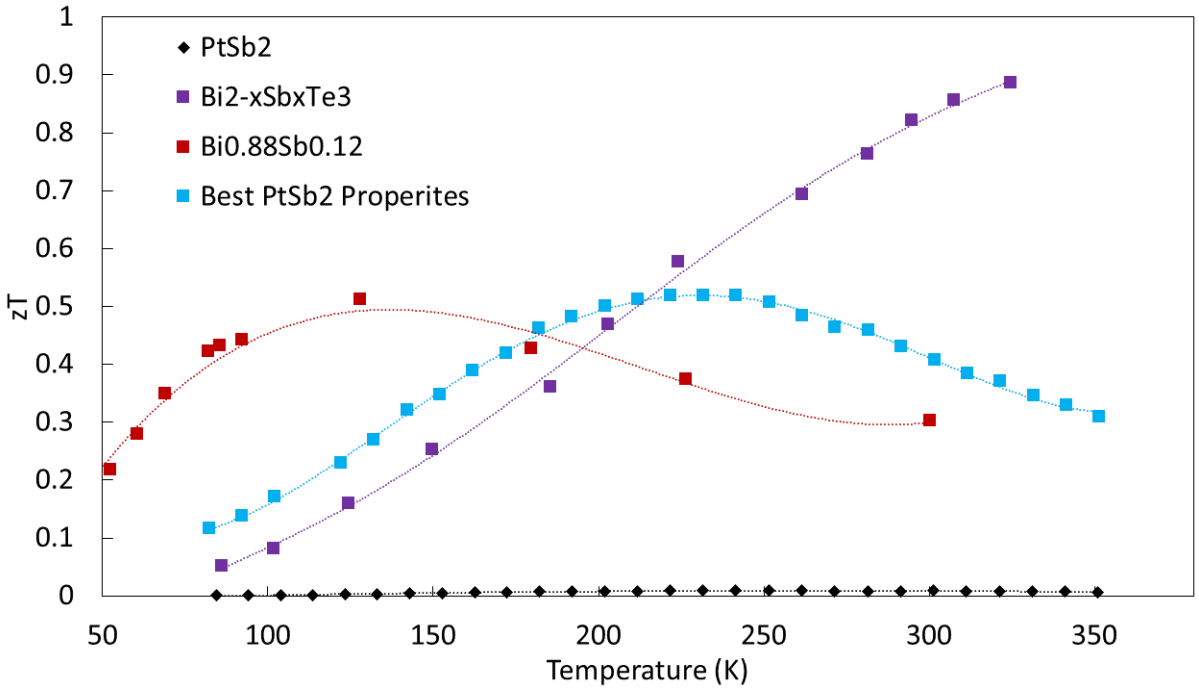

Figure 6.28: Hypothetical zT of the Combined Best Properties of $PtSb_2$ Compared with the measured zT of $Bi_{0.88}Sb_{0.12}$ by Smith and Wolfe and $Bi_{2-x}Sb_xTe_3$ by Chung et al.

In this figure the thermal conductivity of Sn doped, ball milled $PtSb_2$ is combined with the power factor of Yb doped $PtSb_2$ to yield a large zT which surpasses both $Bi_{0.88}Sb_{0.12}$ and $Bi_{2-x}Sb_xTe_3$ in the temperature range from 180 to 200 K. It is unlikely that the zT of $PtSb_2$ could be increased to these values due to the interplay between ball milling and the power factor, however, this demonstrates the substantial enhancements, albeit separately, that were generated in the course of this work. This also motivates further work into minimizing the antimony loss during densification of ball milled samples, as well as an examination of Yb doping on ball milled $PtSb_2$.

6.7 Electron Doping Ball Milled $PtSb_2$

To examine both p- and n-type doping on ball milled $PtSb_2$ a series of samples were synthesized using Te as a dopant due to the success of tellurium doping on un-ball milled samples.

6.7.1 X-Ray Diffraction

The X-ray diffraction patterns of Te doped, ball milled $PtSb_2$ are shown in Figure 6.29.

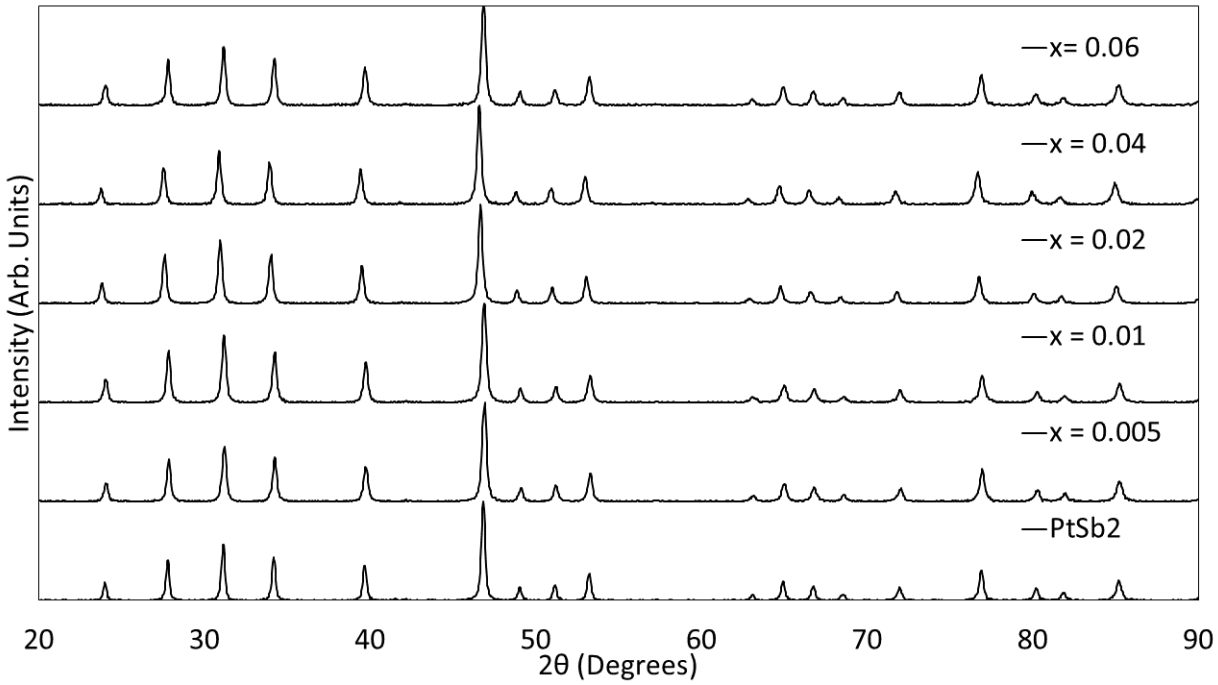

Figure 6.29: X-Ray Diffraction of Te Doped, Ball Milled $PtSb_2$

As was found from Sn doping in ball milled $PtSb_2$, no solubility limit was found for any tellurium composition examined here. The addition of a silicon standard revealed that the apparent shift in peaks in Figure 6.29 was due to a 2θ offset from differing powder heights during X-ray diffraction and did not represent a change in the lattice parameter of these doped samples.

6.7.2 Electronic Properties

Examining the effect of tellurium dopant on the Seebeck coefficient of these samples, the results are shown in Figure 6.30.

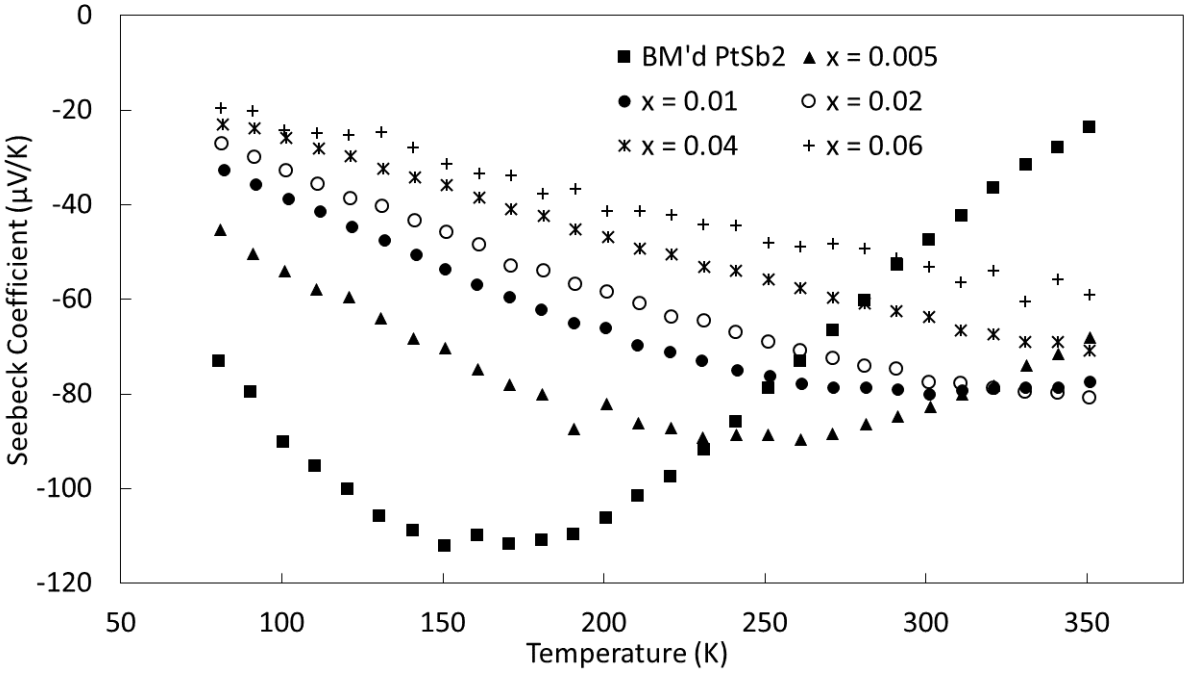

Figure 6.30: Seebeck Coefficient of Te Doped, Ball Milled $PtSb_2$

In this figure the results for nominally undoped $PtSb_2$ have been removed since the comparison being made here is between the ball milled samples only and no scale comparison is necessary to the nominal p-type $PtSb_2$. It was observed that all doped samples displayed the expected trend for same type doping, n-type doping in an n-type material. The expectation was that n-type doping would further increase the concentration of electrons which would lead to a reduction in the magnitude of the Seebeck coefficient. This effect was indeed found for all samples which showed that as the concentration of Te dopant increased the magnitude incrementally decreased. All samples remained n-type over the entire temperature range examined and a peak was observed in the x = 0.005 and 0.01 samples, which had been shifted

to higher temperatures. The existence of a peak in these samples, as with the un-doped sample, indicated the onset of intrinsic carrier population. The x = 0.02, 0.04, and 0.06 samples were found to have continuously increasing values with increasing temperature for the examined region. It is unknown whether these samples would cross back over the x-axis to become p-type at some higher temperature due to the competition of holes with these doped electrons.

The effects of tellurium doping on the electrical resistivity of ball milled $PtSb_2$ may be seen in Figure 6.31.

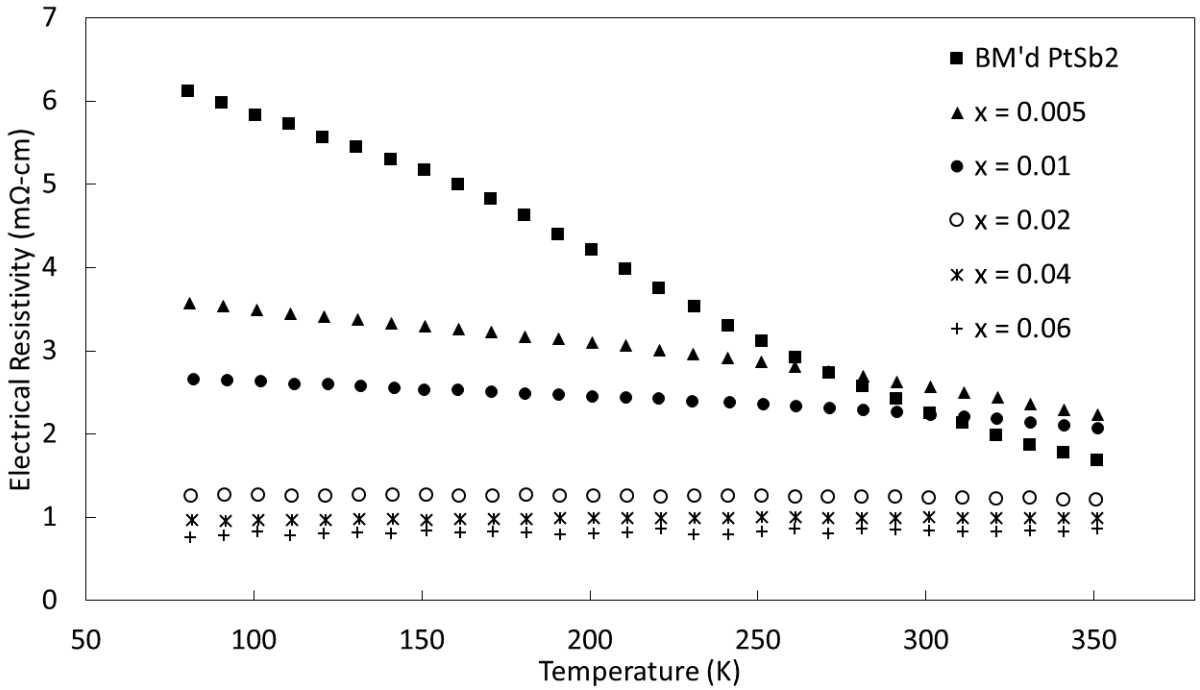

Figure 6.31: Electrical Resistivity of Te Doped, Ball Milled $PtSb_2$

The expected results of n-type doping in an n-type material were found again in these samples. As the concentration of tellurium was increased the electrical resistivity was noted to decrease. In the x = 0.005 and 0.01 samples the electrical resistivity was found to be slightly higher than the undoped sample at approximately room temperature due to the

population of a large concentration of intrinsic carriers in the undoped sample at this temperature. The x = 0.02, 0.04, and 0.06 samples showed very low and flat trends in the electrical resistivity and were not higher than the undoped values for any temperature.

A comparison of the electrical resistivity of these samples with those found for Sn doped, ball milled $PtSb_2$ highlighted a curiosity in the Sn doped samples. Comparing the composition of x = 0.005 for both Sn and Te doping it was found that the electrical resistivity for the Sn sample at 80 K was $\rho = 1.06$ Ω-m and for the Te sample was $\rho = 0.36$ Ω-m. Both samples had the same composition of dopant and would theoretically have very similar degrees of scattering. Additionally, both dopants should be doping a similar concentration of charge carriers into the system for the same composition. The only difference is in the doping type and if reference is made to the electrical resistivities of Te and Sn doped un-ball milled samples a similar disparity in the degree of reduction is found. In the case of un-ball milled samples the Sn dopant generated the largest reduction in the electrical resistivity, while the tellurium dopant, (of opposite type to the parent material), generated a relatively mild reduction. In the ball milled samples, where the parent material became n-type, the Sn dopant was found to generate the mild reduction but only in more heavily doped samples, while the same type dopant, Te, generated the relatively much larger reduction. To more fully probe this effect Hall experimentation should be performed to compare the carrier concentrations and mobilities of these samples.

6.7.3 Thermal Properties

The large reduction in thermal conductivity found from ball milling was again further reduced by doping and is shown in Figure 6.32.

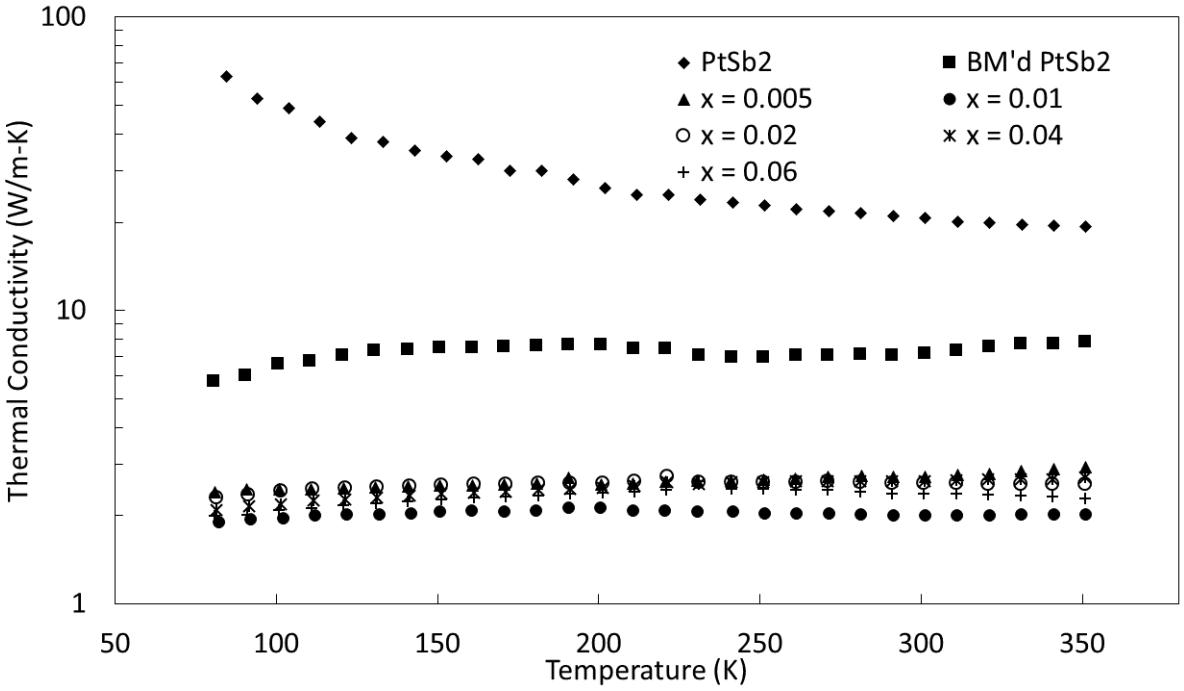

Figure 6.32: Thermal Conductivity of Te Doped, Ball Milled $PtSb_2$

As was found with Sn doping, a large reduction in the thermal conductivity was found in Te doped, ball milled $PtSb_2$. For all doped samples further reduction in the thermal conductivity was obtained beyond that of ball milling by doping. Similar values for all dopant compositions were obtained and it was found that as with the Sn dopant the electronic contribution to the thermal conductivity was a significant portion. From the electrical resistivity data it was known that the electronic contribution increased with increasing concentration of dopant and in the x = 0.06 sample the electronic contribution was approximately 45% at 350 K.

Comparing the total thermal conductivity of both the Sn and Te ball milled samples very similar values were obtained, which displayed the expected similarity in amount of phonon scattering from dopant inclusion. Upon first inspection of this figure, and the figure for the thermal conductivity for Sn doped, ball milled samples, it would appear as though doping

contributed a very large reduction in the thermal conductivity, which was not found in the un-ball milled, doped samples. This conclusion is faulty though due to the logarithmic y-axis giving the illusion of significantly more reduction from doping in these ball milled samples. A comparison of the total thermal conductivity of doped, ball milled samples versus those that were only doped shows that the ratio of the reduction was much larger in those which had been ball milled, but the actual value of that reduction was very similar, which correlates with what would be expected.

6.7.4 zT

The figure-of-merit displayed by these samples is shown in Figure 6.33.

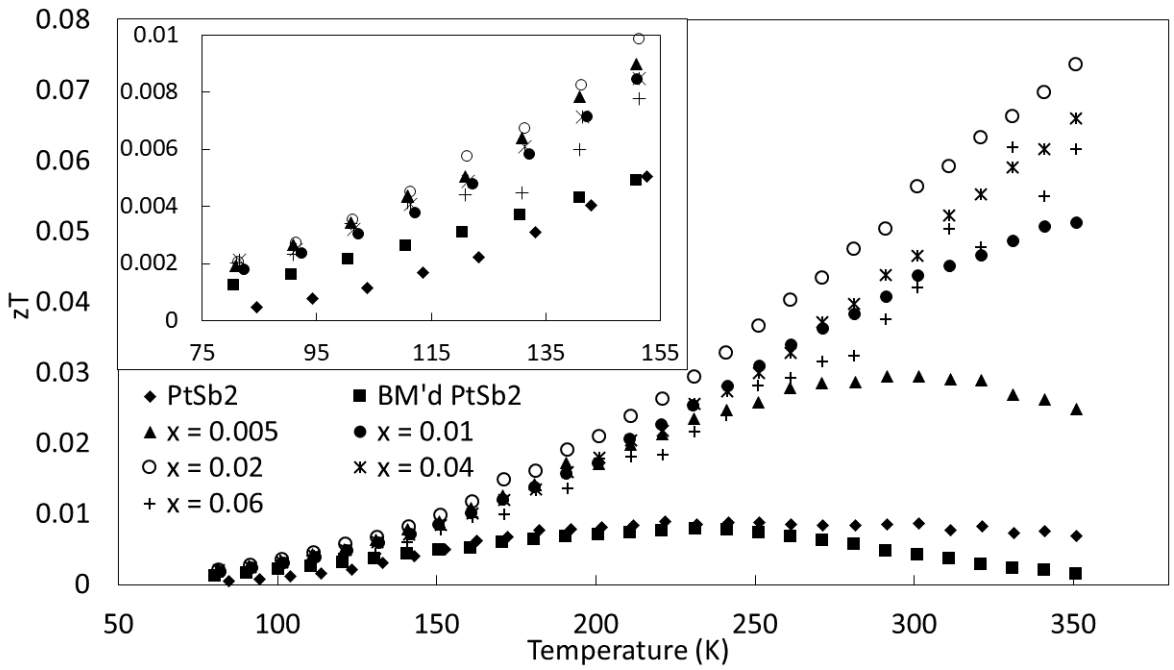

Figure 6.33: zT of Te Doped, Ball Milled $PtSb_2$

It was found that the figure-of-merit of tellurium doped, ball milled $PtSb_2$ was enhanced over nominal $PtSb_2$ over all temperatures measured. The low temperature results shown in

the insert continued to display low values, but demonstrated that all dopant compositions enhanced the figure-of-merit. As temperature increased the x = 0.02 sample showed the highest figure-of-merit of approximately 0.074 at 350 K. Of similar values were the x = 0.04 and 0.06 samples both with values of approximately 0.06 at 350 K. As with all samples discussed, the absolute magnitude of the figure-of-merit in $PtSb_2$, doped or otherwise manipulated, remains low but significant enhancement was made from tellurium doping, ball milled samples.

6.8 Conclusions

From previous research on $PtSb_2$ it was known that significant reduction in the thermal conductivity would be necessary to significantly enhance the thermoelectric performance of this material. Thus, the work in this chapter strove to explore methods of reducing the large thermal conductivity of $PtSb_2$, to explain some of the interesting results occurring from those minimization attempts, and to reap the benefits of a reduced thermal conductivity by tuning the power factor from p- and n-type doping.

The first method of thermal conductivity reduction examined in this chapter concerned the generation of a solid solution between $PtSb_2$ and $PdSb_2$. This method of thermal conductivity reduction is well known and between two materials with the same crystal structure would normally be fully soluble in each other over the entire composition range. It was found though that with only a 10% substitution of Pd that secondary phases were created. The generation of secondary phases created a different scattering mechanism which was a more long range boundary scattering mechanism than the point defect scattering expected from a solid solution. The results from this investigation demonstrated this reduction in

the thermal conductivity most pronounced at low temperatures, yet still substantial around room temperature. The Seebeck coefficient of these samples was found to be diminished due to the inclusion of a secondary phase which was characterized as a metal. The power factor was enhanced in two samples which coupled with a reduced thermal conductivity yielded an enhanced figure-of-merit, but these results were nevertheless lackluster in their magnitude. Future work with this method would examine the creation of a single phased solid solution with $PdSb_2$ and α-$PtBi_2$.

The other well known method of thermal conductivity reduction examined in this work concerned ball milling as a means of reducing particle size. It was found for $PtSb_2$ that the particle size was minimized after a total milling time of 100 minutes in a stainless steel ball mill jar and media. Concurrent with these results it was additionally found that this milling treatment resulted in the generation of a negative Seebeck coefficient. This result was unexpected from ball milling and was the impetus for a series of follow up investigations, which culminated in an examination of the effects of non-stoichiometry in $PtSb_2$.

In the narrow bandgap material, $PtSb_2$, deviations from stoichiometry were thought to have generated a wide dispersion in the transport properties measured in prior literature. Thus, to explore the cause of the change in the Seebeck coefficient of ball milled samples antimony excess and deficient samples were explored. It was found that antimony excess acted as an ionized impurity scattering site which decreased the overall thermoelectric properties of the material. From antimony deficiency it was found that the negative Seebeck coefficient found in ball milled samples was also found for these samples. This led to the conclusion that antimony sublimation during densification of ball milled samples is what created the negative Seebeck coefficient found in these samples. Overall, the thermoelectric potential of $PtSb_2$ was decreased when non-stoichiometry was introduced in the material, and would not

be a future route of enhancement.

To profit from the large reduction in the thermal conductivity found from ball milling two series of doping investigations were performed using Te and Sn as n- and p-type dopants respectively. Focusing first upon the thermal properties both dopant types produced further reduction in the thermal conductivity beyond that which was generated from ball milling. Upon analysis this further reduction was found to be similar to that found from doping in un-ball milled samples, and was of similar magnitude between the two dopants. A few useful comparisons may be made of the two types of dopants concerning the electronic properties found. A comparison of the effects of the dopants on the Seebeck coefficient at 170 K is explanatory of the general results from these dopants. This can be seen in Figure 6.34.

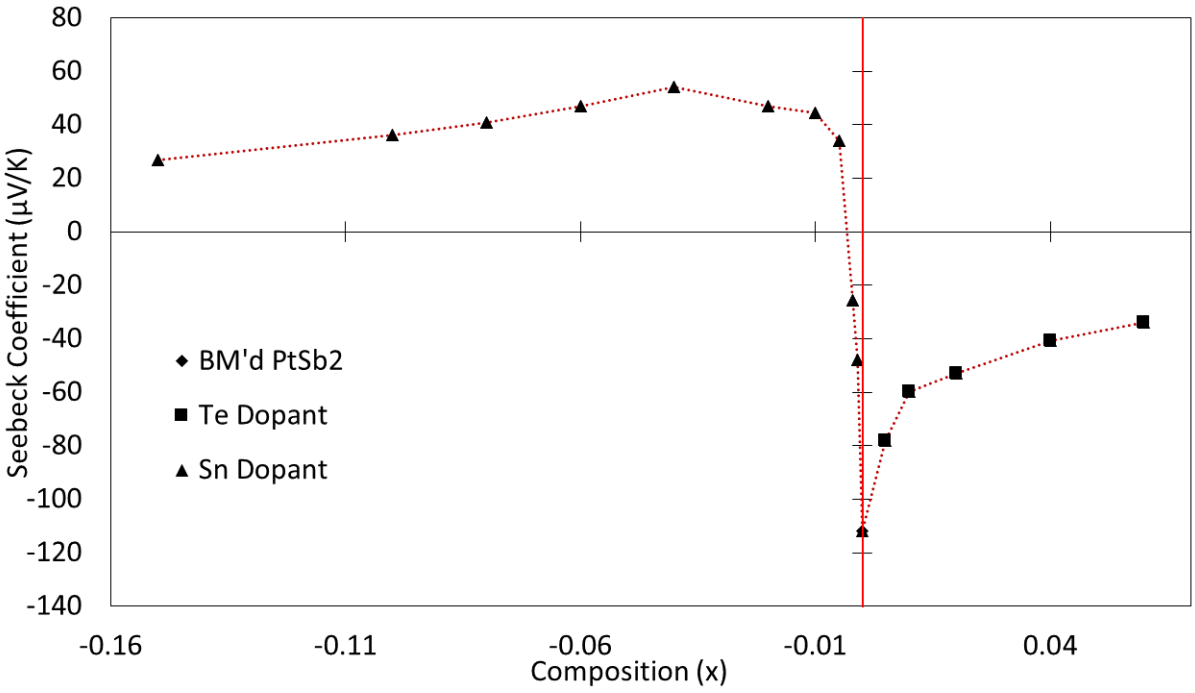

Figure 6.34: Comparison of the Seebeck Coefficients of Sn and Te Doped, Ball Milled $PtSb_2$ at 170 K

This figure hearkens back to that shown in Figure 4.23 and highlights the effect that the same two dopants, Sn and Te, have on a now n-type parent material. As was done before,

the compositions of tin dopant are given as a negative to connote the loss of electrons, while tellurium composition is positive to connote the gain of electrons. The expected trend is found for tellurium dopant where as the concentration is increased of n-type dopant in an n-type material the Seebeck coefficient decreased due to the increasing carrier concentration. In the Sn dopant it would be expected that for compositions less than the the x = 0.04 sample the Seebeck coefficient would continue to increase until a sudden change to negative values was observed for some very low composition. It was instead found that the magnitude decreased in these low dopant concentration samples until a gradual change to negative values were observed. This is thought to have occurred due to the competition between the now intrinsic electron carriers and the extrinsically doped holes.

Also of interest from these results is the increase in the electrical resistivity found for Sn doped, ball milled samples. This increase in the electrical resistivity relative to undoped ball milled samples was found in the same low dopant concentration samples which did not display the expected Seebeck coefficient. In systems with bipolar conduction the addition of extrinsic carriers of opposite type to the dominant carrier in the parent material should not create an increase in the electrical resistivity because they are a non-competing, additive effect. Potential causes for this increase in the electrical resistivity are a decreased mobility from additional scattering, which was not found for tellurium dopants of similar composition, or a change in the electronic band structure which generated a decreased carrier concentration. The only way to determine the answer to this question is through the use of Hall experimentation, which would be a direction of future research in this project.

Ultimately, the figure-of-merit of these doped, ball milled samples showed enhancement over the parent material and similarly doped $PtSb_2$. This further enhancement was largely due to the dramatic reduction in the thermal conductivity of these samples. As was found

for un-ball milled samples, the highest zT obtained in the Sn and Te samples were very similar in magnitude and composition. A zT of 0.07 was obtained in the x = 0.04 sample with Sn doping and a zT of 0.074 was obtained in the x = 0.02 sample with Te doping.

Chapter 7

Conclusions and Future Directions

7.1 Conclusions

This work has concerned the thermoelectric enhancement of the narrow bandgap material $PtSb_2$ for use at low temperatures. The electronic properties of $PtSb_2$ made it a very promising candidate for the low temperature range due to the large Seebeck coefficient it displays, as well as the low electrical resistivity found up to room temperature. The bandgap of $PtSb_2$ is approximately 0.1 eV which offered several avenues of manipulation to probe enhancement mechanisms which are not typically available in middle and high temperature thermoelectric materials. The greatest impediment to the expeditious use of $PtSb_2$ at low temperature is the large thermal conductivity the material exhibits. Thus, in addition to some of the other work offered here on electronic doping are two routes of reducing this large thermal conductivity.

An often used technique to enhance the figure-of-merit of a thermoelectric material is tuning the carrier concentration to maximize the power factor. It is known from the Pisarenko relationship that the power factor of a material is maximized at a specific carrier concentration where the trade off between the Seebeck coefficient and the electrical resistivity are balanced for maximization. In the typical thermoelectric material to meet this carrier

concentration extrinsic carriers will need to be doped into the system. This is typically done by p-type doping in a p-type material, or n-type doping in an n-type material, to avoid any decrease in the Seebeck coefficient which would occur from doping a material with the opposite type of the nominal compound. This is not the case with $PtSb_2$ though due to the narrow bandgap of the material. When $PtSb_2$ is opposite type doped, the Seebeck coefficient will change to the opposite type given sufficient dopant concentrations. This effect was seen in the work performed on antimony site doping in both the ball milled and un-ball milled studies.

Doping on the antimony site in un-ball milled $PtSb_2$ was performed with n- and p-type dopants to great effect for Sn and Te dopants, but was lackluster or incapable for In, Se, and Ge dopants. A large enhancement was found for Sn and Te doping with a factor of six increase in the above room temperature figure-of-merit as well as significant increases found in the power factor for these dopants. However, due to the low figure-of-merit for the nominal material this large enhancement was stymied by its overall low magnitude.

Examining indium as a dopant in comparison to Sn demonstrated a large variability in the electronic properties that were observed for these two p-type dopants. It was expected that for every In atom doped an extra hole would be doped in comparison with Sn doping and that this effect would be indicated by a reduced electrical resistivity for a lower In composition when compared to a similar Sn composition. This was not found though and for a given composition the electrical resistivity was higher. A possible explanation for this effect is the inability of accommodating In in the tetrahedral coordination of the Sb site in $PtSb_2$. Thus, in future work this effect should be taken into account when selecting doping elements.

In the work with Se and Ge doping on the antimony site it was found that Se acted as a

typical n-type dopant, however, compared to Te, Se did not display as large a reduction in the electrical resistivity and also yielded a slightly different behavior in the Seebeck coefficient for similar compositions. This was likely due to a difference in mobility generated from these two dopants since selenium has a larger mass and size difference from antimony than tellurium does. For germanium it was found that even for the lowest dopant concentrations no solubility was observed for this dopant. This was an unexpected result due to the relatively high solubility of tin on the antimony site, as well as the availability of tetrahedral bonding in germanium as compared to indium. It is likely that the size difference of germanium compared to tin created this very limited solubility.

Examining the effects of platinum site doping a few interesting effects were found. Iron doping on the platinum site resulted in a p-type doping effect and generated a large enhancement in the figure-of-merit that was very similar to that created for the Sn and Te doped samples. Unlike the results found for germanium, no solubility limit was found for the iron doped samples examined here. The large mass difference and change in valence shell electron configuration did not impede the incorporation of iron onto the platinum site for these compositions.

Turning to the dopants of niobium and silver the low solubility of these dopants was observed in the x-ray patterns for silver at low compositions and for niobium in the x = 0.05 sample only. The results in the Seebeck coefficient however demonstrated an ionized impurity scattering effect which ultimately led to these two dopants decreasing the figure-of-merit.

Ytterbium dopant was explored due to the possible f-shell electron interactions it may have with the $PtSb_2$ electronic structure. It was found that the power factor of ytterbium doped samples peaked between approximately 180 to 200 K with a very large value close to 42 μW/cm-K^2. This power factor was nearly twice as large as the power factors generated from

Sn or Te doping and was also centered around the temperature region of focus in this work. The figure-of-merit found for this dopant displayed superior properties most pronounced at 250 K of zT = 0.03. In comparison to the Sn and Te antimony site doping this figure-of-merit was not found to be any larger than these dopants at this temperature. It is likely that additional ytterbium dopant concentration would result in further enhancement in this temperature regime and begs for additional work.

It was known that the thermal conductivity of $PtSb_2$ was a major impediment to a large figure-of-merit at low temperature in this material, thus two experimental studies were performed on lowering this thermal conductivity. The first to be examined was the effect of a solid solution of $PdSb_2$ with $PtSb_2$. $PdSb_2$ was expected to have full solid solubility in the parent material $PtSb_2$ because they both crystallize in the same structure and have very similar lattice parameters. It was found though that at approximately 10% substituted palladium a secondary phase of $PdSb_2$ was observed. This secondary phase would cause a different scattering mechanism than the intended point defect scattering from a solid solution. Nevertheless, a decrease in the thermal conductivity was observed for these samples and a slight increase in the power factor for the 5% and 1% substituted samples. This created an overall increase in the figure-of-merit for all samples up to a 25% substitution.

Exploring the effects of ball milling demonstrated the large reduction in thermal conductivity available from reducing the particle size of $PtSb_2$. It was found from using incremental ball milling times that a minimized particle size was met after 100 total minutes of ball milling and that the melting point of the material was drastically reduced due to the reduction in particle size. Unexpectedly, the Seebeck coefficient of these ball milled samples changed sign over the temperatures examined here. After investigations into the effects of non-stoichiometry in $PtSb_2$ it was determined that the change to n-type from ball milling

was likely due to the loss of antimony during densification. Non-stoichiometry in $PtSb_2$ was additionally shown to reduce the figure-of-merit for all temperatures measured and would not likely be an avenue of future examination for enhancement due to the secondary phases found for low deficiency and excess.

The final examinations performed in this work entailed a return to electronic doping with Sn and Te on the antimony site of ball milled samples. This study would make use of the reduced thermal conductivity from ball milling and attempt to tune the carrier concentration of the now n-type material. It was found that using both Sn and Te the power factor was reduced in ball milled samples except for the highest performing concentrations, but due to the large reduction in the thermal conductivity the figure-of-merit was enhanced for several compositions. The highest zT found for Sn doped samples was in the x = 0.04 composition with zT = 0.07 and the highest for Te was in the x = 0.02 composition with zT = 0.074.

It is a remarkable feature of $PtSb_2$ that this material may be made p-type or n-type just by the element with which it is doped, and further, that very similar zTs are found for both types of dopants when maximized. When optimizing the carrier concentration for a typical medium or high temperature thermoelectric material the dopant type chosen will typically be of the same type as the parent material so as to not negatively impact the Seebeck coefficient from the addition of bipolar conductors. While this does indeed happen in $PtSb_2$ the impact is negated due to the low temperature at which intrinsic carriers populate in the system because of its narrow bandgap. As was mentioned previously it is a significant benefit for thermoelectric materials to be capable of being doped n- or p-type for their use in a thermoelectric module. These materials should have a very similar thermal expansion coefficient which will help to reduce the stresses experienced by the materials and decrease the likelihood of fractures and failures.

Table 7.1 gives a comparison of all of the electronic dopants examined in this work and the thermoelectric properties they exhibit at the temperature of maximum figure-of-merit.

Table 7.1: Comparison of the Thermoelectric Properties of Electronically Doped $PtSb_2$ at the Temperature of Maximum zT

	Dopant	Ball Milled	Best Composition	Seebeck Coefficient (μV/K)	Electrical Resistivity (mΩ-cm)	Thermal Conductivity (W/m-K)	zT	Temperature (K)
$PtSb_2$	None		N/A	141.95	1.987	24.79	0.009	220
Antimony Site:	Tellurium		0.02	-93.63	0.41	12.94	0.059	350
	Selenium		0.02	-42.52	0.474	14.61	0.009	350
	Tin		0.04	90.07	0.314	15.41	0.059	350
	Indium		0.01	67.33	0.555	21.46	0.013	340
	Tellurium	X	0.02	-80.84	1.211	2.57	0.073	350
	Tin	X	0.04	84.16	1.642	2.16	0.07	350
Platinum Site:	Ytterbium		0.1	169.76	0.809	29.63	0.03	250
	Iron		0.005	119.68	0.593	14.74	0.057	350
	Niobium		0.01	69.91	0.808	18.13	0.009	270
	Silver		0.02	61.86	0.655	20.69	0.0084	280

It is beneficial to make a brief overview of dopants used in this work and their resultant thermoelectric properties to highlight a few general implications. From Table 7.1 it may be seen that for the purposes of n-type doping, tellurium provides superior enhancement to selenium and for p-type doping, tin is the better dopant when compared to indium. This implies that for doping on the antimony site in $PtSb_2$, and possibly further to all pnictogen sites in narrow-gap semiconductors, proximity in the periodic table of the dopant element to the substituted atom may be key.

When doping on the platinum site, it is likely that proximity is not the only guiding principle for selecting a suitable dopant. It may be observed from the results found in niobium, silver, and iron doping that iron was fully incorporated into the structure and produced a p-type doping effect, while neither niobium nor silver were found to electronically dope. It is likely that size difference, electronegativity, and valency of the dopant are of importance for doping on this site. When examining ytterbium, the cause of the enhancement displayed by this dopant was likely due to a chemical pressure effect on its valency and not

simply the result of a change in the carrier concentration. Of all of the dopants examined in this work, ytterbium may have been the only dopant whose enhancement was not generated through a change in the carrier concentration and may present an independent route of enhancement in the figure-of-merit. It is possible that further optimization of the figure-of-merit may be obtained by combining the effects of ytterbium doping and electronic doping to result in further enhanced power factors and zT values.

Finally, the electronically doped ball milled samples showed the largest improvement in figure-of-merit of all samples examined. A slightly higher figure-of-merit was found for tellurium dopant as compared to tin doping in these ball milled samples. To conclude this overview, it could be stated that for maximal enhancement in the figure-of-merit at temperatures approaching room temperature a ball milled, tellurium doped sample should be used, but for temperatures approaching 250 K ytterbium doped samples display enhanced performance.

7.2 Future Directions

With the large number of materials crystallizing in the pyrite structure it is likely that a solid solution may be able to be synthesized with some compounds, which will result in further enhancement than what was found with $PdSb_2$. Of further interest beyond that of making a solid solution is the substitution of bismuth or arsenic for antimony in $PtSb_2$. It is known that $PtBi_2$ is a metal with fully overlapping conduction and valence bands, similar to $PdSb_2$ [144]. While a solid solution of $PdSb_2$ was unable to be generated $PtBi_2$ may not have the same issue. α-$PtBi_2$ crystallizes in the pyrite structure with a lattice parameter, a = 0.6691 nm [145]. It undergoes a phase change at temperatures greater than 270 °C to β-

$PtBi_2$ in the hexagonal crystal structure [97,146,147]. Hulliger found α-$PtBi_2$ to be metallic and that the compound PtSbBi could be synthesized with a lattice parameter, a = 0.6570 nm, the expected midpoint between the lattice parameters of the two end compounds [97]. While it is expected that large concentrations of a solid solution of $PtSb_2$ with a metal will not result in enhancement, low concentrations of α-$PtBi_2$ may increase the figure-of-merit through a reduction in the thermal conductivity. It is expected that this solid solution may further narrow the bandgap of $PtSb_2$ with very low substitution compositions since PtSbBi was found to be a metal. This bandgap engineering may be a way to lower the temperature where the figure-of-merit is maximized. In the opposite manner $PtAs_2$ has been shown to have a larger bandgap than $PtSb_2$, and while a solid solution with this compound is expected to lower the thermal conductivity, this may also lead to bandgap engineering by increasing the bandgap of $PtSb_2$ [144]. This is likely to lead to an increased temperature for the maximum figure-of-merit, but may lead to enhancement around room temperature.

As mentioned earlier in chapter five further rare earth doping on $PtSb_2$ may yield promising results. Ytterbium doping was the only dopant that generated an increase in the power factor in the low temperature region between 150 to 250 K. Examining greater concentrations of ytterbium may yield increased power factors beyond what was found here, but a new synthesis method would need to be determined. Oxidation of ytterbium and secondary phase formation became a challenge in concentrations beyond x = 0.1 and therefore these concentrations were unable to be examined. Additionally, it is possible that the effect of ytterbium doping may be independent to a reduction in particle size by ball milling, thus a possible avenue of future work would examine those effects. With the enhancement found from ytterbium it is expected that doping with the rare earth cerium may yield similar results. Cerium has one valence electron in the f-shell, and as with ytterbium, may lead to

interesting effects stemming from density of states manipulation near the bandgap.

It has been found that a semiconductor which has been engineered to have a more complex unit cell, for instance by taking a group 4 element and splitting it up into group 3 and 5 elements, often leads to a lower thermal conductivity. This is a common strategy with thermoelectric materials and can lead to enhancement in the figure-of-merit [53]. This engineering may be done with $PtSb_2$ by substitution of the elements Sn and Te for antimony. Tin and tellurium are found on either column of the periodic table of antimony and when crystallized PtSnTe forms the orthorhombic $Pca2_1$ structure with lattice parameters a = 0.6476 nm, b = 0.6461 nm, and c = 0.6445 nm [148]. This structure is only slightly distorted from the pyrite, but the antimony dumbbells found in $PtSb_2$ are replaced by Sn - Te bonded pairs [149]. This is expected to reduce the thermal conductivity dramatically. Early experimental work has been promising with this compound which resulted in nearly an order of magnitude reduction in the thermal conductivity at low temperature. However, in this early experimental work a two phased sample was generated. Further experimentation would require optimization of the synthesis parameters to generate a single phased sample, subsequent doping to tune the carrier concentration, and further thermal conductivity reduction attempts.

Another pyrite structured compound of interest is $MnTe_2$, which from the work of Hulliger et al. was shown to have a wide range of electronic properties depending only upon the synthesis parameters used [90]. The highest Seebeck coefficient for these samples was found to be approximately 500 μV/K between 80 to 120 K, while all other samples showed a range of values greater than 200 μV/K above 150 K. The electrical resistivity of these samples is relatively large for low temperature use but would be expected to decrease with carrier concentration manipulation. It is expected that $MnTe_2$ would have a similar high thermal

conductivity as compared to $PtSb_2$, but may be amenable to reduction attempts. The large variability in the electronic properties is thought to arise due to non-stoichiometry stemming from the tellurium in the system and as such, extensive ball milling may exacerbate this effect. This effect however may be an avenue to explore carrier concentration in the material as it was for $PtSb_2$.

Finally, a compound worthy of investigation is NiP_2, which has been shown to have a narrow bandgap between 0.5 to 0.7 eV [68,150]. Examination of the electronic band structure additionally shows a similarity with that found for $PtSb_2$ with an indirect bandgap [144]. NiP_2 crystallizes in the monoclinic structure with the space group C2/c [151]. Relatively little experimental work has been performed on this material, but the room temperature electrical resistivity has been found to range between 0.42 to 0.09 Ω-cm with a Seebeck coefficient of -392 μV/K [68]. The major benefit of NiP_2 over that of $PtSb_2$ is the lower cost to use nickel and phosphorous compared to that of platinum and antimony. While thermoelectric applications are a niche market where reliability and efficiency are of higher importance than cost, a lowered cost may help by allowing for additional testing and experimentation without as much concern for monetary waste. And it is always a possibility that if costs could be reduced substantially, then extensive adoption may be practical.

As was introduced in the experimental section, some early investigations into this material have been attempted in this work. After separation of NiP_2 and tin flux by reaction with hydrochloric acid and a water wash the recovered powder was found to be single phased from X-ray diffraction in the expected monoclinic structure. This powder required densification by SPS in order to have transport properties measured and after this step the compound was found to have separated into a secondary phase containing nickel phosphide. Thus, for future work, experimentation will be necessary on a densification procedure which does not result

in the sublimation of phosphorous. This material is a promising candidate due to its similar electronic band structure to $PtSb_2$ and its earth abundant constituents. If the synthesis of a single phased sample can be accomplished, further doping and thermal conductivity studies could be performed to create a cost effective thermoelectric material.

As can be seen there are still several open areas and directions in which the work on $PtSb_2$ can be taken to probe some of the interesting results displayed here, as well as to further enhance some of the effects found. Additionally, there are several materials in the pyrite or otherwise structure which show promise as potentially good materials for low temperature thermoelectric use. The cryogenic region of thermoelectric use is a challenging regime to increase the figure-of-merit, but one with many possible applications and benefits for society as well as the world.

REFERENCES

REFERENCES

[1] T. J. Seebeck. Ueber die magnetische Polarisation der Metalle und Erze durch TemperaturDifferenz. *Ann. Phys.*, 82(2):133–160, 1826.

[2] J. C. Peltier. Nouvelles Experiences sur la Caloricite des Courans Electrique. *Ann. Chim. Phys.*, 56:371, 1834.

[3] W. Thomson. Account of Researches in Thermo-Electricity. *Proc. R. Soc. London*, 7(0):49–58, jan 1854.

[4] Nicholas Fuschillo. *Thermoelectric Materials and Devices*. Reinhold Publishing Corp, New York, 1960.

[5] H. J. Goldsmid and R. W. Douglas. The use of semiconductors in thermoelectric refrigeration. *Br. J. Appl. Phys.*, 5:386–390, 1954.

[6] E. Altenkirch. Uber den Nutzeffekt der Thermosaule. *Phys. Zeitschrift*, 10:560–580, 1909.

[7] E. Altenkirch. Elektrothermische Kälteerzeugung und reversible elektrische Heizung. *Phys. Zeitschrift*, 12:920, 1911.

[8] Qiang Wang and Rongrong Li. Drivers for energy consumption: A comparative analysis of China and India. *Renew. Sustain. Energy Rev.*, 62:954–962, 2016.

[9] Melike E. Bildirici and Tahsin Bakirtas. The relationship among oil, natural gas and coal consumption and economic growth in BRICTS (Brazil, Russian, India, China, Turkey and South Africa) countries. *Energy*, 65:134–144, 2014.

[10] Nathan S. Lewis. Powering the Planet. *MRS Bull.*, 32(October):808–820, 2007.

[11] Steven Chu and Arun Majumdar. Opportunities and challenges for a sustainable energy future. *Nature*, 488(7411):294–303, 2012.

[12] J. Yang. Potential applications of thermoelectric waste heat recovery in the automotive industry. *ICT 2005. 24th Int. Conf. Thermoelectr. 2005.*, pages 155–159, 2005.

[13] R. Saidur, M. Rezaei, W. K. Muzammil, M. H. Hassan, S. Paria, and M. Hasanuzzaman. Technologies to recover exhaust heat from internal combustion engines. *Renew. Sustain. Energy Rev.*, 16(8):5649–5659, 2012.

[14] Jihui Yang and Thierry Caillat. Thermoelectric Materials for Space and Automotive Power Generation. *MRS Bull.*, 31(03):224–229, 2006.

[15] M. C. Bennett, M. C. Aronson, D. A. Sokolov, C. Henderson, and Z. Fisk. Ferromagnetism, superconductivity and secondary phases in the dilute magnetic semiconductor Pt1-xRExSb2 (RE = La, Ce, Gd, Yb). *J. Alloys Compd.*, 400:2–10, 2005.

[16] Lester J. Kozlowski and Walter F. Kosonocky. *Handbook of Optics*. McGraw-Hill, New York, 1995.

[17] Antoni Rogalski. Toward third generation HgCdTe infrared detectors. *J. Alloys Compd.*, 371(1-2):53–57, 2004.

[18] Antoni Rogalski. Infrared detectors: An overview. *Infrared Phys. Technol.*, 43(3-5):187–210, 2002.

[19] R. T. Rajendra Kumar, B. Karunagaran, D. Mangalaraj, Sa. K. Narayandass, P. Manoravi, M. Joseph, and Vishnu Gopal. Room temperature deposited vanadium oxide thin films for uncooled infrared detectors. *Sensors Actuators A*, 107:62–67, 2003.

[20] W. D. Hu, X. S. Chen, F. Yin, Z. J. Quan, Z. H. Ye, X. N. Hu, Z. F. Li, and W. Lu. Analysis of temperature dependence of dark current mechanisms for long-wavelength HgCdTe photovoltaic infrared detectors. *J. Appl. Phys.*, 105(10):1–8, 2009.

[21] S. B. Riffat and Xiaoli Ma. Thermoelectrics: A review of present and potential applications. *Appl. Therm. Eng.*, 23(8):913–935, 2003.

[22] F. J. DiSalvo. Thermoelectric Cooling and Power Generation. *Science*, 285(5428):703–706, 1999.

[23] G. S. Nolas, J. Sharp, and H. J. Goldsmid. *Thermoelectrics Basic Principles and New Materials Developments*. Springer, 2001.

[24] H. Julian Goldsmid. *Applications of Thermoelectricity*. Butler and Tanner Ltd., 1960.

[25] G. Jeffrey Snyder, Marco Soto, Randy Alley, David Koester, and Bob Conner. Hot Spot Cooling using Embedded Thermoelectric Coolers. *22nd IEEE SEMI-Therm Symp.*, 2006.

[26] S. B. Riffat and Xiaoli Ma. Improving the coefficient of performance of thermoelectric cooling systems: A review. *Int. J. Energy Res.*, 28(9):753–768, 2004.

[27] H. J. Goldsmid. *Thermoelectric Refrigeration*. Springer US, Boston, MA, 1964.

[28] Hao Lv, Xiao-Dong Wang, Jing-Hui Meng, Tian-Hu Wang, and Wei-Mon Yan. Enhancement of maximum temperature drop across thermoelectric cooler through two-stage design and transient supercooling effect. *Appl. Energy*, 175:285–292, 2016.

[29] B. J. O'Brien, C. S. Wallace, and K. Landecker. Cascading of peltier couples for thermoelectric cooling. *J. Appl. Phys.*, 27(7):820–823, 1956.

[30] T. Metzger and R. P. Huebener. Modelling and cooling behaviour of Peltier cascades. *Cryogenics (Guildf).*, 39(3):235–239, 1999.

[31] P. Drude. Zur Elektronentheorie der Metalle. *Ann. Phys.*, 306(3):566–613, 1900.

[32] A. Sommerfeld. Zur Elektronentheorie der Metalle auf Grund der Fermischen Statistik - I. Teil: Allgemeines, Stromungs- und Austrittsvorgange. *Zeitschrift fur Phys.*, 47(1-2):1–32, 1928.

[33] Felix Bloch. Uber die Quantenmechanik der Elektronen in Kristallgittern. *Zeitschrift fur Phys.*, 52(7-8):555–600, 1929.

[34] C. Kittel. *Introduction to Solid State Physics*. John Wiley and Sons, Inc., New York, third edition, 1953.

[35] A. Bulusu and D. G. Walker. Review of electronic transport models for thermoelectric materials. *Superlattices Microstruct.*, 44(1):1–36, 2008.

[36] S. O. Kasap. *Principles of Electronic Materials and Devices*. McGraw-Hill, New York, 3rd edition, 2006.

[37] Joseph P. Heremans, Vladimir Jovovic, Eric S. Toberer, Ali Saramat, Ken Kurosaki, Anek Charoenphakdee, Shinsuke Yamanaka, and G. Jeffrey Snyder. Enhancement of Thermoelectric of the Electronic Density of States. *Science*, 321(July):1457–1461, 2008.

[38] G. D. Mahan and J. O. Sofo. The best thermoelectric. *Proc. Natl. Acad. Sci. U. S. A.*, 93:7436–7439, 1996.

[39] G. Jeffrey Snyder and Eric S. Toberer. Complex thermoelectric materials. *Nat. Mater.*, 7:105–114, 2008.

[40] A. M. Dehkordi, M. Zebarjadi, J. He, and T. M. Tritt. Thermoelectric Power Factor: Enhancement Mechanisms and Strategies for Higher Performance Thermoelectric Materials. *Mater. Sci. Eng. R.*, 97:1–22, 2015.

[41] R. Peierls. Zur kinetischen Theorie der Wärmeleitung in Kristallen. *Ann. Phys.*, 395(8), 1929.

[42] P. Debye. Zur Theorie der Spezifischen Warmen. *Ann. Phys.*, 344(14), 1912.

[43] T. L. Hill. *An Introduction to Statistical Thermodynamics*. Courier Corporation, New York, 1986.

[44] H. B. G. Casimir. Note on the conduction of heat in crystals. *Physica*, 5(6):495–500, 1938.

[45] J. Callaway. Model for lattice Thermal Conductivity at Low Temperatures. *Phys. Rev.*, 113(4):1046–1051, 1959.

[46] D. M. Rowe, V. S. Shukla, and N. Savvides. Phonon Scattering at Grain Boundaries in Heavily Doped Fine-Grained Silicon-Germanium Alloys. *Nature*, 290(5809), 1981.

[47] F. R. N. Nabarro. The Interaction of Screw Dislocations and Sound Waves. *Proc. R. Soc. A*, 209:278–290, 1951.

[48] M. Asen-Palmer, K. Bartkowski, E. Gmelin, M. Cardona, A. P. Zhernov, A. V. Inyushkin, A. Taldenkov, V. I. Ozhogin, K. M. Itoh, and E. E. Haller. Thermal Conductivity of Germanium Crystals with Different Isotopic Compositions. *Phys. Rev. B*, 56(15):9431–9447, 1997.

[49] I. Pomeranchuk. On Conduction of Heat in Dielectrics below Debye Temperature. *J. Phys. U.S.S.R.*, 6(237), 1942.

[50] Jihui Yang. *Thermal Conductivity Theory, Properties, and Applications*. Springer US, New York, 2004.

[51] P. G. Klemens. The Thermal Conductivity of Dielectric Solids at Low Temperatures (Theoretical). *Proc. R. Soc. A Math. Phys. Sci.*, 208(1092):108–133, 1951.

[52] A. A. Maznev and O. B. Wright. Demystifying umklapp vs normal scattering in lattice thermal conductivity. *Am. J. Phys.*, 82(11):1062–1066, 2014.

[53] Donald T. Morelli and Glen A. Slack. High Lattice Thermal Conductivity Solids. In S. L. Shinde and J. S. Goela, editors, *High Therm. Conduct. Mater.*, page 42. Springer Science, New York, 2006.

[54] Glen A. Slack. The Thermal Conductivity of Nonmetallic Crystals. In *Solid State Phys. - Adv. Res. Appl.*, volume 34, pages 1–71. Academic Press, 1979.

[55] A. Eucken. Über die Temperaturabhängigkeit der Wärmeleitfähigkeit fester Nichtmetalle. *Ann. Phys.*, 339(2):185–221, 1911.

[56] C. Wood. Materials for thermoelectric energy conversion. *Inst. Phys.*, 51:459–539, 1988.

[57] Glen Slack. New Materials and Performance Limits for Thermoelectric Cooling. In D. M. Rowe, editor, *CRC Handb. Thermoelectr.*, chapter 34, pages 407–440. CRC Press, 1995.

[58] R. P. Chasmar and R. Stratton. The Thermoelectric Figure of Merit and its Relation to Thermoelectric Generators. *J. Electron. Control*, 7(1), 1959.

[59] H. Wang, Y. Pei, A. LaLonde, and G. J. Snyder. Material Design Considerations Based on Thermoelectric Quality Factor. In K. Koumoto and T. Mori, editors, *Thermoelectr. Nanomater.*, volume 182, page 389. Springer-Verlag, 2013.

[60] Eric S. Toberer, Alex Zevalkink, and G. Jeffrey Snyder. Phonon engineering through crystal chemistry. *J. Mater. Chem.*, 21(2):15843, 2011.

[61] Wolfgang G. Zeier, Alex Zevalkink, Zachary M. Gibbs, Geoffroy Hautier, Mercouri G. Kanatzidis, and G. Jeffrey Snyder. Thinking Like a Chemist: Intuition in Thermoelectric Materials. *Angew. Chemie - Int. Ed.*, 55(24):6826–6841, 2016.

[62] S. Ganesan. Temperature variation of the grüneisen parameter in magnesium oxide. *Philos. Mag.*, 7(74):197–205, 1962.

[63] G. D. Mahan. Figure of merit for thermoelectrics. *J. Appl. Phys.*, 65:1578–1583, 1989.

[64] J. O. Sofo and G. D. Mahan. Optimum band gap of a thermoelectric material. *Phys. Rev. B*, 49(7), 1994.

[65] Z. A. Munir, U. Anselmi-Tamburini, and M. Ohyanagi. The effect of electric field and pressure on the synthesis and consolidation of materials: A review of the spark plasma sintering method. *J. Mater. Sci.*, 41(3):763–777, 2006.

[66] Jared Williams, Dale Hitchcock, and Jian He. Spark Plasma Sintering: A Brief Survey of Recent Patents. *Recent Patents Mater. Sci.*, 5(3):191–198, 2012.

[67] Mercouri G. Kanatzidis, Rainer Pottgen, and Wolfgang Jeitschko. The metal flux: A preparative tool for the exploration of intermetallic compounds. *Angew. Chemie - Int. Ed.*, 44(43):6996–7023, 2005.

[68] P. Odile, S. Soled, C. Castro, and A. Wold. Crystal Growth and Characterization of the Transition-Metal Phosphides CuP2, NiP2, and RhP3. *Inorg. Chem.*, 17(2):283–286, 1978.

[69] A. L. Patterson. The scherrer formula for X-ray particle size determination. *Phys. Rev.*, 56(10):978–982, 1939.

[70] V. D. Mote, Y Purushotham, and B. N. Dole. Williamson-Hall analysis in estimation of lattice strain in nanometer-sized ZnO particles. *J. Theor. Appl. Phys.*, 6, 2012.

[71] E. H. Hall. On a New Action of the Magnet on Electric Currents. *Am. J. Math.*, 2(3):287–292, 1879.

[72] H. J. Goldsmid. The Thermal Conductivity of Bismuth Telluride. *Proc. Phys. Soc. Sect. B*, 69(2):203–209, 2002.

[73] H. J. Goldsmid. The Electrical Conductivity and Thermoelectric Power of Bismuth Telluride. *Proc. Phys. Soc. London*, 71Goldsmid(460):633–646, 1958.

[74] L. R. Testardi, J. N. Bierly, and F. J. Donahoe. Transport Properties of p-type Bi2Te3-Sb2Te3 Alloys in the Temperature Range 80 - 370 K. *J. Phys. Chem. Solids*, 23:1209–1217, 1962.

[75] M. Stordeur. The Thermoelectric Figure of Merit in the Mixed Crystal System p-(Bi1-xSbx)2Te3. *Phys. Stat. Sol*, 161:831–835, 1990.

[76] H. Julian Goldsmid. Bismuth Telluride and Its Alloys as Materials for Thermoelectric Generation. *Materials (Basel).*, 7(4):2577–2592, 2014.

[77] G. E. Smith and R. Wolfe. Thermoelectric properties of bismuth-antimony alloys. *J. Appl. Phys.*, 33(1962):841–846, 1962.

[78] W. M. Yim and A. Amith. BiSb alloys for magneto-thermoelectric and thermomagnetic cooling. *Solid State Electron.*, 15(10), 1972.

[79] Duck-Young Chung, Tim Hogan, Paul Brazis, Melissa Rocci-lane, Carl Kannewurf, Marina Bastea, Ctirad Uher, and Mercouri G Kanatzidis. CsBi4Te6: A High-Performance Thermoelectric Material for Low-Temperature Applications. *Science*, 287(5455):1024–2027, 2000.

[80] V. Jaccarino, G. K. Wertheim, J. H. Wernick, L. R. Walker, and Sigurds Arajs. Paramagnetic excited state of FeSi. *Phys. Rev.*, 160(3):476–482, 1967.

[81] B. C. Sales, E. C. Jones, B. C. Chakoumakos, J. A. Fernandez-Baca, H. E. Harmon, J. W. Sharp, and E. H. Volckmann. Magnetic, transport, and structural properties of Fe1-xIrxSi. *Phys. Rev. B*, 50(12):8207–8213, 1994.

[82] Brian C. Sales, Olivier Delaire, Michael A. McGuire, and Andrew F. May. Thermoelectric properties of Co-, Ir-, and Os-doped FeSi alloys: Evidence for strong electron-phonon coupling. *Phys. Rev. B - Condens. Matter Mater. Phys.*, 83(12):1–7, 2011.

[83] Stephen R. Boona and Donald T. Morelli. Structural, Magnetic, and Thermoelectric Properties of Some CePd3-Based Compounds. *J. Electron. Mater.*, 42(7):1592–1596, 2013.

[84] Gloria J. Lehr, Donald T. Morelli, Hyungyu Jin, and Joseph P. Heremans. Enhanced thermoelectric power factor in Yb1-xScxAl2 alloys using chemical pressure tuning of the Yb valence. *J. Appl. Phys.*, 114:223712, 2013.

[85] Sigrid Furuseth, Kari Selte, and Arne Kjekshus. Redetermined Crystal Structures of PdAs2, PdSb2, PtP2, PtAs2, PtSb2, PtBi2, and AuSb2. *ACTA Chem. Scand.*, 19(3):735–741, 1965.

[86] Nathaniel E. Brese and Hans Georg. Bonding Trends in Pyrites and a Reinvestigation of the Structures of PdAs2, PdSb2, PtSb2, and PtBi2. *Zeitschrift fur Anorg. und Allg. Chemie*, 620:393–404, 1994.

[87] P. E. Ngoepe, P. S. Ntoahae, S. S. Mangwejane, H. M. Sithole, S. C. Parker, K. V. Wright, and N. H. De Leeuw. Atomistic simulation studies of iron sulphide, platinum antimonide and platinum arsenide. *S. Afr. J. Sci.*, 101:480–483, 2005.

[88] Koichi Momma and Fujio Izumi. VESTA 3 for three-dimensional visualization of crystal, volumetric and morphology data. *J. Appl. Crystallogr.*, 44(6):1272–1276, 2011.

[89] R. C. Miller, D. H. Damon, and A. Sagar. Etch-Pit Patterns and Crystal Structure of PtSb2. *J. Appl. Phys.*, 35(12):3582, 1964.

[90] W. D. Johnston, R. C. Miller, and D. H. Damon. Electrical Properties of Some Compounds having the Pyrite or Marcasite Structure. *J. Less-Common Met.*, 8:272–287, 1965.

[91] Sigrid Furuseth, Kari Selte, and Arne Kjekshus. Solid Solubility and Structural Properties of Rare-Earth Pnictogens. *Acta Chem. Scand.*, 21(2):527–536, 1967.

[92] G. T. Mallick and P. R. Emtage. Nuclear Magnetic Resonance in PtSb2 and PtAs2. *Phys. Rev. B*, 2(5):1251–1260, 1970.

[93] Jerry Bell. *Chemistry*. W. H. Freeman and Company, New York, 1st edition, 2005.

[94] H. D. Lutz, G. Schneider, and G. Kliche. Far-infrared reflection spectra, TO- and LO-phonon frequencies, coupled and decoupled plasmon-phonon modes, dielectric constants, and effective dynamical charges of manganese, iron, and platinum group pyrite type compounds. *J. Phys. Chem. Solids*, 46(4):437–443, 1985.

[95] Jinming Liu, Yinghui Zhang, and Cuiping Guo. Thermodynamic Assessment of the Pt-Sb System. *Int. J. Nonferrous Metall.*, 02:95–99, 2013.

[96] V. P. Itkin and C. B. Alcock. The Pt-Sb (Platinum-Antimony) System. *J. Phase Equilibria*, 17(4):356–361, 1996.

[97] F. Hulliger. Electrical Properties of Pyrite-Type and Related Compounds with Zero Spin Moment. *Nature*, 200:1064–1065, 1963.

[98] D. H. Damon, R. C. Miller, and A. Sagar. Semiconducting Properties of PtSb2. *Phys. Rev.*, 138(2A):636–645, 1965.

[99] P. R. Emtage. Band structure of Platinum Antimonide. *Phys. Rev.*, 138(1A):246–259, 1965.

[100] Martin Søndergaard, Mogens Christensen, Lasse Bjerg, Kasper A. Borup, Peijie Sun, Frank Steglich, and Bo B. Iversen. Investigation of the correlation between stoichiometry and thermoelectric properties in a PtSb2 single crystal. *Dalt. Trans.*, 41:1278, 2012.

[101] D. H. Damon, R. C. Miller, and P. R. Emtage. Valence-Band Structure of PtSb2. *Phys. Rev. B*, 5(6):2175–2185, 1972.

[102] C. T. Elliot and S. E. R. Hiscocks. On the Preparation and Electrical Properties of PtSb2. *J. Mater. Sci.*, 3:174–177, 1968.

[103] R. A. Reynolds, M. J. Brau, and R. A. Chapman. Preparation and Semiconducting Properties of Platinum Antimonide. *J. Phys. Chem. Solids*, 29:755–770, 1968.

[104] A. Abdullaev, A. Angelova, V. Kuznetsov, B. Ormont, and Yu. Pashintsev. Galvano- and Thermomagnetic Properties of Platinum Antimonide. *Phys Stat Sol*, 18:459–463, 1973.

[105] J. O'Shaughnessy and C. Smith. Absorption-Edge Structure in Platinum Antimonide. *Solid State Commun.*, 8:481–484, 1970.

[106] Pantelija Nikolic, Stevan Vujatovic, Dragan Todorovic, Milan Miletic, Aleksandar Golubovic, Aleksandar Bojici, Ferenc Kermendi, Stevan Duric, Katarina Radulovic, and Jovan Elazar. Thermal and Electronic Transport Properties of Single Crystal PtSb2 Obtained by the Photoacoustic Method. *Jpn. J. Appl. Phys.*, 36:1006–1011, 1997.

[107] Spencer L. Waldrop and Donald T. Morelli. Effect of non-stoichiometry on the thermal and electrical properties of polycrystalline PtSb2 at low temperature. *J. Alloys Compd.*, 701:23–26, apr 2017.

[108] A. Dargys and J. Kundrotas. Electrical properties of narrow gap semiconductor PtSb2. *J. Phys. Chem. Solids*, 44(3):261–267, 1983.

[109] R. A. Laudise, W. A. Sunder, R. L. Barns, G. W. Kammlott, A. F. Witf, and D. J. Carlson. Czochralski Crystal Growth in the System PtMnxSb2-x. *J. Cryst. Growth*, 102:21–30, 1990.

[110] M. C. Bennett, M. C. Aronson, D. A. Sokolov, C. Henderson, and Z. Fisk. Ferromagnetism, superconductivity and secondary phases in the dilute magnetic semiconductor Pt1-xRExSb2 (RE = La, Ce, Gd, Yb). *J. Alloys Compd.*, 400:2–10, 2005.

[111] B. T. Matthias. Transition temperatures of superconductors. *Phys. Rev.*, 92(4):874–876, 1953.

[112] Yoshihiro Nishikubo, Seiya Nakano, Kazutaka Kudo, and Minoru Nohara. Enhanced thermoelectric properties by Ir doping of PtSb2 with pyrite structure. *Appl. Phys. Lett.*, 100:1–4, 2012.

[113] Kouta Mori, Hidetomo Usui, Hirofumi Sakakibara, and Kazuhiko Kuroki. Corrugated flat band as an origin of large thermopower in hole doped PtSb2. *AIP Adv.*, 2, 2012.

[114] Y. Saeed, N. Singh, D. Parker, and U. Schwingenschlögl. Thermoelectric performance of electron and hole doped PtSb2. *J. Appl. Phys.*, 113, 2013.

[115] Spencer Waldrop and Donald Morelli. Low-Temperature Thermoelectric Properties of PtSb2-xTex for Cryogenic Peltier Cooling Applications. *J. Electron. Mater.*, 44(6):1562–1565, jun 2015.

[116] Kazutaka Kudo, Seiya Nakano, Tasuku Mizukami, Toshiro Takabatake, and Minoru Nohara. Enhancing high-temperature thermoelectric properties of PtAs2 by Rh doping. *Appl. Phys. Lett.*, 103:2012–2015, 2013.

[117] A. Bentien, S. Johnsen, G. K. H. Madsen, B. B. Iversen, and F. Steglich. Colossal Seebeck Coefficient in Strongly Correlated Semiconductor FeSb2. *Euro Phys. Lett.*, 80, 2007.

[118] N. Oeschler, P. Sun, F. Steglich, S. Johnsen, and B. B. Iversen. Enhanced Thermopower of the Narrow-Gap Semiconductor FeSb2. *ETC 2008 - line Proc.*, 2008.

[119] A. Bentien, G. K. H. Madsen, S. Johnsen, and B. B. Iversen. Experimental and theoretical investigations of strongly correlated FeSb2-xSnx. *Phys. Rev. B - Condens. Matter Mater. Phys.*, 74, 2006.

[120] C. Petrovic, Y. Lee, T. Vogt, N. Dj. Lazarov, S. L. Bud'ko, and P. C. Canfield. Kondo insulator description of spin state transition in FeSb2. *Phys. Rev. B - Condens. Matter Mater. Phys.*, 72(4):1–7, 2005.

[121] Z. Fisk, J. L. Sarrao, S. L. Cooper, P. Nyhus, G. S. Boebinger, A. Passner, and P. C. Canfield. Kondo insulators. *Phys. B Condens. Matter*, 223-224(1-4):409–412, 1996.

[122] Peter S. Riseborough. Heavy fermion semiconductors. *Adv. Phys.*, 49(3):257–320, 2000.

[123] G. D. Mahan. *Good Thermoelectrics*, volume 51. ACADEMIC PRESS, 1997.

[124] Gloria J. Lehr and Donald T. Morelli. Thermoelectric Properties of Yb1-x(Er, Lu)xAl3 Solid Solutions. *J. Electron. Mater.*, 42(7):1697–1701, 2013.

[125] H. J. Van Daal, P. B. Van Aken, and K. H. J. Buschow. The Seebeck Coefficient of YbAl2 and YbAl3. *Phys. Lett.*, 49A(3):246–248, 1974.

[126] T. Graft, J. M. Lawrence, M. F. Hundley, J. D. Thompson, A. Lacerda, E. Haanappel, M. S. Torikachvili, Z. Fisk, and P. C. Canfield. Resistivity, Magnetization, and Specific-Heat of YbAgCu4 in High Magnetic Fields. *Phys. Rev. B*, 51(21):53–61, 1995.

[127] R. Casanova, D. Jaccard, C. Marcenat, N. Hamdaoui, and M. J. Besnus. Thermoelectric power of YbMCu4 (M = Ag, Au and Pd) and YbPd2Si2. *J. Magn. Magn. Mater.*, 90-91:587–588, 1990.

[128] T. Ohyama, J. Skurai, and Y. Komura. Thermoelectric Power of Antiferromagnetic RIn3 Compounds. *Solid State Commun.*, 60(12):975–977, 1986.

[129] J. R. Thompson, S. T. Sekula, C. K. Loong, and C. Stassis. Electrical resistivity and magnetization of the intermediate valence compound CePd3. *J. Appl. Phys.*, 53(11):7893–7895, 1982.

[130] B. Stalinski, Z. Kletowski, and Z. Henkie. Electrical Resistivity of RESn3 Single Crystals (RE=La, Ce, Pr, and Nd). *Phys. Stat. Sol*, 19:165–168, 1973.

[131] Jeffrey S. Dyck, Wei Chen, Ctirad Uher, Lidong Chen, Xinfeng Tang, and Toshio Hirai. Thermoelectric properties of the n-type filled skutterudite Ba 0.3 Co 4 Sb 12 doped with Ni. *J. Appl. Phys. J. Appl. Phys. J. Appl. Phys*, 91(90):163503–1864, 2002.

[132] Shanyu Wang, Jiong Yang, Lihua Wu, Ping Wei, Wenqing Zhang, and Jihui Yang. On Intensifying Carrier Impurity Scattering to Enhance Thermoelectric Performance in Cr-Doped CeyCo4Sb12. *Adv. Funct. Mater.*, 25(42):6660–6670, 2015.

[133] A. F. Ioffe. *Semiconductor Thermoelements and Thermoelectric Cooling*. Infosearch Limited, London, UK, 1957.

[134] Tiejun Zhu, Yintu Liu, Chenguang Fu, Joseph P. Heremans, Jeffrey G. Snyder, and Xinbing Zhao. Compromise and Synergy in High-Efficiency Thermoelectric Materials. *Adv. Mater.*, page 1605884, 2017.

[135] P. G. Klemens. The Scattering of Low-Frequency Lattice Waves by Static Imperfections. *Proc. Phys. Soc. Sect. A*, 68(12):1113–1128, 1955.

[136] J. Callaway and H. von Baeyer. Effect of Point Imperfections on Lattice Thermal Conductivity. *Phys. Rev.*, 120(4):1149–1154, 1960.

[137] B. Abeles. Lattice Thermal Conductivity of Disordered Semiconductor Alloys at High Temperatures. *Phys. Rev.*, 131(5):1906–1911, 1963.

[138] G. Meisner, D. Morelli, S. Hu, J. Yang, and C. Uher. Structure and Lattice Thermal Conductivity of Fractionally Filled Skutterudites: Solid Solutions of Fully Filled and Unfilled End Members. *Phys. Rev. Lett.*, 80(16):3551–3554, 1998.

[139] Bed Poudel, Qing Hao, Yi Ma, Yucheng Lan, Austin Minnich, Bo Yu, Xiao Yan, Dezhi Wang, Andrew Muto, Daryoosh Vashaee, Xiaoyuan Chen, Junming Liu, Mildred S. Dresselhaus, Gang Chen, and Zhifeng Ren. High-thermoelectric performance of nanostructured bismuth antimony telluride bulk alloys. *Science*, 320(5876):634–8, 2008.

[140] Shuo Chen and Zhifeng Ren. Recent progress of half-Heusler for moderate temperature thermoelectric applications. *Mater. Today*, 16(10):387–395, 2013.

[141] Wenjie Xie, Anke Weidenkaff, Xinfeng Tang, Qingjie Zhang, Joseph Poon, and Terry Tritt. Recent advances in nanostructured thermoelectric Half-Heusler compounds. *Nanomaterials*, 2(4):379–412, 2012.

[142] Tiejun Zhu, Chenguang Fu, Hanhui Xie, Yintu Liu, and Xinbing Zhao. High Efficiency Half-Heusler Thermoelectric Materials for Energy Harvesting. *Adv. Energy Mater.*, 5(19):1–13, 2015.

[143] H. Okamoto. Pd-Sb (Palladium-Antimony). *J. Phase Equilibria*, 13(5):578–579, 1992.

[144] Kouta Mori, Hidetomo Usui, Hirofumi Sakakibara, and Kazuhiko Kuroki. Theoretical expectation of large seebeck effect in PtAs2 and PtP2. *J. Phys. Soc. Japan*, 83:1–4, 2014.

[145] L. J. Cabri and D. C. Harris. The New Mineral Insizwaite (PtBi2) and New Data on Niggliite (PtSn). *Mineral. Mag.*, 38:794–800, 1972.

[146] H. Okamoto. The Bi-Pt (Bismuth-Platinum) System. *J. Phase Equilibria*, 12(2):207–210, 1991.

[147] N. N. Zhuravlev, T. A. Mingazin, and G. S. Zhdanov. Structure of Superconductors : Xi Investigation of Alloys of Bismuth with Platinum, Ruthenium, Osmium and Iridium. *Sov. Phys. JETP*, 5(6):566–571, 1957.

[148] Richard Weihrich, Daniel Kurowski, Andrea C. Stückl, Samir F. Matar, Franz Rau, and Thomas Bernert. On the ordering in new low gap semiconductors: PtSnS, PtSnSe, PtSnTe. Experimental and DFT studies. *J. Solid State Chem.*, 177:2591–2599, 2004.

[149] Frederik Bachhuber, Alexander Krach, Andrea Furtner, Tilo Söhnel, Philipp Peter, Jan Rothballer, and Richard Weihrich. Phase stabilities of pyrite-related MTCh compounds (M=Ni, Pd, Pt; T=Si, Ge, Sn, Pb; Ch=S, Se, Te): A systematic DFT study. *J. Solid State Chem.*, 226:29–35, 2015.

[150] F. Hulliger. Crystal chemistry of the chalcogenides and pnictides of the transition elements. *Struct. Bond.*, pages 83–229, 1968.

[151] H. Okamoto. Ni-Sb (Nickel-Antimony). *J. Phase Equilibria Diffus.*, 30(3):301–302, 2009.